Studies of Background Reduction via angular-selective Electron Detection in the KATRIN Experiment

Inauguraldissertation
zur Erlangung des Doktorgrades (Dr. rer. nat.)
der Naturwissenschaften im Fachbereich Physik
der Mathematisch-Naturwissenschaftlichen Fakultät
der Universität Münster

vorgelegt von
Kevin Gauda
aus Ahaus-Ottenstein
– 2024 –

Erster Gutachter: Prof. Dr. C. Weinheimer
Zweiter Gutachter: Prof. Dr. C. Klein-Bösing

Dekan:	Prof. Dr. Rudolf Bratschitsch
Erster Gutachter:	Prof. Christian Weinheimer
Zweiter Gutachter:	Apl. Prof. Dr. Christian Klein-Bösing
Tag der mündlichen Prüfung:	15.07.2024
Tag der Promotion:	15.07.2024

"Let's think the unthinkable, let's do the undoable.
Let us prepare to grapple with the ineffable itself,
and see if we may not eff it after all."

Douglas Adams, Dirk Gently's Holistic Detective Agency.

Abstract

The phenomenon of neutrino oscillations predicts massive neutrinos, whose exact mass remains unknown in particle physics. A model-independent method for a more precise determination is applied in the kinematic measurement of the end-point energy of tritium decay: The Karlsruhe Tritium Neutrino Experiment (KATRIN) performs high-precision endpoint spectroscopy of the tritium β-spectrum and has been able to constrain the neutrino mass to $m_\nu < 0.8\,\mathrm{eV/c^2}$ (90% C.L.) since its beginnings. The electrons in KATRIN are guided adiabatically from the tritium source from a $\sim 2.5\,\mathrm{T}$ magnetic field to the focal plane detector (FPD) in a similarly strong magnetic field. In between, an approximately $0.6\,\mathrm{mT}$ magnetic field, combined with a gradually changing electrical retardation potential, forms the spectrometer. Electrons with sufficient energy can overcome the retardation potential and are accelerated to the FPD.

Low-energy electrons in the spectrometer volume from decays of Rydberg and autoionizing atoms, which enter the spectrometer volume due to radioactive contamination, can also be accelerated from there to the FPD. The energy of the background, therefore, does not differ from the energy of the tritium β-decay electrons within the energy resolution of the FPD. However, the background has a significantly lower transverse energy and, thus, a cyclotron motion with smaller pitch angles compared to most β-decay electrons.

This work focuses on the development of a modified detector with strongly angle-selective electron detection efficiency to replace or complement the original FPD. This principle is called "active Transverse Energy Filter" (aTEF). The aTEF is intended to suppress electrons with a low pitch angle and preferentially measure electrons with a large pitch angle.

In this work, commercial microchannel plates (MCPs) were used as aTEF detectors in a laboratory experiment in Münster. After the differentiation of electrons based on their pitch angle was successful, the development of an aTEF based on Si-PIN diodes (Si-aTEF) was pursued. Hexagonal channels were introduced into the surface of commercial Si-PIN detectors to a certain depth. Up to this depth, a large part ($\sim 90\%$) of the detector material was removed via deep silicon etching. The remaining surfaces, which were inserted vertically into the surface, were intended to primarily detect electrons with large pitch angles. Electrons with low pitch angles should be stopped in the inactive bottom of the channels.

The angular selectivity of the electron detection was measured using a specially designed setup. A photoelectron source with electrons with energies of a similar order of magnitude as in KATRIN was used. The electrons were magnetically guided onto the Si-PIN detector or Si-aTEF prototype at a variable angle. Angular selectivity was measured in two of the prototypes presented, representing a milestone in the development of the Si-aTEF. By cooling, a reduction of the reverse current and the intrinsic background as well as an improvement of the charge collection efficiency of the Si-aTEF prototypes could be achieved. The detector perfomance was limited due to nanofabrication issues, which will be resolved in the future.

The experimentally found angular-selectivity was supported by semiconductor simulations that predicted the potential curve and the propagation of the depletion zone in microstructured Si-aTEF prototypes. An important difference between the commercial diodes of the Si-aTEF prototypes and the FPD used in KATRIN is their reversed doping order. The simulations suggest that the bottoms of the channels in an aTEF with FPD-like doping order should be active, which requires further investigation and, possibly, an additional blocking layer.

Zusammenfassung

Das Phänomen der Neutrinooszillationen sagt massive Neutrinos voraus, deren genaue Masse bis heute eine Unbekannte in der Teilchenphysik ist. Eine modellunabhängige Methode zur genaueren Bestimmung wird in einer kinematischen Messung der Endpunktenergie des Tritiumzerfalls angewandt: Das Karlsruhe Tritium Neutrino Experiment (KATRIN) führt hochpräzise Endpunktspektroskopie des Tritium-β-Spektrums durch und konnte die Neutrinomasse bislang auf $m_\nu < 0.8\,\mathrm{eV/c^2}$ (90% C.L.) eingrenzen. Die Elektronen in KATRIN werden adiabatisch von der Tritiumquelle aus einem 2.5 T-Magnetfeld kommend zum Fokalebenendetektor (FPD) in ähnlich starkem Magnetfeld geführt. Dazwischen bildet ein $\sim 0.6\,\mathrm{mT}$-Magnetfeld in Kombination mit einem stufenweise veränderten elektrischen Retardierungspotential das Spektrometer. Elektronen mit ausreichend Energie können das Retardierungspotential überwinden und werden zum FPD beschleunigt.

Niederenergetische Elektronen im Spektrometervolumen aus Zerfällen von Rydberg- und autoionisierenden Atomen, die durch radioaktive Kontamination in das Spektrometervolumen gelangen, können von dort ebenso zum FPD beschleunigt werden. Die Energie des Untergrunds unterscheidet sich daher im Rahmen der Energieauflösung des FPD nicht von der Energie der β-Elektronen am Endpunkt des Spektrums. Die Untergrundelektronen besitzen aber eine signifikant geringere Transversalenergie und daher eine Zyklotronbewegung mit kleineren Neigungswinkeln im Vergleich zu den meisten β-Elektronen.

Diese Arbeit konzentrierte sich auf die Entwicklung eines modifizierten Detektors mit stark winkelselektiver Elektronendetektionseffizienz, der den ursprünglichen FPD ersetzen oder ergänzen soll. Dieses Prinzip wird "active Transverse Energy Filter" (aTEF) genannt. Mit dem aTEF sollen Elektronen geringen Neigungswinkels unterdrückt und Elektronen großen Neigungswinkels bevorzugt gemessen werden.

In dieser Arbeit wurden kommerzielle Mikrokanalplatten (MCPs) in einem Laborexperiment in Münster als aTEF-Detektoren verwendet. Nachdem die Unterscheidung von Elektronen anhand ihres Neigungswinkels gelang, wurde vor allem die Entwicklung eines aTEF basierend auf Si-PIN-Dioden (Si-aTEF) verfolgt. Hexagonale Kanäle wurden in die Oberfläche kommerzieller Si-PIN-Detektoren bis zu einer bestimmten Tiefe eingebracht. Bis zu dieser Tiefe wurde via tiefem Siliziumätzen ein Großteil ($\sim 90\%$) des Detektormaterials entfernt. Die verbleibenden, vertikal zur Oberfläche eingebrachten Oberflächen sollten vor allem Elektronen großer Neigungswinkel detektieren. Elektronen mit geringen Neigungswinkeln sollten im inaktiven Boden der Kanäle gestoppt werden.

Die Winkelselektivität der Elektronendetektion konnte mithilfe eines eigens konzipierten Aufbaus vermessen werden. Dabei wurde eine Photoelektronenquelle mit Elektronen mit Energien in ähnlicher Größenordnung wie bei KATRIN verwendet, die unter variablem Winkel magnetisch auf den Si-PIN-Detektor oder Si-aTEF-Prototypen geleitet wurden. Bei zwei der vorgestellten Prototypen konnte eine Winkelselektivität gemessen werden, welches einen Meilenstein der Si-aTEF-Entwicklung darstellte. Kühlung führte zu einer Reduktion des Sperrstroms und des intrinischen Untergrunds sowie zu einer Verbesserung der Ladungssammeleffizienz der Si-aTEF-Prototypen. Die Performance der Detektoren war durch Probleme in der Nanofabrikation limitiert, die in Zukunft behoben sein werden.

Die gefundene Winkelabhängigkeit wurde durch Halbleiter-Simulationen unterstützt, die den Potentialverlauf und die Ausbreitung der Verarmungszone in mikrostrukturierten Si-aTEF-Prototypen voraussagten. Ein gewichtiger Unterschied zwischen den kommerziellen Dioden der Si-aTEF-Prototypen und dem in KATRIN verwendeten FPD war die umgekehrte Dotierungs-Reihenfolge. Die Simulationen ließen darauf schließen, dass die Böden der Kanäle in einem aTEF mit FPD-Dotierungsreihenfolge aktiv sind, was weiterer Untersuchungen und womöglich einer blockierenden Beschichtung bedarf.

Erratum

The ideas of the transverse energy filter and their further refined active and passive variants were described within this work. The original transverse energy filter (TEF) was envisioned by R.G.H. Robertson, the active transverse energy filter (aTEF) by C. Weinheimer and the passive transverse energy filter (pTEF) by K. Gauda. The variants were not (aTEF, pTEF) or not noticeably (TEF) associated with these names within this work. To credit their respective inventor, the names of the initiators of the three variants were added to chapters 3 and 4 of this work. Further, S. Schneidewind had a co-leading role within the aTEF project. A mark was added in chapter 6 to state that she steered the design of setup II, which was used in this and in her work for characterization of aTEF-prototypes. Lastly, corrections of minor mistakes and typographical errors were added to this version. These do not affect any of the results or their implications found within this work.

Contents

1 Introduction

After the postulation of neutrinos by W. Pauli in his famous letter dedicated to the radioactive gentlemen and -women [1], the vital field of neutrino physics evolved as essential cornerstone of particle physics. The neutrino was able to solve the problem that arose in β-decay from the continuous electron energy spectrum – which was incompatible with energy conservation in a two-body decay. Already in 1934, Fermi's theoretical description of the β-spectrum predicted a shape distortion of the eletron spectrum's endpoint region depending on the neutrino mass [2], see figure 1.1. The first direct evidence of neutrinos was obtained in 1956 [3] in the famous Poltergeist experiment by Cowan and Reines, of whom the latter was awarded the Noble prize for the detection [4].

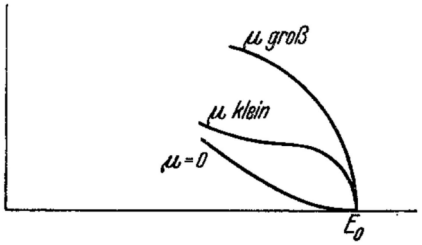

Fig. 1.

Figure 1.1 – Published in 1934 by E. Fermi [2], the sketch shows the influence of the neutrino mass (here: μ) on the endpoint shape of the β-decay electron energy spectrum.

The Standard Model of particle physics predicts that neutrinos are massless particles. There is, however, undeniable evidence of flavor oscillations that alter the occurrence of flavors with travel distance and energy. These oscillations are generally explained by massive neutrinos. While the differences in squared neutrino masses are measured by oscillation experiments and known to be non-zero, the exact mass of these eigenstates could not yet be determined.

The KATRIN experiment aims to determine the neutrino mass with unprecedented precision from kinematics of the β-decay of tritium. It utilizes the sophisticated operation of electric and magnetic fields in a so-called MAC-filter (see section 3.1.2) to allow high-precision spectroscopy of the spectral endpoint. The most recent result was found to be an upper limit on the effective neutrino mass, $m_\nu < 0.8\,\mathrm{eV/c^2}$ (90% C.L.), which is the world's first sub-eV measurement from a direct neutrino-mass experiment [5]. The final sensitivity after 1000 days of β-decay measurements is planned to be $0.2\,\mathrm{eV/c^2}$ [6]. That aim, however, is threatened by background components that did not occur as major background during its predecessor experiments: Radioactive decays in the hull of the main

spectrometer allow highly-excited, uncharged atoms to enter the spectrometer, where they release low-energetic electrons. When they reach the detector, they are not differentiable from β-electrons in energy. Their specific generation mechanism, however, induces a sharp angular distribution at the detector. Filtering electrons based on their so-called pitch angle to the magnetic field line is the strategy pursued via so-called Transverse Energy Filters (TEF) in order to reduce this background. Passive TEF-variants can efficiently reduce the background, but they will inevitably reduce the signal amplitude as well and, thereby, harm the neutrino mass sensitivity. Nevertheless, the TEF-concept initiated further development processes: This work will set forth the active Transverse Energy Filter (aTEF)-concept as a decisive progression to reduce the background while maintaining most of the signal. After an introduction to neutrino physics in chapter 2 and an overview of the KATRIN-experiment in chapter 3, a first experimental implementation of the aTEF-concept is achieved by commercial microchannel plate detectors, which is laid out in chapter 4. Further, a modification of the planar Si-PIN diode that serves as KATRIN's focal plane detector is introduced as silicon-based aTEF (Si-aTEF). The Si-aTEF-prototype fabrication based on commercial Si-PIN diodes is explicated in chapter 5. Chapter 6 is dedicated to the principal understanding and the characterization of the prototypes and concludes this work.

2 Introduction to Neutrino Physics

Neutrinos are of elusive nature and great expense needs to be and already has been taken to experimentally assess their properties. They are described in the Standard Model of particle physics as massless leptons without electric charge that exclusively undergo neutral (NC) or charged current (CC) weak interactions. As fermions, they carry spin 1/2. The neutrino family consists of neutrinos of three possible (active) lepton flavors e, μ, τ and their respective antineutrino counterparts. Contrary to the Standard Model assumption, they violate lepton flavour as they propagate. This phenomenon is known as neutrino oscillation and described by the Pontecorvo-Maki-Nakagawa-Sakata (PMNS) matrix[1]. The neutrino oscillation phenomenon implies the existence of non-zero neutrino masses. The value of their mass, the neutrino-mass production mechanism as extension of the Standard Model, whether they appear as Dirac- or Majorana-type particles, and the ordering of the neutrino mass eigenstates belong to the key puzzles of neutrino physics and, in general, particle physics. The following chapter presents details of these topics and motivates the importance of enlightening the neutrino properties – which KATRIN attempts for its mass. The KATRIN experiment aims to directly detect the neutrino mass. Thus, the focus of this introductory chapter will be laid on the mass, its generation mechanisms, and the carried out and planned experimental possibilities to measure it. Other unresolved mysteries of the neutrino are not considered here, e.g. its magnetic moment, the existence of sterile neutrinos, or their astrophysical role as dark matter candidate and relic neutrino background.

2.1 Neutrino Oscillations

There is overwhelming evidence from many decades of experiments that neutrino flavours undergo mass-induced oscillation. These experiments are carried out over a variety of neutrino sources. The first evidence for solar neutrino oscillation was found in the Homestake Solar Neutrino Detector from the late 1960s on [9], for which R. Davis was awarded the Nobel prize in 2002, together with M. Koshiba and R. Giaconni [10].The measured neutrino flux in the Homestake experiment was only approximately 30% of the expected rate, which became known as the *solar neutrino problem*. Thirty years later, the Super-Kamiokande experiment was able to resolve the problem by detection of atmospheric electron neutrinos ν_e and, in addition, muon neutrinos ν_μ [11]. The total solar neutrino

[1]The PMNS is based on a two-neutrino particle mixture theory by Z. Maki, M. Nakagawa, S. Sakata [7], extended and applied to neutrino oscillations, which were predicted by B. Pontecorvo in 1957 [8].

flux including tau neutrinos ν_τ was measured by the Sudbury Neutrino Observatory (SNO), further validating the oscillation of neutrino flavours [12]. The Nobel prize of 2015 was awarded to Takaaki Kajita and Arthur B. McDonald for their contributions to these experiments and their work on the discovery of neutrino oscillations [13].

The mixing angles, amplitudes and mass splittings were subsequently quantified more and more precisely with neutrinos from different sources: Atmospheric neutrino oscillations were measured, e.g., by Super-Kamiokande [14] and IceCube/DeepCore [15]. Solar neutrino oscillation parameters were deducted, e.g., from results of the radiochemical experiment Gallex/GNO [16] and from SNO [17], Super-Kamiokande [18], and Borexino [19]. Reactor and accelerator neutrinos can be detected at different baselines and are generally differentiated in long-baseline (LBL), medium-baseline (MBL) and short-baseline (SBL) experiments[2]. Results from LBL accelerator experiments come, e.g., from NOvA (810 km) [20] and T2K (295 km) [21]. Reactor experiments measure the $\bar{\nu}_e$ from nuclear fission processes. Among them are the SBL experiments Daya Bay (1.65 km) [22], RENO (1.38 km) [23], and Double Chooz (1.05 km) [24]. The different neutrino sources allow access to the various parameters that describe neutrino oscillation, which are introduced below in eq. (2.1.2): Solar neutrino experiments, for example, are most sensitive to the mixing angle θ_{12}, while reactor MBL experiments dominate the accuracy of θ_{13}. The CP-violating phase δ_{CP} is best observed in LBL accelerator experiments [25]. By now, the neutrino mixing parameters are precisley known. Results of a global fit of the oscillation parameters by the NuFIT collaboration are listed in table 2.1, as published in [25].

Table 2.1 – Neutrino mass splittings and mixing angles, according to the global neutrino parameter fit framework NuFIT, which uses the Standard Model with a minimal extension with three massive neutrinos as its framework [25]. The CP-violating phase δ_{CP} was not directly measured yet, but deducted from the global fit. Values for normal (NO) and inverted (IO) mass ordering are shown. The mass ordering is explained in figure 2.1. Note, that $\Delta m^2_{3\ell} \equiv \Delta m^2_{31} > 0$ for NO and $\Delta m^2_{3\ell} \equiv \Delta m^2_{32} < 0$ for IO.

Parameter	**Value (NO)**	**Value (IO)**
$\sin^2\theta_{12}$	$0.304^{+0.013}_{-0.012}$	$0.304^{+0.012}_{-0.012}$
$\sin^2\theta_{23}$	$0.573^{+0.018}_{-0.023}$	$0.578^{+0.017}_{-0.021}$
$\sin^2\theta_{13}$	$0.02220^{+0.00068}_{-0.00062}$	$0.02238^{+0.00064}_{-0.00062}$
$\delta_{\mathrm{CP}}/^\circ$	194^{+52}_{-25}	287^{+27}_{-32}
$\Delta m^2_{21}/(10^{-5}\,\mathrm{eV}^2)$	$7.42^{+0.21}_{-0.20}$	$7.42^{+0.21}_{-0.20}$
$\Delta m^2_{3\ell}/(10^{-}\,\mathrm{eV}^2)$	$2.515^{+0.028}_{-0.028}$	$-2.498^{+0.028}_{-0.029}$

All of these and many other experiments show that the lepton flavour $\alpha = e, \mu, \tau$ is not conserved when neutrinos propagate. Consequently, neutrinos must have non-zero masses

[2]The decisive quantity here is the baseline divided by the energy L/E, since the sensitivity to the squared difference of two neutrino mass eigenstates $|\Delta m^2_{ij}|$ is determined by that, if L corresponds to the oscillation length $L = L^{\mathrm{osc}}_{0,ij}$ (see equation 2.1.5)

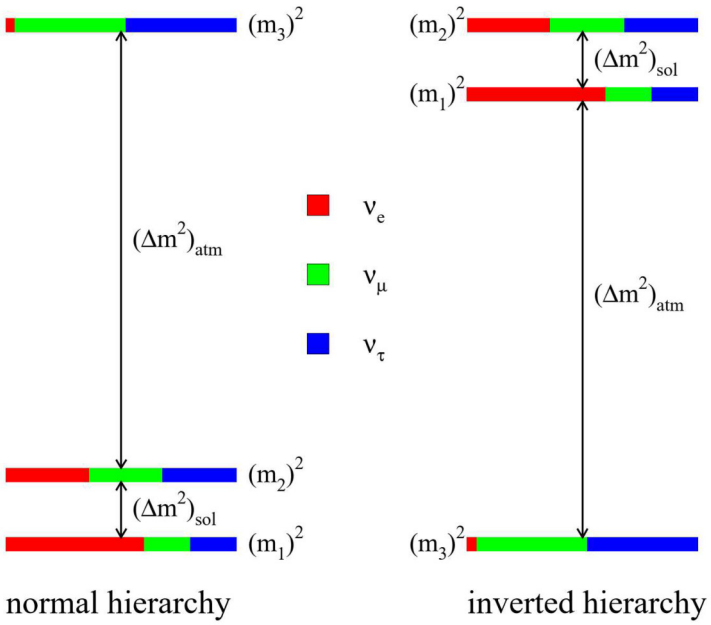

Figure 2.1 – Scenarios for different neutrino mass hierarchies: Either m_1 or m_3 is the lightest neutrino mass. Their ordering cannot be determined from oscillation experiments alone. The appearance probability of the different flavours e, μ, τ in the mass eigenstates $1, 2, 3$ is indicated by the colour-coding. Figure taken from [26].

and lepton flavors in weak charged current interactions are mixed states. The number of different (active) neutrinos is $N_\nu = 2.9840 \pm 0.0082$, as known from the width of the Z-resonance [27] and, fittingly, all oscillation phenomena can be explained by three-neutrino mixing, which is described by the PMNS-matrix U. The weak eigenstate, as it is produced in a weak charged current interaction of a charged lepton ℓ_α, is a linear combination of the mass eigenstates ν_i,

$$|\nu_\alpha\rangle = \sum_{i=1}^{n} U_{\alpha i}^{*} |\nu_i\rangle. \tag{2.1.1}$$

The matrix element $U_{\alpha i}$ is the amplitude of the mass eigenstate i at a given lepton flavor α. The mixing matrix is typically parameterized by three mixing angles $\theta_{12}, \theta_{23}, \theta_{13}$, and a CP-violating phase δ_{CP}:

$$U = \begin{pmatrix} 1 & 0 & 0 \\ 0 & c_{23} & s_{23} \\ 0 & -s_{23} & c_{23} \end{pmatrix} \begin{pmatrix} c_{13} & 0 & s_{13} e^{-i\delta_{\mathrm{CP}}} \\ 0 & 1 & 0 \\ -s_{13} e^{i\delta_{\mathrm{CP}}} & 0 & c_{13} \end{pmatrix} \begin{pmatrix} c_{12} & s_{12} & 0 \\ -s_{12} & c_{12} & 0 \\ 0 & 0 & 1 \end{pmatrix} \tag{2.1.2}$$

with $c_{ij} = \cos\theta_{ij}$ and $s_{ij} = \sin\theta_{ij}$ In case of Majorana-type neutrinos, two additional Majorana phases that do not directly affect neutrino oscillations need to be considered by multiplying $\mathrm{diag}(e^{i\alpha_1}, e^{i\alpha_2}, 1)$ to the mixing matrix [28]. The state $|\nu_\alpha\rangle$ propagates with time t, so that after distance $L \approx ct$ (for relativistic neutrinos) the eigenstate is described

by

$$|\nu_\alpha(t)\rangle = \sum_{i=1}^{n} U^*_{\alpha i}|\nu_i(t)\rangle. \tag{2.1.3}$$

That $\nu_\alpha(t)$ produces a lepton ℓ_β in a charged current interaction via $\nu_\alpha(t)N' \to \ell_\beta N$ has a probability

$$P_{\alpha\beta} = |\langle\nu_\beta|\nu_\alpha(t)\rangle|^2 = \left|\sum_{i=1}^{n}\sum_{j=1}^{n} U^*_{\alpha i}U_{\beta j}\langle\nu_j|\nu_i(t)\rangle\right|^2. \tag{2.1.4}$$

The oscillation length

$$L^{\text{osc}}_{0,ij} = \frac{4\pi E}{|\Delta m^2_{ij}|} \tag{2.1.5}$$

is found from the assumption of $|\nu\rangle$ being a plane wave and neutrinos with energy E being relativistic. Neutrinos must have masses, since their evidently oscillatory nature

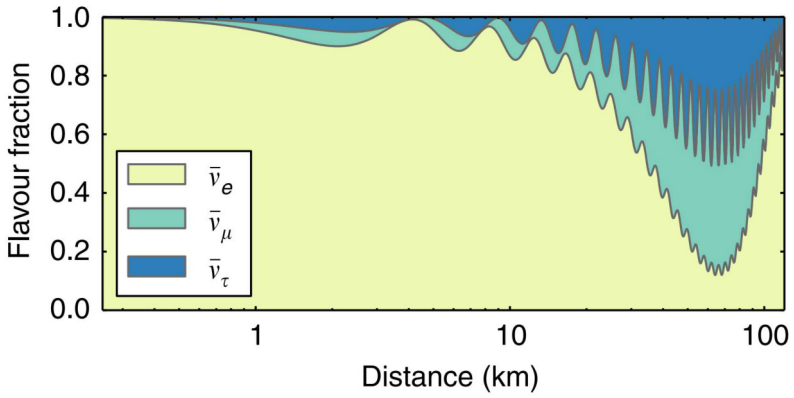

Figure 2.2 – Oscillation of (anti-)neutrino flavours with propagation distance [29]. Neutrinos have 4 MeV energy in this example.

requires $|\Delta m^2_{ij}| \neq 0$. Further, the amount of mixing is non-vanishing, i.e., $U_{\alpha i}U_{\beta i} \neq 0$. Since the (potentially existent) lepton-number violating Majorana phases cancel out in the calculation of the probability, the flavour oscillation conserves the total lepton number. The composition of flavour eigenstates in an exemplary neutrino beam of 4 MeV electron antineutrinos changes as shown in figure 2.2. Dedicated neutrino oscillation experiments – especially on short baselines – are seldom provided with monoenergetic neutrino beams. Thus, the measured oscillation amplitude at a certain length depends on the given neutrino energy spectrum.

Oscillation experiments are not able to determine the sign of the mass splitting $\Delta m^2_{ij} = m^2_i - m^2_j$ and, thus, rely on other phenomena to measure the neutrino mass ordering. Matter effects in the sun allow the fixing of Δm^2_{21} to be positive[3].

[3] More accurately, but depending on convention, the matter effects in the sun constrain $\Delta m^2_{21}\cos 2\theta_{12} > 0$.

2.2 Neutrino Mass

Details on the neutrino mass generation mechanism and the various kinds of measurement approaches of the neutrino mass are presented in the following sections.

With the evidence of their mass – and the disagreement with the Standard Model – an extension is needed to correctly incorporate the mass generation mechanism. One of the big challenges is their unknown nature as Dirac- or Majorana-particles: If neutrinos are of Majorana-nature and, therefore, their own antiparticles, the mathematical description is different than for Dirac-neutrinos. Section 2.2.1 examines these issues.

Neutrino mass searches are, i.a., carried out within cosmological observations. They give the – by date – most stringent limits on the sum of neutrino masses, but they rely on the accuracy and correctness of the underlying models and assumptions. Section 2.2.2 addresses the observations and challenges.

A second method to get precise insights on the neutrino mass and their nature arises from the spectroscopy of double-β decaying isotopes, e.g. ^{76}Ge or ^{136}Xe. If neutrinos are Majorana particles (see section 2.2.1), there is the chance that the emitted neutrino from one nucleon is directly absorbed by another nucleon. That process is called neutrinoless double-β decay and induces the consequence of two-electron-emission with the Q-value of the decay $Q_{\beta\beta}$. That would result in a sharp peak at $Q_{\beta\beta}$ in the spectrum. This decay channel is only possible in case of Majorana-neutrinos, but their nature is not clear, yet. The neutrinoless double-β decay is explained in more detail in section 2.2.3.

A third measurement principle – mopel-independent, in contrast – is the precision spectroscopy of β-decay or electron capture, as discussed in section 2.2.4. The kinematics of the β-decay have to be as simple as possible, i.e. the intial state and final state distributions have to be very sharp and well known, which is the case for tritium (T or T_2), holmium (^{163}Ho), and rhenium (^{187}Re), which are utilized for experiments. The neutrino mass has a distinct effect on the position and shape of the electrons' energy spectrum.

The effective neutrino mass can be related to the lightest neutrino mass, as shown in figure 2.3 for tritium β-decay and $0\nu\beta\beta$-decay. In case of inverted ordering, the lightest neutrino mass will have a minimum value of $m_{\nu_e}^{eff} \approx 50\,\mathrm{meV}$ [28].

2.2.1 Neutrino Masses and the Standard Model

The Standard Model of particle physics is able to describe the strong, weak, and electromagnetic interactions between all known elementary particles. Its particle content consists of three fermion generations (quarks and leptons, see table 2.2), gauge bosons that mediate particle interactions via electromagnetic, strong, or weak force, and the scalar Higgs boson. Different symmetry groups form the Standard model: The combination of the unitary group $U(1)_{\mathrm{Y}}$ and the special special unitary group $SU(2)_{\mathrm{Left}}$ defines the electroweak theory as a combination of quantum electrodynamics and weak interaction in the electroweak theory. $SU(3)_{\mathrm{Color}}$ is the symmetry group of the quantum field theory that describes strong interactions. The Standard Model is expressed in the $SU(3)_{\mathrm{Color}} \times SU(2)_{\mathrm{Left}} \times U(1)_{\mathrm{Y}}$ gauge

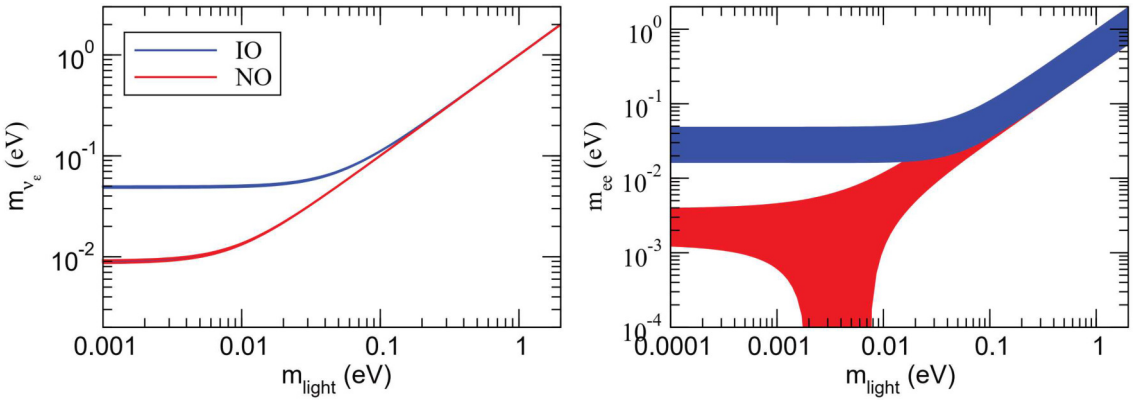

Figure 2.3 – The allowed 95% C.L.-ranges of the neutrino mass observables of tritium β-decay (left) and $0\nu\beta\beta$-decay (right) are shown for the 3ν case depending on the lightest neutrino mass [28, 30].

Table 2.2 – Standard model fermions and anti-fermions consist of the quarks and leptons in this table. The quarks form eigenstates of the strong interaction instead of weak isospin doublets. These can transform into another flavor via weak interaction. There is a strong tendency to transform into a quark of the same generation, with the transition probability being described by the CKM matrix. Charged leptons and neutrinos form weak isospin doublets, where their flavor $\ell = e, \mu, \tau$ defines their generation I, II, or III. Similar to quarks, neutrino flavors can transform with probabilities described by the PMNS matrix, see eq. (2.1.2).

	I		**II**		**III**	
quarks	u d′	ū d̄′	c s′	c̄ s̄′	t b′	t̄ b̄′
leptons	e ν_e	$\bar{e}$ $\bar{\nu}_e$	μ ν_μ	$\bar{\mu}$ $\bar{\nu}_\mu$	τ τ	$\bar{\tau}$ $\bar{\nu}_\tau$

symmetry, which is spontaneously broken by the Higgs mechanism to $SU(3)_{\text{Color}} \times U(1)_{\text{EM}}$, where the unitary group $U(1)_{\text{EM}}$ couples to the electromagnetic charge Q_{EM}.

Standard Model leptons are grouped into doublets with one neutrino for each charged lepton $\ell = e, \mu, \tau$. The Yukawa term of the Lagrangian is

$$\mathcal{L}_{\text{Yuk}} = -f_e \bar{l}_L \Phi e_R - f_u \bar{q}_L \tilde{\Phi} u_R - f_d \bar{q}_L \Phi d_R + h.c. \tag{2.2.1}$$

for the first fermion generation. The left-handed fermions are arranged as doublets

$$l_L = \begin{pmatrix} u \\ d \end{pmatrix}_L, \quad \begin{pmatrix} \nu_e \\ e \end{pmatrix}_L \tag{2.2.2}$$

and the right-handed fermions as singlets e_R, u_R, d_R. The fermion mass after spontaneous electroweak symmetry breaking is denoted as

$$m_i = \frac{f_i v}{\sqrt{2}} \tag{2.2.3}$$

with the Yukawa coupling f_i, $i = e, \mu, \nu$ and the Higgs vacuum expectation value v.

The Standard Model generates masses of gauge bosons and fermions differently, but its formalism prevents to assign masses to neutrinos: Gauge boson masses are produced by the Higgs mechanism. Fermion masses are exclusively generated by Yukawa-type interactions with the Higgs field. The Standard Model assigns left-handed fermions to the $SU(2)_{\text{Left}}$ doublets and right-handed fermions to the $SU(2)_{\text{Left}}$ singlets. The scalar Higgs doublet Φ couples to a right-handed singlet and a left-handed doublet, e.g. to the left-handed lepton doublets L_L and the right-handed charged lepton fields E_R. That generates the charged lepton masses after spontenaous symmetry breaking. While right-handed charged leptons are included, the Standard Model does not contain right-handed neutrinos. That prevents such a Yukawa interaction to be generated for neutrinos, leaving them massless at the level of the Lagrangian formulation.

Two possible gauge invariant and renormalizable operators lead to the Dirac mass term and the Majorana mass term in the Lagrangian formulation. The Dirac mass term

$$\mathcal{L}_\nu = -m_D(\bar{\nu}_L \nu_R + \bar{\nu}_R \nu_L) \tag{2.2.4}$$

conserves the total lepton number, but may violate lepton flavour number symmetries. The introduction of right-handed neutrinos via an additional Dirac mass term is possible, but not favored, since the Yukawa coupling f_ν for neutrinos would have to be much smaller than $f_e \approx f_u \approx f_d$ due to the small neutrino mass [31].

Alternatively, the neutrino masses can be generated via a Majorana mass term, which implies that neutrinos and antineutrinos are identical. The Majorana mass term is a singlet of the Standard Model gauge group and can appear as a bare mass term in the Lagrangian formulation:

$$\begin{aligned} \mathcal{L}_\nu &= -\frac{1}{2}\left(m_D(\bar{\nu}_L \nu_R + \bar{\nu}_R^c \nu_L^c) + m_M^L(\bar{\nu}_L \nu_L^c) + m_M^R(\bar{\nu}_R^c \nu_R)\right) + h.c. \\ &= -\frac{1}{2}\begin{pmatrix}\bar{\nu}_L & \bar{\nu}_R^c\end{pmatrix} \boldsymbol{M} \begin{pmatrix}\nu_L^c \\ \nu_R\end{pmatrix} + h.c. \end{aligned} \tag{2.2.5}$$

with the complex and symmetric mass matrix

$$\boldsymbol{M} = \begin{pmatrix} m_M^L & m_D^T \\ m_D & m_M^R \end{pmatrix}. \tag{2.2.6}$$

The Majorana mass term involves two right-handed neutrino fields and breaks the lepton number by 2. The neutrino states and antineutrino states are described by one field. While the charged fermions are described by four-component spinors, a Majorana neutrino can be described by a two-component spinor.

If $m_M^L = 0$ and $m_M^R = 0$, the neutrino mass is exclusively generated by the Dirac mass term and the eigenvalues of $\boldsymbol{M}$ are $m = m_D$. These would not explain why the charged leptons are much heavier than the corresponding neutrinos, since they all acquire their

mass via the same mechanism. In case of Majorana neutrinos, however, the mass terms read $m_L^M = 0$ and $m_M^R \gg m_D$ with light (l) and heavy (h) mass eigenstates,

$$\begin{aligned} m_l &\approx \frac{m_D^2}{m_M^R} \\ m_h &\approx m_M^R. \end{aligned} \tag{2.2.7}$$

Instead, this difference in mass can be explained by the (type I) seesaw mechanism, where a very heavy neutrino is paired with each of the light neutrinos [32]. The larger the mass of the heavier neutrinos m_h is, the smaller the mass of the lighter neutrino m_l becomes, hence explaining the "seesaw". There are many possible extensions of the Standard Model that explain neutrino masses via a Dirac mass term, a Majorana mass term, or both, and obtaining a correct and experimentally substantiated description is the challenge for current- and next-generation experiments.

2.2.2 Cosmology and Supernovae

Strong bounds on the effective neutrino mass are found within cosmological observations. The standard cosmological model ΛCDM describes the evolution of the universe, consisting of the cosmological constant Λ and the abbreviation CDM for cold dark matter. A combination of many observations is necessary for a concise cosmological model, which is described by a range of parameters like its curvature and expansion rate, its matter composition and others. Oscillation experiments suggest that non-degenerate neutrino masses have a lower limit $m_{\nu_e} \geq 0.0085\,\mathrm{eV/c^2}$ in the normal ordering and $m_{\nu_e} \geq 0.048\,\mathrm{eV/c^2}$ in the inverted ordering [28]. Even at this small limit, neutrinos play a significant role in structure formation and clustering in the universe [28].

The ΛCDM model assumes zero neutrino masses. Non-zero masses would have a distinct effect on the cosmic microwave background (CMB) and anisotropies in its power spectrum. The power spectrum is measured to high precision by Planck [33]. Comparison of the galaxy power spectrum with a model consisting of baryons, cold dark matter, a cosmological constant and massive neutrinos allows to determine neutrino mass limits. The Planck 2018 data on temperature and polarization of the CMB gives an upper limit on the neutrino mass of $\sum_{i=1}^{3} m_\nu < 0.26\,\mathrm{eV/c^2}$ at 95% C.L. [33]. A careful combination of these data with baryon acoustic oscillation (BAO) measurements leads to $\sum_{i=1}^{3} m_\nu < 0.13\,\mathrm{eV/c^2}$ at 95% C.L. [34]. Addition of further observations allows more and more stringent limits on the neutrino mass – some of them even down to a level, where the neutrino masses of inverted ordering should be measurable [33, 34]. ΛCDM model extensions lead to a release of the rather stringent limits, but even with twelve instead of seven free parameters, the bound from Planck 2018 is at $\sum_{i=1}^{3} m_\nu < 0.52\,\mathrm{eV/c^2}$ (95% C.L.) [28, 35]. With the lower bound on the neutrino mass from oscillation experiments, the direct detection within cosmological observations can be expected [36].

Since neutrinos with their non-zero mass travel at less than the speed of light, the

spread in arrival times of neutrinos from a very short neutrino emission event like a nearby supernova allows to set rather stringent limits on the average (electron) neutrino mass, as first published in [37]. The type II supernova 1987A in approximately 157 kly distance allowed a time-of-flight measurement of neutrinos, only depending on the free-streaming of neutrinos, the supernova modelling, and the average (electron) neutrino mass. Due to its proximity a large number of neutrinos could be detected, but the supernova occured still sufficiently far away from earth to measure a significant arrival time spread. The supernova neutrinos arrived earlier than photons in a time interval of $\Delta t_{\mathrm{arr}} \approx 13\,s$ and were measured by underground neutrino observatories Kamiokande and IMB [38, 39]. A mass limit comparable to laboratory experiments could be set to $m_\nu < 5.7\,\mathrm{eV/c^2}$, although the estimated emission time spread depends on the supernova model [40]. With experiments like JUNO, DUNE, and Hyper-Kamiokande being in preparation, future nearby supernova explosions will encounter more sophisticated and abundant neutrino detectors, which may be able to measure the time spread and possibly the neutrino mass with higher accuracy.

2.2.3 Neutrinoless Double-β Decay

In 1981, J. Schechter and J. W. F. Valle developed the hypothesis that the existence of neutrinoless double-β decay ($0\nu\beta\beta$) in the reaction

$$(A, Z) \rightarrow (A, Z+2) + e^- + e^- \tag{2.2.8}$$

implies a Majorana-nature of neutrinos [41]. If, however, neutrinos are of Dirac nature, then a vanishing term in the $0\nu\beta\beta$ probability – due to the neutrino and the antineutrino state being orthogonal – leads to a zero amplitude of the probability. Wether neutrinos are of Dirac nature is, thus, a direct consequence of the non-existence of $0\nu\beta\beta$ [41].

When neutrinos are Majorana particles and their own antiparticles, there are non-vanishing probabilities – depending on the nuclear matrix element and the effective Majorana mass of ν_e, including the CP-violating phase δ_{CP} and the Majorana phases $\alpha_{1,2}$ – that the neutrino and antineutrino annihilate upon double-β decay. That would result in a sharp peak at the end of the energy spectrum, caused by the two emitted electrons. This process is described in the Feynman diagram in figure 2.4.

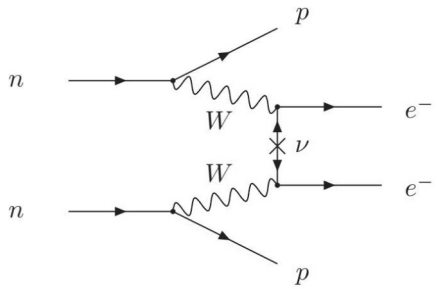

Figure 2.4 – Feynman diagram for neutrinoless double-β decay [28].

The effective neutrino mass of light neutrinos is

$$m_{\beta\beta} \equiv \sum_l \left| U_{el}^2 m_l \right| \tag{2.2.9}$$

with $l = 1, 2, 3$, denoting the neutrino mass eigenstate. When the Majorana neutrino mass is the only source of lepton number violation, the half-life of the decay at low energies, according to [28], is given by

$$\left(T_{1/2}^{0\nu}\right)^{-1} = G^{0\nu} \left| \boldsymbol{M}^{0\nu} \right|^2 \left(\frac{m_{\beta\beta}}{m_e} \right)^2 . \tag{2.2.10}$$

It contains the phase space integral $G^{0\nu}$ and the nuclear matrix $\boldsymbol{M}^{0\nu}$. Further parameters enter the experimentally available half-life, resulting in the sensitivity to the decay

$$\left(T_{1/2}^{0\nu}\right) \propto \begin{cases} aM\epsilon t, & \text{background-free} \\ a\epsilon\sqrt{\frac{Mt}{B\Delta E}}, & \text{with background} \end{cases} \tag{2.2.11}$$

with isotope abundance a, source mass M, measurement time t, total efficiency for detecting $0\nu\beta\beta$ decays ϵ, background rate B, and energy resolution ΔE. Further, the nuclear structure calculation is subject of large uncertainties for all 2β-decaying isotopes, which induce a spread by a factor 2 to 3 in $m_{\beta\beta}$ for a given half-life $T_{1/2}^{0\nu}$ [42]. The GERDA experiment achieved the absence of background in the region of interest. The spectrum of the double-β decay of ^{76}Ge including a hypothetical peak at $Q_{\beta\beta}$ is shown in figure 2.5. The

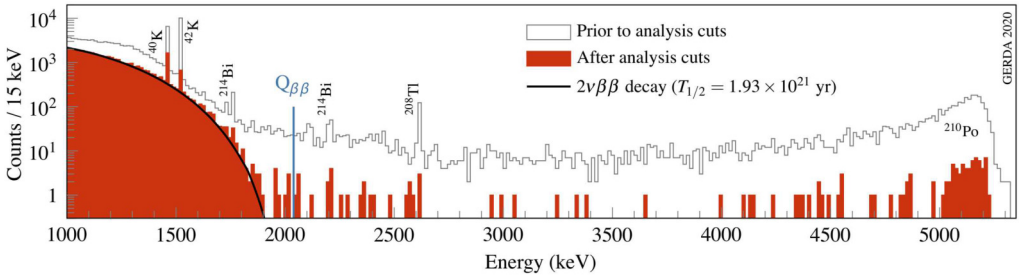

Figure 2.5 – Spectrum of ^{76}Ge, published as final results from the GERDA experiment [43]. All background components are identified, as well as the $2\nu2\beta$-spectrum and the position of $Q_{\beta\beta}$.

GERDA detectors were made of ^{76}Ge-enriched high-purity germanium within a liquid-argon cryostat, which is an efficient shielding and scintillating veto. That and the sophisticated pulse-shape discrimination proved to be a successful combination: The GERDA experiment measured the lower limit on the half life to be $T_{1/2} > 1.8 \times 10^{26}$ years (90% C.L.) with ^{76}Ge and $m_{\beta\beta} < (79 - 180)\,\mathrm{meV/c^2}$ [43]. Another successful experiment, among others, was CUORE, which investigated the decay of ^{130}Te with a sophisticated cryogenic calorimeter – operated at temperatures of 10 mK – and found $m_{\beta\beta} < (0.11 - 0.52)\,\mathrm{eV/c^2}$ [45].

2.2.4 Kinematic Measurements

Energy-momentum conservation experiments are the only model-independent way to measure the (anti-)neutrino mass. Typically, the isotopes used for these experiments have a small endpoint energy and, therefore, a relatively large number of counts in the endpoint region that is affected by the neutrino mass. It is, further, experimentally easier to achieve the required energy resolution ΔE at low energies. Experiments utilize for example rhenium (^{187}Re) with a Q-value $Q_\beta = 2470.9 \pm 1.3\,\mathrm{eV}$ [46] or tritium (T) with a Q-value of $Q_\beta = 18592.071 \pm 0.022\,\mathrm{keV}$ [47] for β^--decay and ^{163}Ho with a Q-value of $Q_{\mathrm{EC}} = 2.838 \pm 0.014\,\mathrm{keV}$ for the electron capture process [48].

The β-decay is described via the reaction

$$(Z, A) \rightarrow (Z + 1, A) + e^- + \bar{\nu}_e \tag{2.2.12}$$

or

$$n \rightarrow p + e^- + \bar{\nu}_e. \tag{2.2.13}$$

It represents the decay of a neutron's constituent d quark, mediated by a charged weak interaction boson W^-, into a u quark, leaving a proton.

Fermi's golden rule with phase-space density $\rho(E)$ and nuclear matrix element M describes the differential decay rate as

$$\frac{\mathrm{d}\dot{N}}{\mathrm{d}E} = \frac{2\pi}{\hbar}|M|^2\rho(E). \tag{2.2.14}$$

The phase-space factors of the nucleus and the electron and neutrino can be separated due to the large mass of the nucleus and the contribution of nuclear recoil energy can be neglected. The nuclear matrix element can then be expressed with a hadronic part M_{nuc} and a leptonic part M_{lep}:

$$|M| = G_{\mathrm{F}} \cos\theta_{\mathrm{C}} M_{\mathrm{nuc}} M_{\mathrm{lep}}, \tag{2.2.15}$$

with the Fermi coupling G_{F} and the Cabbibo angle $\theta_{\mathrm{C}} \approx 13°$. In case of tritium, the decay is super-allowed, i.e. the electron and the neutrino do not take away angular momentum, and the nuclear matrix element M_{nuc} is independent of the electron energy. The leptonic part of the nuclear matrix element is

$$|M_{\mathrm{lep}}|^2 = \frac{1}{V^2} F(Z + 1, E), \tag{2.2.16}$$

containing a normalization volume V and the Fermi function F (with $Z = 1$ in case of tritium), which accounts for the Coulomb attraction between the emitted electron and the daughter nucleus.

The phase-space density of energy levels is given by

$$\begin{aligned}\rho(E) &= \frac{\mathrm{d}n_e}{\mathrm{d}E_e}\frac{\mathrm{d}n_\nu}{\mathrm{d}E_\nu} \\ &= V^2\frac{p_e E_e p_\nu E_\nu}{4\pi^4\hbar^6} \\ &= \frac{V^2}{4\pi^4\hbar^6}\sqrt{E^2+2m_e c^2 E}(E+m_e c^2)(E_0-E)\sqrt{(E_0-E)^2-m_\nu^2 c^4}\end{aligned} \tag{2.2.17}$$

The above expressions yield the β-decay spectrum,

$$\frac{\mathrm{d}\dot{N}}{\mathrm{d}E} = \frac{G_\mathrm{F}^2\cos^2(\theta_\mathrm{C})}{2\pi^3\hbar^7}|M_\mathrm{nuc}|^2 F(E,Z+1)p_e(E+m_\mathrm{e}c^2)\sum_f P_f\epsilon_f\sqrt{\epsilon_f^2-m_{\nu_e}^2c^4}\Theta(\epsilon_f-m_{\nu_e}c^2). \tag{2.2.18}$$

The momentum p and the energy of the emitted electron form the phase-space factor $p_e\cdot(E+m_e) = \sqrt{(E+m_ec^2)^2-m_e^2c^4}\cdot(E+m_ec^2)$. The neutrino energy $\epsilon_f = E_0 - V_f - E$ contains the energy correction from the final state f of molecular tritium T_2, the effective β-decay endpoint energy, and the molecular excitation energy V_f with probability P_f from quantum chemical theory. The Heaviside function $\Theta(\epsilon_f - m_\nu c^2)$ is added for energy conservation. The main influence on the shape of the spectrum comes from the neutrino phase space factor, which contains the neutrino momentum

$$p_{\nu_e} = \sqrt{\epsilon_f^2 - m_{\nu_e}^2c^4}. \tag{2.2.19}$$

The energy-independent parameters can be condensed into

$$A = \frac{G_\mathrm{F}^2\cos^2(\theta_\mathrm{C})}{2\pi^3\hbar^7}|M_\mathrm{nuc}|^2. \tag{2.2.20}$$

Due to the neutrino mixing, the spectrum contains the mass eigenstates ν_i $(i=1,2,3)$, weighted with the mixing matrix U_{ei}:

$$\frac{\mathrm{d}\dot{N}}{\mathrm{d}E} = AF(E,Z+1)p_e(E+m_\mathrm{e}c^2)\sum_f P_f\epsilon_f\sum_i |U_{ei}|^2\sqrt{\epsilon_f^2-m_{\nu_i}^2c^4}\Theta(\epsilon_f-m_{\nu_i}c^2). \tag{2.2.21}$$

This formalism and more details are found in [49]. The limited experimental resolution $\Delta E \ll m_{\nu_e}c^2$ only allows to measure the incoherent sum of neutrino mass eigenstates[4], which is expressed as the experimental observable

$$m_{\nu_e} \equiv \sqrt{\sum_i |U_{ei}|^2 m_i^2}, \tag{2.2.22}$$

with $m_{\nu_e} \equiv m_{\bar{\nu}_e}$ from CPT-conversion [50].

[4]This expression can be identified as the mass of the propagating neutrinos, not its virtual/effective values m_{ν_e} or $m_{\beta\beta}$), with mass eigenstates contributing to the flavor e. It can be written this way, if the experimental resolution is considerably worse than the neutrino mass difference.

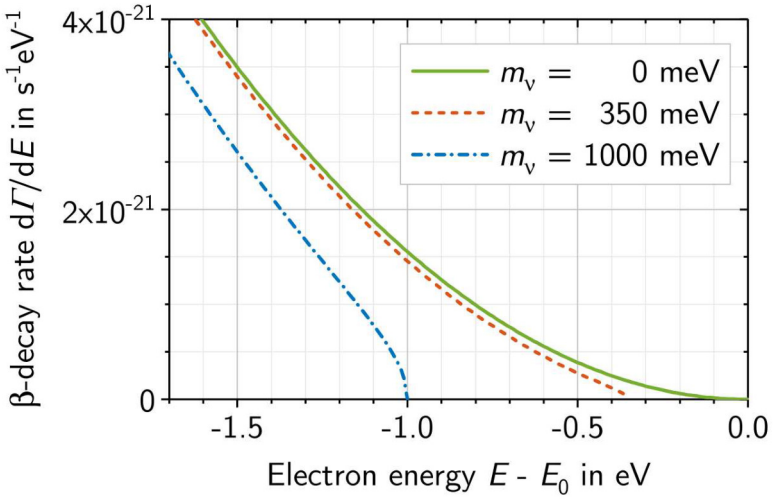

Figure 2.6 – Endpoint region of the tritium β-decay spectrum. The distortion of the spectrum becomes less pronounced for smaller values of m_ν. Image from [49].

The influence on the shape and endpoint position of the tritium β-decay spectrum of different neutrino mass values is shown in figure 2.6. The most recent result from β-decay spectroscopy of tritium was achieved by the KATRIN experiment with a first sub-eV limit from a direct search, $m_\nu < 0.8\,\mathrm{eV/c^2}$ (90% C.L.) [5]. In its predecessors in Mainz and Troitsk upper limits of $m_\nu < 2.05\,\mathrm{eV/c^2}$ (95% C.L.) and $m_\nu < 2.3\,\mathrm{eV/c^2}$ (95% C.L.) were achieved [51, 52].

These experiments used a so-called MAC-E filter technique to achieve their respective precision, see chapter 3.1.2. The presence of molecular tritium and the, thereby, broadened final state distribution limits the sensitivity of kinematic neutrino mass measurements. The next-generation experiment Project 8 will attempt to measure the spectrum of atomic tritium via cyclotron radiation emission spectroscopy and can – in principle – achieve a sensitivity of $m_{\nu_e} \approx 0.04\,\mathrm{eV/c^2}$ [53].

An alternative isotope to tritium for the neutrino mass estimation is found in ^{187}Re with a much lower endpoint $E_0 \approx 2.8\,\mathrm{keV}$. The ^{187}Re β-decay is a forbidden transition, which increases the half-life and an excessively large source mass would have to be acquired for a comparable neutrino mass limit. That outweighs the benefit of the low endpoint value and limits the achievable neutrino mass sensitivity[5] [55].

There are experiments that make use of the electron capture process with ^{163}Ho, which aim for a sub-eV sensitivity on m_{ν_e}: The ECHo experiment, for instance, uses magnetic microcalorimeters as highly precise detectors for the ^{163}Ho-spectrum resulting from the electron capture process [56], while the HOLMES experiment uses ^{163}Ho-implanted gold absorbers coupled to transition edge sensors [57]. ^{163}Ho has a remarkably low Q-value, $Q \approx 2858(11)\,\mathrm{eV}$ [58], and the endpoint region of the spectrum depends on m_{ν_e} in the same way as for tritium.

The incoherent sum given in equation 2.2.22 is analogously expressed for the μ and τ

[5] A limit of $m_{\nu_e} < 15\,\mathrm{eV/c^2}$ (90% C.L.) was reached via calorimetry [54].

flavors [55]. The best upper limit on the (effective) neutrino masses associated with the μ was found in pion decay at rest, $\pi^+ \to \mu^+ + \nu_\mu$: $m_{\nu_\mu} < 0.17\,\mathrm{MeV/c^2}$ (90% C.L.) [59]. An upper bound on the incoherent sum of τ neutrino masses was measured by the ALEPH collaboration to be $m_{\nu_\tau} < 18.2\,\mathrm{MeV/c^2}$ (95% C.L.) [60].

3 The KATRIN Experiment

The KATRIN experiment aims to directly measure the squared sum of neutrino masses m_ν^2 with a final sensitivity $\Delta m_\nu = 0.2\,\mathrm{eV/c^2}$ after 1000 days of data taking at a background level of 10 mcps [6]. From 2018 onwards, at least 210 measurement days are the annual operation goal, which was steadily reached [61]. The experiment is located in Karlsruhe and embedded into the infrastructure of the Tritium Laboratory Karlsruhe (TLK).

The β-decay of tritium,

$$\mathrm{T} \rightarrow {}^3\mathrm{He} + e^- + \bar{\nu}_e, \tag{3.0.1}$$

contains information on the neutrino mass in its endpoint's shape and energy $E_0 \approx 18.6\,\mathrm{keV}$, as described in the previous chapter 2.2.4. Electrons from the tritium decay are transported from the *source and transport section* into the *spectrometer and detector section* and are, if their energy suffices, counted by the detector. Both areas of the beamline are explained in more detail in section 3.1.

In 2022, KATRIN set the best upper limit from a direct neutrino mass experiment of $m_\nu < 0.8\,\mathrm{eV/c^2}$ (90% C.L.) with data taken in two campaigns in spring and fall 2019 [5]. It became apparent during the initial measurement campaigns that the background level is higher than expected. Extensive research was needed to find that the elevated background originates in radioactive sources and stems from a secondary, low-energetic-electron generation mechanism that was not anticipated during planning, see section 3.3.2 [62, 63, 64]. There are various, often complementary approaches to reduce the background level – partially already implemented, partially in different stages of research and development. The main ones are discussed in section 3.3.3. Further operation with the elevated background level of currently $R_{\mathrm{bg}} \approx 140\,\mathrm{mcps}$[1] in the recent science runs will impair the sensitivity and a final sensitivity better than 300 meV is expected. In order to improve the sensitivity and allow a sensitivity closer to the design value the background reduction requires special efforts.

The KATRIN experiment is scheduled to run until the end of 2025. It will be modified afterwards for sterile neutrino mass search in the Tritium Sterile Anti-Neutrino (TRISTAN) phase of KATRIN with a novel multichannel silicon drift detector that has the capability to precisely measure the energy of incoming electrons at a large rate [65].

[1] mcps = "millicounts per second", $R_{\mathrm{bg}} \approx 140\,\mathrm{mcps}$ after data quality cut of pixels on the outer radius of the detector wafer. The background is $R_{\mathrm{bg}} \gtrsim 160\,\mathrm{mcps}$ without quality cuts.

3.1 Setup

The tritium plasma in the windowless gaseous tritium source (WGTS) is contained via superconducting magnets. A sophisticated loop system controls the amount and purity of tritium within the WGTS. Electrons that move upstream[2] to the rear end of the beam line hit a gold plated stainless steel disk, the so-called rear wall (RW). The electrons that move into the downstream direction are guided through the differential pump section (DPS) and the cryogenic pump section (CPS). The number of tritium atoms between the windowless source and the spectrometer is reduced by 14 orders of magnitude, which results in a neglible amount of tritium within the spectrometer.

Electrons reaching the spectrometer are slowed down by the electric potential qU. The magnetic adiabatic guiding with an electrostratic (MAC-E) filter acts as a spectrometer: Electrons are registered by the focal plane detector (FPD) when they have sufficient velocity into longitudinal direction, which corresponds to a kinetic energy high enough to overcome the so-called analyzing plane. An integral β-spectrum is recorded by step-wise change of the electric potential. For the analysis the response function of the spectrometer needs to be unfolded from the spectrum.

The following section will provide details on each segment of the beamline. Figure 3.1 gives a schematic overview of the experiment's components and of the predominant background processes.

3.1.1 Source and Transport Section

The source and transport section consists of the rear section, the source section, and the DPS and CPS. The rear section of KATRIN contains the rear wall, which absorbs electrons emitted in the upstream direction. Further, it controls the work function of the source system. A monoenergetic, angular-selective photoelectron source for, i.a., spectrometer calibration and energy loss measurements is housed in the rear section. The source section provides the tritium plasma and is connected to the tritium loop system, where the isotopologue composition is established. To prohibit tritium from entering the spectrometer, the DPS and CPS efficiently remove neutral and ionized tritium from the beamline.

Rear Section

The WGTS potential and the rear wall potential define the starting potential of the β-electrons [66]. Ions and electrons can move between the rear wall and the plasma in the direction of the magnetic field line, but not perpendicular to it. To counter local space charges in the source, which induce potential inhomogeneities, a conducting plate – the rear wall, a gold-plated stainless steel disk of 145 mm diameter – was installed at the rear end of the source that allows charge transfer between different radii in the source. The

[2] Downstream means the direction from the source to the detector, upstream vice versa.

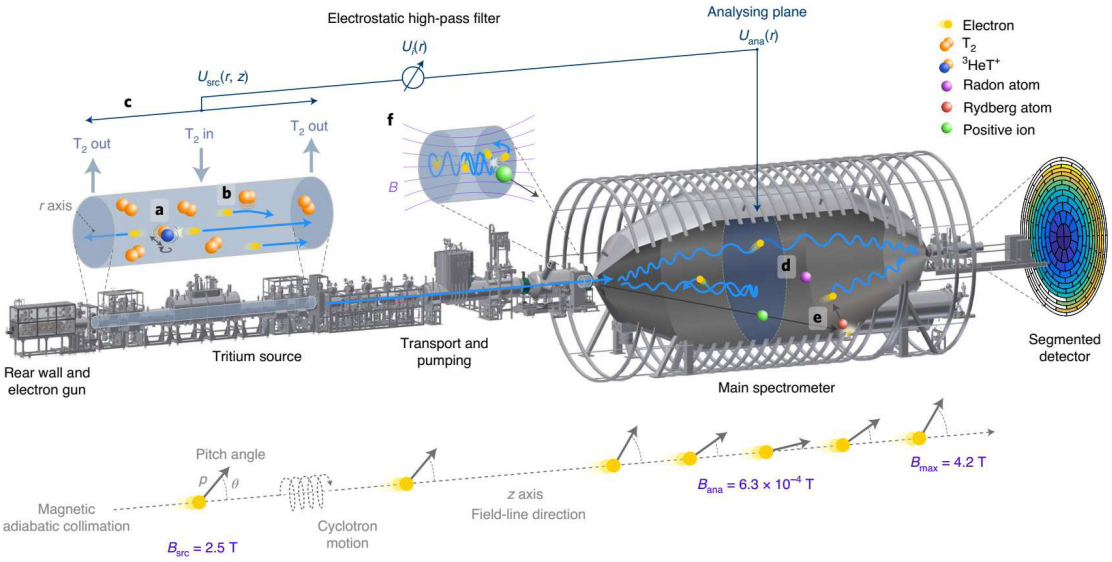

Figure 3.1 – KATRIN beamline, taken from [5]. The tritium β-decay in the windowless gaseous tritium source releases the β-electrons. They are magnetically guided through the transport section, where remaining tritium is pumped-off. The electrons are analyzed by energy in the spectrometer and measured by the segmented focal plane detector. Molecular final-state excitations of the remaining atom (a), electron-scattering off gas molecules (b), and electric potential variations within the source induce systematic effects in the source. In the spectrometer, there are various background processes: Electrons are released from radon-decay (d) and from de-excitation of Rydberg-atoms (e). Positive ions are created in Penning traps between the main spectrometer and the (now deactivated) pre-spectrometer.

magnetic flux tube is mapped onto its surface, so that β-electrons, secondary electrons, and ions are absorbed. An optimal bias voltage point, where the work function difference between rear wall and beam tube is minimized, can be found experimentally [67].

Further, the beta-induced X-ray spectrometer system (BIXS) is housed in the rear section to directly measure the source activity.

Electrons from the monoenergetic, angular-selective UV-photoelectron source can be used to measure the transmission properties of the beamline [68]. Its electrons are guided magnetically through a small hole in the rear wall and guided downstream. It is a calibration tool that is used, for example, to measure the initial energy-dependent energy loss from inelastic electron scattering in the source [69, 70].

Windowless Gaseous Tritium Source and Source-gas Circulation

A strong source, on the one hand, provides the necessary statistics for the neutrino mass search. On the other hand, the electrons from the tritium β-decay with an endpoint energy $E_0 \approx 18.6\,\mathrm{keV}$ need to reach the spectrometer without previously losing an (unknown) amount of energy due to scattering. That means, a trade-off between these two aspects needs to be found. The source, further, needs to be thoroughly stabilized in activity, temperature, and source potential. The WGTS is schematically shown in figure 3.2.

The tritium in KATRIN's WGTS is present in molecular form. While a high purity of

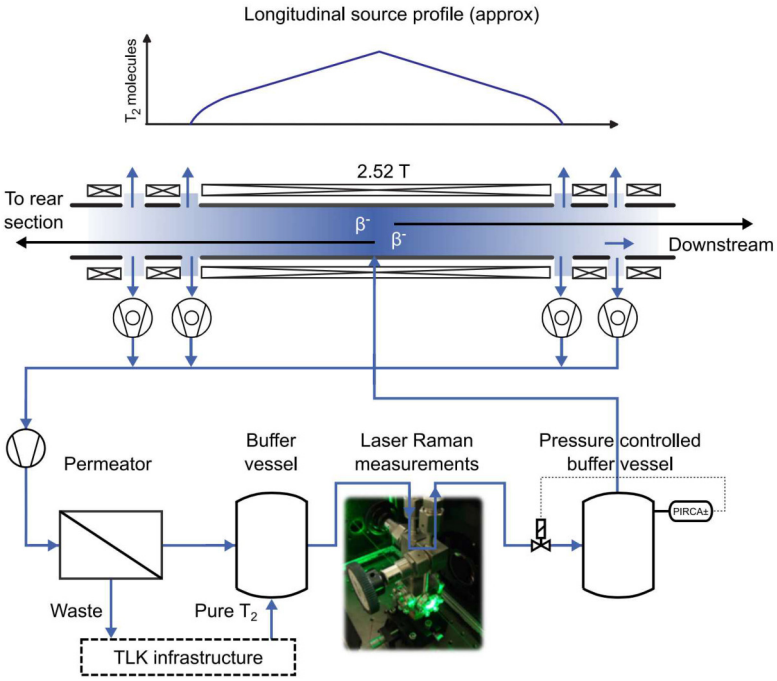

Figure 3.2 – The WGTS system of KATRIN [61]. The longitudinal gas density profile is schematically shown atop. Electrons are released isotropically. In upstream direction they reach the rear wall, in downstream direction they move towards the spectrometer. Differential pump ports remove tritium at the rear and front end.

95% T_2 is achieved, there is a small proportion of HT and DT. Non-hydrogen impurities are removed by a permeator before (re-)injection. The gas composition that enters the source is monitored via Raman spectroscopy [71]. The source gas-density profile is kept constant by continuous inflow and outflow: Tritium is fed via capillaries into an injection chamber and then into the central part. At the rear and front end of the source, two differential pumping ducts remove tritium and its decay products.

Besides the tritium circulation, a simultaneous circulation of ^{83m}Kr and tritium or a pure ^{83m}Kr circulation are possible modes of operation. ^{83m}Kr is a metastable isotope of krypton with half-life $T_{1/2} = (1.8620 \pm 0.0019)$ h [72], which is ideally suited to avoid long-term contamination of the experiment. Krypton is used as calibration source for various purposes: It helps, for example, to understand the energy loss of β-electrons in tritium, and it allows investigation of the spatial inhomogeneity of the source plasma potential, as an additional potential shifts the well-known line positions of the conversion electrons [61, 67]. Further, KATRIN can be used to improve the knowledge on ^{83m}Kr transition energies [73]. It decays mainly via internal conversion with transition energies 32.2 keV and 9.4 keV or in a suppressed direct transition of 41.6 keV [74].

The neutrino mass measurement and calibration measurements should be performed at the same temperature in order to easily switch between the different WGTS modes. Similar operating conditions are beneficial, especially with indications that plasma effects in the source are larger than simulations would predict [61]. Since krypton would freeze at

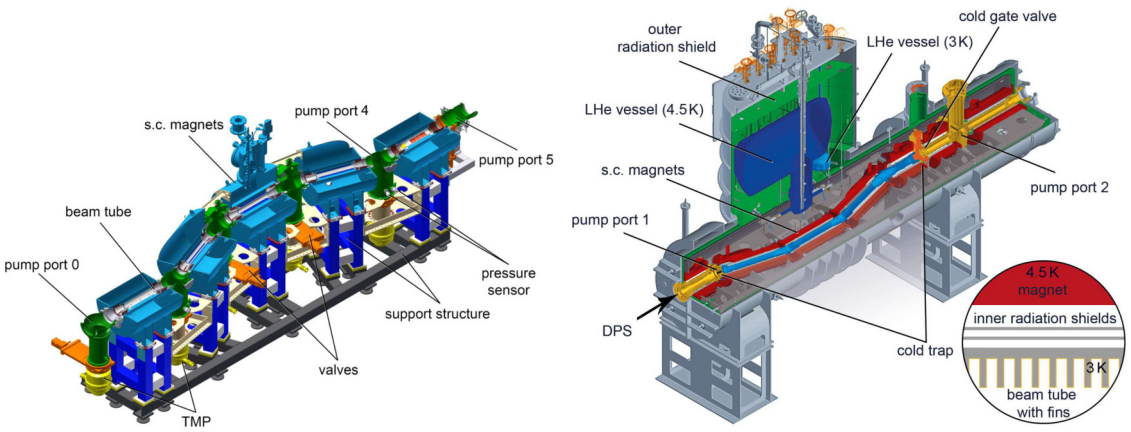

(a) DPS **(b)** CPS

Figure 3.3 – The differential pump section (DPS) and cryogenic pump section (CPS) remove the residual tritium from the beamline [67, 75].

source temperatures of 30 K, the operation temperature is 80 K [61] via two-phase nitrogen cooling.

The requirements on the source are a stability $< 0.1\%$ of the integrated number of tritium molecules per cross-sectional area over the beam tube axis (so-called column density) and a high tritium purity $> 95\%$. After the source activity was at roughly one fifth of the design value in the first measurement campaign KNM1, the source activity could be increased to $9.5 \cdot 10^{10}$ Bq – approximately 75% of the design value – in the following campaigns [61].

The WGTS is a windowless source, i.e., no energy is lost at an exit window. Consequently, tritium can leave the source in the direction of the spectrometer, if it is not prohibited by other systems. The amount of tritium that leaves the WGTS in the direction of the beamline after the tritium retention pump ducts is $< 0.1\%$ [67]. Preventing it from reaching the spectrometer is left to the subsequent pumping systems in the transport section.

Differential & Cryogenic Pump Sections

The differential pump section (DPS) and the cryogenic differential pump section (CPS) further reduce the tritium flow rate in total by more than twelve orders of magnitude. Both are shown in figure 3.3.

Trapezoidal chicanes of 20° angle block neutral particles in the DPS, while electrons and ions are guided by the magnetic field of five superconducting magnets. Electrons can pass through, but heavier tritium ions are removed via $E \times B$-drift and neutralized upon impact on the dipole electrodes. The neutral tritium is then differentially pumped off by the turbomolecular pumps.

The CPS adiabatically guides the β-electrons further towards the spectrometer, while it achieves a tritium flow rate reduction of more than seven orders of magnitude [76]. A sorption pump is directly integrated into the beamline. Its inner surface is gold plated and an argon layer is frozen upon, which is – in conjunction with the adsorbed tritium –

removable by heating. The argon layer is kept at a temperature of 6 K, where its surface area is enlarged [77] and, thus, the sticking time for tritium is maximized compared to higher temperatures [78]. The CPS is kept at cryogenic temperatures during neutrino mass measurements, so that the tritium on its walls is retained. The argon frost pump is regenerated before its activity reaches 1 Curie – once per year typically suffices [67].

The CPS section houses important monitoring and calibration devices that can be inserted into the beamline on demand: The forward beam monitor (FBM) and the condensed ^{83m}Kr source (CKrS). The FBM tracks the source activity and can be used to scan the rate across the flux tube. The condensed krypton source, on the other hand, provides conversion electrons from krypton decay from a solid source with stable ^{84}Kr and metastable ^{83m}Kr frozen onto HOPG substrate. It allows to hit only a few pixel at once and is, therefore, suited to precisely measure the electric potentials and magnetic fields in the analyzing plane of the main spectrometer. Additionally, a new method allows to directly measure a previously undetected conversion line with KATRIN and determine the energy scale with unprecedented precision [73, 79, 80].

3.1.2 Spectrometer and Detector Section

The electrons that leave the CPS are guided magnetically into the pre- and the main spectrometer and finally measured by the focal plane detector (FPD), if their energy suffices to overcome the retarding potentials of the spectrometers. The MAC-E filter allows for very sharp distinction of electrons with insufficient energy with a filter width of $\mathcal{O}(\Delta E) \sim 1\,\mathrm{eV}$ at the β-spectrum endpoint $E_0 \approx 18.6\,\mathrm{keV}$ [6].

Spectrometer Principle

The pre- and main spectrometer of KATRIN are both of MAC-E filter type, which was extensively described in [82]-[83]. It utilizes the collimation of isotropically emitted electrons from a source via inverse magnetic mirror effect. The consequential minimization of their transverse energy in the lowest magnetic field and the adiabatic guidance is, together with an electrostatic potential, used to form a very sharp energy filter. Figure 3.4 demonstrates the principle. The x-y plane of minimal magnetic field B_{ana} and maximal electrostatic potential $|U_{\mathrm{ret}}|$ is called analyzing plane. An integral spectrum is recorded in multiple retarding potential steps that are predetermined by a dedicated measurement time distribution. The detected count rate in dependence of the retarding potential voltage is a convolution of the response function, which contains the transmission function of the spectrometer, and the β-decay spectrum, see section 3.2.1.

Electrons within a magnetic field follow the magnetic field line. The relation of the electron's transverse and longitudinal energy to the pitch angle $\theta = \angle(\vec{p}, \vec{B})$ and magnetic

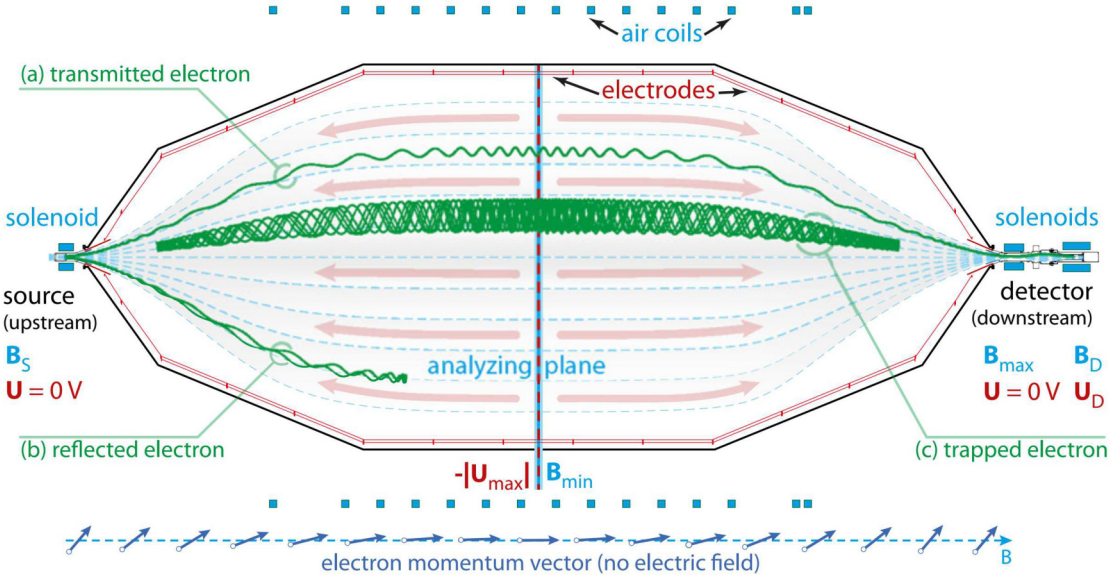

Figure 3.4 – MAC-E filter principle [81]. The electrons are transmitted (a), if their longitudinal energy suffices to overcome the retarding potential. Otherwise, they are reflected (b) ultimately at the analyzing plane. High-energetic electrons may become trapped between the strong magnetic fields of the entrance and exit and induce low-energetic secondary electron emission as background, see section 3.3.

field strength $B = |\vec{B}|$ is

$$E_{\text{kin}} =: E_{\parallel} + E_{\perp} \tag{3.1.1}$$

$$= E_{\text{kin}} \cdot \cos^2\theta + E_{\text{kin}} \cdot \sin^2\theta \tag{3.1.2}$$

Electrons in a magnetic field move on a cyclotron path with the gyroradius

$$r_{\text{g}} = \frac{m_e v_{\perp}}{eB} = \frac{\sqrt{2m_e E_{\perp}}}{eB}, \tag{3.1.3}$$

which can be calculated (here: non-relativistically) from the equality of Lorentz force. The magnetic moment $\vec{\mu}$ of an electron can be expressed as

$$\mu = |\vec{\mu}| = \frac{e}{2m_e}|\vec{l}| = \frac{E_{\perp}}{B} \tag{3.1.4}$$

with $\vec{l}$ being the orbital angular momentum $\vec{l}$ of the electron. The magnetic moment is conserved during adiabatic motion, i.e., the fraction

$$\frac{E_{\perp}(z)}{B(z)} = \frac{E_{\perp}(z')}{B(z')} = \text{const} \tag{3.1.5}$$

holds at any position z or z'. With equation 3.1.2, the adiabatic transformation of the pitch angle θ is given by

$$\sin^2\theta(z') = \sin^2\theta(z) \cdot \frac{B(z')}{B(z)}. \tag{3.1.6}$$

Electrons are transmitted, if their longitudinal energy is larger than the retarding potential. The transmission condition is

$$E_{\parallel} = E_{\mathrm{kin}} \cos^2 \theta_{\mathrm{ana}} > qU_{\mathrm{max}}, \tag{3.1.7}$$

where θ_{ana} is the pitch angle of the electron in the magnetic field of the analyzing plane. The energy resolution is the width of the filter, i.e. the maximum remaining transverse energy of an electron in the analyzing plane with maximum pitch angle in the WGTS:

$$\Delta E = E_0 \cdot \frac{B_{\mathrm{min}}}{B_{\mathrm{max}}} \tag{3.1.8}$$

with an unprecedented $\Delta E = 0.93\,\mathrm{eV}$ at $E_0 = 18.6\,\mathrm{keV}$ in KATRIN when operated under conditions specified in the Technical Design Report [6] with $B_{\mathrm{ana}}^{\mathrm{DR}} = 0.3\,\mathrm{mT}$. The magnetic field in the analyzing plane was enlarged to $B_{\mathrm{ana}} = 0.6\,\mathrm{mT}$ for the neutrino mass campaigns, mainly because the overall background rate depends on the flux tube volume in the spectrometer that decreases with magnetic field strength. An increased filter width of $\Delta E = 2.8\,\mathrm{eV}$ was deemed acceptable in the first campaigns [84]. The electromagnetic configuration in later campaigns was further adapted for enhanced background reduction, see section 3.3.3.

When moving from B_{ana} into a region of higher magnetic field, the electrons are decollimated, i.e. their pitch angles increase, see equation 3.1.6. That means, the spectrometer's acceptance angle θ_{max}, i.e. the initial angle that allows electrons to be transmitted from the source to the detector, depends on the starting magnetic field B_{S} and the highest magnetic field B_{max}:

$$\theta_{\mathrm{max}} = \arcsin\left(\sqrt{\frac{B_{\mathrm{S}}}{B_{\mathrm{max}}}}\right). \tag{3.1.9}$$

Depending on their initial angles, electron pitch angles can be enlarged to more than 90° and, consequentially, reflected via magnetic mirror effect.

Pre- and Main Spectrometer Setup

The KATRIN beamline contains two subsequent MAC-E filter spectrometers. The first one is called pre-spectrometer and was used to reduce the amount of electrons that reach the main spectrometer in the first place. The second one is the main spectrometer, which is used as the fine energy filter. The simultaneous operation of both spectrometers on high voltage, however, induces a Penning trap in the spectrometer. That is a known phenomenon and an ion removal system was installed [85]. However, the removal of stored particles leads to an increased background rate with increasing high-voltage step length [5]. If unaccounted, that can induce a systematic shift in the measured neutrino mass, since the measurement time in the most m_ν^2-sensitive energy region with the lowest β-electron count rate is typically the longest. The pre-spectrometer was set to ground potential in 2022 to neutralize the Penning trap [5].

The magnetic field is provided by superconducting magnets at the entrance and the exit of the spectrometer. Air coils are used to hold and fine-tune the magnetic field within the main spectrometer. Further, a set of air coils is used for the earth magnetic field compensation.

The retarding potential in the analyzing plane is provided by the high voltage system with the WGTS potential as common ground potential. The two custom-made K35 [86] and K65 [87] high-voltage dividers in conjunction with 8.5-digit precision digital voltmeters allow the necessary ppm (10^{-6}) level precision of the electric potential on the spectrometer vessel relative to its set value [67]. The high voltage is stable on time intervals from sub-µs to entire measurement campaigns of 60 days and equipped with an additional post-regulation system against high-frequency noise [67]. An inner electrode system is operated with an offset of up to $-400\,\mathrm{V}$ and provides an efficient shielding for charged particles from the vessel walls, e.g. released by cosmic muons or radioactive decays [88]. The high-voltage configuration of the inner electrode is highly versatile by the utilization of various offset power supplies for different regions of the IE within the spectrometer [67]. Thereby, the electric potential can be fine-tuned.

Detector

The focal plane detector (FPD) is embedded into the detector section as shown in figure 3.5. Two superconducting magnets provide nominal magnetic fields of 4.2 T at the pinch magnet and 2.52 T at the detector magnet [67]. That allows adiabatic guidance of the β-electrons and the flux tube to be fully mapped onto the FPD. Before the electrons from the main spectrometer reach the detector, their energy is enhanced by the post-acceleration electrode, nominally by 10 keV, into a region of lower intrinsic detector background in the recorded spectrum and reduced backscattering probability on the blank silicon surface [67]. The detector is connected to the main spectrometer vacuum system and operates at 10^{-9} mbar.

The detector is passively shielded against γ-background and X-rays. It is, further, surrounded by a veto system based on plastic scintillators, as described in [89]. The veto system was updated for higher light output, resulting in higher efficiency and better stability [67].

The FPD wafer is described in detail in [89, 91]. A photograph of its segmented back side and its electrical contact layout are shown in figure 3.6. It is a single-wafer Si-PIN diode of 503 mm thickness. It was decided to use a backside-illuminated[3] detector in order to optimize the energy resolution by a thinner dead layer. The manufacturer Canberra™[4] specified a dead layer thickness of 100 nm. From its total diameter of 125 mm the active area has a diameter of 90 mm. It is front side-pixelated in 13 concentric rings. Except for the inner four pixels, these rings are interrupted into 12 pixels. All pixels are of equal

[3]The electrons hit the backside of the detector, which is the $n+$-side of the $n+/n/p+$ diode. The pixel-segmented front side is read-out by the electronics and provides the signal.

[4]Canberra Semiconductor NV (now: Mirion Technologies), Lammerdries 25, B-2430 Olen, Belgium.

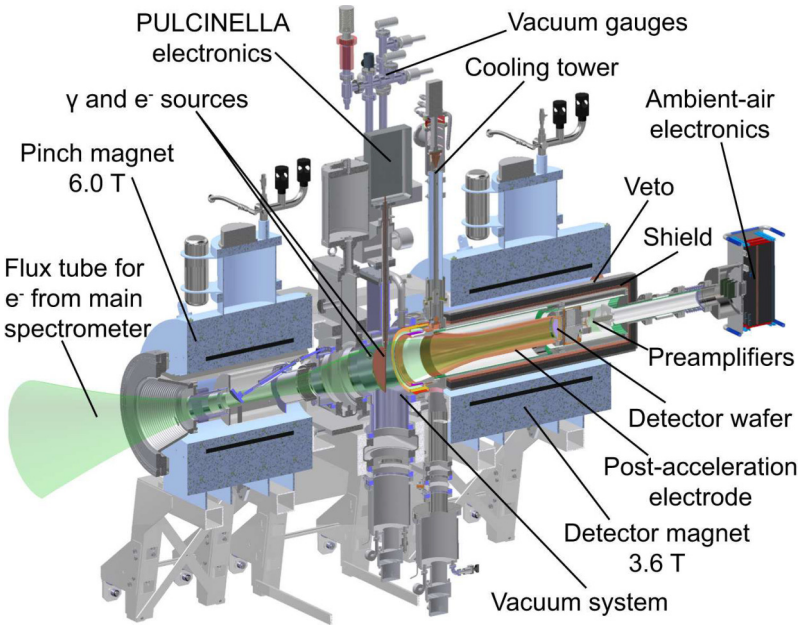

Figure 3.5 – Main components of the detector section [89]. The electron flux tube coming from the spectrometer is compressed by the pinch and detector magnet and mapped onto the focal plane detector. Before they arrive at the detector wafer, the post-acceleration electrode enhances the electron energy by 10 keV.

area 44.1 mm^2. The separate pixels have a design capacitance of 8.2 pF and an inter-pixel resistance $> 1\,\mathrm{G\Omega}$[89]. They are coated with non-oxidizing TiN with separation of 50 µm between pixels. For full-depletion of the detector and optimal performance, a bias voltage of 120 V is applied and the detector wafer is cooled to $-25°\mathrm{C}$. All electrical connections are established from the front side: The bias voltage is applied to the front side-connection of the bias ring. The single pixels are connected to the read-out electronics by a spring-loaded pogo pin mechanism: For optimal contact, the pins are compressed by a certain length and, consequently, they put the wafer under mechanical stress. The induced wafer deformation does, however, not increase the leakage current [91].

The detector readout-system is able to process single-channel events of up to 100 kcps and total rates – without storing the full waveform – to > 1 Mcps [67]. The readout chain consists of analog filters, digitization, digital signal processing, PCI-to-PCIe bridge, and external readout system [67]. A run control PC is used to manage, monitor, and control the detector data via ORCA software [92], which also provides a graphical user interface.

The mean energy resolution per channel of the detector is $\Delta E = (1.52 \pm 0.01)\,\mathrm{keV}$ [89]. The detector is calibrated and tested for linearity and efficiency with electronic and radioactive sources, for example Am-241 [67, 89].

3.2 Neutrino Mass Analysis

Accurate knowledge of the β-spectrum model and the spectrometer's response function are required in order to infer the neutrino mass information from the measured integrated

(a) Dartboard patterned back side [89].

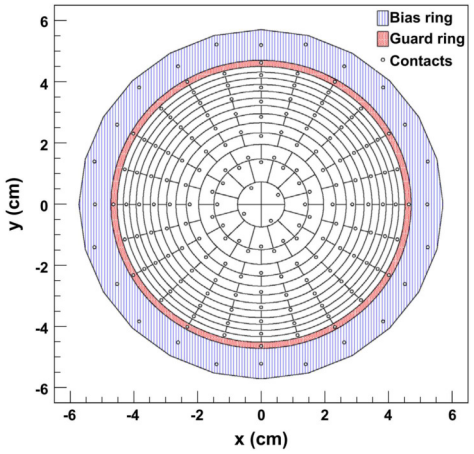

(b) Electrical contacts on front side [90].

Figure 3.6 – The focal plane detector has a pixelated frontside, see (a). The frontside is electrically contacted via pogo pins as specified in (b). The blank, non-segmented backside faces towards the incoming electrons.

spectral data. The response function contains the transmission function of β-electrons through KATRIN's beamline, the energy loss on their way through the source, and other corrections, which are summarized in section 3.2.1. The integral data is fitted with a β-spectrum model that contains an analytical description of the tritium β-decay and the experimental response of the spectrometer. The statistical methods to derive a result on the neutrino mass m_ν are based on frequentist and Bayesian parameter inference. They are outlined in 3.2.2.

3.2.1 β-Decay Spectrum of T_2 and Experimental Response Function

The recorded data is described by the theoretical β-decay spectrum of tritium (T_2) in conjunction with the instruments' response. Section 2.2.4 introduces the Fermi-theory of β decays. Tritium decays to helium with the proton number $Z = 2$ of the daughter nucleus. Its differential decay rate $R_\beta (= \frac{\mathrm{d}\dot{N}}{\mathrm{d}E})$ is – without theoretical corrections – given by equation 2.2.21. Additional theoretical corrections, e.g. the Doppler broadening due to the source temperature and the energy loss ϵ from scattering within the source, are included in the final model [49, 93].

The experimental response is given by

$$R(qU_i, r_j) = A_\mathrm{s} N_\mathrm{T} \int_{qU_i}^{E_0} R_\beta(E) \cdot f(E, qU_i, r_j) \mathrm{d}E + R_\mathrm{bg}(qU_i, r_j) \tag{3.2.1}$$

with the retarding potential U_i and rate r_j at pixel, ring, or patch j (see section 3.2.2). It is shown in figure 3.7. The normalization N_T is calculated from the column density or the number of tritium atoms in the source, the acceptance angle, and the detection efficiency. The signal amplitude A_s is included as free parameter and absorbs any systematic effects on the absolute rate [93]. The response function $f(E, qU_i, r_j)$ contains the transmission

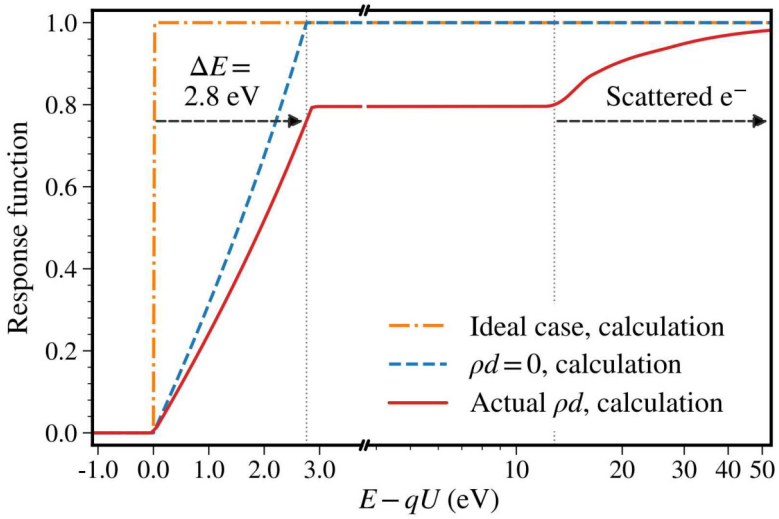

Figure 3.7 – The response function of a MAC-E filter of infinitesimally sharp filter width (orange dash-dotted line), of a realistic MAC-filter without scattering-losses in the source (blue dashed line), and of a realistic MAC-E filter including scattering-losses in the source (solid red line) [93]. Any electron with surplus energy larger than ΔE will overcome the spectrometer. The transmission probability of electrons with surplus energies lower than 0 eV will be reflected. The transmission probability of electrons with surplus energy up to ΔE depends on their starting pitch angle, compare figure 3.8.

function as well as energy losses due to electron scattering and synchrotron radiation [5]. The transmission function $T(E, qU_i, r_j)$ depends on the retarding potential and is characterized by the magnetic fields in the spectrometer and the analyzing plane. The acceptance angle of the spectrometer due to the magnetic mirror effect, see equation (3.1.9), needs to be included: It reduces the number of transmitted electrons with angles larger than $\theta_{\max}$ and, on one side, hampers the overall count rate. On the other side, it sharpens the filter width ΔE of the spectrometer, which allows a higher spectroscopic precision. The transmission function is depicted in figure 3.8 and given by

$$\begin{aligned} T(E, qU) &= \int_0^{\theta_{\max}} \mathcal{T}(E, \theta, qU) \cdot \sin(\theta) \mathrm{d}\theta \\ &= \begin{cases} 0 & , \quad (E - qU) < 0, \\ 1 - \sqrt{\left(1 - \frac{E - qU}{E}\right) \frac{B_\mathrm{S}}{B_\mathrm{ana}}} & , \quad 0 \leq (E - qU) \leq \Delta E, \\ 1 - \sqrt{1 - \frac{B_\mathrm{S}}{B_\mathrm{max}}} & , \quad (E - qU) > \Delta E \end{cases} \end{aligned} \tag{3.2.2}$$

with surplus energy $(E - qU)$. If the largest magnetic field equals the source magnetic field, $B_{\max} = B_\mathrm{S}$, all of the electrons that are emitted in forward direction and have an energy $E > qU + \Delta E$ are able to pass the filter. The acceptance angle and thereby the maximal transmission probability is reduced, if $B_{\max} > B_\mathrm{S}$.

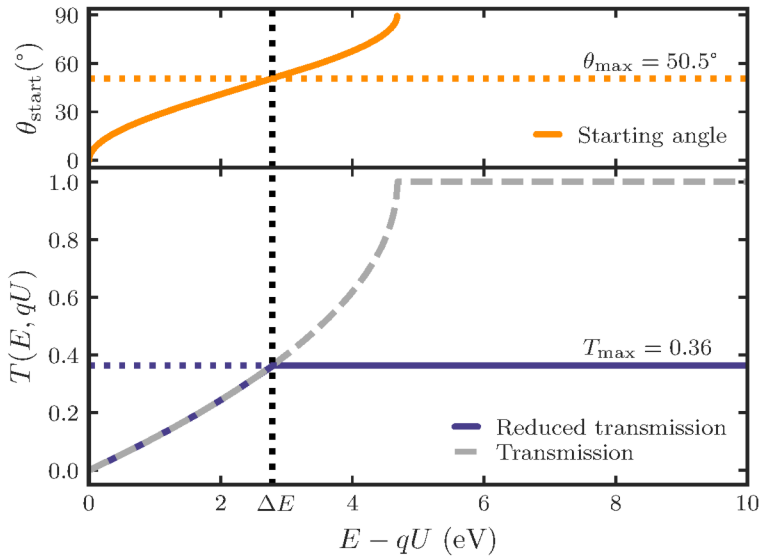

Figure 3.8 – Isotropic electron start angle distribution (upper panel) and transmission function of the MAC-E filter (lower panel). Electrons of starting angles $\theta_{\mathrm{start}} > \theta_{\mathrm{max}} = 50.5°$ are not transmitted due to a magnetic mirror, see eq. (3.1.9). That lowers the number of transmitted electrons, but reduces the filter width to $\Delta E \approx 2.8\,\mathrm{eV}$. Electrons with a starting angle $\theta_{\mathrm{start}} = \theta_{\mathrm{max}}$ pass the filter with surplus energy $E - qU > \Delta E$, while electrons with $\theta_{\mathrm{start}} = 0°$ will pass the filter with $E - qU \leq 0\,\mathrm{eV}$.

3.2.2 Neutrino Mass Analysis Methods and Results

The neutrino mass is inferred from fitting the analytical spectrum prediction $R(qU_i, r_j)$ to the measured spectrum $R_{\mathrm{meas}}(qU_i, r_j)$ by minimizing $\chi^2 = R_{\mathrm{data}} C^{-1} R$ [5]. The neutrino mass m_ν is one of four free fit parameters for equation (3.2.1) – the others are the endpoint E_0, the signal amplitude A_{S}, and the background rate R_{bg}. When the data set is divided in pixels, rings, or patches r_j, $E_0(r_j)$, $A_{\mathrm{S}}(r_j)$, and $R_{\mathrm{bg}}(r_j)$ are fitted separately for each subdivision, while m_ν^2 is shared between all fits. There is, however, a variety of additional fit parameters.

In KATRIN, four parallel strategies are used [5, 93] to obtain a result. In addition, a novel neural network fitting procedure reduces the computational load by three orders of magnitude [94].

Systematic uncertainties can, for example, be included via covariance matrix approach: While the diagonal matrix entries contain uncorrelated uncertainties for each data point $R(qU_i, r_j)$, the off-diagonal entries take correlated uncertainties between different data points into account. The covariance matrix is pre-computed with $O(10^4)$ simulated spectra and the systematic parameters are varied within their uncertainty probability density.

Another way to consider systematic uncertainties in the neutrino mass analysis is by utilization of pull terms, which are added as a penalty to the χ^2 function and are composed of the squared difference of the parameter value and its expectation, divided by the squared uncertainty value.

Systematic uncertainties can further be included via Monte Carlo propagation, where –

in statistically randomized Monte Carlo spectra – single systematic parameters are varied within their probability density function. The resulting randomized model is fitted to a reference spectrum for the systematic uncertainty breakdown. When the randomized model is fit to the data, the resulting likelihood value is used to weigh the corresponding sample.

The fourth strategy applies a Bayesian analysis. The spectrum is calculated as in the previous strategy and systematic uncertainties are mainly included via model variation technique [5].

When all systematic uncertainties are included and the fitting teams, which apply different strategies and software, agree on their results on model-blinded data, the neutrino mass result is inferred from the best-fit value to non-blinded data. Many experiments throughout the history of kinematic neutrino mass measurements delivered negative best-fit values, which is only allowed as an extension of the model. The confidence belt for experiments with low count rates is typically calculated with the Feldmann-Cousins approach. There, larger negative best-fit values lead to stricter upper limits. In KATRIN and its predecessors, however, most of the systematic uncertainties – if unaccounted for – lead to a larger negative best-fit values. Since negative m_ν^2 results are unphysical, the specifically designed Lokhov-Tkachov approach enables to set a more conservative upper limit on m_ν, even if the best-fit value reaches particularly negative values [95].

The first measurement campaign of the KATRIN experiment started in spring of 2019 and lasted four weeks. The source activity was reduced to approximately 25% of the nominal value, since methane-freezing within the tritium injection capillary did not allow stable operation at the nominal source activities. 117 out of 148 detector pixels were used for the final analysis [5]. The data was combined to a single spectrum and delivered a best-fit value of $m_\nu^2 = -1.0^{+0.9}_{-1.1}\,\mathrm{eV^2/c^4}$ with the endpoint at $E_0 = 18573.7(1)\,\mathrm{eV}$ [84]. The upper limit $m_\nu < 1.1\,\mathrm{eV/c^2}$ (90% C.L.) was obtained with the confidence belt according to Lokhov-Tkachov.

The second measurement campaign was carried out during fall 2019. A higher source activity of 75% of the nominal value was achieved and the scan time was increased by 30% [5]. The largest uncertainty, which was the radon-induced non-Poissonian background, was reduced by a bake-out of the radon-removal system. The 25% lower background and an optimized high-voltage reproducibility allowed a stronger best-fit value $m_\nu^2 = 0.26^{+0.34}_{-0.34}\,\mathrm{eV^2}$ with the endpoint $E_0 = 18573.69(3)\,\mathrm{eV}$ and yielded an upper limit of $m_\nu < 0.9\,\mathrm{eV}$ (90% C.L.) for both, Feldmann-Cousins and Lokhov-Tkachov, confidence belt construction approaches. A combination of both campaigns delivered the (to date) most stringent upper limit on the neutrino mass from kinematic measurements of $m_\nu < 0.8\,\mathrm{eV}$ (90% C.L.)[6] [5].

In both measurement campaigns the statistical uncertainties exceeded the systematic uncertainties. The largest systematic uncertainty stemmed from an elevated radon-

[5]The pixels on the outer rings are typically not usable for neutrino mass measurements due to increased noise or misalignments between WGTS and FPD [67].

[6]The value is rounded to the digit where both frequentist methods agree

background, which induced a (partially) non-Poissonian distributed background rate and, thereby, enlarged the statistical uncertainty [5], see section 3.3.1. Variations in the source potential impact the energy scale and were, therefore, considered as another highly-relevant systematic uncertainty. Also, a background component from a Penning trap between the spectrometers was deemed a major systematic uncertainty, since it induces a higher background count rate with larger scan-step-duration, which may be mistaken for a neutrino mass signal. Background-related systematic uncertainties were among the largest contributors to the systematic error budget. Refining the knowledge of the background generation mechanisms and reducing the background is crucial for future campaigns.

3.3 Background

The statistical uncertainty δm_ν^2 of the squared neutrino mass depends on both, the signal and the background count rate. The approximate formula

$$\delta m_\nu^2 c^4 \approx \left(\frac{16}{27}\right)^{1/6} r^{-2/3} b^{1/6} t^{-1/2} \tag{3.3.1}$$

shows that the uncertainty decreases stronger with signal rate than it increases with background rate [6]. It is, however, of utmost importance to decrease the background count rate: With currently approximately 140 mcps it is significantly higher than the value of 10 mcps that is stated in the design report [6] and, therefore, introduces further systematic uncertainties.

An overview of the most important mechanisms of background creation, its treatment and, in the best case, its mitigation are explained here.

3.3.1 Overview

There are various sources of background in the KATRIN experiment, of which many are well understood and under control. The greatest concern of KATRIN in terms of background are charged particles of low and high energies within the spectrometer. Low-energetic electrons can reach the detector, if they have (just) enough energy to overcome the retarding potential, or if they are born downstream of the analyzing plane. Further, trapped high-energetic charged particles scatter with residual gas and finally induce low-energetic secondary electrons, as well. Low-energetic are accelerated towards the detector in conjunction with the signal electrons, so that both end up at approximately $E = 18.6\,\mathrm{keV}$, leaving them indistinguishable by energy for the FPD with its energy resolution of $\Delta E \approx 1.5\,\mathrm{keV}$ at this energy.

There is only a small contribution of cosmic-ray muons and of γ-radiation, which can introduce false counts from secondary electrons produced within the spectrometer. The majority of muon-induced or γ-induced secondary electrons is hindered from entering the spectrometer by the efficient magnetic and electrostatic shielding [96, 97].

Low-energetic (negatively) charged particles can be trapped if they are created in a potential that is smaller than the surrounding potential, so that the Lorentz force binds them radially. Electrons that move through this region and lose energy can be trapped, as well. Such a trap used to be prevalent in the space between the pre- and main spectrometer. An accumulated amount of trapped particles can lead to a discharge, which may have severe consequences if it, for example, induces a high-voltage breakdown or damages the detector. The Penning trap between the spectrometers can be emptied by so-called electron catchers, i.e., grounded metal rods that are moved through the flux tube radius [85]. The background from Penning traps is especially critical, since the duration of the high-voltage-steps is chosen longer close to the endpoint. Thus, an unaccounted Penning background will resemble a neutrino-mass-like signal. The pre-spectrometer was grounded from 2021 in order to close the Penning trap.

The main spectrometer's entrance and exit magnets act as a magnetic bottle for high-energetic charged particles, which can be trapped within the spectrometer volume due to their magnetic field-induced decollimation to pitch angles larger than 90°, see eq. (3.1.9). The ultra-high vacuum of 10^{-11} mbar allows very efficient trapping, since scattering is efficiently prohibited. Upon scattering, they can ionize residual gas atoms and generate low-energetic electrons, which can find their way to the detector and induce background events. These high-energetic charged particles stem from α-decays of radon, which is emanated from the non-evaporable getter pumps [98, 99]. ^{219}Rn with a half life of ($T_{1/2} = 4\,\mathrm{s}$) will decay in the main spectrometer, while ^{220}Rn ($T_{1/2} \approx 56\,\mathrm{s}$) and ^{222}Rn ($T_{1/2} \approx 3.8\,\mathrm{d}$) will be pumped out. The background events from radon α-decays are typically detected as clusters of events, i.e. in a non-Poissonian temporal distribution, and in principle reducible via analysis cuts. Radon is prevented from entering, in the first place, via cold traps in the spectrometer, where it decays before it can enter the spectrometer [100, 101].

The mitigation of radon-induced background is further efficiently provided by an altered electromagnetic field configuration of the spectrometer, the so-called shifted analyzing plane (SAP), that is explained in section 3.3.3.1. It was intended as a countermeasure against the largest share of background, which is the result of the radon-contamination of the spectrometer surfaces during the experiment assembly, but also proved to be efficient in reduction of radon-induced magnetic trapping.

The surface contamination with radon during installation of the inner electrode system of the main spectrometer leads to the so-called "Rydberg background", i.e. secondary electrons from the black body radiation (BBR)-induced ionization of highly excited states prevalent in the spectrometer, see section 3.3.2. It is indistinguishable via energy, as it possesses energies of the same order as the β-decay electrons. According to the Rydberg background generation model [62, 63], its angular distribution at the detector will be significantly sharper than the β-decay electrons.

In the history of KATRIN, direct or indirect measurements of the energy spectrum of the background were attempted with different methods [64, 102, 103]. The $\sim 1.5\,\mathrm{keV}$ energy resolution of the FPD makes other means of energy measurements necessary.

Electron traps were released via blocking potentials in a slightly changed electromagnetic field configuration [102]. These suggest a background energy spectrum that consists of mainly low-energetic electrons, but also contains energies significantly larger ($\mathcal{O}(1\,\mathrm{eV})$) than expected from BBR-induced Rydberg ionization electrons ($< k_\mathrm{B}T > \approx 0.025\,\mathrm{eV}$).

Another measurement was the artificial creation and stepwise opening or closing of electric and magnetic traps [103]. There, a significant part of E_bg, again, lies above the BBR-induced Rydberg-ionization energies.

Finally, the measurement of the angular distribution of the background is an important indication of the prevalent production mechanism. That was – in a first measurement campaign and with subsequent campaigns in preparation – attempted in [64]. Due to experimental limitations, the angular distribution was not determined exactly. However, it was found that the energy distribution is most likely larger than that of BBR-induced Rydberg-ionization energies. That makes alternative background production mechanisms of electron energies above the prediction from Rydberg background hypothesis and below the spectrometer resolution necessary. The generation of auto-ionizing states may explain the elevated energies [64], see section 3.3.2.

3.3.2 Rydberg background

Secondary electrons from ionization of Rydberg atoms are a straightforward way to link α-activity to KATRIN's background from low-energetic electrons in the spectrometer: The Rydberg atoms in the main spectrometer most likely originate from the 5-year installation period of the inner electrode when the spectrometer was in contact with dust-filtered, but not radon-filtered ambient air [63]. The Rydberg background mechanism is shown in figure 3.9. ^{222}Rn adsorbed onto the spectrometer surfaces. ^{218}Pb from its α-decay was implanted into the surface where subsequent decays lead to ^{210}Po, which finally decays to ^{206}Pb. The ^{238}U-decay chain is shown in figure 3.10. The high recoil of this α-decay can sputter off many secondary electrons and atoms, mainly hydrogen and oxygen that are partly in excited states, as shown in simulations based on SRIM[7] in [62]. Charged particles are efficiently reflected by the inner electrode potential. Neutral atoms pass the electromagnetic barrier of the inner electrode. They can be in highly-excited Rydberg states, which are characterized by a large quantum number n.

The ionization of Rydberg atoms via BBR-photons is described in [62]. The Rydberg atoms have small binding energies,

$$E_n = -\frac{E_R}{n^2} = -\frac{13.6\,\mathrm{eV}}{n^2}. \tag{3.3.2}$$

so that they can be ionized via BBR and, upon ionization, emit low-energetic electrons. These electrons, typically, have energies below 0.15 eV [62]. The half-life is long enough for Rydberg atoms to distribute in the spectrometer, but there is a significant radial

[7] Simulation software for stopping and range of ions in matter [105].

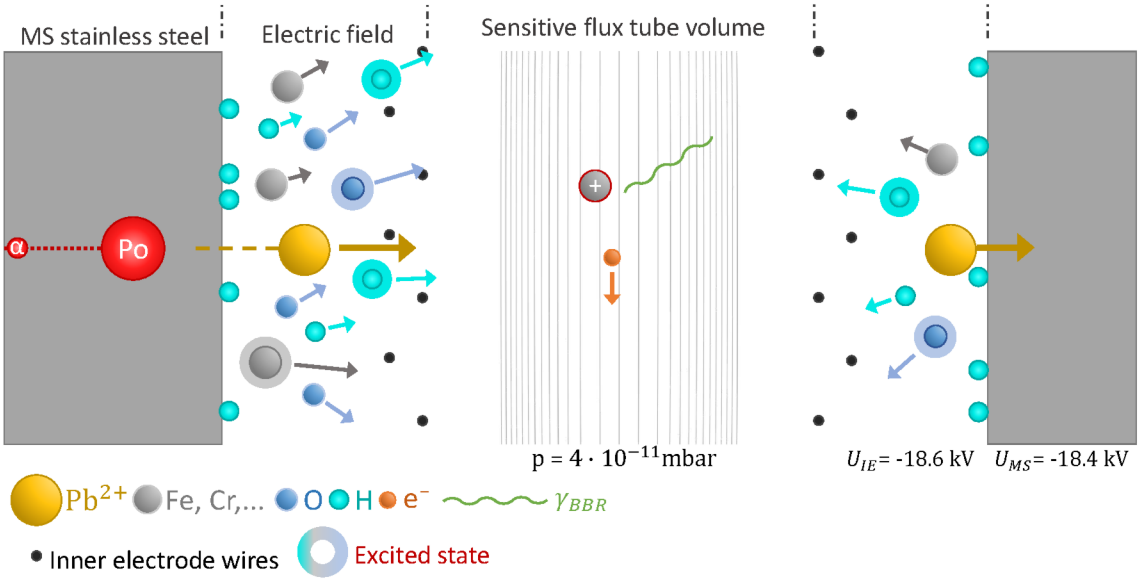

Figure 3.9 – Rydberg background process mechanism. The decay of ^{210}Po sputters of charged and uncharged particles from the main spectrometer walls – either directly upon decay or at the impact site of the daughter nucleus. Neutral highly-excited Rydberg atoms can overcome the electric field provided by the inner electrode and reach the flux tube volume, where they emit low-energetic electrons. If the de-excitation occurs downstream of the analyzing plane, the emitted electrons are accelerated towards the detector, where they are indistinguishable from β-electrons. Image taken from [61].

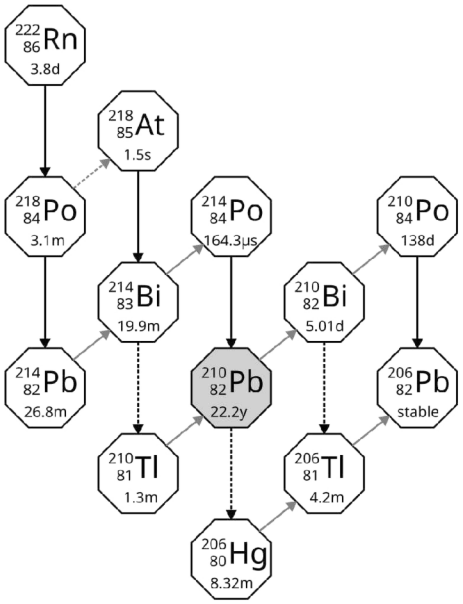

Figure 3.10 – ^{222}Rn-decay chain. β-decays are shown as grey arrows and α-decays black arrows. The Rydberg background is produced by the decay of ^{210}Po (highlighted in grey) within the inner surface of the spectrometer. The diagram is based on [104].

dependence of background events on the detector, indicating that background comes from the outer region of the spectrometer. Measurements with ^{228}Th and ^{223}Ra show that α-activity on the inner spectrometer is associated with an elevated background and

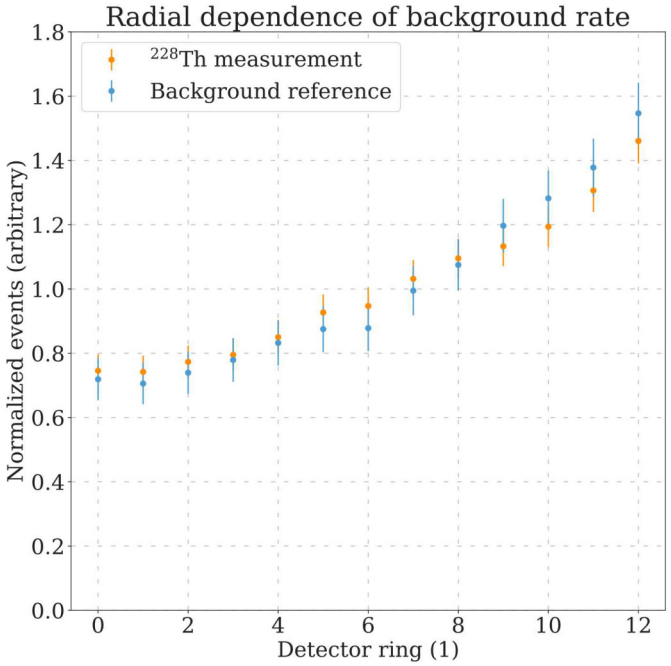

Figure 3.11 – Radial dependence of artificial α-background and spectrometer background rate, normalized [63]. Both measurements show an increased background component from the outer pixel-rings of the detector. The similarity of the curves may indicate a similar production mechanism, as supposed by the Rydberg hypothesis.

shares further properties like the radial dependency, see figure 3.11, and inner electrode offset potential[8] dependency with the actual main spectrometer background [63]. The volume downstream of the analyzing plane is critical: Electrons from this volume are very likely to hit the detector, which is very unlikely for any low-energetic electron that was born elsewhere. The downstream-volume dependency of the background-contribution was, further, measured accurately during the search for an optimal setting of the shifted analyzing plane, see section 3.3.3.1.

In order to derive the expected angular distribution of Rydberg background electrons in the magnetic field of the detector, simulations from [62] are combined with electron tracking simulations by C. Weinheimer, which were further developed in [106]. The energy distribution of the sputtered atom species from the stainless steel surface of the spectrometer is found in figure 3.12. The electron energy from photoionization via BBR is shown in 3.13 for different initial quantum numbers n. Further, the quantum number n distribution of electrons that reach the detector is shown in 3.14. The energy spectrum of these electrons in the analyzing plane is derived directly. The kinetic energy of the Rydberg atom itself adds a Doppler broadening to the initial energies of the ionization electrons in the laboratory system. Only the main elements, oxygen (64%) and hydrogen (36%), are considered for the calculation of the angular distribution of background electrons [106]. It is assumed that the Rydberg atoms are emitted via $\cos\theta$-distribution with θ being the emission angle to the

[8]The inner electrode on the inside of the spectrometer walls is used for fine-tuning of the retarding potential and shielding of the inner volume against charged particles from the walls, see 3.1.2.

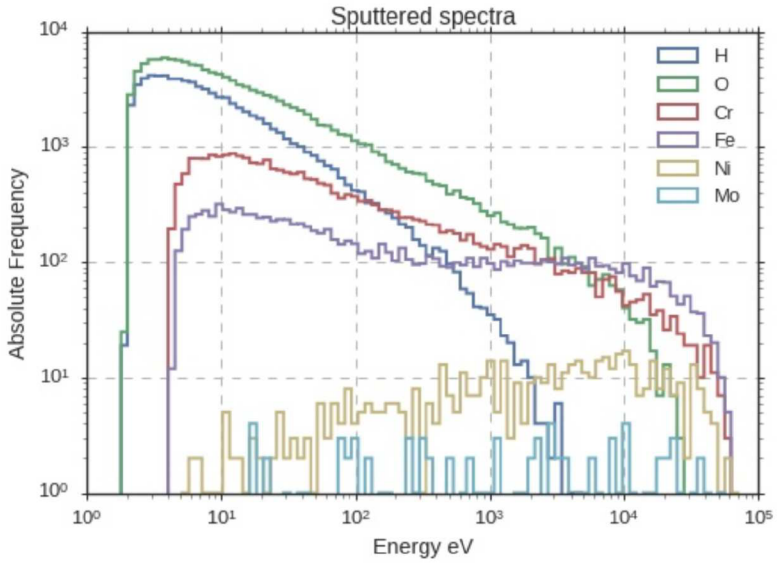

Figure 3.12 – Energy spectra of the atoms sputtered off the spectrometer wall by the recoil of the ^{206}Pb decay [62].

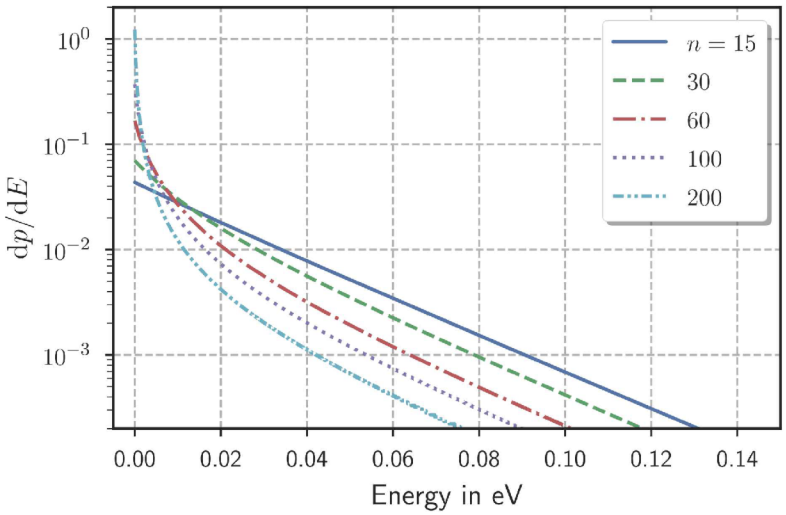

Figure 3.13 – Energy spectra of electrons from BBR-induced photoionization for different quantum numbers n (at $l = 1, T = 293\,\mathrm{K}$) [62].

spectrometer wall perpendicular to the beam axis. The distributions of electrons from the Rydberg-ionization of oxygen and hydrogen are weighted with the respective occurrence of oxygen and hydrogen. The velocity of the ionization electron in the Rydberg atom system is calculated via isotropic emission in the analyzing plane[9] before it is Doppler-shifted to the laboratory system. The surface binding energy (2 eV for hydrogen and oxygen) is subtracted, as SRIM gives the energy within the surface. On their way to the detector the electrons gain kinetic energy of ≈ 18.6 keV from the potential difference[10]. Ultimately,

[9]The distribution within the whole spectrometer volume would be more exact. The result, therefore, has to be taken as upper limit estimation of the angular distribution.

[10]In order to maximize the difference between signal and Rydberg background, the post-acceleration is

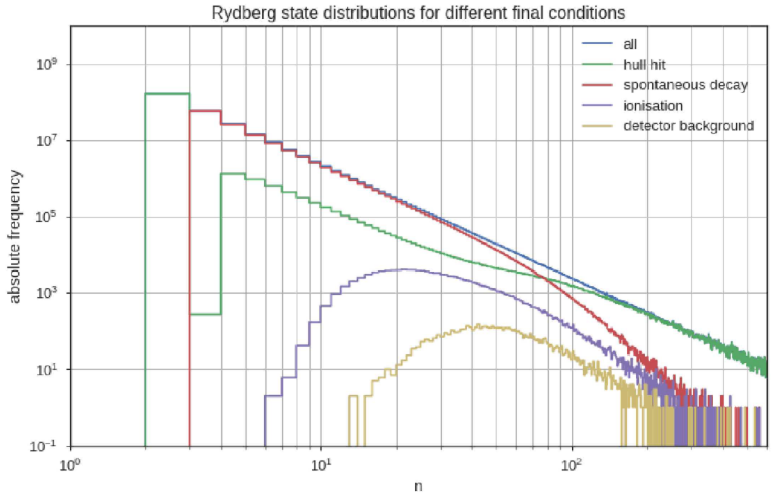

Figure 3.14 – Quantum number n distribution of Rydberg states in the spectrometer [62]. Only the "detector background"-labeled states induce background counts at the detector.

the angular distribution of the Doppler-broadened Rydberg background electrons at the detector can be calculated via adiabatic guidance of electrons from the analyzing plane to the detector and equation 3.1.6. The expected angular distribution at the detector is shown in figure 3.15.

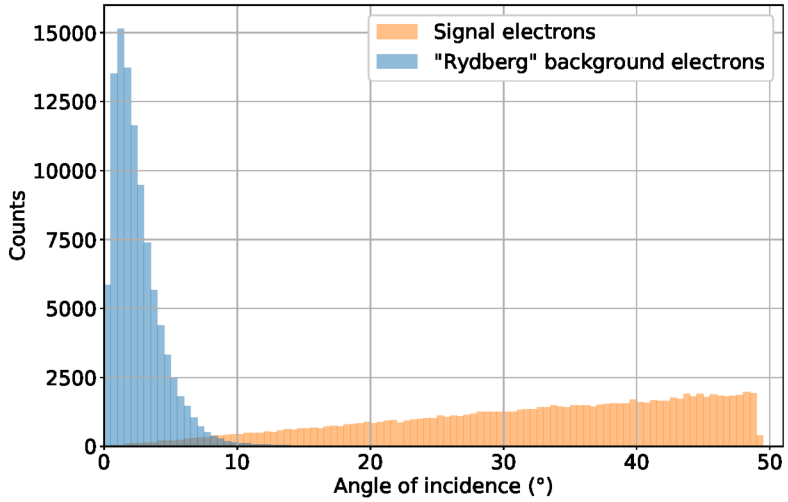

Figure 3.15 – Simulation of the angular distribution at the detector of 10^5 Rydberg background electrons and β-electrons in a magnetic field of 2.4 T [106]. The simulation of the Rydberg background is based on [62]. As figure 3.12 reveals, the majority of sputtered atoms consists of oxygen and hydrogen, which are considered in the simulation with a fraction of 64 % and 36 %, respectively. Other species are neglected. The Doppler-broadening due to movement of Rydberg atoms is included.

assumed to be inactive. Otherwise, another 10 keV of kinetic energy need to be added.

3.3.3 Rydberg Background Reduction Strategies

The electrons from Rydberg background are energetically indistinguishable from tritium β-decay electrons. That means, other strategies than energy separation are necessary. The reduction of the volume downstream of the analyzing plane by the SAP-configuration proved to be very successful, as section 3.3.3.1 describes. Further, the nature of the Rydberg states allows THz-radiation-induced transitions. Section 3.3.3.2 explains how a cascade of THz sources may prove successful to de-excite Rydberg atoms and reduce the associated background.

It is in principle possible to exploit the time-of-flight to gain information on the β-electrons and, thereby, generate a differential spectrum[11] [107, 108].

A promising method for background reduction is possible due to the sharp angular distribution of the Rydberg background electrons at the detector: Geometrical suppression of small pitch angles is obtained, when electrons are mainly measured in a plane with surface normal perpendicular to the magnetic field lines: Electrons of small pitch angles (i.e., of small transverse energy) will not hit the detecting surface, while electrons of large pitch angles that possess a significant transverse energy are measured. The currently installed FPD obtains a plane surface perpendicular to the field lines and will measure electrons of all pitch angles. Therefore, a significant modification of the detector would be required for this kind of background suppression. A suggested kind of modification is the active transverse energy filter (aTEF) concept, which is described in more detail in section 3.3.3.3. Development of the aTEF concept and fabrication and examination of first prototypes is the main topic of this work.

3.3.3.1 Shifted Analyzing Plane

The elevated background of > 350 mcps during the first tritium campaign [84] lead to the decision of increasing the magnetic field in the analyzing plane and, thereby, reducing the flux tube volume in the main spectrometer. Since low-energetic electrons do not have enough energy to overcome the retarding potential the fiducial volume between detector and analyzing plane is crucial: Low-energetic electrons released there contribute to the background. An alternative, asymmetric field configuration – so-called shifted analyzing plane (SAP) configuration, which was introduced in [102] – allows to further reduce the flux tube volume between detector and analyzing plane. Extensive tests lead to a background reduction by a factor of 2 [81] by shifting the minimum of the magnetic field and the maximum of the absolute retarding potential, i.e. the analyzing plane, towards the detector and, consequentially, reducing the flux tube volume. Even stronger background reduction

[11] That requires large efforts: Either, a longer flight path and fast-switching electric fields are necessary for the time-focusing time-of-flight method presented in [107], or, the development of an "electron tagger" device in order to register electrons with a certain starting energy is required for the method presented in [108]. This registration must, either, only alter the energy by an insignificant amount, or, cost a fixed amount of energy. The electron tagger development is actively driven within the KATRIN collaboration and was subject of studies [108, 109].

would, in principle, be possible [81]. The trade-off between background level, energy resolution, and field homogeneity in the analyzing plane, however, lead to the decision for the current SAP configuration. The magnetic field minimum and the electric potential maximum do, other than in the very symmetric normal analyzing plane, not lie at the same z-position. They are shaped in a curve, as indicated in figure 3.16 (top).

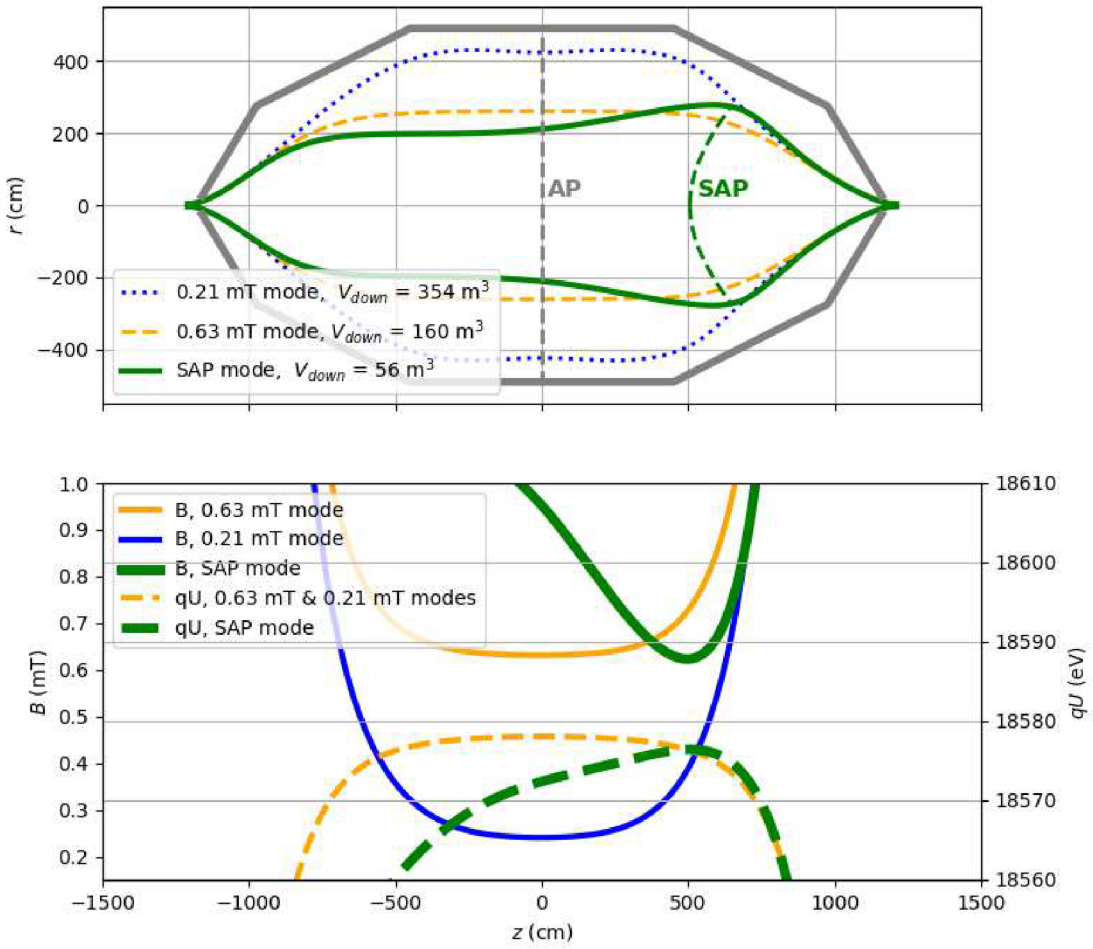

Figure 3.16 – The upper panel shows the originally proposed analyzing plane (AP) in conjunction with the optimized shifted analyzing plane (SAP) configuration of the KATRIN main spectrometer [81]. The lower panel shows the associated magnetic field strength and electric potential, orange for the AP configuration and green for the SAP configuration. The curved shape of the SAP is caused by the radial dependence of the z-position of potential and magnetic field minimum. The resulting transmission function broadening can be compensated by dividing the FPD pixels into certain patches of similar transmission conditions.

The increased field variation can be accounted for by utilizing the pixelization of the FPD. The computational load of the neutrino mass analysis in comparison to a fully pixel-wise

analysis can be reduced when groups of pixels are analyzed in patches[12] that have common differences in fields of $\delta B \leq 0.014\,\mathrm{mT}$ and $\delta qU \leq 0.25\,\mathrm{eV}$ [81]. The improvement on the squared neutrino mass sensitivity from the background reduction in the SAP configuration is about 13 % [81]. Further, the trapping conditions in the SAP-configuration are worse than in the original field configuration, so that there is a lower prevalence of radon-induced trapped electrons. That eliminates the non-Poissonian overdispersion of the background, since the number of time-correlated events per primary electron is significantly reduced [81].

The SAP configuration became the default operation mode after successful, extensive tests since 2020 [81].

3.3.3.2 THz Radiation

The excited state of Rydberg atoms is susceptible to manipulation with THz radiation [110, 111]. The Rydberg-state distribution from the predominant charge-exchange sputtering mechanism tends to be of low principal quantum numbers n and high angular quantum numbers l [61, 62]. Rydberg atoms can undergo spontaneous decay, BBR-induced (de-)excitation, or BBR-induced ionization.

The aim of using THz light sources of appropriate frequencies is to induce multiple $\Delta n = -1$ transitions to shorter-lived states, as indicated in figure 3.17, since the decay time $\tau = n^3 l(l+1) \cdot 10^{-10}\,\mathrm{s}$ is proportional to n^3 [61]. It is inevitable, that the THz irradiation ionizes lower excited states and, thereby, elevate the background level. Narrow-band sources may reduce the amount of this effect.

While eight sources of $5\,\mathrm{mW\,m^{-2}}$ power for transitions from $n = 32$ to $n = 24$ could reduce the Rydberg background by $> 50\%$, this kind of source with high power is not easily available [61].

3.3.3.3 aTEF

The aTEF is a novel concept proposed by Christian Weinheimer that allows angle-selective electron detection within KATRIN's conditions [106]. Conventional methods of angle-selective electron detection are, e.g., gas-filled drift chambers, $\Delta E/E$-arrangements, or trace reconstruction via (multiple) thin-layered Si-detectors as they are used at particle accelerators. Different methods of angle-dependent electron detection and reasons for prohibition within KATRIN are described in [106]: The low electron energy of up to 18.6 keV in tritium decay prohibits the use of a window between the main spectrometer and the detector, i.e. gas-filled drift chambers cannot easily work. Further, the electrons are absorbed in a few µm of silicon, so that a trace reconstruction via layered Si-detectors is hardly possible with today's detectors. For $\Delta E/E$-arrangements the amount of energy loss in a thin detector before the main detector allows estimation of the angle. The tritium

[12] Ideally, every patch should contain a ringwise structure of pixels. Due to misalignments, these patches are slightly displaced and broadened.

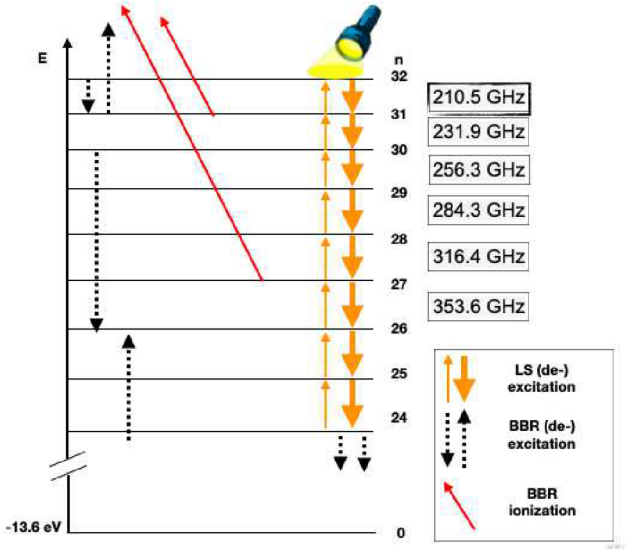

Figure 3.17 – Simplified diagram of Rydberg state binding energies and transition. The de-excitation rate via the THz light source (LS) is considered to be five orders of magnitudes higher than the ionization rate via black body radiation (BBR) [61].

decay electrons, again, are too low-energetic for these detectors. The large magnetic field of 2.4 T and the resulting cyclotron motion – tightly wound with sub-mm radius around the magnetic field line – give further constraints on usable detector types.

These constraints are met by the aTEF concept – an active (i.e., detecting) microstructured filter made from parallel channels of certain diameter with axes parallel to the magnetic field lines. It is based on a passive variant, the transverse energy filter (TEF), that is explained in detail in section 4.1 and was inventend by R.G.H. Robertson. Electrons with small pitch angles are suppressed due to the, for the most part, elimination of active areas with surface normal parallel to the field line. The active surface normals are parallel to the field lines and, thereby, allow detection of electrons with higher probability when they have a larger pitch angle. The general idea can be illustrated at the example of a microchannel plate (MCP) detector placed in front of KATRIN's FPD, as shown in figure 3.18. Electrons can either enter the MCP and travel through without interaction, or they are absorbed in the channel wall upon impact. In the first case, they are counted by the FPD, but in the latter case a secondary electron avalanche is triggered, which induces a distinguishable signal in the FPD. Thereby, differentiation of electrons based on their pitch angles becomes possible in KATRIN's environment. The geometry of an aTEF needs to be tailored to KATRIN's background, but knowledge on the actual composition is complicated to measure, see 3.3.1. The neutrino mass sensitivity is to be maximized, that means the reduction in background and signal needs to be carefully balanced. The knowledge of the background angular distribution can be investigated with a passive transverse energy filter (pTEF), as explained in section 4.1.

This work is devoted to the development of the concept, including prototyping and

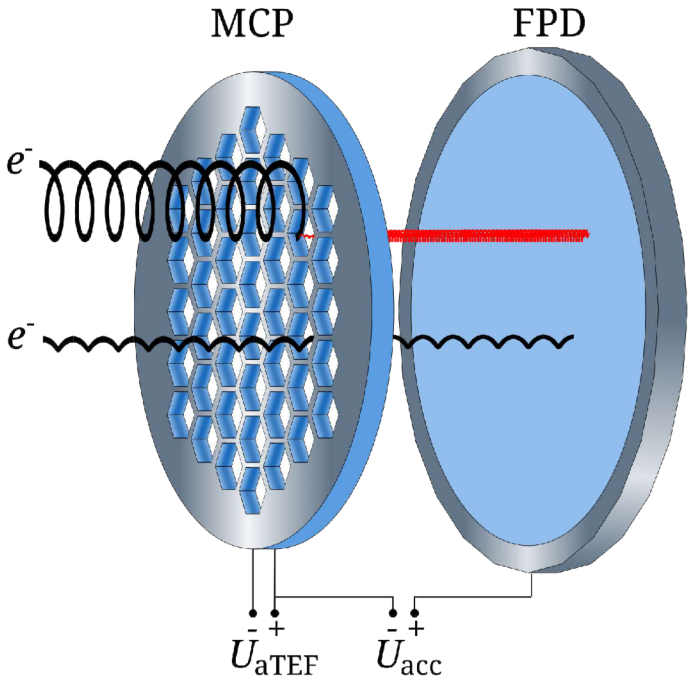

Figure 3.18 – MCP-aTEF in front of KATRIN's FPD. Electrons of small pitch angles have a higher chance to reach the detector without interaction with the MCP-aTEF. Electrons of large pitch angles are more likely to induce a secondary electron avalanche (red) in the MCP-aTEF, which is generated by the bias voltage U_{aTEF} and accelerated by U_{acc}. The electron avalanche will arrive at the detector with a larger spatial and temporal distribution. Its total signal imprint on the FPD will be different from the primary electron's energy. That allows to differentiate background electrons and β-electrons.

testing of first aTEF detectors. Deeper investigation of the influence of the geometry and detection efficiency on the neutrino mass sensitivity will be examined in [69], where additional post-processing steps and extended prototype tests will be described.

4 Angle-selective Electron Filtering and Detection

This chapter summarizes different concepts of angle-selective measurement methods in the frame of Transverse Energy Filters (TEF) within the specific requirements of the KATRIN experiment. These ideas sparked from the narrow angular distribution of Rydberg background electrons at the detector that is predicted by the Rydberg hypothesis, see chapter 3.3.2. They can be grouped into passive and active filters: A passive transverse energy filter, pTEF or – originally – TEF, acts as a physical barrier that shields electrons from the detector. An active transverse energy filter, aTEF, measures electrons with large incident angles[1] while it allows differentiation or suppression of electrons with small incident angles.

The chapter gives an overview on approaches to implement both concepts and their proof-of-principle realization in a test setup. In section 4.1 the passive electron filters are described as motivation of the aTEF. The first aTEF concept based on microchannel plates is introduced in section 4.2 and a demonstration experiment for the pTEF and aTEF is described in section 4.3. Lastly, further aTEF concepts are illuminated in section 4.4.

4.1 Overview on passive Transverse Energy Filters for KATRIN

The passive filters were envisioned in two varieties that should be installed in front of the detector in a homogeneous magnetic field: They are either intended to increase the signal-to-noise ratio [112], or to directly measure the angular distribution of the background. The original TEF idea was proposed as measure to increase the signal-to-noise ratio. The pTEF was a subsequently expressed idea to assess the angular distribution of background electrons at the detector. The pTEF is named "passive" to differentiate it from the "active" filters. The original, eponymous TEF is a passive filter, too. This section differentiates between the TEF, which was not implemented, and the pTEF, which was manufactured and used in KATRIN [64].

[1] "Incident angle" means the angle of the incoming electron to the normal of the focal plane of the detector. In KATRIN, electrons of large transverse energy possess a larger pitch angle to the magnetic field line.

4.1.1 TEF for Background Reduction

The idea of Transverse Energy Filters within KATRIN was introduced by R.G.H. Robertson[2]: The intended position of the TEF was a homogeneous magnetic field between the detector and the pinch magnet of the beamline at the PULCINELLA disc[3], see figure 3.5. The original TEF should consist of two layers of slit arrays with width-to-space-ratio of 50:50. Both layers are shifted, so that the direct line-of-sight is blocked. Such a two-layered grid can decrease the number of electrons with small transverse energies and, consequently, small pitch angles, that reach the detector. That is illustrated in figure 4.1. With the electromagnetic field configuration stated in the design report the fraction of background electrons from Rydberg atom decays in the main spectrometer could be reduced by more than 95% at the cost of a $\sim 73\%$ loss of signal rate [112] with such a device. Such a strong signal reduction would have a detrimental effect on KATRIN's neutrino mass sensitivity, which lead to discarding the original concept [112].

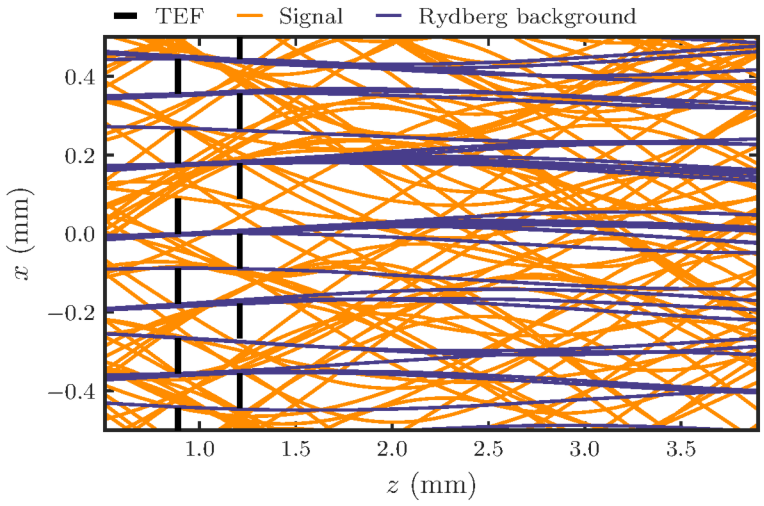

Figure 4.1 – TEF concept. Grid (black) in front of the focal plane detector, in a magnetic field of maximal homogeneity, which points in z-direction. The electrons spiral around their respective field line in a cyclotron motion that is, in 2d, projected onto a sinusoidal trajectory. The signal electrons from tritium β-decay (orange) have a higher probability of transmission than the Rydberg background electrons (blue). Only the electrons that were not blocked by the TEF are depicted. The combination of two layers efficiently blocks electrons of small pitch angles.

However, an improvement in signal retention and background reduction compared to the original TEF can be reached by adding layers to the two-layered grid, as suggested by C. Weinheimer. The width-to-space ratio of each of the n layers would be $1/(n-1)$ in order to block the direct line of sight without overlap of the layers. The concept was further elaborated in a Monte Carlo study within this work: The background was, for

[2]Center for Experimental Nuclear Physics and Astrophysics and Department of Physics, University of Washington, Seattle, WA 98195, USA.

[3]The PULCINELLA is a device that can be used as Faraday cup to precisely measure currents from different sources upstream of the beamline [67, 89].

simplicity, modeled as electrons of $E_{\mathrm{Ryd}} = 25\,\mathrm{meV} \approx k_{\mathrm{B}}T$ energy, which is a typical energy according to the Rydberg background model. They were isotropically emitted in the analyzing plane of the spectrometer and adiabatically guided to the TEF via eq. (3.1.6). The relevant magnetic field of the source, the spectrometer, and at the TEF-position were $B_{\mathrm{source}} = 2.52\,\mathrm{T}$, $B_{\mathrm{ana}} = 0.6\,\mathrm{mT}$, and $B_{\mathrm{TEF}} = 0.517\,\mathrm{T}$.

The approximate neutrino mass sensitivity[4] – as shown in a m_ν-sensitivity study under consideration of only statistical errors and with Monte Carlo data of the third neutrino mass campaign (KNM3) and electrons filtered via an analytical model of the TEF – is impacted by the reduction in signal and background amplitude. All TEF-variants worsen the statistical neutrino mass sensitivity, as table 4.1 shows. A higher number of stages was

Table 4.1 – Influence of a hypothetical TEF of two, three, or four layers in front of the focal plane detector. The distance and width of the layers was varied and optimized for signal retention. The sensitivity worsens by 34% to 64% if a TEF is considered, which deems it as unfavorable background reduction method.

Number i of TEF layers	**2**	**3**	**4**
Signal reduction (%)	74	68	66
Rydberg background reduction (%)	95	93	95
$\Delta m^2_{\nu,\mathrm{TEF},i}/\Delta m^2_{\nu,\mathrm{ref}}$	1.64	1.46	1.34

not simulated, since the alignment of the TEF layers to each other and to the magnetic field lines would be drastically more difficult with more layers. In the end, the unaltered beamline, i.e. without the TEF, delivers the best statistical neutrino mass sensitivity, even though the normal analyzing plane configuration with especially high background contribution was considered.

While it is crucial to reduce the background, only a very limited reduction of the signal is allowed in order to preserve the statistical sensitivity. The TEF as a multilayered grid in the beamline in front of the detector is, therefore, not suited to approach KATRIN's design neutrino mass sensitivity. However, it sparked the development of the aTEF, which aims to overcome the limitations of the TEF, and of the pTEF, which is used to further characterize KATRIN's background.

[4]The influence on the sensitivity is evaluated via means of the 1σ-interval of the statistical uncertainty. The KATRIN beamline parameters (electric and magnetic field configuration, analyzing plane position, pixel positions, etc) are taken from the file `GlobalKNM3Simulation-PeriodSummary_Jul2020b_18600V_6.0G-000002.json`. The KATRIN neutrino mass run #63308 with the run summary file `RunSummary-Prompt6e-fpd0063308.json` was taken as reference run for the Monte Carlo study. The generated data corresponded to three years of measurement time and was fit with the `KaFit` program in `KASPER v3.5.0`. Systematic errors, e.g. misalignment of the TEF, backscattering from its surface, or others are not included. The column density was assumed to be at 75% of its nominal value. The spectrometer was assumed to be operated in the nominal analyzing plane mode and not in the optimized SAP mode, as explained in section 3.3.3.1. The background rate without TEF was 293 cps, which was taken from the first measurement campaign of KATRIN [84].

4.1.2 pTEF for Background Characterization

The angular distribution of the Rydberg background electrons at the detector is based on the experimentally supported Rydberg hypothesis, as described in chapter 3.3.2. However, the direct measurement of the angular distribution relies on sophisticated methods, since KATRIN's focal plane detector is not able to resolve the incoming electrons by their incident angles directly.

4.1.2.1 Original pTEF Idea

Based on the TEF and aTEF ideas, the pTEF was proposed on the 39th KATRIN collaboration meeting by K. Gauda [113] with the aim to directly obtain information on the angular distribution with a passive structure. A filter with i radially separated sections would show a different response $R(\theta_{\text{inc}})$ for electrons of incident angle θ_{inc}, see figure 4.2. A region of homogeneous magnetic field throughout the flux tube diameter, behind the

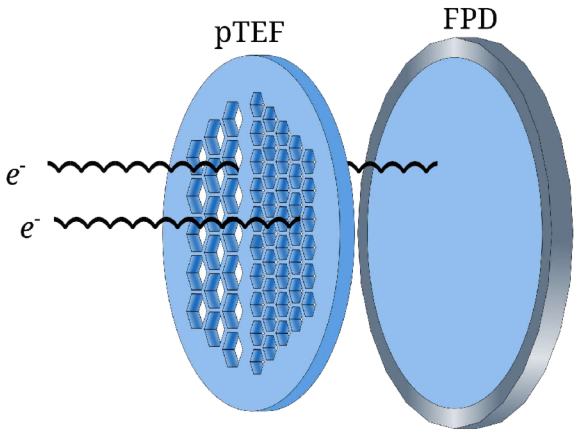

Figure 4.2 – An exemplary pTEF could posses different segments, here $i = 2$. Electrons of a certain pitch angle have different probabilities to pass the different segments. The count rate on the focal plane detector (FPD) behind different segments will contain information on the shape of the background angular distribution. It will, however, affect the statistics (per segment), so that a long measurement period or complementary measurements become necessary.

spectrometer and in front of the detector, would be a suitable location – for instance, the same location that was proposed for the TEF before. Each segment of the pTEF is perforated by channels of one certain diameter. The diameter of the channels differs between different segments. The transmission of electrons would depend on their cyclotron radii or pitch angles, as shown in 4.3. The transmission efficiency T_i per segment i is then given by

$$\boldsymbol{T} = \begin{pmatrix} T_1 \\ \vdots \\ T_n \end{pmatrix} = \int_0^{\theta} N(\theta_{\text{inc}}) \cdot \boldsymbol{R}(\theta_{\text{inc}}, E) \cdot \sin\theta \, \mathrm{d}\theta \tag{4.1.1}$$

with the angles θ_{inc} being drawn from the angular distribution N and $\boldsymbol{R}$ being the response of each segment of the pTEF to mono-angular electrons. $\boldsymbol{R}$ depends on the electron's

incident angle and its energy. This method may distinguish between different models of the angular distribution of the background. A more accurate measurement is achieved when a larger number of parameters is varied. The magnetic field in the analyzing plane, for example, changes the field in which the Rydberg background electrons are released and, thus, its angular distribution and the response. The magnetic starting field may, however, somehow influence the production mechanism of background electrons and has to be applied with care.

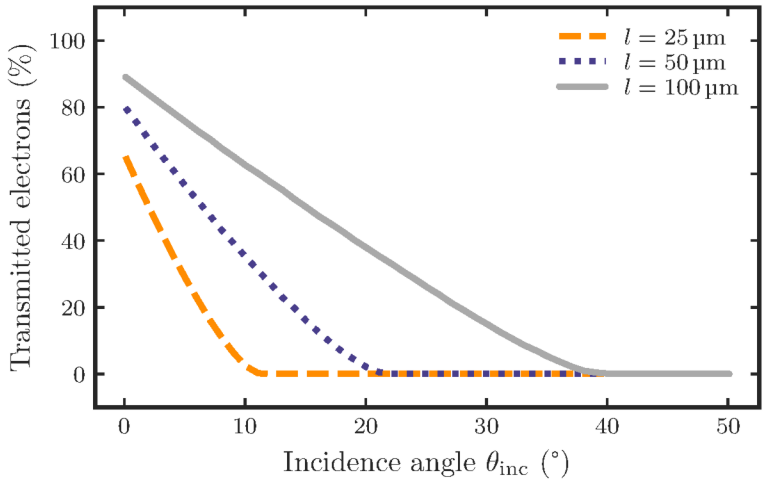

Figure 4.3 – The transmission probability of electrons through a pTEF segment depends on the electron incident angle θ_{inc} and the dimension of the single channels. In this simulation of 100000 electrons through a pTEF with hexagonal channels, the electrons which hit the pTEF are not transmitted. Other effects, e.g. backscattering, were not taken into account. A channel depth of 250 µm was simulated with different side lengths l. The wall thickness is fixed to 10 µm, since smaller structures may become too fragile. The open area is, therefore, reduced for smaller l, which is resembled by the transmission at $\theta_{\mathrm{inc}} = 0°$. The electron energy is the endpoint $E_0 = 18.6\,\mathrm{keV}$ of the tritium β-spectrum, which resembles the energy of signal and Rydberg background electrons. The number of transmitted electrons further depends on the magnetic and electric field configuration. The simulation was initiated by C. Weinheimer and A. Fulst and further developed within this work.

4.1.2.2 Implementation in KATRIN and Results

The pTEF idea has been further developed and was, finally, realized by members of the KATRIN-group of KIT[5] in a first pTEF-measurement campaign during a maintenance break of KATRIN at the end of 2021. The results of the first pTEF campaign are summarized here. The preparation and analysis can be found in detail in [64]. Since no tritium, krypton, or photoelectron source was available for the pTEF measurements due to the maintenance status of KATRIN, no independent calibration could be obtained. The background was measured at different magnetic and electric field configurations to influence the initial field configuration of the background and, thereby, the angular distribution

[5]Karlsruhe Institute of Technology, Institut für Astroteilchenphysik, Hermann-von-Helmholtz-Platz 1, 76344 Eggenstein-Leopoldshafen, Germany.

at the pTEF. Figure 4.4 illustrates the different transmission probability for electrons depending on their pitch angle. The pTEF consisted of two half segments of a circle of

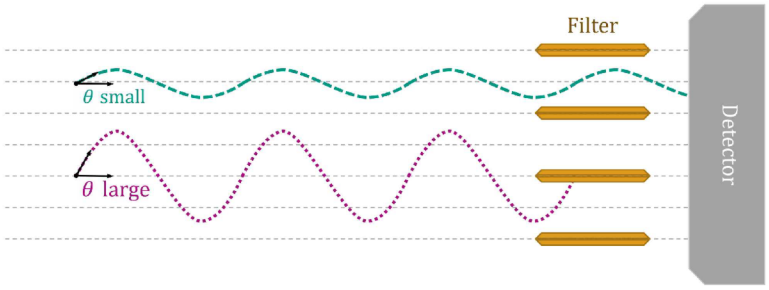

Figure 4.4 – Schematic of a pTEF installed in front of the detector [64]. Electrons of larger pitch angles θ have a higher probability to interact with the filter and to not reach the detector.

5 cm radius: One half was structured with hexagons, the other half was open and used as a reference. The manufacturer Microworks[6] specified the hexagon side length to be 100 µm, the wall thickness to be 8 µm, and the thickness to be 250 µm. As described in [64], the pTEF was made via X-ray lithography: The pTEF photomask was illuminated with synchrotron radiation from the Karlsruhe Research Accelerator KARA. A negative photoresist mask was manufactured, where the non-illuminated parts were filled up with gold in a galvanic process. The photoresist was removed afterwards, leaving the gold structure, as it is shown in figure 4.5. A low-Z material would have been beneficial due to

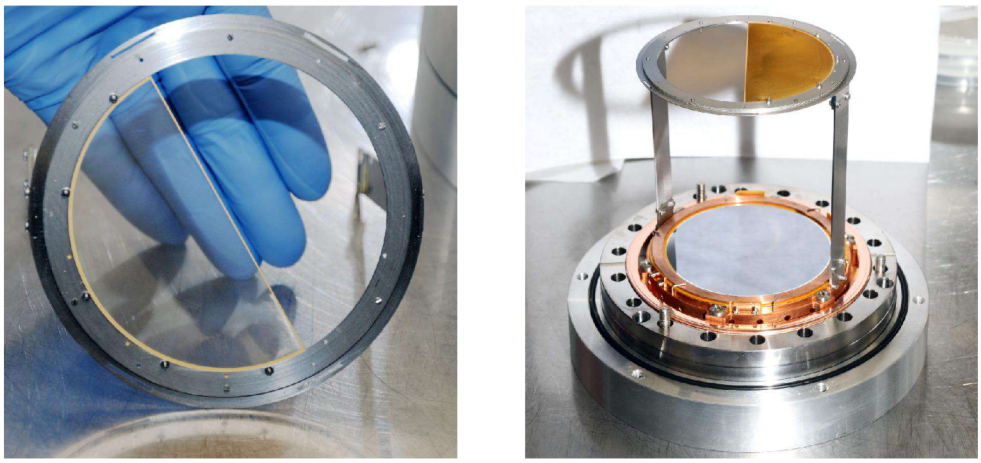

(a) pTEF front view **(b)** pTEF on detector flange

Figure 4.5 – Due to the large OAR of approximately 90% the pTEF appears transparent when viewed from the front. The pTEF is mounted onto the focal plane detector flange within a stainless steel frame. Images from [64].

its lower backscattering probability for electrons. Thus, a significant part of the electrons that hit the pTEF-structure undergoes scattering, but this effect is in first order canceled by the prevalence of backscattering at the focal plane detector surface, according to [64].

The pTEF was assembled onto a stainless steel structure onto the detector flange and

[6]Microworks GmbH, Hermann-von-Helmholtz-Platz 6, 76344 Eggenstein-Leopoldshafen, Germany.

in a distance of about 11 cm in front of the FPD. As a first test, a rather simple pTEF without different-sized hexagons was chosen. That way, the number of whole pixels that are hit by electrons is larger and the count rate does not rely that strongly on the accuracy of rate corrections, which account for shadowing of pixels by the pTEF.

The pTEF-measurement in KATRIN was accompanied by Monte-Carlo simulations with the particle tracking software `KASSIOPEIA`[7] [64]. There, isotropically emitted electrons of 0.1 eV to 0.7 eV were started at different z-positions of the spectrometer. Their ringwise[8] count rate with and without pTEF at different magnetic field and electric potential configurations was compared with the associated measurements. The measurements lead to the conclusion that a component with larger transverse energies in the analyzing plane than possible from BBR-induced Rydberg ionization is prevalent, which is in accordance with previous, complementary measurements [102, 103]. It has to be remarked, however, that the works [102, 103] were prepared before the background from secondary electrons from high-energetic radon decay, which is known to produce clusters of secondary electrons of larger energies than Rydberg background electrons in the spectrometer, was drastically reduced. The new work by [64] still finds larger energies, which neither stem from this process, nor from secondary electrons from black body radiation-induced Rydberg atom ionization: The initial transverse energies of background electrons in the spectrometer, as found in [64], are of mean energy between 200 meV and 420 meV, corresponding to a total initial kinetic energy of 300 meV to 630 meV.

Thus, an additional mechanism for the generation of larger electron angles at the detector – resembling the dependence on the flux tube volume and the radial distribution – is needed that accompanies the Rydberg background hypothesis. Previous works mentioned the possibility of atoms in autoionizing states in the spectrometer [103, 115]. That hypothesis was further worked out in [64]: There, autoionization processes of double-excited oxygen were rendered as the most likely additional contributor to the background. The lifetime of double-excited oxygen is enhanced due to forbidden electronic core excitations to $\tau = 0.7\,\mathrm{s}$ or $\tau = 108.9\,\mathrm{s}$ [116, 117]. It is, however, too short to explain the radial distribution of the background [64]. Double-excited oxygen can produce Rydberg-states with two valence electrons in excited states, which can be spatially apart. The overlap of the electron clouds of their electron's states n_1 and n_2 can be non-existent, so that the lifetime is enhanced to the µs regime. That allows them to distribute in the spectrometer volume, where the different autoionizing states can decay under emission of electrons in the range of 420 meV up to 2.77 eV [64]. Prevalence of these states in the spectrometer can explain the higher-than-expected transverse energies that was measured in the pTEF campaign. The low-energetic electron background of KATRIN may, therefore, consist of the known-of Rydberg atoms of hydrogen and oxygen, the fast autoionization of double-excited oxygen,

[7] KASSIOPEIA is developed for tracking particles in electromagnetic fields and through complex geometries. It is published in [114] and a detailed documentation can be found at https://katrin-experiment.github.io/Kassiopeia/index.html.

[8] Detector rings are the rings of pixels at the same radius of the focal plane detector.

and slow autoionization of the Rydberg state of double-excited oxygen [64].

A subsequent campaign with an adapted geometry and – as originally proposed, see section 4.1.2.1 – an increased number of filter segments is currently planned in order to refine the measurement. Further, calibration sources should be available. However, since its installation incorporates an alignment and hardware change of the detector region, the magnetic field alignment on the detector has to be remeasured after each pTEF campaign. That is linked to risks of introducing systematic uncertainties and should be done as seldom as possible.

The additional component in the angular distribution shown in figure 4.6 needs to be considered in the planning of the geometry of an aTEF, as it negatively impacts its maximal signal-to-noise ratio and the possible improvement on the neutrino mass sensitivity.

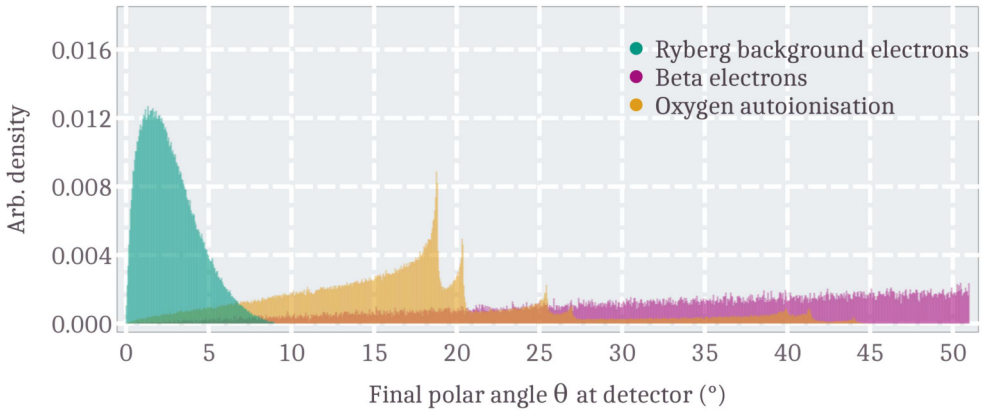

Figure 4.6 – Angular distribution of Rydberg background electrons and of autoionizing oxygen, which can account for the additional components in the pTEF measurement [64].

4.2 Microchannel Plate-based Active Transverse Energy Filter: MCP-aTEF

The suppression of Rydberg background electrons with simultaneous measurement of tritium β-decay electrons may be realized with an aTEF detector, which can be realized based on different detector types. Variants of the aTEF are illuminated in section 4.4. The initial approach to build an aTEF is based on custom microchannel plate (MCP) detectors and is described in this section: An MCP may allow suppression of electrons with small cyclotron radii, while electrons of large cyclotron radius trigger an electron avalanche that can be registered by a subsequent detector. That allows to use it as so-called MCP-aTEF [106].

Microchannel plates allow detection of different particle species and feature excellent time resolution in the order of a few nanoseconds and below. They consist of a lead glass capillary array of $\mathcal{O}(10^4 - 10^7)$ parallel single channels with diameters of typically 5 µm to 10 µm, each of them representing an electron multiplier with a continuous dynode. The

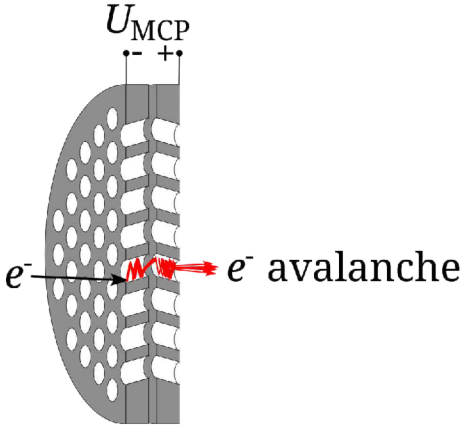

Figure 4.7 – Illustration of the working principle of an MCP-detector, consisting of two MCPs in chevron stack. The electron avalanche is generated from a single primary electron that induces repeated emission of secondary electrons, which are further multiplied by the second MCP.

lead glass channels are coated with a strip-resistivity layer and a $\mathcal{O}(10\,\mathrm{nm})$-thin secondary electron emission (SEE) layer. While the SEE layer allows electrons to be released in an avalanche, the strip-resistivity layer replenishes the lost electrons and offers an overall resistance of the MCP in the order of $10^8\,\Omega$. A potential difference of typically 1 kV between front and back is applied via NiCr electrodes. It allows acceleration of secondary electrons in an avalanche that results in a measurable signal when it arrives at the anode. The reduction of ion-feedback is crucial for longevity in high-rate applications of these detectors. Ion-feedback can be reduced via a slight channel tilt of typically 5° to 12° to block the direct line of sight, which simultaneously allows for a larger electron gain than a single MCP [118]. MCP-detectors reach higher signal discrimination when two (chevron stack) or three (Z-stack) plates are put in row. Their operation requires high vacuum environment.

A schematic of an MCP in the common chevron stack is shown in figure 4.7. A dark count rate on the order of 1 cps/cm^2 of these stacks is inherent due to the material choice that comes with radioactive impurities (e.g. ^{40}K). The dark count rate of a single MCP is lower, but still on the order of 0.1 cps/cm^2 [119]. The high background rate immediately disqualifies commercial MCPs for background reduction within KATRIN. For an MCP-aTEF of 10 cm diameter a total dark count rate of 0.5 cps would be higher than the Rydberg background that shall be fought with an MCP-aTEF. The glass material used for commercial MCPs is, thus, not suited for KATRIN's background requirement.

An MCP-aTEF for KATRIN requires further key characteristics:

The channels must be parallel to the magnetic field lines, i.e. without bias angle, so that background electrons of small pitch angles can pass mostly unhindered.

The MCP-aTEF needs to allow for a significant secondary electron gain. Therefore, it must differ in its structure and geometry from commercially available MCPs. Silicon is considered as base material instead of the classically used borosilicate or lead glass: It is generally very radiopure, for example the inherent radioactive ^{238}U and ^{232}Th content

of silicon lies below a few $^{\mu Bq}/_{kg}$ [120]. Silicon can, further, be processed via well-known standard semiconductor industry tools. These allow the basic structure with a channel diameter in the order of 100 µm and the necessary aspect ratio in the order of 1 : 2 to 1 : 4 to be fabricated.

A total resistance of $10^8\,\Omega$ is a typical value for MCPs and ensures a balance between excessive heat generation and too sparse charge replenishment into the detector for sustained secondary electron avalanche generation. Since silicon is intrinsically too conductive, an insulating layer of, e.g., SiO_2 needs to be applied. Then, the overall resistance of $10^8\,\Omega$ can be achieved by a combination of the strip resistance layer and SEE layer with the SiO_2 substrate [121]. A promising approach to reach the aimed-for overall resistance is a composite of thin layers of TiO_x and Al_2O_x as strip resistivity layer, which is possible with an atomic layer deposition procedure [121, 122].

Another layer on top allows SEE. The optimal SEE material and its thickness depend on the type and energy of the incoming particle. Only few materials have a secondary electron gain $\delta_{\mathrm{SEE}} > 1$ for electrons in the energy range of the tritium endpoint at $E_0 \approx 18.6\,\mathrm{keV}$ or even higher. The electron gain δ_{SEE} needs to be greater than 1 for optimal detection efficiency. Silicon dioxide is used in traditional MCPs as secondary electron emitter, but the reachable gain is insufficient. Therefore, a better suited material, e.g. MgO or Al_2O_3, must be used to ensure a sufficient performance of an MCP-aTEF for KATRIN.

Silicon-MCPs were already successfully produced [123] and, also, atomic layer deposition (ALD) was used to create long-lasting and efficient MCP plates [124]. Modern high-performance MCPs use ALD to bring other materials with a very controlled growth rate onto the substrate [125].

However, building an MCP-aTEF in its entirety with sufficient secondary electron gain and, if successful, test it rigorously before operation in KATRIN would require an immense effort. The optimal SEE layer, the overall device resistance, the secondary gain for electrons of different energies and incident angles, and the dark count rate of such a device would need to be studied extensively. That is a very demanding challenge, especially in the face of the end of KATRIN's regular neutrino mass measurement schedule in 2025. Therefore, the research on MCP-aTEF detectors remained to be proof-of-principle tests with commercial MCPs, which were partially published in [106]. They are complemented by measurements in section 4.3. The aTEF concept is, however, applicable to other detector types, as expressed in section 4.4.

4.3 Proof-of-Principle of aTEF and pTEF Concept

The transverse energy filters are supposed to measure magnetically guided electrons (of certain energy) with preferably large transverse energies or incident angles and reject electrons with small transverse energies or incident angles. Experiments in a test setup with a photoelectron source, magnetic guiding field, and an MCP-detector provided a general proof of the method: Electrons were discriminated based on their incident angle

onto an MCP that was operated either as aTEF or as pTEF. In a first experiment the MCP-detector itself was used as aTEF to show angle-selective electron detection. A second experiment utilized an additional, custom-made MCP-filter module that served as aTEF/pTEF. For the second experiment, the aTEF/pTEF module is referred to as MCP-filter and, in order to distinguish from that, the detector is referred to as MCP-detector, that registers the amplified or filtered electrons.

Details on the setup and its components can be found in section 4.3.1, while section 4.3.2 presents the experiments and the findings.

4.3.1 Test Setup

On its 2.7 m overall length[9] the test setup featured magnetic guidance for electrons from a UV-photoelectron source that was formerly used as calibration source in KATRIN [68]. The setup is shown in figure 4.8. The electrons were started in the source with a sharp initial energy distribution and are detected at the end of the flight path in a detector, e.g. an MCP or a Si-PIN diode. The central cubic vacuum chamber allows access to the electron beam from different sides and was later used as port for an MCP that served as aTEF/pTEF. The (ultra-)high vacuum with pressure in the order of 10^{-7} to 10^{-8} mbar was provided by a turbomolecular pump Leybold[10] TURBOVAC 340M with TURBOTRONIC NT 340M controller and a scroll pump Pfeiffer[11] ACP 15M ahead. The vacuum chamber, source, and detector were the same for both experiments, which are explained below. For the second experiment, the MCP-filter was added and the magnetic field configuration was changed. The setup consisted of multiple parts, which are listed here in the order of appearance in figure 4.8 as seen from the electron source: The photoelectron source itself was housed in a chamber with vacuum feedthroughs for the UV fiber, high-voltage supply, and the mechanics to adjust the angle of its parallel electrode plates. The source is described in more detail below. The chamber was geometrically aligned with the aluminum profile frame. The electrons were guided via magnetic fields from four coils made from anoxal®[12] that could provide magnetic fields in the order of 50 mT in their center without overheating. The coils were equipped with water-cooled copper plates at their end surfaces that limit the maximum temperature to approximately 50 °C. The coils were placed close the photoelectron source's emission point, symmetrically around the central part of the vacuum chamber, and around the detector. The vacuum tubes left and right of the central cubic vacuum chamber were each approximately 1.2 m long and covered by coils that were manufactured in the precision-mechanical workshop associated to the Institute of Nuclear Physics Münster. Each beam tube was equipped with four separate coils made from 2.1 mm copper magnet wire. The region around the CF40-flange featured additional windings to balance the gap at the flange position. The optimal geometry of the compensating coil

[9] The length of the setup was originally optimized for time-of-flight applications.

[10] Leybold GmbH, Bonner Strasse 498, 50968 Cologne, Germany.

[11] Pfeiffer Vacuum GmbH, Berliner Strasse 43, 35614 Asslar, Germany.

[12] Manufacturer: Umwelttechnik Wesselmann GmbH, Auf dem Knuf 21, 59073 Hamm, Germany.

turns was determined in [126]. All coils were driven by Delta Elektronika[13] DC-power supplies SM15-200D (with max. 15 V and 200 A) or SM30-100D (with max. 30 V and 100 A). The magnetic field configurations for the experiments are shown in figures 4.9 and 4.10.

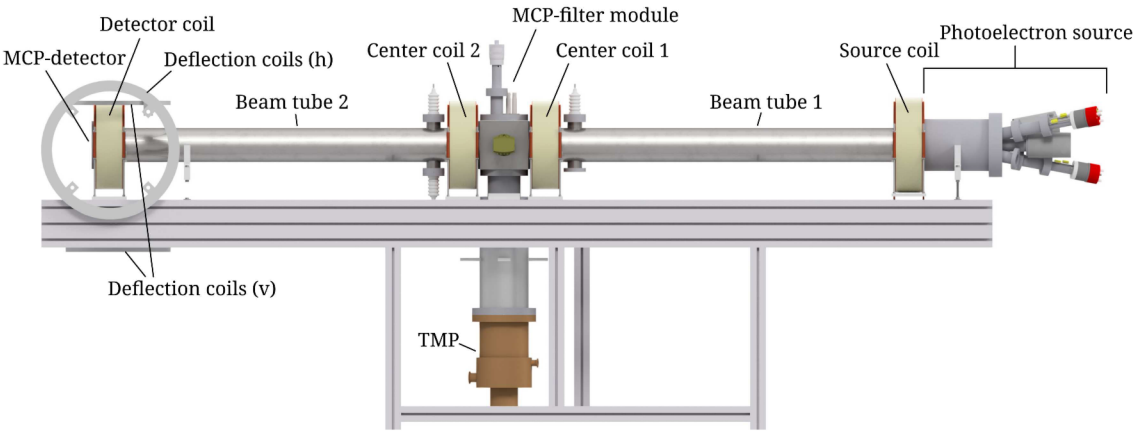

Figure 4.8 – Electrons were guided from the electron source via magnetic guiding fields to the MCP-detector. The magnetic fields were provided by free-standing air coils and additional beam tube coils directly wound onto the beam tube vacuum chamber. The setup was equipped with pairs of deflection coils that allowed deflection of the electron beam in the detector area and were used in experiment 1. Later, the MCP-filter module, which acted as aTEF and pTEF and was used in experiment 2, was installed. CAD drawing by H.-W. Ortjohann.

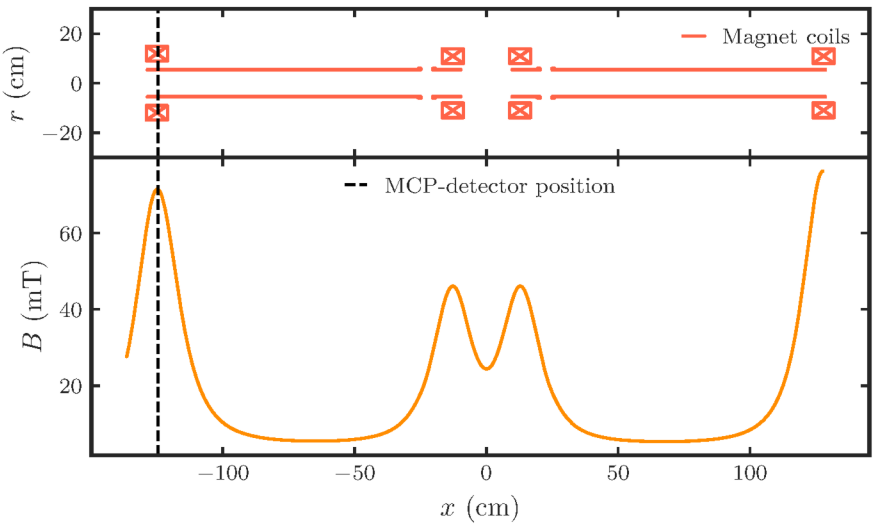

Figure 4.9 – Simulated magnetic field (neglecting perpendicular coils) as used in experiment 1 without the field generated by the deflection coils. Simulated with `bfield_3d` [127]. The electrons move from the source magnetic field on the right into the detector magnetic field on the left.

The turbomolecular pump was placed below the central cubic chamber. The cold cathode pressure sensor Leybold ITR 90 was attached to the side of the cubic chamber. The magnetic field of the free-standing air coils was aligned to the magnetic field of the

[13]Delta Elektronika, Vissersdijk 4, 4301 ND Zierikzee, The Netherlands.

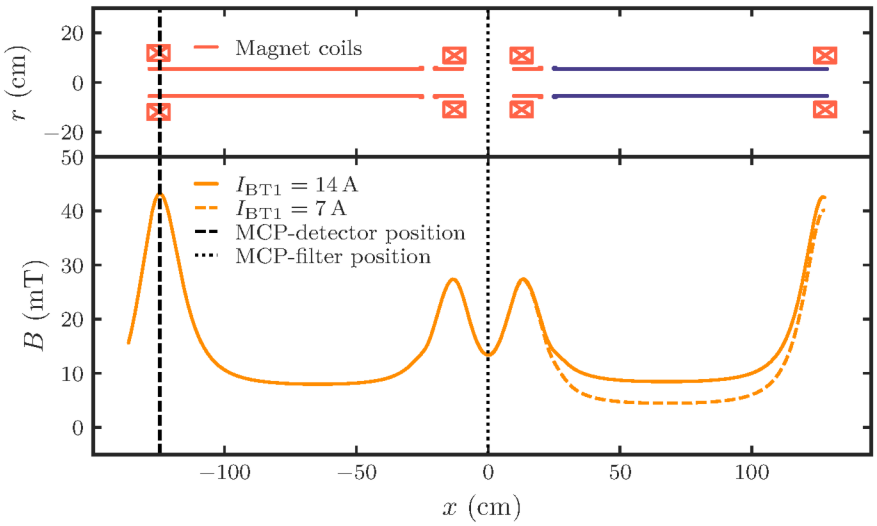

Figure 4.10 – The setup used for experiment 2 was modified with the aTEF/pTEF module in the central cubic chamber in figure 4.8. The single MCP plate that was used as aTEF/pTEF was inserted into and removed from the beamline via linear vacuum feedthrough fed by high-voltage feedthroughs. More details are shown in figure 4.16. The deflection coils were not used. The magnetic field strength is shown. The beam coils on the vacuum chamber were split in experiment 2: Beam coil 1 extended from the photoelectron source to the CF40-flange right of center coil 1 and is highlighted in blue. The variation of currents through beam coil 1 affected the electron motion on a $\sim 1\,\mathrm{m}$ length.

fixated beam coils: The magnetic field in a few decimeters distance from the air coils was measured radially symmetric at four points around the beam coils and the difference in magnetic field strength was minimized by slight adjustments of the air coils.

Photoelectron source Pulsed, angular-selective UV-photoelectron sources with sharp energy distribution of the emitted electrons are essential calibration and measurement tools in KATRIN. They are used, e.g., for the measurement of the energy loss of electrons upon scattering on tritium (and deuterium) in the WGTS and can, thereby, help to predict the systematic influence of the electron scattering on the neutrino mass [128]. The model that was used in the test setup was developed over the course of multiple years and used within KATRIN, e.g. for the measurement of transmission properties of the beamline [68, 129]. A schematic design is shown in figure 4.11.

The photoelectron source resembled a plate capacitor in a grounded cylindrical cage. Its back plate contained the thin gold cathode with a UV-fiber of 200 µm diameter glued into its backside, which illuminated the gold cathode. A UV-LED was coupled via optical fibers and a vacuum feedthrough to the back plate. The UV-light source was a LVL TO39 250-270 nm deep UV-LED, which allowed maximal input power of 200 mW[14] It was driven by a Tektronix[15] AFG 3102 frequency generator. The electrons were emitted from the gold

[14]Further maximum ratings at $T = 25\,^{\circ}\mathrm{C}$ are max. operation current (CW) of 20 mA, max. operation current (pulsed, length $< 5\,\mu\mathrm{s}$ @ 1 kHz), operation voltage 8 V (CW) or 10 V (pulsed).

[15]Tektronix GmbH, Heinrich Pesch Strasse 9-11, 50739 Köln, Germany.

cathode, if the UV photons had enough energy to overcome its work function. Their energy distribution is typically of 100 meV width and depends on the wavelength[16]. A potential difference between back plate and front plate accelerated the electrons non-adiabatically. The high voltage was provided by a Knürr-Heinzinger[17] PNC5 30000-5 neg power supply and was distributed to the plates via a 4/5-high-voltage divider that was built in the electronic workshop of the Institute for Nuclear Physics Münster. The back plate was provided with the full voltage of the voltage supply, $U_{\mathrm{back}} = U_{\mathrm{HV}}$, and the front plate with $U_{\mathrm{front}} = 80\% \cdot U_{\mathrm{HV}}$.

An aperture in the front plate allowed the electrons to pass through. Afterwards, they were accelerated due to the difference to the ground potential of the surrounding cage. A tilt in all directions around the emission point $\mathrm{P_e}$ was possible up to plate angles $\alpha_{\mathrm{p}} \leq 16°$. In the specific magnetic fields in KATRIN, this allowed to imprint angles $\theta = \arcsin\left(\alpha_{\mathrm{p}} \cdot k \cdot \sqrt{\frac{B_{\mathrm{max}}}{B_{\mathrm{start}}}}\right)$, with the factor k coming from the non-adiabatic acceleration of electrons in the photoelectron source. In a constant magnetic field, the relationship of the emission angle $\theta^*_{\mathrm{start}}$ at the exit of the source cage with the plate angle α_{p} in first approximation is $\theta^*_{\mathrm{start}} = \arcsin(\alpha_{\mathrm{p}} \cdot k)$. The value of k was not directly measured in the various fields of the test setup, since an estimation of the emission angle distribution was not pursued.

The tilt angle α_{p} of the photoelectron source plates was measured by Attocube ANR240 piezo-electric motors with an accuracy of 0.05° on the rotation angle. The angle was changed by linear motors Bibus Tesla 1620 that were driven by pressurized air, which are suited for operation in the strong magnetic fields of the KATRIN beamline.

The LabView™ program that was used to control the plate angle was an alteration of a program described in [129].

MCP-Detector: The MCP-detector was a Tectra[18] MCP 050-D-L-A-F in chevron stack with ≥ 44 mm active diameter, 12 µm channel pitch, 10 µm pore diameter, $\geq 60\,\%$ open area ratio (OAR) and an overall plate thickness of 0.48 ± 0.05 mm at an aspect ratio of 40:1 of channel length to channel pitch. It was attached to a CF100 flange that fitted the beam tube vacuum chamber. The MCP was operated with up to 1 kV voltage difference per plate. First-time operation required conditioning with gradually increased voltages up to a value 200 V above operation voltage for a few hours [130]. The high voltage was distributed by a voltage divider. Plain MCPs in general do not allow sharp energy discrimination, but they excel in temporal resolution. A rate measurement was, therefore, carried out with a

[16] If the UV wavelength is tuned to lie slightly above the work function, the electron energy distribution is cut-off and only a fraction reaches the vacuum level. That leads to a sharp energy distribution of emitted electrons and a lowered electron yield. Here, the UV-photon energy does not perfectly match the work function: The diode was chosen for its large output and the electron energy was not needed to be on the level of accuracy that was necessary for the source's operation in KATRIN.

[17] Knürr-Heinzinger GmbH (now: Heinzinger electronic GmbH), Anton-Jakob-Strasse 4, 83026 Rosenheim, Germany.

[18] tectra GmbH, Reuterweg 51–53, 60323 Frankfurt/M, Germany.

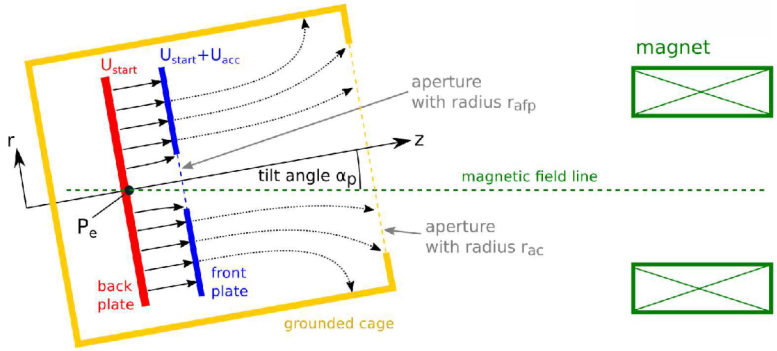

Figure 4.11 – Schematic of the UV-photoelectron source [68]. The homogeneous electric field between back plate and front plate accelerated electrons, which were emitted through the aperture in the front plate. The grounded cage further accelerated electrons towards the exit of the source. The source was gimbal-mounted around the emission point P_e on the back plate and could be tilted by the plate angle α_p.

pulse counter based on NIM[19]-modules and LabView®, as schematically shown in figure 4.12. For the second experiment, a gate generator allowed to halt the data acquisition after an event for the length of a gate signal in order to prohibit multiple counting of signals generated in the same event, see figure 4.13. The anode readout signal was connected via a 47 µF capacitor to an ORTEC 474 timing filter amplifier. The signal is discriminated by a CAEN N417 discriminator module. Finally, a NIM/TTL converter allowed the signal to be registered in the event counter of a National Instruments[20] NI6008 USB-Box for LabView.

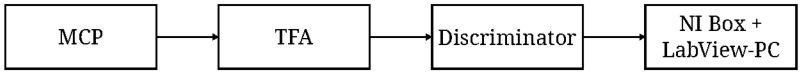

Figure 4.12 – The DAQ chain was used for aTEF-measurements with the MCP-detector in experiment 1. The MCP anode signal was guided to the timing filter amplifier, which enlarged it and altered its shape. The amplified signal was guided to the discriminator, which sent a digital signal to the counter module of the NI Box. An accompanying LabView program was used to write the count rates and the associated magnet coil currents into a file.

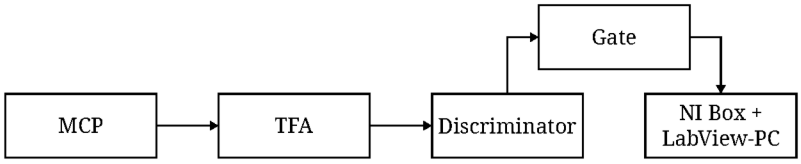

Figure 4.13 – This DAQ chain was used for measurements with the aTEF/pTEF module in experiment 2. The original data acquisition system (see figure 4.12) was provided with an additional gate generator. That allowed to blind the counter for the length of the gate time and, thereby, to count temporarily spread-out events once only and to exclude the counting of afterpulses.

[19]Nuclear Instrumentation Module Standard [131].

[20]National Instruments Corporation,11500 North Mopac Expressway, Austin, TX 78759, United States.

Electron detection was possible without considerable energy threshold in the MCP-detector that was used in the experiments. There was, however, a strongly deteriorating detection efficiency for electron energies below 500 eV. The MCP-detector was mounted on a CF100 flange, which was equipped with various vacuum feedthrough connectors for the signal-readout and iseg[21] NHQ 224M high-voltage supply, see figure 4.14. It was installed with an additional adapter in the setup in figure 4.8. That adapter was a CF100 flange, which was inclined by 6°. The bias angle of the channels was, thereby, compensated and electrons of small pitch angle were able to move in parallel to the channels, which allowed to perform the experiments in the following section.

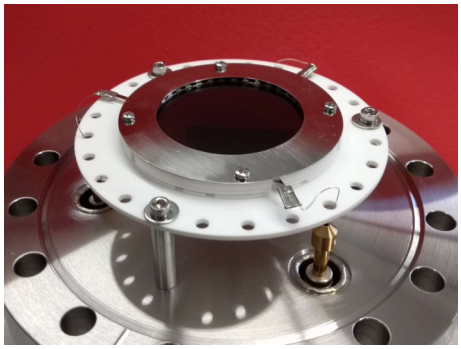

Figure 4.14 – The Tectra MCP-detector in chevron stack was mounted on a CF100 flange, which was provided with feedthrough ports for high-voltage supply and signal read-out.

4.3.2 Experiments on MCPs as aTEF or pTEF

In order to induce angle-selective detection effects in MCPs, the movement of electrons through the setup needs to be understood: An electron is bound to a cyclotron movement by the Lorentz force and the centripetal force. The cyclotron motion of electrons with electron rest mass m_e through vacuum and in the absence of electric fields, is (non-relativistically) described by the velocity $v_\perp$ perpendicular to the magnetic field B

$$e \cdot v_\perp \cdot B = m_e \cdot \frac{v_\perp^2}{r_c}. \tag{4.3.1}$$

An electron in the setup passed regions of different magnetic field strength that affected the cyclotron radius r_c via

$$r_c = \frac{v_\perp \cdot m_e}{e \cdot B}. \tag{4.3.2}$$

The pitch angle $\theta(E, B)$ of an electron of energy E in the magnetic field B can be directly calculated from the cyclotron radius:

$$\theta(E, B) = \arcsin\left(\frac{\sqrt{2 \cdot E \cdot m_e}}{r_c \cdot e \cdot B}\right). \tag{4.3.3}$$

[21] iseg GmbH, Bautzner Landstr. 23, 01454 Radeberg, Germany.

With the angular velocity $\omega = v/r$, the time T of a cyclotron period is

$$T = \frac{2\pi \cdot m_e}{e \cdot B} \tag{4.3.4}$$

and, consequentially, the displacement h per cyclotron period is

$$h = v_{\parallel} \cdot T = \frac{2\pi \cdot m_e \cdot v_{\parallel}}{e \cdot B}. \tag{4.3.5}$$

In the setup used for the experiments the cyclotron radius r_c can become large in regions of low magnetic field strength, so that collisions with the vacuum chamber may occur, depending on the initial electron angle and energy.

The setup allowed to conduct different experiments to find whether MCPs are suited to suppress and amplify electrons depending on their incident angle. While here a short summary of the findings is given, complementary details on the experiments can be found in [106, 132, 133].

Experiment I:

For the first experiment, the setup in figure 4.8 was equipped with pairs of coils to magnetically deflect the electrons in the region of the MCP-detector. There were two coil pairs, each connected in series. The coils of each pair possessed the same central axis. One pair was installed vertically, the other pair horizontally to the beam tube axis. The distance of the vertical coil pair to the detector was not equal. The small deflection coil pair could generate a field of $B_s = 1.0\,\mathrm{mT}$ at the position of the MCP-detector when $I_s = 4.54\,\mathrm{A}$ was provided. The large deflection coil pair could generate $B_l = 1.0\,\mathrm{mT}$ at $I_l = 2.03\,\mathrm{A}$. It was intended to actively influence the path of the magnetic field line and, thereby, the incident angle on the detector by variation of the currents through each deflection coil pair. Electrons were started in the photoelectron source with an acceleration voltage of $U_{\mathrm{back}} = -50\,\mathrm{V}$. With large magnetic fields at the source and at the detector, the cyclotron radius and the pitch angle of an electron at the source and at the detector was of comparable size. The plate angle of the photoelectron source was set to $\alpha_{\mathrm{p}} = 0°$ (with respect to the optical axis), but – since the magnetic field was not perfectly aligned to the beam tubes and to the photoelectron source – the electrons did most likely travel with $\theta \gtrsim 0°$.

The cyclotron radius (see eq. 4.3.2) was drastically reduced in contrast to 18.6 keV electrons at the same plate angle α_{p} and collisions with the vacuum chamber were prevented. The displacement per full radius of a cyclotron motion in the setup can be assumed to be macroscopical, i.e. $\mathcal{O}(\mathrm{cm})$, depending on the exact electron energy, local magnetic field and pitch angle.

The first experiment aimed for the suppression of electron detection from the photoelectron source with the MCP-detector under certain incident angles. The incident angles were directly influenced by the deflection coil currents. With the rest of the coils being operated

with constant current, the deflection coil currents were changed in a grid-scan. The expected outcome was a reduction of the detection rate at a certain amount of deflection coil current: The electrons could pass the first MCP of the chevron stack without hit, because their pitch angle was aligned to the first MCP channel angle. That way, they would not trigger secondary electron amplification in the first MCP. They could be amplified in the second MCP, but the amplification factor of a single plate would not be large enough to overcome the noise level and induce a measurable pulse. On the contrary, other deflection coil currents would lead to larger incident angles and induce an electron avalanche, as long as the electron beam was not deflected off the MCP-detectors surface.

As expected, the count rate diminished for certain deflection coil currents, while at other deflection coil currents there was no such drastic rate decrease. That is shown in figure 4.15.

The expected rate-decrease at certain deflection coil currents was measured. A decrease by a factor > 55 in the minimum compared to the baseline was measured in [132]. That can be interpreted as a proof-of-principle of angle-selective electron detection. The first MCP served as MCP-aTEF detector. Further evaluation of experiment 1 can be found in [132].

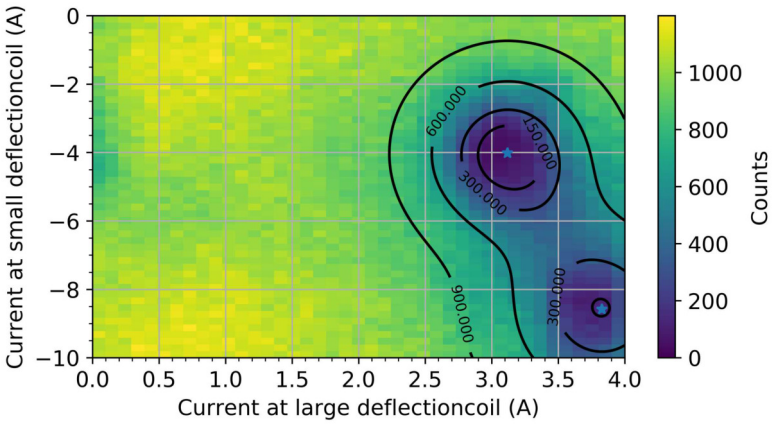

Figure 4.15 – Electrons of 50 eV were guided towards the MCP-detector. The beam was deviated by the deflection coils at the detector position. The "small deflection coils" were pair-wise installed horizontally and generated deflection of the magnetic field lines in vertical direction. The "large deflection coils" were pair-wise installed vertically and, consequently, lead to horizontal deflection of the magnetic field lines. At two close-by areas, the deflected beam did not induce a count rate in the MCP. That can be interpreted as the suppression of electrons with pitch angles that were very close to the MCP channel orientation. A secondary electron avalanche was probably generated in the second plate, but due to its low signal-to-noise ratio not measured. The result can be interpreted as demonstration of the aTEF-principle. It is suspected that the manufacturing process of the MCP, which involves bundle-wise stacking of channels with possibly different orientations, induces the two distinct minima.

Experiment 2:

Based on the findings of the first experiment, the angle-selective detection and suppression of electrons was tested in a second experiment with a separate aTEF/pTEF module, or

"MCP-filter" as distinctive from the "MCP-detector" at the end of the beamline. The MCP-filter consisted of a single MCP in a custom-made housing that was intended to filter the electrons based on their incident angle on the plate. It could be inserted via a linear vacuum feedthrough as aTEF/pTEF in the central part of the beam tube, see figure 4.8 and 4.16. A detailed description of the experiment is found in [133]. With a differential high-voltage supply FuG[22] HNC 35M-5000 and a high-voltage supply iseg NHQ 224M, a voltage difference between front and back could be applied and, additionally, the reference potential could be raised or lowered with respect to ground. The MCP-filter was installed

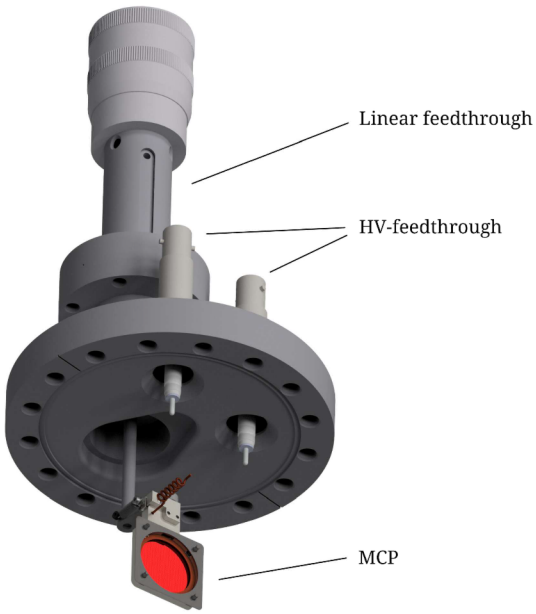

Figure 4.16 – The MCP filter was mounted on a CF100 flange and equipped with a custom-made PEEK housing. High voltage vacuum feedthrough connectors allowed to supply the MCP-filter with potentials on its front- and backside. Both sides could be set to a potential and, thereby, act as retarding potential barrier for incoming electrons. A potential difference could be applied. That allowed SEE avalanche generation at a sufficiently large potential difference between front- and backside. The filter was inserted into or retracted from the beamline via linear vacuum feedthrough. The MCP-filter module was constructed and drawn by Hans-Werner Ortjohann and used in [133]. The cable connection between the high-voltage feedthrough and the MCP front and back is not shown.

under 12° to the beam tube in order to align the channels with the central beam tube axis[23]. That allowed electrons of small pitch angles to be transmitted [133]. The front side of the MCP-filter is defined as the side exposed to the photoelectron source. The potential

[22]FuG Elektronik GmbH, Gewerbegebiet Schechen-Nord, Am Eschengrund 11, 83135 Schechen, Germany.

[23]The aim was the alignment of the channels to the magnetic field lines, but that could not be controlled in the setup due to inevitable misalignments of the magnetic fields with respect to the photoelectron source and the MCP-detector channel axes. Although the MCP-filter was precisely aligned to its vacuum flange [133], the pitch angle of electrons was unknown. It is unlikely that electrons of 0° pitch angle would have been transmitted, since exact alignment of the magnetic field remained unsuccessful.

$U_{\mathrm{MCP,front}}$ was set to a negative value to accelerate secondary electrons in the direction of the MCP-detector and to allow the formation of an electron avalanche. The electrons from the photoelectron source were able to reach the MCP-filter only when they could overcome the front side potential, i.e., they required the corresponding longitudinal energy. The MCP-detector was read out via the DAQ chain illustrated in figure 4.13.

A sufficient potential difference between front and back of the MCP-filter was necessary to allow for significant gain, although too high voltages can increase the dark count rate or damage the device by discharges. A potential difference $\Delta U = U_{\mathrm{MCP,back}} - U_{\mathrm{MCP,front}}$ implied acceleration of secondary electrons in the channels and, for $\Delta U \geq 700\,\mathrm{V}$ (in case of the RoentDek Det25), the formation of secondary electron avalanches from primary electrons occurred.

In the so-called "active" mode with $\Delta U \geq 700\,V$, electrons arrived at the MCP-detector as secondary electron cloud or, if they moved through the channels without interaction, as single electrons. The MCP-filter was able to provide a measurable secondary electron avalanche when hit by a primary electron.

In the "passive" mode, on the contrary, there was no voltage difference between the front side and backside of the MCP-filter and, therefore, no secondary electron avalanche was triggered. Electrons were either absorbed or scattered by the MCP-filter, if they hit a part of the structure, or passed it without hit, if their pitch angle was aligned with the MCP's channel orientation. The OAR of 60 % of the MCP-filter reduced the number of traversing or amplified electrons in both modes, active and passive.

Electrons were sent from the photoelectron source towards the MCP-filter and were registered with different DAQ-settings for the passive and the active mode. If they passed the MCP-filter without collision, the single primary electrons reached the MCP-detector at the end of the beamline. They were registered in the passive mode and likely not registered in the active mode. The count rate of single electrons was additionally affected by the OAR of the MCP-detector depending on the incident angle, while the count rate of secondary electron clouds was not affected due to the larger number of electrons and their broader distribution in energy and arrival time and space.

If the primary electrons collided with the MCP-filter in the passive mode, they were scattered or absorbed and they were not registered by the MCP-detector. In the active mode, they triggered a secondary electron avalanche in the MCP-filter and were registered by the MCP-detector as a larger and broader pulse than single electrons would induce.

The experiment aimed to provide a proof for the pTEF and aTEF working principle by changing the incident angle on the MCP-filter when operated in passive and active mode. The incident angle was not directly accessible, but it was adjustable with changes of the magnetic field as explained in the following: The electrons started in the magnetic field $B(z_0)$ at the photoelectron source. The beam coils that were installed between the photoelectron source and the CF40-flange in front of the MCP-filter were controllable independently from the other coils: Changes of the beam coil current affected the magnetic field over a length of approximately 1 m, see figure 4.10. The magnetic field provided by

the beam coil had a minor effect on the magnetic field at the electron emission point and at the MCP-filter position.

When the electrons left the influence of the first beam tube, all electrons possessed the same cyclotron radius, independent from the magnetic field in the first beam tube[24]. However, the displacement h per cyclotron period is affected via $h \propto v_{\parallel}/B(z)$. That means, the variation of the current through the beam coil 1 only influenced the phase of the electrons' cyclotron motion at the MCP-filter, while their pitch angles at the MCP-filter were not affected. Although the MCP-filter was aligned by eye to the vacuum chamber, the MCP-filter channels and the magnetic field lines were slightly misaligned. That allowed the electron trajectories to be aligned to the channels of the MCP-filter only at certain beam coil 1 currents.

Figure 4.17 visualizes the change, which was implied by the magnetic field to the incident angle on the filter: In the active mode, certain phases lead to a parallel motion of electrons to the channels, so that electrons can pass the MCP-filter without triggering an avalanche. The other phases resulted in non-parallel motion of electrons to the channels. The active MCP-filter multiplied these electrons, resulting in avalanches that were detected at the MCP-detector.

The current I in beam coil 1 that is needed to displace the cyclotron phase by n whole turns [132]:

$$I = \frac{2\pi m_e v_{\parallel}}{e\mu_0 N} n. \tag{4.3.6}$$

The number of windings in beam coil 1 up to the CF40 flange is given by $N = 473$. The periodicity of cyclotron motion was $\Delta I \approx 1\,A$ for the used magnetic fields [133]. That allowed to finely tune the cyclotron phase and, thereby, the angle of the electrons towards the channels of the filter, by sub-Ampere adjustments. The displacement h for a full cyclotron period was typically in the order of a few cm. Since the MCP-filter is only 400 µm thin, the curvature of the trajectory within the MCP-filter can be neglected.

Figure 4.18 presents typical MCP-detector pulse shapes in the passive and in the active mode of the MCP-filter. The signals were obtained with shaping time $T_{\mathrm{shape,s}} = 20\,\mathrm{ns}$ or $T_{\mathrm{shape,l}} = 500\,\mathrm{ns}$ of the timing filter amplifier [25]. The gate prevented multiple counting of long pulses from secondary electron avalanches and their subsequent afterpulses as separate events. The pulse shape in passive mode was typically short and without subsequent afterpulses, since it stemmed from single electrons from the photoelectron source that passed the MCP-filter without hit. The secondary electron avalanches in the active mode were typically spread out in their arrival time, since the secondary electrons had divergent starting energies. The active mode resulted in longer pulses from the spread-out avalanches. Often, afterpulses from the release of electron traps in the MCP-filter were measured subsequently. The single electrons that passed the MCP-filter without triggering secondary

[24] The magnetic field at the source is assumed to be constant. Further, adiabaticity is assumed

[25] Remark: Figures 4.22 and 4.23 were conducted with shaping time $T_{\mathrm{shape,l}} = 200\,\mathrm{ns}$ and with a shorter gate $T_{\mathrm{gate}} = 10\,\mu\mathrm{s}$. That weakened the suppression of single electron detection in the active mode.

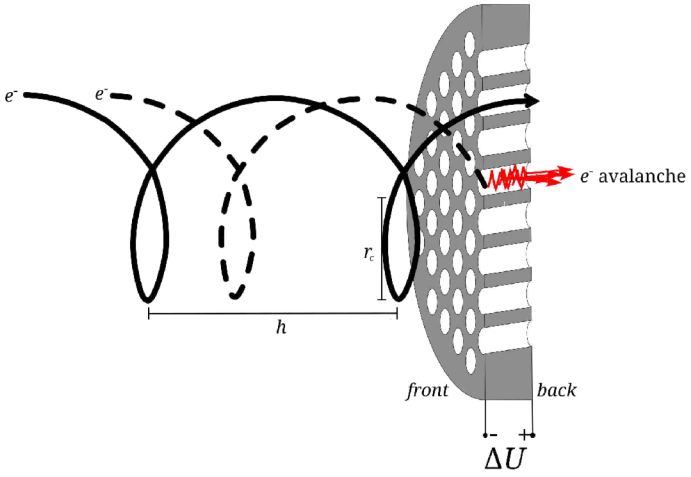

Figure 4.17 – An electron with cyclotron radius r_c and cyclotron displacement h – both large compared to the MCP channel radius – that moves through a magnetic field on a certain cyclotron path (solid line) reaches the MCP parallel to its channels axes and can be transmitted without hitting the channel wall. A phase-shifted electron (dashed line) with the same cyclotron radius r_c and displacement h can possess a larger angle to the MCP channel, although their pitch angles are the same, and generate a secondary electron avalanche upon impact on the channel wall. If the voltage difference between the front and back is $\Delta U \gtrsim 700\,\mathrm{V}$, secondary electron avalanches are generated upon impact of a primary electron.

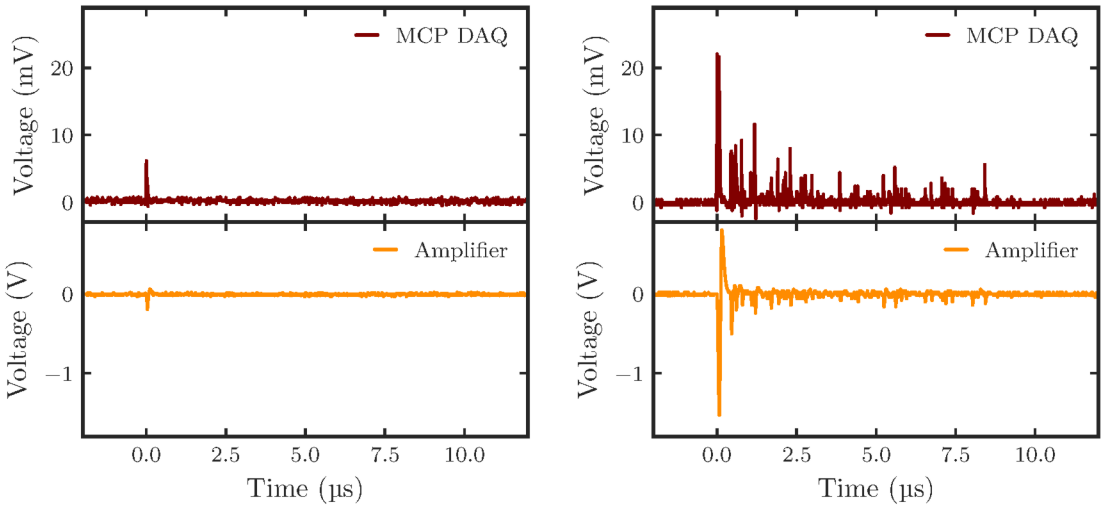

(a) Passive MCP-filter

(b) Active MCP-filter

Figure 4.18 – Oscilloscope traces for typical events during in measurements with a passive (a) and active (b) MCP-filter. The signals were measured after the MCP-detector's anode read-out (upper panel) and after the timing filter amplifier (lower panel). A single primary electron generates a short signal, as visible in (a). The broad pulses in (b) are generated by the spread-out electron avalanche and subsequent afterpulses of the active MCP-filter. While the oscilloscope trace was measured with $T_{\mathrm{shape,l}} = 200\,\mathrm{ns}$, later measurements were taken with $T_{\mathrm{shape,l}} = 500\,\mathrm{ns}$. After detection of a signal, the gate does not allow another count for T_{Gate}.

electron avalanches induced short, mostly singular pulses.

Figure 4.19 shows the suppression of single-electron counts in passive mode, when the large shaping time of the active mode is applied. A mean reduction by $(76.0 \pm 3.9)\%$

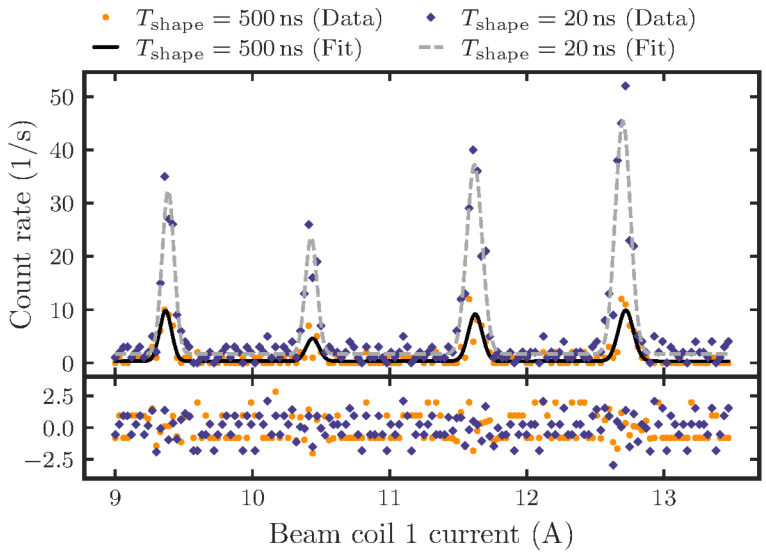

Figure 4.19 – Suppression of single MCP counts in passive mode, similar to a measurement shown in [133]. The electron energy was 1 keV and the MCP front and back voltage $U_{\mathrm{MCP,front}} = U_{\mathrm{MCP,back}} = -750\,\mathrm{V}$. Electrons were able to pass the MCP at certain beam coil 1 currents, where their pitch angle matched the channel orientation. When the timing filter amplifier was set to the longer shaping time, shorter and smaller pulses were suppressed. The origin of the difference in height of the maxima in each dataset and the spread in periodicity is not clear, but may stem from a small influence from the change in magnetic field in beam tube 1 on the field at the source or at the aTEF/pTEF-module. The Poisson-likelihood estimation resulted in $\chi^2_r = 220.2/137 = 1.61 \pm 0.12$ ($T_{\mathrm{shape}} = 500\,\mathrm{ns}$) and $\chi^2_r = 203.08/137 = 1.48 \pm 0.12$ ($T_{\mathrm{shape}} = 20\,\mathrm{ns}$).

between the integrated gaussian count rate distributions with a constant background being subtracted is found between the two datasets. That means, the single electron events are suppressed approximately to a quarter when the longer shaping time $T_{\mathrm{shape,l}} = 500\,\mathrm{ns}$ and the gate $T_{\mathrm{gate}} = 100\,\mu\mathrm{s}$ are applied.

The shaping time $T_{\mathrm{shape}} = 500\,\mathrm{ns}$ filtered single electrons, background events from, e.g., field emission from the MCP-filter, and unintentionally suppressed electron avalanches. In the active mode that allowed to predominantly measure the amplified events, which is shown in figure 4.20. That means, the active mode allowed to measure predominantly electrons of large angles to the channels of the MCP-filter and to suppress those of small incident angles, which traveled through the filter without hit.

A direct comparison between passive and active mode is shown in figure 4.21. The difference voltage between front and back of the MCP-filter of $\Delta U = 750\,\mathrm{V}$ in the active mode was chosen high enough to produce secondary electrons and low enough to not generate excessive dark counts. The offset potential of the MCP-filter was chosen such that it was smaller than the kinetic energy of the electron in order to not repel it. The overlapping positions of the count rate maxima in passive mode and the minima in active mode stand out. Their common positions are the expected outcome from the pTEF and aTEF considerations above: Electrons experience an electric field from the applied voltages

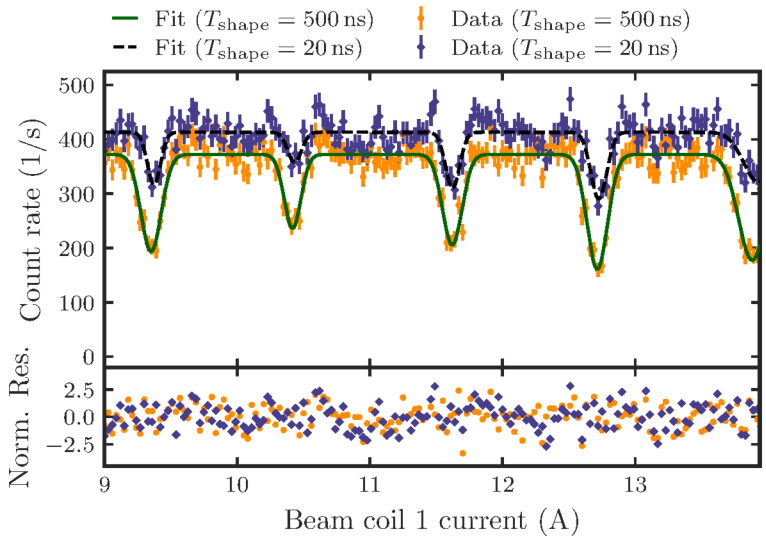

Figure 4.20 – The MCP-filter was operated in active mode with $\Delta U = 750\,\mathrm{V}$ and $U_{\mathrm{MCP,front}} = -50\,\mathrm{V}$. The baseline count rate is reduced by $(40.8 \pm 2.6)\,\mathrm{cps}$ between the two shaping times. The suppression of short events via adjustment of the shaping time from $T_{\mathrm{shape}} = 20\,\mathrm{ns}$ to $T_{\mathrm{shape}} = 500\,\mathrm{ns}$ is shown for 1 keV-electrons: The ratio of the minima between $T_{\mathrm{shape,s}} = 20\,\mathrm{ns}$ and $T_{\mathrm{shape,l}} = 500\,\mathrm{ns}$ is 1.90 ± 0.26, which stems from the suppression of single events and afterpulses from the longer shaping time. With $T_{\mathrm{gate}} = 100\,\mu\mathrm{s}$, the gate was sufficiently long to suppress afterpulses in the active mode.

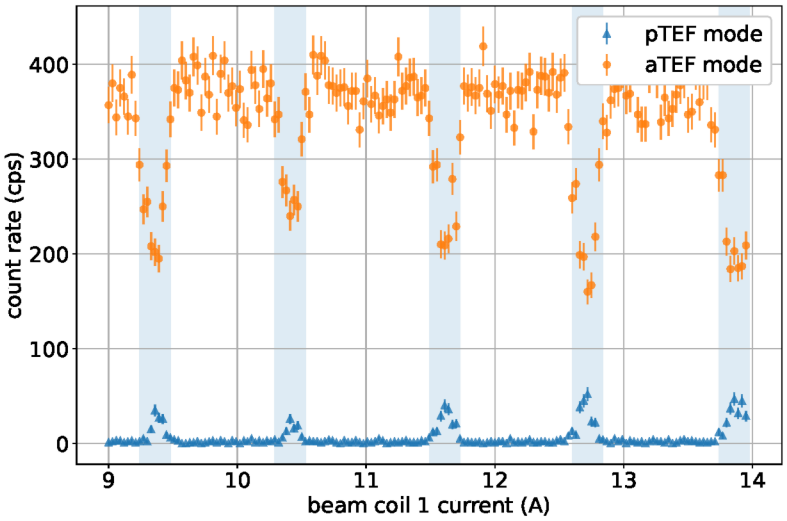

Figure 4.21 – The shaping time $T_{\mathrm{shape,l}} = 500\,\mathrm{ns}$ in active and $T_{\mathrm{shape}} = 20\,\mathrm{ns}$ in passive mode in conjunction with the gate time $T_{\mathrm{gate}} = 100\,\mathrm{ns}$ allowed to measure electrons from predominantly amplified events in the active (aTEF) mode and, in contrast, to measure mainly single events in the passive (pTEF) mode. Taken from [106].

$U_{\mathrm{MCP,front}}$ and $U_{\mathrm{MCP,back}}$ and are decelerated as a consequence. The MCP-filter is set to the offset voltage ΔU to compensate the change in cyclotron displacement h. In both cases, the back-plate voltage was chosen to $U_{\mathrm{MCP,back}} = -750\,\mathrm{V}$. The front plate voltage is less relevant for the movement of the electrons, since the cyclotron displacement h is

significantly larger than the MCP-filter thickness.

In summary, the measurement confirmed the conceptual assumption of the aTEF and pTEF: When primary electrons hit the channels of the MCP-filter, they were filtered-out in passive mode and amplified in active mode. When primary electrons pass the MCP-filter they were detected in passive mode and suppressed in active mode.

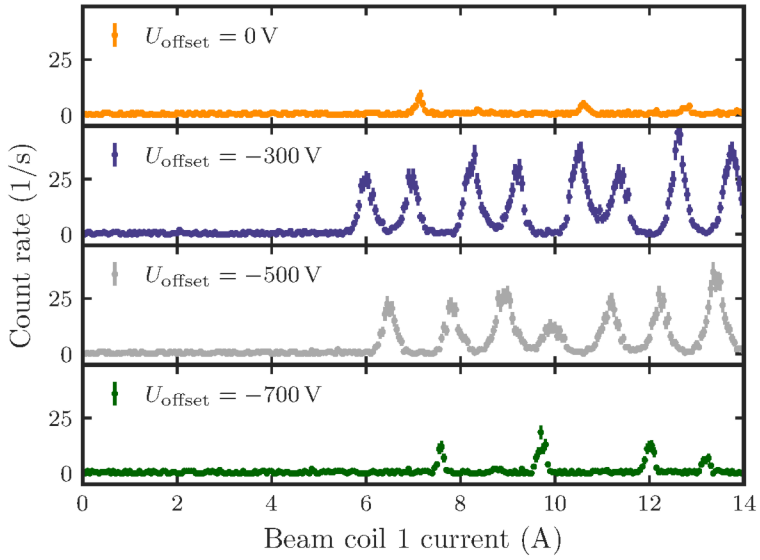

Figure 4.22 – The transmission of electrons of 1 keV energy through the MCP-filter in passive mode depends strongly on the cyclotron phase. Different retarding energies change the transmission maxima positions and height, as the flight path and cyclotron phase of the electrons depends on the electron energy, which is affected by the offset voltage U_{offset} of the MCP-filter.

Complementary measurements with different offset potential in passive mode are displayed in figure 4.22. There, the MCP-filter was operated without difference voltage, but with varying offset voltage $U_{\text{offset}} = U_{\text{back}} = U_{\text{front}}$. The retarding potential reduced the velocity of the passing electrons. Since the retarding potential mainly affected $v_{\parallel}$ – and, thus, the cyclotron displacement h – the influence on the cyclotron radius at the filter position was small. Thereby, the incident angles of electrons on the MCP-filter were varied. For small retarding voltages most of the electrons possessed too small cyclotron radii that did not match the channel angles, so that changing the phase only let through a small number of electrons with particular large cyclotron radii. At $U_{\text{off}} = -300\,\text{V}$ and $U_{\text{off}} = -500\,\text{V}$ retarding voltage the number of passing electrons was largest. For higher retarding voltages the incident angle apparently became too large and most of the electrons were absorbed by the MCP-filter.

Another indication that the suppression and amplification depends on the incident angle is given by a direct comparison of different photoelectron source plate angles in figure 4.23. The panels of each plot display measurements in passive mode (top panel) and active mode (lower panel). The rate in the active mode was generally higher due to the large number of secondary electrons, which strongly increased the detection efficiency at the MCP-detector compared to single electrons. Although predictions on the exact pitch angles in the test

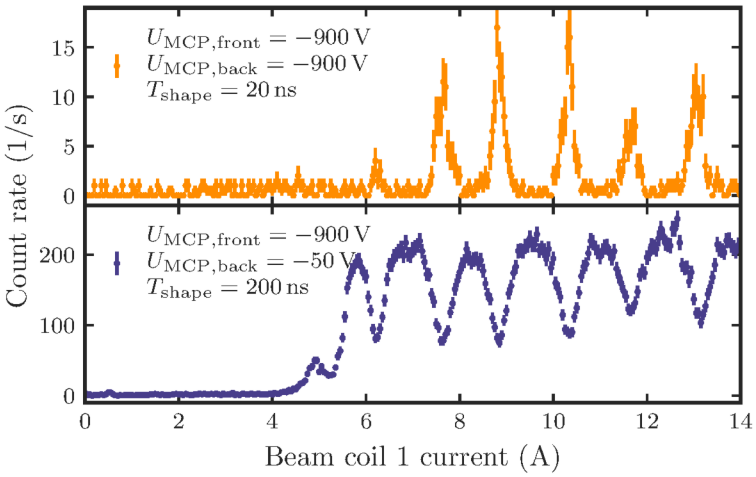

(a) $\alpha_{\mathrm{p}} = 0°$

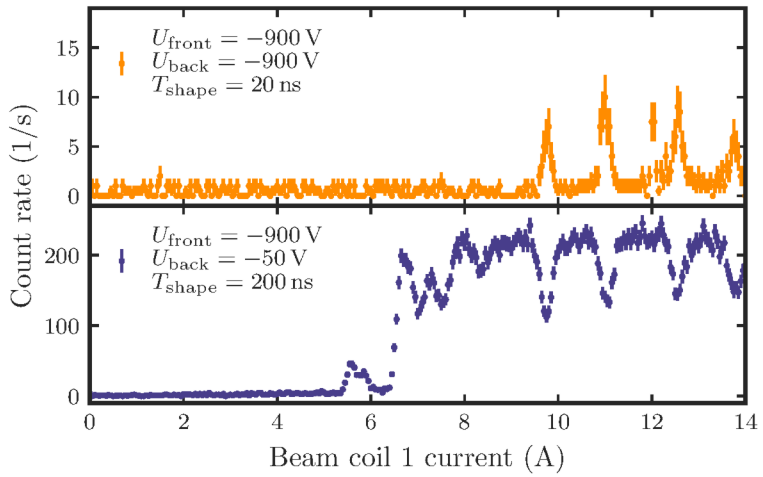

(b) $\alpha_{\mathrm{p}} = 4°$

Figure 4.23 – Comparison of the pTEF and aTEF measurements with the photoelectron source plate angle at $\alpha_{\mathrm{p}} = 0°$ (a) and at $\alpha_{\mathrm{p}} = 4°$ (b). The onset of the modulation in aTEF and pTEF mode is at smaller currents for $\alpha_{\mathrm{p}} = 0°$, where the electrons started with smaller pitch angles and cyclotron radii, so that they did not collide with the beam tube vacuum chamber wall. Note: Due to the smaller gate time $T_{\mathrm{gate}} = 10\,\mu\mathrm{s}$ and the smaller shaping time $T_{\mathrm{shape}} = 200\,\mathrm{ns}$ compared to e.g. figure 4.21, the suppression of afterpulses and single events in the active mode was less pronounced.

setup were difficult due to adiabaticity violations and misalignments [134], a significant increase of the plate angle was associated with larger pitch angles. Due to the increased perpendicular component of the momentum at larger α_{p}, the magnetic guiding field and, thereby, the beam coil 1 current needed to be larger to allow transmission. Further, the height of the transmission maxima in passive mode and the depth of the minima in active mode were smaller for $\alpha_{\mathrm{p}} = 4°$. That means, the electrons of larger pitch angle could not move as similar to the channel orientation of the MCP-filter as electrons of smaller pitch angle.

To conclude, this and previous works applied active and passive filtering with MCPs on low-energetic electrons in a qualitative measurement. The experiments 1 and 2 showed the possibility of active measurement or suppression of electrons based on their angle towards the MCP channels and, thus, the general possibility of active and passive transverse energy filters. Among other things, the unknown extent of the misalignments between the magnetic field and the MCP-filter channels, however, did not allow for a quantitative estimation of the angle-dependent efficiency of the used MCP-filter. Nevertheless, since the proof-of-principle test remained successful, first steps to implement a silicon-based MCP with a KATRIN-suited geometry were undertaken, as previously reported in section 4.2.

4.4 aTEF-Concepts based on other Detector Types

The background mitigation via active transverse energy filters became an important research topic within the KATRIN collaboration [61]. C. Weinheimer suggested to use different, broadly used types of detectors like MCPs, Si-PIN diodes, or scintillators as aTEF. These are investigated for their potential to suppress and detect electrons based on their incident angle and help to reduce the background. The MCP-aTEF was explained previously and initiated research on further types of detectors. The Si-aTEF is a variant based on microstructured Si-PIN diodes, see chapters 4.4 and 6. Both, MCP-aTEF and Si-aTEF, are concepts that are researched in the group of C. Weinheimer [69, 121, 126, 132, 133, 134, 135, 136]. Another approach is a scintillator-based aTEF (Scint-aTEF). It consists of a 3d-printed microstructure out of a scintillating material, which is combined with a CMOS-based single-photon avalanche diode detector array, as shown in figure 4.24. It is developed at the KIT in the group of G. Drexlin [137].

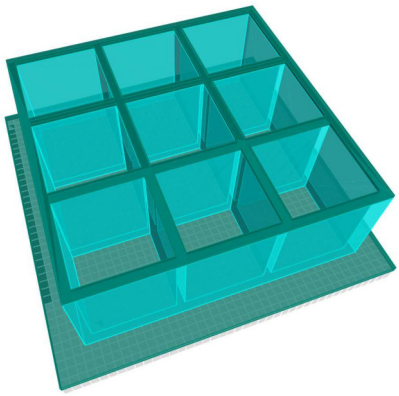

Figure 4.24 – The image shows the geometry of a GEANT4-simulation of the scint-aTEF [137]. It consists of a microstructured scintillator and a read-out device for the scintillation light – e.g., an SPAD array can be used. In this view electrons enter the scint-aTEF from the top. Scintillation light is generated if channels are hit by electrons, predominantly of large pitch angles. No light and no signal is generated if electrons directly impact into the SPAD.

MCPs can generally be used in strong magnetic fields. The strongly curved trajectory of secondary electrons in the KATRIN beamline, however, could make it necessary to increase

the acceleration voltage in order to allow the electrons to gain enough energy to induce an electron avalanche [138]. The effect of the unusual aspect ratio of diameter to channel length of an MCP-aTEF (1:2 to 1:4) compared to commercial MCPs (1:40 to 1:60), that is necessary to allow for sufficient background reduction and signal detection, needs to be thoroughly investigated, as it will affect the gain and dark count rate. Further, the material choice is crucial to minimize the background rate: MCPs made from intrinsically low-radioactive silicon may be suited for usage as MCP-aTEF for KATRIN. A description of possible manufacturing processes of the different layers and possible materials is given in section 4.2. The layered structure and the uncommon geometry require an extensive development process and optimization of parameters, which are, i.a., the layer materials, layer thicknesses, the overall geometry, and the applied voltage difference between front and back electrode.

In contrast to the MCP-aTEF, the Si-aTEF concept aims to utilize KATRIN's focal plane detector, which makes it the most accessible of the aTEF-variants. The scenario of a

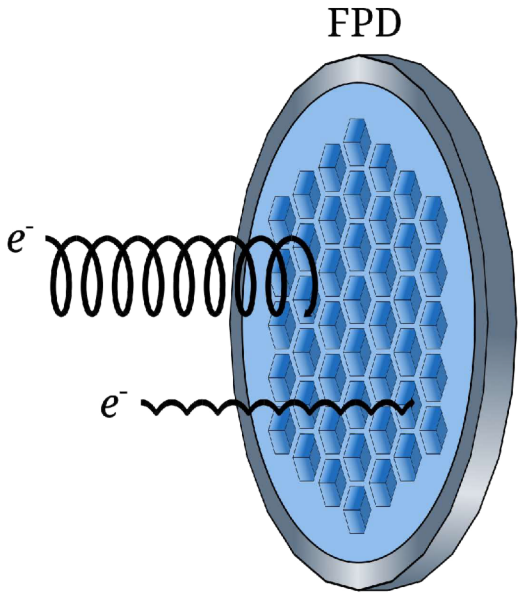

Figure 4.25 – The Si-aTEF is a microstructured Si-PIN diode, where the individual channels feature active sidewalls. The bottom of each channel should be inactive, so that electrons of small pitch angles are absorbed without generating a detector response. Electrons with small pitch angles will have a higher probability to hit the sidewall of a channel, where they induce a detectable signal. The channels can be etched into the surface with silicon nanofabrication tools. The substitution of the KATRIN focal plane detector with a microstructured Si-aTEF can be a solution to significantly reduce the background and to enhance the achievable neutrino mass sensitivity of the experiment.

Si-aTEF in KATRIN would be the following: The low-energetic electrons of the tritium β-decay only penetrate a few µm into the Si-surface. To allow the aimed-for angle-selective detection of electrons, a microstructure[26] needs to be inserted into the – initially planar – surface via deep silicon etching, where a hexagonal photomask shadows the area that

[26]The feasibility of Si-PIN diodes with microstructured active surfaces was already proven in other works, where they were used, for example, as neutron detectors [139].

needs to remain unaltered by the etch process. The non-covered Si-material is removed by the anisotropic etch process in a vertical direction to the surface. That way, the detector obtains vertical side walls. These are intended to register electrons of large incident angle[27], as indicated in figure 4.25. The surface at the bottom of the channel needs to be inactive, so that electrons of small incident angle are not registered. Either, the altered structure of the diode leads to the bottom surface being inactive, or an additional blocking layer is necessary to block electrons of small incident angles. The hexagonal microstructure exhibits a maximized OAR, while the side wall thickness is chosen thick enough to allow for a stable detector. The mask geometry is chosen based on the maximized neutrino mass sensitivity via suppression of background electrons and maintaining most of the signal electrons. The side wall thickness was fixed to $d \leq 10\,\mu\text{m}$ to maintain stability of the structure, but the stability of the final detector still needs to be tested before installation in KATRIN. Initially, a side length of $s = 100\,\mu\text{m}$ of a single hexagon and a channel length of $l = 400\,\mu\text{m}$ was considered to optimize the neutrino mass sensitivity [106]. However, the optimal geometry depends on the exact angular distribution of the background. After the introduction of the autoionizing oxygen states in the spectrometer (see section 4.1), the favored geometry was slightly altered to $s = 80\,\mu\text{m}$ and $l = 250\,\mu\text{m}$, which is based on sensitivity studies and simulations by S. Schneidewind [140] and C. Weinheimer, who developed the initial aTEF idea.

[27] In KATRIN, pitch angle and incident angle have the same value.

5 Fabrication of Microstructures in Silicon

Microstructured silicon-based electron detectors could be a key technology to reduce KATRIN's excessive background. This chapter is dedicated to the microstructuring process that is used to manufacture Si-aTEF prototypes. At first, a recipe for microstructuring silicon is developed. The fabrication steps for both, Si-aTEF and MCP-aTEF, and exemplary samples are shown in this chapter.

The MCP-aTEF and Si-aTEF approach, as they were introduced in the previous chapter 4, require certain steps of semiconductor engineering in order to apply the microstructure: In general, they need to undergo a cleaning protocol to remove anorganic and organic contaminations. Then, a photomask is applied before the etching procedure. The intended microstructure is imprinted in a deep-etch process and, eventually, the remaining photomask is removed.

The process of silicon deep etching was established throughout this work and a recipe was found by testing on blank silicon chips of $2 \times 2\,\mathrm{cm}^2$ area and $500\,\mu\mathrm{m}$ thickness.

A very first aim for the realization of the MCP-aTEF concept was to generate silicon samples with hexagonal channels, so that they can be activated with further layers generate secondary electron avalanches and work as particle detectors as described in chapter 4.2. Thus, the etch process was applied to silicon chips of $200\,\mu\mathrm{m}$ thickness for a duration long enough to completely etch through. The aim was the fabrication of a regular silicon structure, which could serve as basic structure for an MCP-aTEF. Being able to fabricate an MCP-aTEF would also allow to create a Si-based pTEF, as described in section 4.1.2.1. The activation of the MCP structure was not followed within this work, but ensued as a research project within the working group [121].

The recipe was then applied to (commercial) Si-PIN diodes with the aim to fabricate Si-aTEF prototypes. These underwent a less stressful cleaning procedure than pure silicon to reduce risk of damage. Si-aTEF prototypes need to be able to detect electrons based on the incident angle with a high efficiency. They should, further, be fully operating at a temperature that can be reached within KATRIN's detector section, $T_{\mathrm{op}} > 40°\mathrm{C}$.

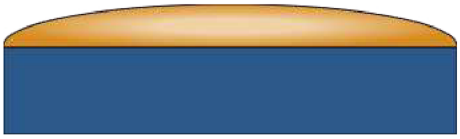

(a) Sample with SU-8 film

(b) Sample with spin-coated SU-8 film

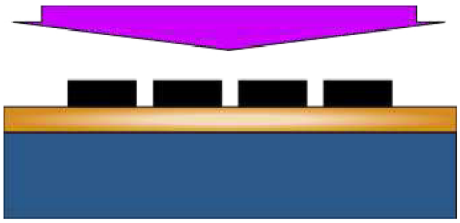

(c) UV-Lithography

(d) Photoresist mask

(e) Sample after ICP-RIE process

Figure 5.1 – Nanofabrication procedure of microstructured silicon and Si-aTEF prototypes. The SU-8 3035 photoresist (orange) is applied on the surface of the sample (blue) in (a) and evenly distributed (b). The lithography mask (black) transmits the UV-light (purple) in non-covered areas only (c). After development, the photoresist mask persists on the sample (d). The ICP-RIE process generates vertical structures in the sample and, further, deteriorates the SU-8 film (e). Optionally, the remaining SU-8 film can be removed (not shown), e.g. with suitable resist stripper solutions.

Two main kinds of etching samples were used in this work: Pure silicon chips and fully-functioning (commercially available) Si-PIN diodes. In addition, a piece of the FPD was etched to test the feasibility of the etch process on the FPD. Samples from pure silicon can be handled via standard protocols, while Si-PIN diodes need a more sensitive handling without strong solvents and at lower temperatures. The etch process recipes were

developed in close consultation with M. Stappers[1] and A. Fulst[2]. The fabrication process was carried out in the Münster Nanofabrication Facility[3] (MNF). The preparation and cleaning protocols are listed in section 5.1, the UV-lithography is described in section 5.2, and the etch process and the procedure to find a suitable recipe is presented in section 5.3. The removal of the photomask concluded the process and is shown exemplary in section 5.4. Microstructured Si-PIN diodes and silicon chips are found in section 5.5.

The process flow is summarized in figure 5.1.

5.1 Sample preparation

Si-chips were cut via dicing tool into $2 \times 2\text{cm}^2$ chips, which then were prepared via the following cleaning protocols. Commercial Si-PIN diodes were handled with less potent solvents and at lower temperatures in order to preserve their functionality.

5.1.1 Sample Cleaning Recipes

The standard protocol for pure silicon chips consisted of the following steps in this order:

- Submerge sample in acetone.
- Apply ultrasonic cleaning (for the device VWR Ultrasonic Cleaner USC-THD/HF: level 9, room temperature, approx. 5 min).
- Rinse with isopropyl alcohol (IPA).
- Blow dry with N_2 gas.
- Low-pressure oxygen plasma via Diener Zepto W6[4] plasma asher to further remove organic contaminants.
- Heat to 150°C to remove condensed water.

The silicon chips were then heated to 150°C to remove water prior to the application of the (supposed-to-be) permanent epoxy negative photoresist Kayaku Microchem[5] SU-8 3035 [141].

The established protocol for Si-PIN diodes considers that they are fragile devices. In order to keep the non-sealed electrodes, the passivation layer, and the protective epoxy around the wire bonds intact, the usage of the strong solvent acetone was avoided. For the same reason, the plasma asher was not used. Organic and non-organic surface contamination

[1] University of Münster, Physikalisches Institut, AG Pernice, Heisenbergstraße 11, 48149 Münster, Germany.

[2] University of Münster, Institut für Kernphysik, AG Weinheimer, Wilhelm-Klemm-Str. 9, 48149 Münster, Germany.

[3] University of Münster, Münster Nanofabrication Facility, Busso-Peus-Str.10, 48149 Münster, Germany.

[4] Diener electronic GmbH&Co. KG, Nagolder Straße 61, 72224 Ebhausen, Germany.

[5] Kayaku Advanced Materials®, 200 Flanders Road, Westborough, MA 01581, USA.

could, therefore, be more abundant than after the standard cleaning protocol and may have contributed to a non-ideal final result. The protocol consisted of these steps:

- Submerge sample in IPA.
- Blow dry with N_2 gas.
- Heat to 95°C for 10 minutes.

5.2 UV-Lithography

The UV-lithography utilized a reusable (negative) lithography mask to scribe a (positive) photoresist mask – resistant against plasma etching – with the targeted geometry directly onto the substrate.

5.2.1 Lithography Mask

The (negative) lithography masks were based on commercial blank masks from UV-transmitting soda lime glass substrate with a 90 nm Cr-layer. "Negative" means that the Cr-layer shadowed the photoresist from UV-illumination and polymerization, as figure 5.1c illustrates. The resulting photomask was a negative of the lithography mask.

In order to produce the mask, an electron beam resist is applied via spin coating. The subsequently executed electron beam lithography requires a data file with the geometric mask information in `.gds`-format and was prepared in Python with the GDSHelpers package [142]. The lithography mask manufacturing involved usage of the sophisticated electron beam lithography machine Raith[6] EBPG5150, which involved multiple training sessions and required an experienced user. Since the aTEF-project does not involve regularly repeated mask preparation, the masks were kindly prepared by M. Stappers. The next step is development of the resist in a suitable developer. Then, the non-coated Cr-layer needs to be removed by an etchant and, finally, the mask is cleaned with water and blow-dried with N_2. For fine structures it is recommended to remove the resist layer to prohibit static charge accumulation. Here, the resist was not removed because of the rather large structure size in the order of 10 µm.

Two masks were prepared: The first mask M1 had 4" diameter and hexagons of 100 µm side length and 10 µm sidewall thickness. It was not directly suited for Si-PIN diodes, where the microstructure needed to be applied in the central part. It was necessary to manually cover the outer area, where the electrodes are located. Mask M2 contained two masks on one substrate: One with an area of $7.5 \times 7.5\,\mathrm{mm}^2$ and another one with an area of $15 \times 15\,\mathrm{mm}^2$. Both featured hexagons with 100 µm side length and 20 µm sidewall thickness.

[6] Raith GmbH, Konrad-Adenauer-Allee 8, 44263 Dortmund, Germany.

5.2.2 Photoresist Mask

After application of the cleaning protocol as described in section 5.1 the sample was inserted into a POLOS Spin 150i SPS europe spin coater. There, a layer of Kayaku Microchem SU-8 3035 photoresist was applied thickly. That allowed for silicon structures with depth in the order of a few 100 µm. The SU-8 variant 3035 is of high viscosity, which, on the one hand, allowed the thick application but, on the other hand, impeded even distribution of the photoresist. The photoresist could not be handled via a standard pipette method due to its high viscosity. So, the photoresist was carefully poured onto the sample distributed with a pipette tip as evenly as possible. The spin coating was a two-step process: It started with an acceleration of 100 rpm/s until 1500 rpm was reached and held for 10 s. Then, it accelerated with 300 rpm/s, until 4000 rpm was reached, which was held for 90 s. An accumulation of photoresist at the sample edges was inevitable, but in most of the application cases not relevant. In order to not accidentally polymerize the photoresist, the sample needed to be handled in a UV-free clean room environment until the photoresist mask was illuminated, developed and sufficiently hardened.

The sample was heated for 10-15 minutes to 95°C to remove solvents before the UV-illumination. A heating duration of 15 minutes was favored for the handleability of the samples to reduce the adhesiveness of the photoresist. However, it could occur that the substrate with its photoresist mask sticked to the lithography mask during the lithography process. If not yet baked, the SU-8 photoresist was soluble in acetone or – less efficiently – in isopropyl alcohol and could, thereby, be removed.

5.2.3 UV-Lithography

The sample and the UV-lithography mask were installed in the lithography system EVG® 620 NT[7], which allowed precise mask alignment to the substrate and exposure with UV light of 350 nm to 450 nm. The lithography mask was brought into close proximity of the (photoresist-covered) substrate and exposed with UV-light, which caused cross-linking of the photoresist molecules in the exposed areas. The optimal exposure dose depends on the film thickness and is 150 mJ/cm² to 250 mJ/cm² for thickness above 20 µm [141]. Recipes of parameters that controlled the distance of the mask and substrate during the process are listed in table A.1 in the appendix.

A post-exposure bake of 1 min at 65°C and 10 min at 95°C was carried out to evaporate the remaining solvent from the photoresist and induce polymerization. Afterwards, the photomask was developed in propylene glycol methyl ether acetate (PGMEA), where gentle swirling of the sample was advised (that mainly applies for high aspect ratios). After 8 minutes, the sample is immersed in IPA to interrupt the development process. The sample is prepared for the etching process after blow-drying with N_2.

[7]EV Group Europe&Asia/Pacific GmbH, DI Erich Thallner Strasse 1, A-4782 St. Florian am Inn, Austria.

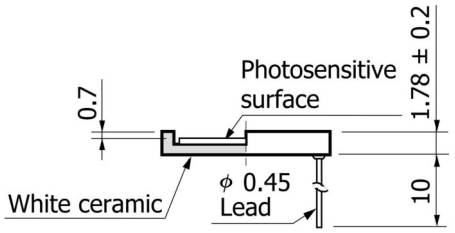

Figure 5.2 – The commercially available Hamamatsu S3509-09 PIN-diode had a ceramic packaging that overtopped the detector surface. The resulting enlarged gap between photoresist and lithography mask was problematic, since the UV-light was strongly refracted and distributed to non-masked regions [143].

The typical proximity parameter value that resulted in good photoresist masks lied around 200 µm to 300 µm, as tests on blank silicon chips showed. For the Hamamatsu[8] S3590 PIN diodes that were used as Si-aTEF-prototypes throughout this work, the optimal proximity cannot be set due to an inherent problem from their packaging: The ceramic packaging extended above the detector surface, see figure 5.2, and induced a minimum proximity of 700 µm between lithography mask and detector surface. The UV-light was distributed to regions of the photoresist that were intended to be masked and effectively enlarged the minimum structure size. Thus, the achieved structure sizes of photoresist masks on the Hamamatsu S3590 PIN diodes were systematically larger than aimed for. Since the spread-out induced a reduced total intensity in the illuminated regions, the amount of cross-linking reactions of the photoresist polymers was lower than anticipated. This lead to less robust photoresist layer – probably with detrimental effects on the etch result. That problem was later solved with a custom packaging from Hamamatsu, see e.g. in [69, 144].

5.3 Cryogenic Inductively Coupled Plasma Reactive Ion-Etching

In general, Si can be micromachined via different fluorine- (or chlorine-)containing plasma-based methods. These are categorized into sputtering, chemical etching, ion-enhanced energetic etching and ion-enhanced inhibitor etching [145]. In contrast to SiO_2 and photoresist, Si has a lower Arrhenius activation energy for reaction of F-radicals [145]. Therefore, the F-based methods with a chemical etching component preferably etch Si and affect the photoresist- and SiO_2-covered areas by a much smaller amount [146]. A highly-directional etch is achieved in reactive-ion etching (RIE) where an inhibitor mechanism prevents contact of F-radicals with the vertical areas. RIE is a well-established tool in semiconductor chip production and widely used, with experiments on the process beginning in the mid 1970's [147]. A first deep RIE process was invented with the Bosch-process

[8] Hamamatsu Photonics Deutschland GmbH, Arzbergerstr. 10, 82211 Herrsching am Ammersee, Germany.

in 1992 [148, 149] by F. Laermer and A. Schilp. It is a dry etching[9] process and a well-regarded tool for structure etching. Highly anisotropic etching of deep structures in silicon is crucial for the aTEF-fabrication, with the two mainly used plasma-etching processes with that ability being the Bosch-process and inductively coupled plasma reactive ion-etching (ICP-RIE). The main idea in both procedures is to completely passivate the silicon surface, to remove the passivation layer in the horizontal layers via ion bombardment and to bring an etch gas (containing fluorine, e.g. CF_4 or SF_6) in contact with the uncovered silicon surface. Thereby, the etch is directed vertically to the surface. While the deep RIE or Bosch process alternates between the steps of surface passivation and of etching in conjunction with ion bombardment, leaving a slightly undulating sidewall structure, the ICP-RIE process achieves both - etching and passivation - in one continuous process that allows for straight sidewalls.

The ICP-RIE is available in the Münster Nanofabrication Facility (MNF) with an Oxford[10] PlasmaLab 100 machine. Two different plasma sources are installed in ICP-RIE instruments: The inductively coupled plasma (ICP) source and the conductively coupled plasma (CCP) source.

The ICP is generated via radio frequency (RF)-driven magnetic induction. The ion species are produced via collisions of electrons, atoms and molecules until equilibrium is reached. Increased voltage raises the number of ions according to Paschen's law and, thus, allows to control the ion density.

The conductively coupled plasma (CCP) is generated by a RF voltage oscillation between cathode and anode. There, the mobile electrons ionize the rather inert injected gas molecules or atoms. There is self-bias in CCP, i.e. there are negative charges accumulating on the cathode via the capacitor between anode and RF supply. Thereby, it accelerates ions vertically and provides the ion bombardment. A static plasma voltage results from the loss of electrons to the grounded walls.

Both modes – ICP and CCP – are operated in superposition in the ICP-RIE process, which allows to independently alter the ion density and ion flux. The etching process can be described as interplay of a chemical and a mechanical etch component, which allows for great versatility and is a great advantage of the ICP-RIE process. The *chemical etch* is obtained with the utilized process gases SF_6 and O_2 by the plasma-generated radicals:

$$\begin{aligned} SF_6 &\rightarrow SF_x + F_y \\ O_2 &\rightarrow O + O \end{aligned} \tag{5.3.1}$$

There are two chemical etch reactions with Si: The reaction

$$Si + F + O \rightarrow SiO_xF_y \tag{5.3.2}$$

[9] Dry etching is opposed to wet etching, where a liquid etchant is used. Most wet etching processes etch isotropically, while dry etching obtains a chemically reactive plasma.

[10] Oxford Instruments GmbH, 62505 Wiesbaden, Borsigstrasse 15a, Germany.

removes Si and provides the passivation of the side walls, when SiO_xF_y attaches to the silicon surface and obstructs the F radicals from reaching the surface. This effect is temperature dependent and allows for anisotropic etching at temperatures below approx. $-75°C$ [150]. At temperatures below $-140°C$, however, SF_6 begins to condense and prohibits the etch process [151]. The ion bombardment via ICP source sputters the passivation layer from the horizontal surfaces (*mechanical etch*). That allows F-radicals to come in contact with the silicon surface and react chemically via

$$Si + F \rightarrow SiF_4, \tag{5.3.3}$$

with the gaseous SiF_4 being removed. The etch via F-radicals also erodes the photoresist and other surfaces, for example SiO_2 layers, but does this with much lower rates. The ICP-RIE process is illustrated in figure 5.3.

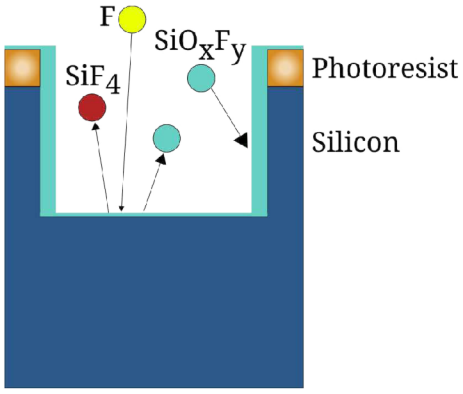

Figure 5.3 – Schematic ICP-RIE process on a silicon sample. The passivation layer is built from the reaction products and contained on the vertical walls at cryogenic temperatures. The horizontal passivation layer of SiO_xF_y is constantly removed by the impact of ions. That exposes the horizontal surface to F-radicals and results in a highly anisotropic etch process.

Many parameters affect the etching rate of silicon and photoresist, the anisotropy of the process and the overall result: While an increased CCP power P_{CCP} raises the ion energy and induces a stronger mechanical etch, an increased ICP power P_{ICP} raises the ion density in the plasma and thereby induces a stronger chemical etch. The sample temperature changes the sidewall passivation by influencing the volatility of SiO_xF_y: An increase in temperature reduces the attachment rate and, thereby, the sidewall passivation. The sample temperature is affected by the He-pressure P_{He} on the sample backside and via the LN_2-cooled table temperature T_T. The process gas ratio and the total gas flow F_{O_2} and F_{SF_6} influence the etch chemistry, i.e. etch rate and anisotropy, of substrate and photoresist.

Section 5.3.1 shows the established workflow for the etch process. A general overview of the ICP-RIE parameters and their correlations is given in section 5.3.2, while section 5.3.3 shows a way to find a proper recipe for deep vertical structures and presents an overview of the treated samples.

5.3.1 Etching Procedure

The Oxford PlasmaPro® 100 Cobra used in this work is a versatile plasma etch machine for wafers up to 4" or ≈ 100 mm diameter (with the option to process wafer sizes of up to 8" diameter, which would require an expensive modification). It is shown in figure 5.4 The sample was installed on a carrier wafer in the load lock chamber of the Oxford

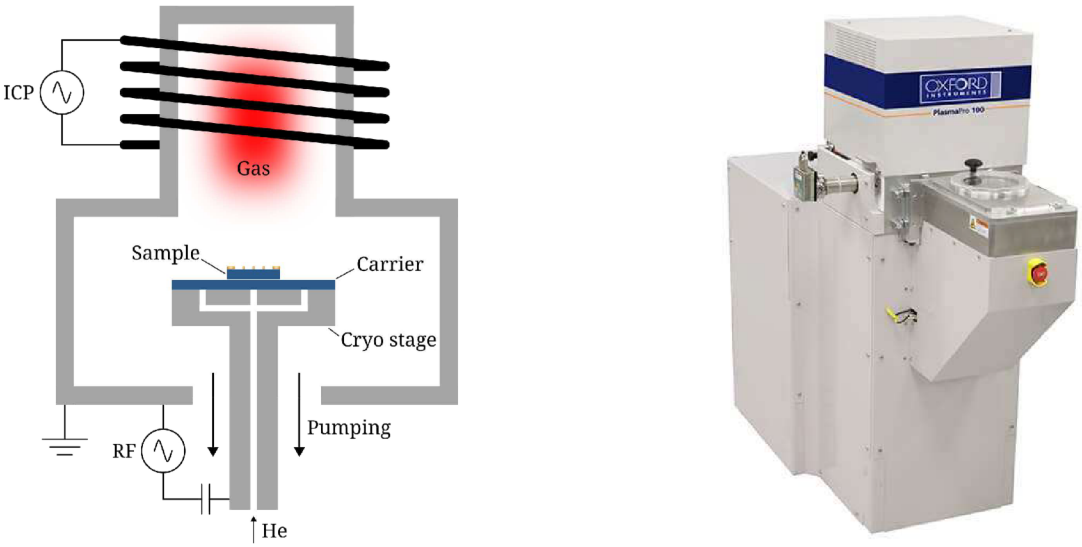

(a) ICP-RIE chamber **(b)** Oxford PlasmaPro® 100 Cobra [152]

Figure 5.4 – A schematic of an ICP-RIE instrument is shown in (a). The chamber is evacuated via the pump ports. The process gases are constantly supplied. The plasma is generated by the ICP source. The RF source accelerates charged plasma particles onto the sample and carrier wafer. Cooling of the carrier wafer is provided by He, which allows heat conduction. The clamp, which fixates the wafer onto the cryo stage, is not shown here. The instrument in (b) is located in the MNF and used for the etch processes in this work. The carrier wafer with the sample on top is placed in the load-lock chamber, which can be quickly evacuated. The load-lock chamber is flushed with nitrogen after completion of the process in order to remove any – potentially hazardous – process gas residues.

PlasmaPro® 100 machine. Sufficient attachment of the sample to the carrier wafer was achieved with a thin layer of Santovac® 5 polyphenol ether vacuum oil between the two, which is easily removable with IPA. It increased the temperature conductance and held the sample in place. The load lock chamber was evacuated and the carrier wafer was automatically transferred into the aluminum main chamber. There, the ICP-RIE process was executed according to the previously specified recipe. Afterwards, the carrier wafer was driven back into the load lock chamber. The load lock chamber was purged with nitrogen, evacuated once more to remove traces of the (possibly hazardous) process gases, and vented in the end. Then, the carrier wafer was removed from the chamber. The sample was carefully separated from the carrier wafer and cleaned with IPA. The result was finally checked with an optical microscope or, if the sample is not electrically sensitive, a scanning electron microscope (SEM). The carrier wafer was a SiO_2-coated Si-wafer. Si allowed for sufficient temperature conduction to cool the sample to the required temperature. The wafer's multiple µm thick SiO_2 layer was significantly more etch-resistant than silicon.

The ICP machine was supplied with LN_2 via a cryogenic storage dewar, which was placed next to the machine for the first etch tests. Since the machine was placed in a cleanroom environment, this dewar had to be cleaned thoroughly after every filling procedure, which took place out of the cleanroom. A direct liquid nitrogen supply line was, therefore, installed to feed the machine from a dewar outside of the cleanroom area.

5.3.2 Cryogenic ICP-RIE Parameters

There exist different methods to navigate through the adjustment of the great number of parameters to achieve an etch result in an affordable number of optimization steps. The set of optimal parameter values further depends on the machine (and its contaminations) and is generally not directly transferable to other machines. There are multiple correlations between parameters [153], which are listed here.

The oxygen flow is correlated to the CCP power: Since the CCP power affects the ion energy, it directly influences the effectiveness of the sidewall-passivation SiO_xF_y. Combining increased CCP power with lowered oxygen flow increases sputtering properties and, thus, lowers the effectivity of the sidewall-passivation.

The temperature of the lower electrode (or table temperature) directly affects the wafer temperature. It plays a crucial role and can be seen in context to CCP power, to O_2 flow, and to SF_6 flow: Combining increased CCP power, for example, with higher table temperatures can lead to a more isotropic etch result, because the sidewall passivation is reduced by the volatile SiO_xF_y. Too low CCP power, on the other hand, may induce the formation of silicon micro-pillars – so-called black silicon. Black silicon is created via micromasking from, i.a., insufficient removal of the passivation layer from the horizontal surfaces or from surface contamination. It is a sought-after phenomenon for example for sensor or catalysis applications due to its very high absorption also of visible and near-infrared light [154]. Here, it is an unwanted product, as it disturbs the etching process by reducing the etch rate and probably increases surface leakage currents of the final Si-aTEF detectors.

While too high table temperatures reduce the sidewall-passivation and lead to a more isotropic etch or a negative taper, excessive wafer cooling, on the contrary, can lead to narrowing of the sidewalls with depth (positive taper) from an increased sidewall-passivation.

Irregular and underetched structures may result from a low O_2/SF_6 gas flow ratio, since they deliver the etch reactants. If the ratio is too large, tapered structures can develop and, further, black-silicon may be created.

Increasing the ICP power has a similar effect as increasing the SF_6 flow, since they both enhance the F-concentration and lower the sidewall-passivation [153]. That can lead to a more anisotropic etch.

Enhanced main chamber pressure increases the ion angular distribution and, as a consequence, removal of the SiO_xF_y-passivation is increased.

It is suggested in [153] to start with a set of parameter values and, due to the correlation of different parameters, only change key parameters in order to balance deposition of the passivation and etching. Such a parameter set can be, for example, the table temperature, the CCP power and O_2 and SF_6 gas flow. The He-backing pressure and, also, the ICP power have tremendous effects, but these can be also reached by changes within the chosen parameter set.

5.3.3 ICP-RIE Parameter Tuning for Deep Silicon Etch

The very first set of deep-etched samples was produced solely to find promising start parameters. These values were chosen by M. Stappers. The samples and their parameters are listed as Si-chips 1 to 10 in table 5.1. The influence of the different ICP-RIE parameters is visible in the images in figure 5.5, where the broken chips reveal the etch profile. During the manufacturing-series of the chips 1 to 10 every parameter except for the CCP-power P_{CCP} and total time t was changed. All of the chips 1 to 10 showed black silicon, grassing, or other defects. The formation of black silicon drastically increases the surface and it was observed to lower the etch rate when it was excessively prevalent.

The change in table temperature from $-100°\mathrm{C}$ to $-120°\mathrm{C}$ between chips 1 and 2 did not have a remarkable effect on the result. The warmer table temperature of $-80°\mathrm{C}$ and, additionally, the weaker He-backside cooling was responsible for the so-called grassing, i.e. short silicon needles, that is seen in figure 5.5c. The shortness of the needles hints to a thin passivation layer, i.e. insufficient protection from F-radicals in horizontal direction. Further, the region close to the mask showed a bottling effect. Bottling directly beneath the mask can be caused by a too thin passivation layer and a higher number of ions that hit the surface compared to deeper parts of the sample. The O_2 gas flow was increased and the SF_6 flow was reduced at chip 5. The higher oxygen content lead to a stronger passivation and the reduced amount of F-radicals lowered the etch rate. That resulted in a positive taper of the structures.

Strongly increasing the ICP power to $P_{\mathrm{ICP}} = 900\,\mathrm{W}$ for chip 7 resulted in an isotropic etch, such that the structures beneath the photomask were etched away. The reduction of temperature from $-100°\mathrm{C}$ to $-120°\mathrm{C}$ in chip 8 did not prevent this behaviour, as figures 5.5e and 5.5f show. Despite the decrease in ICP power to $P_{\mathrm{ICP}} = 700\,\mathrm{W}$, an increase in chamber pressure to $P_{\mathrm{Ch}} = 25\,\mathrm{mTorr}$ drastically increased the ion angular distribution and, thereby, reduced the sidewall passivation, resulting in rather isotropic etch, too. Finally, the higher temperature of $T_{\mathrm{T}} = -80°\mathrm{C}$ of chip 10 caused a lowered sidewall passivation, although it was combined with an increase in O_2 flow (stronger passivation) and lowered SF_6 flow (weaker etch).

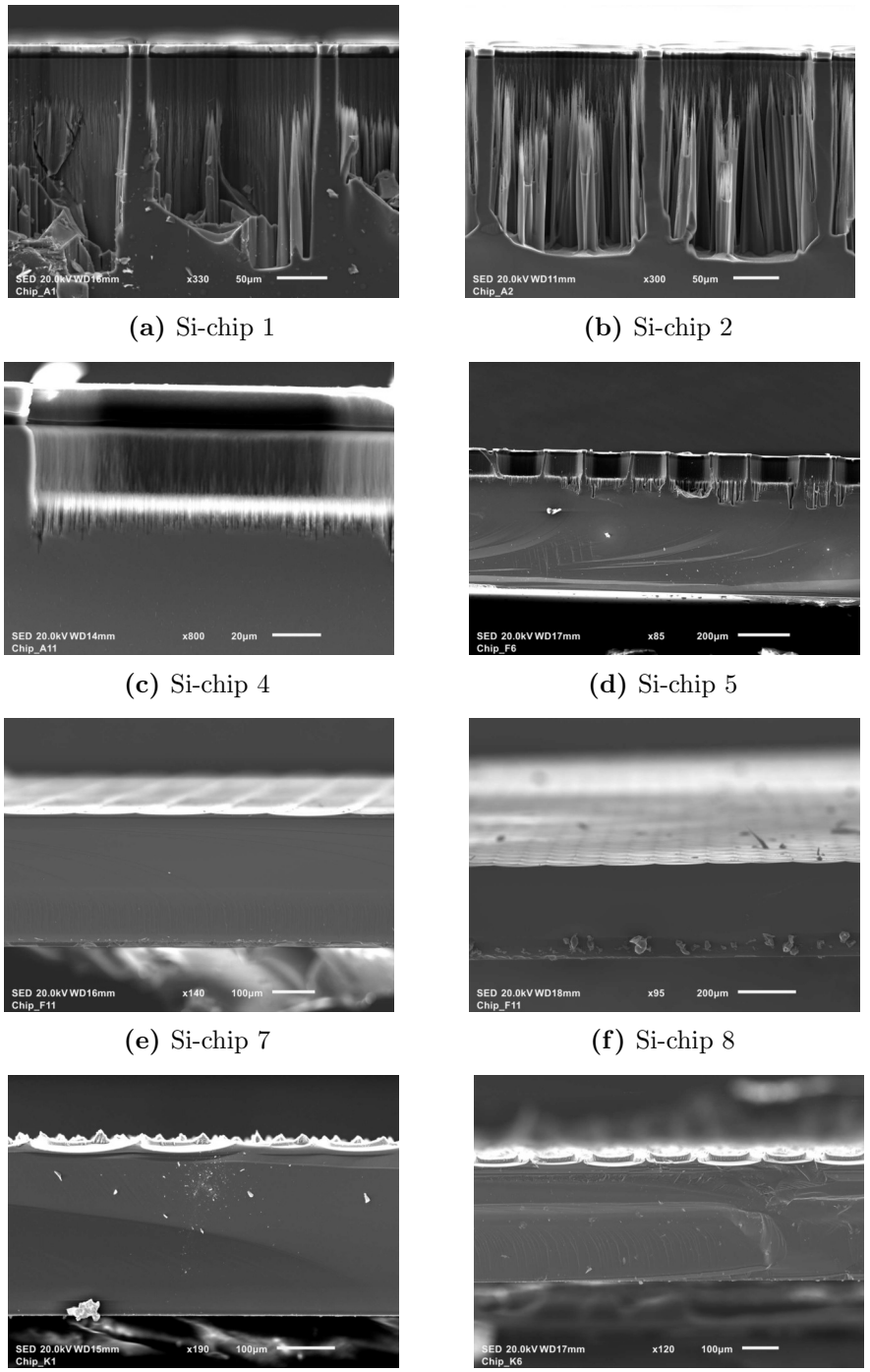

(a) Si-chip 1 **(b)** Si-chip 2

(c) Si-chip 4 **(d)** Si-chip 5

(e) Si-chip 7 **(f)** Si-chip 8

(g) Si-chip 9 **(h)** Si-chip 10

Figure 5.5 – First ICP-RIE process series with silicon samples. Images were taken with a JEOL JSM-IT100 scanning electron microscope after the etch. The parameters were varied as summarized in table 5.1. More information is given in section 5.3.3. Parameters can be found in table 5.1. The dust particles on the images stem from breaking the chips in order to access the etch profile. The chips are viewed from the side. The etch is brought on the sample from the top. The photoresist is visible as thin layer in (a) to (d), as well as the vertical sidewalls and silicon needles and other artifacts. In the other images, a too large horizontal etch component removed the sidewalls.

The chips 1 to 10 were etched with variation of every parameter of the ICP. This helped

tremendously to understand their specific influence on the etch result. The chips B1 to B10, though, were etched with variation of the subset P_{ICP}, P_{CCP}, and P_{Ch} with the aim to find a working set of parameter values. The results are shown in figure 5.6.

The chip B4 was etched with increased $P_{\mathrm{CCP}} = 20\,\mathrm{W}$, which removed the passivation layer more efficiently than in chips 1 to 10, where $P_{\mathrm{CCP}} = 10\,\mathrm{W}$ was used. That still resulted in a certain amount of black silicon, but it is reduced compared to the previous chip 1. Chip B4 shows positively tapered sidewalls. That taper seems to have been removed in chip B6, where the CCP power was drastically increased to $P_{\mathrm{CCP}} = 50\,\mathrm{W}$. The number of silicon needles was strongly reduced and the sample looks overall much cleaner.

In order to slightly enhance the anisotropy of the etch, the ICP power was reduced to $P_{\mathrm{ICP}} = 600\,\mathrm{W}$ in chip B7. That led to the intended etch result with clean structures mainly free of silicon needles and straight channel walls, as visible in figures 5.6g and 5.7.

The chips B1 and B5 were etched simultaneously, as well as chips B3 and B9 and chips B2, B8, and B10. The larger silicon area changed the etch rate by occupying more F-radicals, but revealed the important implication that the etch rate strongly depended on the etched surface. A full-scale Si-aTEF with the size of KATRIN's focal plane detector will, therefore, require a separate etch parameter adjustment. It was, further, seen in a large area etch of a silicon blank wafer of 10 cm diameter that the etch rate slightly depends on the radius and is higher towards outer radii, see section 5.5. That effect may be avoidable with a larger ICP-RIE etching instrument that provides a more homogeneous plasma within the inner 10 cm.

To conclude, the variation of the parameter set of ICP power, CCP power and pressure turned out successful and a standard etch recipe was developed. It is assumed that the results obtained with pure silicon are directly applicable to the doped silicon of PIN diodes. Examples of etched PIN-diodes are given in section 5.5.

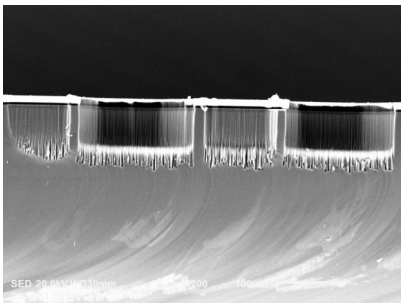

(a) Si-chip B1

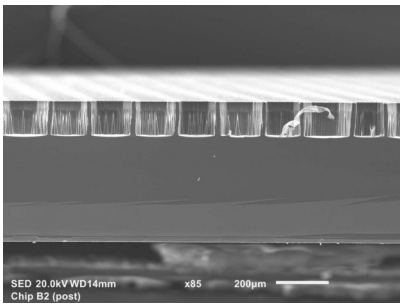

(b) Si-chip B2

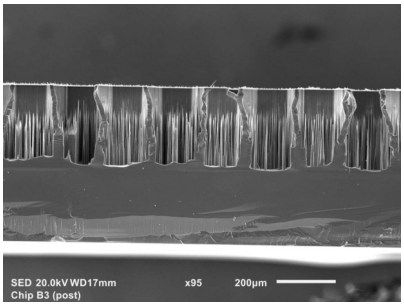

(c) Si-chip B3

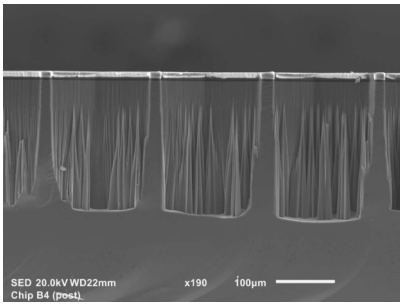

(d) Si-chip B4

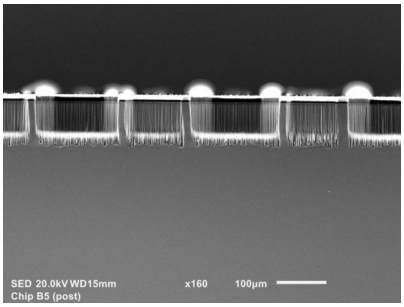

(e) Si-chip B5

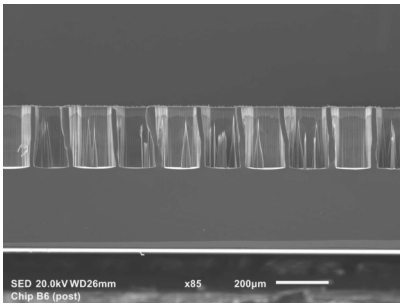

(f) Si-chip B6

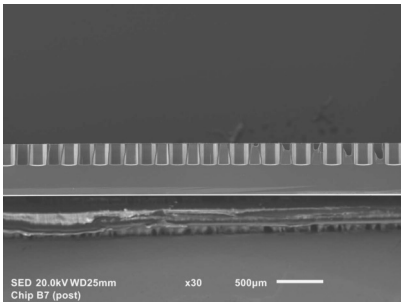

(g) Si-chip B7

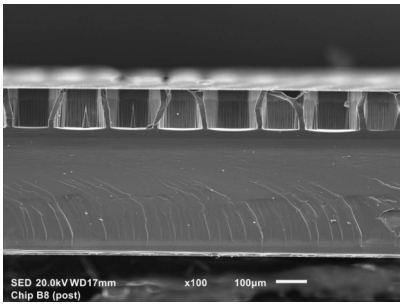

(h) Si-chip B8

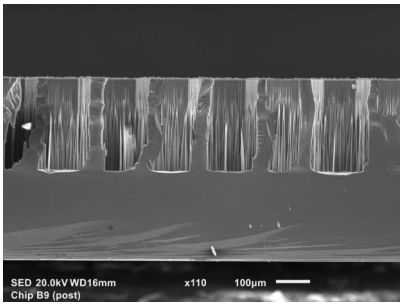

(i) Si-chip B9

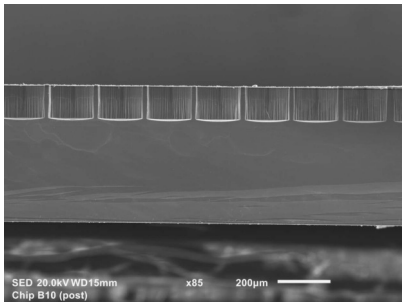

(j) Si-chip B10

Figure 5.6 – Systematic ICP-RIE parameter study, as explained in section 5.3.3. Parameters can be found in table 5.1.

Table 5.1 – Main ICP-RIE parameter study with variation of a subset of ICP-RIE parameters. Missing chip-numbers were not etched. The photoresist application was (visibly) thinner for chips 1, 2, and 5, and the recipe was exchanged to a thicker application. Consequently, the resist thickness parameter for the UV-lithography was enlarged significantly to prevent contact and adhesion between lithography mask and photoresist. Parameters: ICP-power P_{ICP} (W), CCP-power P_{CCP} (W), O_2 gas flow F_{O_2} (sccm), SF_6 gas flow F_{SF_6} (sccm), chamber pressure P_{Ch} (mTorr), table temperature T_{T} (°C), He-backing pressure P_{He} (Torr), etch time t (min), etched depth d (µm). The resulting standard recipe of chip B7 is highlighted in gray.

Si-chip	P_{ICP} (W)	P_{CCP} (W)	F_{O_2} (sccm)	F_{SF_6} (sccm)	P_{Ch} (mTorr)	T_{T} (°C)	P_{He} (Torr)	t (min)	d (µm)
1	700	10	9	61	20	-100	10	30	209
2	700	10	9	61	20	-120	10	30	220
4	700	10	9	61	20	-80	8	30	193
5	700	10	15	55	20	-100	10	30	60
7	900	10	9	61	20	-100	8	30	218
8	900	10	9	61	20	-120	8	30	207
9	700	10	9	61	25	-100	8	30	245
10	700	10	15	55	20	-80	8	30	210
B1	700	10	9	61	20	-100	8	30	95
B2	600	50	9	61	15	-100	8	30	130
B3	600	50	9	61	20	-100	8	40	190
B4	700	20	9	61	20	-100	8	30	237
B5	700	10	9	61	20	-100	8	30	88
B6	700	50	9	61	20	-100	8	30	230
B7	600	50	9	61	20	-100	8	30	225
B8	600	50	9	61	15	-100	8	30	130
B9	600	50	9	61	20	-100	8	40	270
B10	600	50	9	61	15	-100	8	30	125

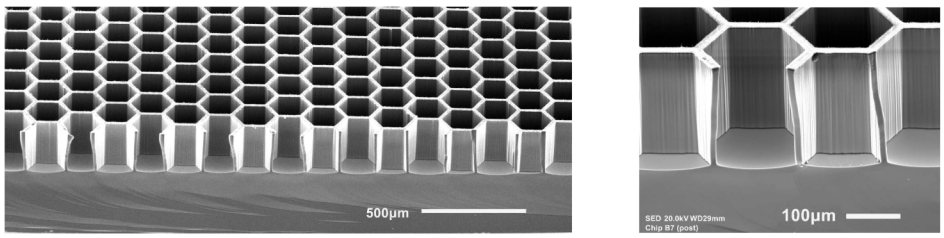

(a) Si-chip B7 **(b)** Si-chip B7, zoomed

Figure 5.7 – Views on chip B7, taken with the JEOL JSM-IT100 SEM. The depth of chip B7 was $\sim 225\,\mu\mathrm{m}$ [106].

5.4 Photoresist removal

The photoresist SU-8 3035 is highly-persistent against solvents. A way to remove the photoresist and other organic residues from silicon is a solution of sulfuric acid (H_2SO_4)

and hydrogen peroxide (H_2O_2), so-called piranha etch[11]. It is an established process for pure silicon samples. However, when applied to Si-aTEF prototype diodes, it removed parts of the electrode materials of the Hamamatsu S3590 diodes and is, therefore, not suited for these diodes.

Another, non-toxic and safer method, is the solvent dimethyl sulfoxide (DMSO[12]): Covering the sample in DMSO and heating it to 60°C to 80°C for multiple hours lead to detachment of the SU-8 photoresist from the silicon surface, see figure 5.8. The time and the result depended, i.a., on the DMSO temperature, the photoresist thickness, the open area ratio and etch quality. DMSO did not solve SU-8, but swells it and, thereby, loosens or breaks the adhesion to the silicon surface. It was less efficient on very thin structures of less than 10 µm. It did, however, not attack the electrode material and was, due to its non-toxicity and usability, the method of choice for the aTEF-prototypes. Remaining DMSO was removed via IPA.

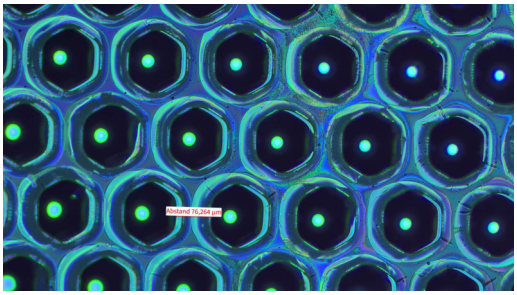

(a) Before DMSO-cleaning

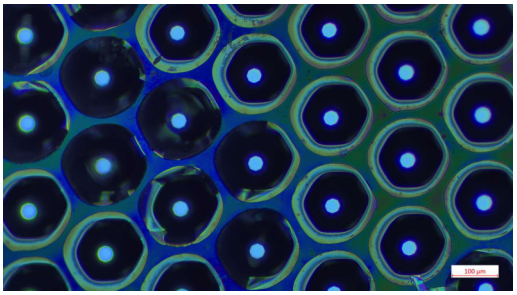

(b) After DMSO-cleaning

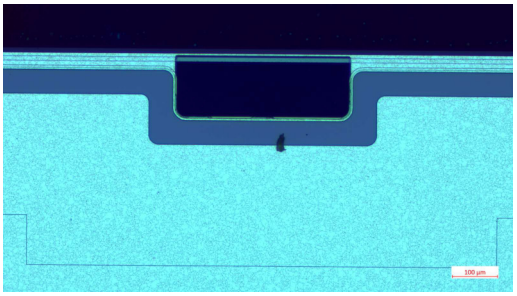

(c) After Piranha cleaning

Figure 5.8 – Top view of two microstructured Si-PIN diodes showing the result of two removal methods of photoresist: The sample in (a) was treated with DMSO, resulting in the clean surface (b) With DMSO, small pieces of epoxy resist may have persisted on the surface. Further, the color gradient in (b) may hint to residues, which can affect the performance of the diode. The sample in (c) was treated with Piranha solution. Both methods reveal a clean Si-surface. Although Piranha solution removes the SU-8 resist very efficiently, the process was not suited for the Si-PIN diodes: The electrode pads, which are used for the electric contacts via wire bonds, were removed by the acid.

[11] It has to be prepared by trained personnel in a fumehood for hydrofluoric acid due to its reactivity and toxicity and it has to be handled with greatest care. Therefore, the qualified and experienced group of Prof. Pernice kindly tested the procedure on one of the samples

[12] DMSO is listed as less potent alternative to *N*-methyl-2-pyrrolidone (NMP). NMP is toxic and its use, therefore, avoided.

5.5 Examples

Throughout the aTEF-prototype development hexagonal microstructures were imprinted in a variety of different samples. There were Si-chips to study the ICP-RIE process parameters, as described in the previous section 5.3.2. Further, the possibility of etching channels through silicon was explored as a preparation for an MCP-aTEF. Pieces of a spare FPD showed that the KATRIN-detector allows for a clean etch result with the intended large open area ratio. The main object were Hamamatsu S3590 Si-PIN diodes, which were used to study the Si-aTEF and its angular-selectivity, as it is described in detail in chapter 6.3.

The etch rate of the samples depended on the non-covered silicon surface. The samples were placed on a SiO_2-coated carrier wafer and in order to reduce excessive material consumption, these carrier wafers were reused with the SiO_2 layer being partly removed in each etch process. However, when the underlying silicon layer of the surfaced, the etch rate of the samples was drastically reduced, which had to be anticipated for a correct process.

Throughout all samples silicon needles or black silicon could occur. Cleaner substrate surfaces helped to reduce localized differences in the etch rate on the chip surface. If they remained, these differences could enlarge during the process and lead to micromasking and, consequently, to the formation of silicon needles. However, the sensitive diodes were not treated with an ultrasonic bath and acetone or other too strong solvents in order to keep the electrodes and the surfaces fully intact. Thus, the risk of black silicon persisted for this kind of samples. Further, the SU-8 photoresist exceeded its expiration date. The contained solvents may have evaporated or degenerated to some extent, inducing performance issues.

The SEM (scanning electron microscope) images throughout this work were obtained with a JEOL[13] JSM-IT100. The optical microscope images were taken with a Zeiss[14] Axiolab 5. Functioning diodes were photographed exclusively with the optical microscope to not damage them by the large voltage differences of multiple keV in the SEM.

The examples shown in this work were etched with the recipes specified in table 5.2

5.5.1 Silicon chips and wafers

Blank Si-chips were not only used to find optimal recipes: In a first attempt to build the basic structure of a silicon-based MCP-aTEF, the etching of hexagonal channels through entire silicon chips (and wafers) was attempted. In figure 5.9, an example of an originally 200 µm thick silicon chip is shown. A strong difference between the top and the bottom of the etched chips was observed: The front was clean and resembled the mask, the back showed defects and deviated from the hexagonal shape. Not all hexagons were etched through and, conclusively, the etch rate over the chip surface was inhomogeneous. It seems that any irregularity of the mask, e.g. uneven edges, has propagated down and amplified.

[13]JEOL (Germany) GmbH, Gute Änger 30, 85356 Freising, Germany.

[14]Carl Zeiss Microscopy Deutschland GmbH, Carl-Zeiss-Strasse 22, 73447 Oberkochen, Germany.

Table 5.2 – Parameters and results of the different samples that are described in this work. The samples consisted of plain Si-chips or Si-wafers and active Si-PIN diodes. A piece of the KATRIN focal plane detector (FPD) was etched in order to prove the feasibility of production of hexagonal structures to allow the transformation of an FPD into a Si-aTEF. More samples were prepared, but are not shown here. The standard spin coating recipe with SU-8 film was 10 s @ 500 rpm and 90 s @ 4000 rpm on a "POLOS Spin 150i SPS europe" spin coater. The lithography recipes are shown in table A.1 in the appendix. The lithography mask was either version M1 or M2, see section 5.2. The ICP-RIE recipe "ICP1" is the standard recipe that was used for chip B7 in table 5.1. Diodes A, B, C, and D were renamed for this work and are, in this order, referred to as D3, D4, Diode 2, and K1 in the laboratory journal and further records. The etched depth of diode D was measured with the attached photomask of unknown thickness.

Object	Recipes	ICP-RIE time (min)	Approx. depth (µm)
Si chip E2	2×(SC1, L-Chip), M1, ICP1	49	360
Wafer W1	SC1, L-Wafer, M1, ICP1	~ 170	
Diode A	SC1, L-S3590v2, M1, ICP1	20	
Diode B	SC1, L-S3590v2, M1, ICP1	20	100 ± 10
Diode C	SC1, L-S3590v3, M2, ICP1	30	111 ± 14
Diode D	SC1, L-S3590v2, M2, ICP1	40	130 ± 15
FPD	SC1, L-FPD, ICP1	30	122 ± 15

These irregularities can be reduced by higher electron-beam lithography precision during fabrication of any future lithography mask (refer to section 5.2).

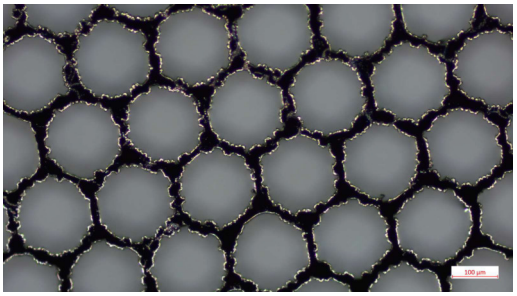

Figure 5.9 – A 200 µm thin Si-chip that was prepared and etched with the standard ICP-RIE recipe (see table 5.1). While a clean top was reached consistently with Si-chips, the surface structure on the backside was very rough and irregular. That is shown in the image, but also visible in later iterations, see [121].

Upon the etch of a whole Si-wafer of 4" diameter, a slight radial dependence of the etch rate was seen, as figure 5.10 shows. The radial etch rate is reducible with a larger ICP-RIE etching instrument that provides a more homogeneous plasma within the inner region. Further, an uneven distribution of the SU-8 photoresist during spin coating may have left the inner region with a thinner SU-8 layer and, after its complete erosion in the central part, the sidewalls were etched from atop, as well.

The performance of a Si-aTEF in general highly depends on the angular distribution of KATRIN's background electrons at the detector and on the Si-aTEF detector geometry and efficiency. There were scenarios in which a structure depth of approx. 400 µm at 100 µm hexagon side length was targeted. Thus, the reachable depth was tested on a

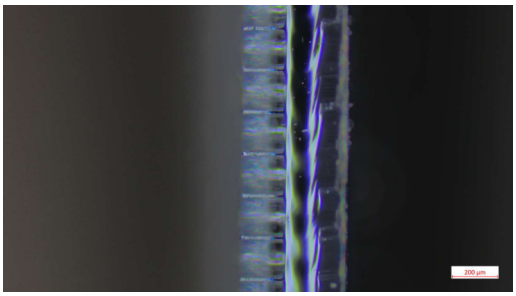

(a) −14.25 mm from center

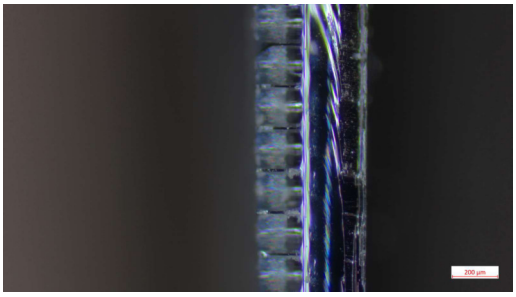

(b) 0 mm from center

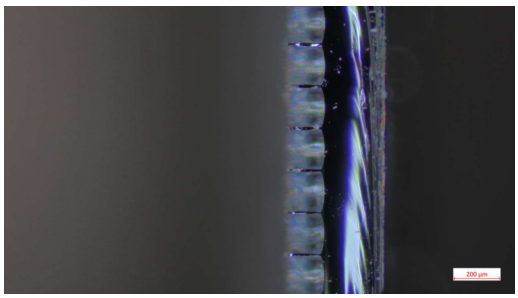

(c) 14.25 mm from center

Figure 5.10 – The inner and outer region of the cut through an etched 4" Si-wafer of 200 µm thickness reveals differences in depth of the hexagon structure. At larger radii the overall thickness of the wafer is reduced. That means, the SU-8 photoresist was fully removed and the exposed frontal parts hexagonal structures were eroded by the etch process. That radial dependence can be reduced when a larger ICP-RIE instrument is used. The wafer, further, features a slight negative taper of the sidewalls. Thus, a slight adjustment of the etch recipe is necessary for large samples.

few examples and an etched depth of $d \approx 360\,\mu m$ was achieved, which had a promising constitution of the sidewalls. To avoid the full removal of the photomask during the etch process the SU-8 layer was applied twice by repeating the spin-coating and pre-bake. A slight non-vertical etch rate was visible, inducing the formation of ledges. When carried out on a Si-PIN diode, the influence of these ledges on the detector performance is unknown, but it is likely that a visibly cleaner and smoother surface would reduce the amount of surface traps and leakage currents. In principle, the twofold application of photoresist does work and it is likely that deep etches of satisfactory quality at approximately 400 µm depth are feasible. Further experiments with such deep etches were not made within this work.

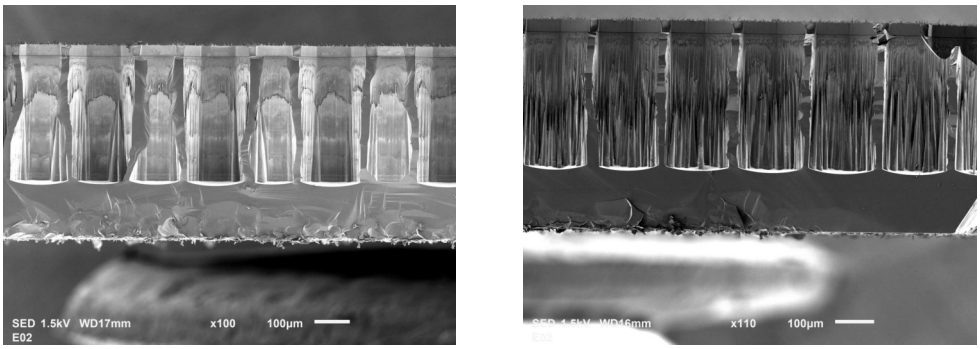

(a) Cleanly etched region **(b)** Region with silicon needles

Figure 5.11 – The silicon chip E2 was prepared with a two-fold application of SU-8 photoresist and was etched for 49 min, which was significantly longer than the typical etch duration of 30 min. A final depth of 360 µm was measured, but more would have been possible, since the photomask is still visible in the images. While the sidewalls are very straightly vertical, the SEM-images show artifacts: In (a), small ledges are seen, which come from a small horizontal etch component. Slight improvements of the etch recipe may be necessary to avoid these. In (b) black silicon is found, which will have detrimental effects on the leakage current of a deep-etched Si-aTEF and should be avoided. Contaminants on the surface or in the SU-8 photoresist itself can be responsible for micromasking, which can induce the formation of silicon needles.

5.5.2 Si-PIN Diodes

The Si-aTEF prototypes prepared in this work were front side-illuminated Hamamatsu S3590-09 Si-PIN diodes of 300 µm thickness. The open area ratio was much smaller than anticipated due to the increased distance between mask and substrate during the UV-lithography, which is the case for every Hamamatsu S3590 diode in this thesis. Section 5.2.3 explains the UV lithography issues in more detail. As a consequence, the shape of the channels, which was intended to be hexagonal, is rather circular[15]. The occasional formation of black silicon needles and other artifacts persisted throughout the samples. Further optimization is, therefore, advised. However, a final Si-aTEF would have to be manufactured by a company with the required equipment and expertise in deep reactive-ion etching. There, a cleaner etch result can be expected, i.e. straighter vertical channel walls, less defective areas and a lower amount of silicon needles. The performance of the diodes after the treatment is studied in chapter 6.

[15] Future S3590 etches will be of better quality due to custom-made ceramic casings by Hamamatsu. These will be examined in [69].

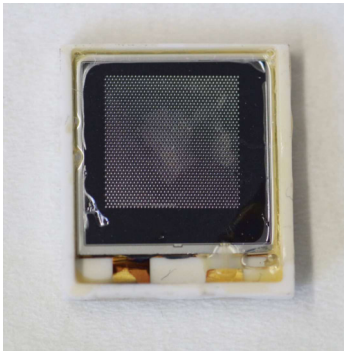

Figure 5.12 – Hamamatsu S3590-09 Si-PIN diode after ICP-RIE, namely diode D. The surface is still covered in photoresist. There are damaged regions, where the photoresist cracked due to the cryogenic temperature during the etch process. The etch process damaged the underlying surface. The lower left golden electrode was not fully covered in SU-8 and tarnished. In order to process the diode with nanofabrication tools, the 10 mm long leads on the backside of the ceramic housing were removed.

Diodes A and B:

Diode A and B were simultaneously etched. Afterwards, diode B was mainly studied, since A malfunctioned. The open area ratio of the photomask on diode B is estimated to OAR $\approx (47.0 \pm 0.5)\%$, which is the percentage of the masked area compared to the total image area, estimated with GIMP (GNU Image Manipulation Program). As described beforehand, the lithography mask was too distant from the photoresist mask during the lithography process. The hexagons were, therefore, recognizable but with broader sidewall thickness $s = (45.3 \pm 1.7)\,\mu\text{m}$ throughout the microstructured area. There was no black silicon visible and an overall clean etch was reached. The channel bottoms show a structure of unknown origin, which was be observed in other samples and it was suspected to not induce performance issues, since it appears very flat.

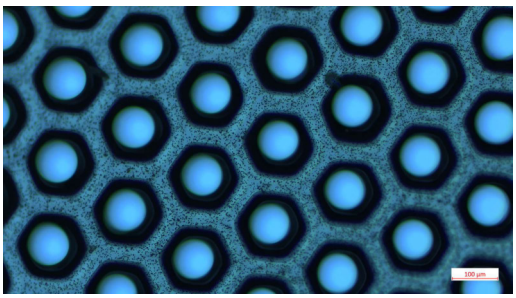

(a) Diode B, focus on top

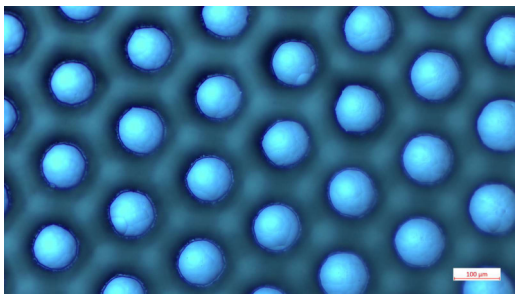

(b) Diode B, focus on bottom

Figure 5.13 – The diode B shows a very regular hexagonal structure. Its open area ratio was reduced compared to the aimed-for geometry, which is due to an enlarged distance during UV-lithography. The bottom region was flat and did feature only very few silicon needles or other artifacts. The bright spot in the center is the reflection off the planar channel ground.

Diode C:

The microstructure of diode C is shown in figure 5.14 Diode C was examined for its performance as a Si-aTEF prototype, see chapter 6.3.3.2. The photoresist of diode C after the etch process was in similar shape as that of diode B. The underlying silicon structure was not as regular as the photoresist, compare the clear blue areas in figure 5.14b, which resemble the silicon surface of diode C. There was a certain amount of isotropic etching that narrowed the side walls, possibly due to the deficient mask quality that negatively affected the etch process. The open area ratio with photoresist, i.e. the non-covered area, was OAR = $(39.0 \pm 0.5)\%$. The OAR without photoresist, i.e. the microstructured area in the channels, was $(73.3 \pm 0.6)\%$. No silicon needles were visible under the microscope.

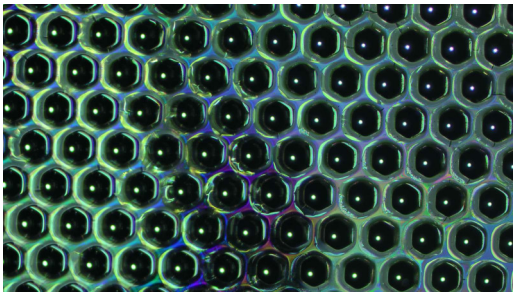

(a) Diode C, with photoresist

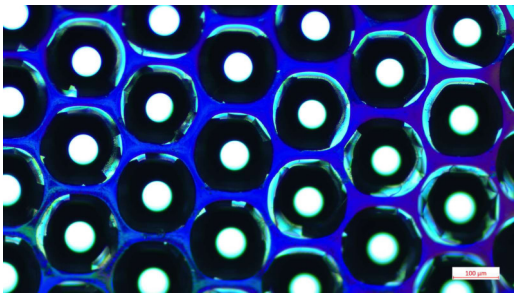

(b) Diode C, focus on top

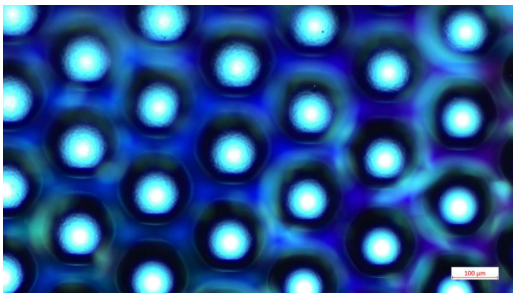

(c) Diode C, focus on bottom

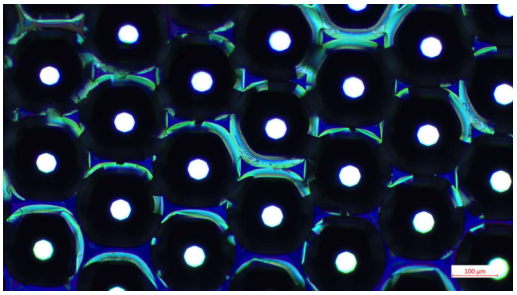

(d) Diode C, focus on top

Figure 5.14 – The diode C with and without photomask features a very different open area ratio width. The sidewall thickness of the photomask is $s = (63.2 \pm 1.7)$ µm. The hexagons appeared round after removal of the photoresist, so that the sidewall thickness varied strongly. The mean sidewall thickness (measured at the thinnest part) in b is $s = (26.8 \pm 7.3)$ µm. The bottom in c showed marginal artifacts. In d, however, the sidewalls were partly missing. The bright spots in the hexagon centers were a reflection of the optical microscope illumination on the planar channel ground.

Diode D:

The etch result of diode D was of similar quality as the previous examples. The photoresist of diode D was not removed in order to preserve its functionality for future tests. Thus, the status of the surface and the side walls beneath the photomask remains unclear. The bottom of the channels was cleanly etched and a mainly regularly, unpatterned surface is visible in figure 5.15. There, a small amount of single silicon needles was visible. The open area ratio with photoresist mask was OAR = $(43.0 \pm 0.2)\%$. The mean sidewall thickness of the photomask was $s = (60.12 \pm 1.1)\,\mu\text{m}$, which was close to the previous examples of the photomasks on the Si-aTEF prototype diodes.

The lithography mask used for the preparation of diode D was M2. The larger side wall thickness of 20 µm did not alter the result, as the comparably large OAR of diode B showed. The processing, however, was significantly easier, as the $7.5 \times 7.5\,\text{mm}^2$ mask could be aligned centrally on the active area. No further shadowing of the electrodes was necessary, in contrast to the previously prepared examples.

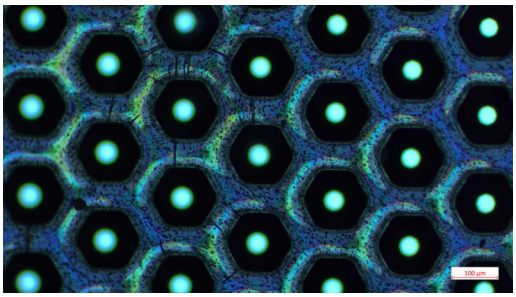

(a) Diode D, focus on top

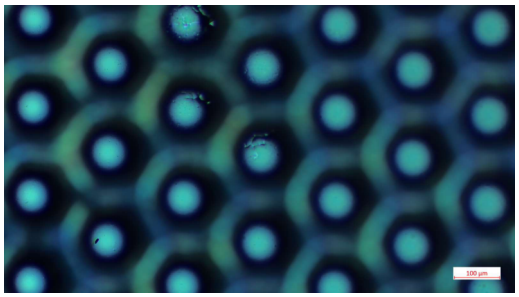

(b) Diode D, focus on bottom

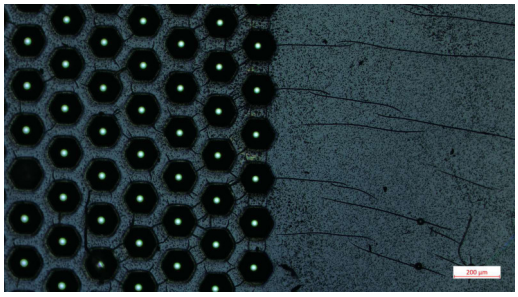

(c) Diode D, transition between etched and non-etched region

Figure 5.15 – The diode D appeared similar to the previous examples. The photoresist was not removed. Therefore, the constitution of the diode beneath the photoresist was unknown. In (c) there are cracks from the thermal stresses during the etch process visible in the SU-8. The material beneath these cracks can unintentionally be etched, which can be problematic, e.g. for underlying electrodes.

FPD:

A single piece of a spare Focal Plane Detector of $\sim 500\,\mu m$ thickness was used to study the possibility of a direct microstructuring of KATRIN's detector. First, the detector of 9 cm diameter was diced into rectangular pieces of side lengths $2 \times 4\,cm^2$. One piece was cleaned, underwent the lithography procedure, and was etched. Due to an appropriate proximity of the lithography mask M1 to the photoresist, the SU-8 mask and also the etched channels reached the same wall thickness as the photomask. The OAR with photoresist was OAR $= (81.0 \pm 0.3)\%$. After removal of the photoresist, the silicon surface was revealed. The OAR without photoresist was OAR $= (85.6 \pm 0.6)\%$, although areas with slightly smaller open area due to larger sidewall thicknesses existed. A small amount of silicon needles was present, but apart from that the etch result appeared very clean, see figure 5.16. Parts of the surface, however, featured a higher black-silicon occurrence.

The FPD is in principle well suited to be etched via ICP-RIE. If upscaling to the size of an FPD is feasible, the intended microstructure can be manufactured. Since the ICP-RIE machinery and the lithography machine of the Münster Nanofabrication Facility would require major upgrades, it cannot be done there and, thus, a full-size Si-aTEF would have to be manufactured by a specialized company.

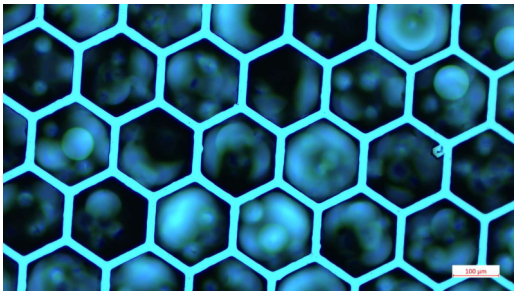

(a) FPD, focus on top (with resist)

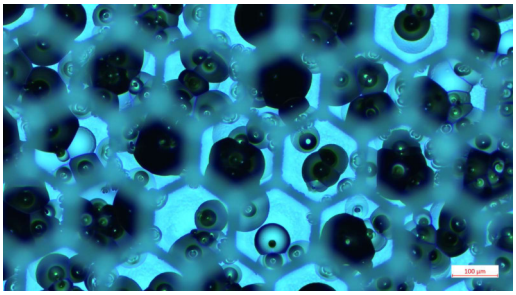

(b) FPD, focus on bottom (with resist)

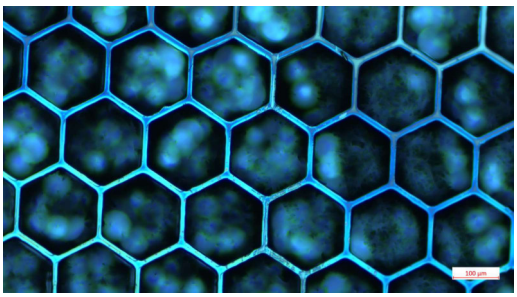

(c) FPD, focus on top (without resist)

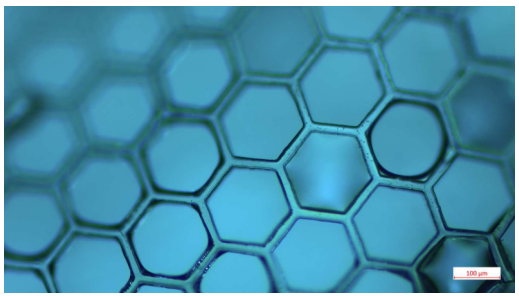

(d) SU-8 photoresist piece

Figure 5.16 – Optical microscope image of a piece of a spare KATRIN focal plane detector (FPD). In contrast to the Si-aTEF prototypes based on Hamamatsu S3590 Si-PIN diodes, the piece of the FPD had a photomask with thin sidewalls of $s = (17.7 \pm 0.6)\,\mu m$ (a). The bottom region of the etched area showed an irregular occurrence of silicon needles (b). After removal of the photoresist via DMSO, the very regular remaining hexagon structure with mean sidewall thickness $s = (11.6 \pm 1.3)\,\mu m$ was revealed (c). A piece of the photoresist was studied under the microscope, as well (d). There, one featured artifact is a single filled-out hexagon, which is a manufacturing error of the lithography mask.

6 Si-aTEF Prototype Development and Tests

The Si-aTEF as a concept for background suppression is briefly introduced in chapter 4.4 and the production of prototypes is presented in the previous chapter 5.5. This chapter is dedicated to the understanding of the detector principle and the experimental test of the Si-aTEF prototype detectors. All Si-aTEF prototypes investigated in this chapter are based on Hamamatsu S3590 PIN diodes. A hexagonal microstructure with maximized open area ratio was etched deep into the detector surface with the intention to add angular-selectivity for incoming electrons as key feature.

The aim of this work is to examine whether such a microstructured PIN diode can suppress electrons with small incident angles, which would – in principle – allow to reduce the detected amount of KATRIN's Rydberg-background electrons. The chapter begins with a brief overview of the working principle of PIN detectors. The modification process based on silicon etching (ICP-RIE) is described in chapter 5. A large part of either the p^+ or n^+ layer of the PIN diode is removed – along with a significant amount of the intrinsically n-doped silicon bulk – which affects the behavior of the diode when a bias voltage is applied. A brief introduction to the signal formation in Si-PIN detectors is given in section 6.1. In section 6.2 the one-dimensional Poisson-equation is solved from basic assumptions and the spread of the depletion zone as a function of the bias voltage is described. These analytic calculations are verified and extended by simulations in COMSOL[1] Multiphysics® for one- and two-dimensional detector geometries. Section 6.3 describes a variety of measurements on first Si-aTEF prototypes. Especially, their angle-dependent detection property is examined. Section 6.4 concludes the chapter with requirements for a Si-aTEF detector in KATRIN.

6.1 Silicon PIN Detector Introduction

The majority of semiconductor detectors is based on silicon, with the PIN diode being a common detector type for different kinds of radiation. For instance, the KATRIN focal plane detector is a backside-illuminated, pixel-segmented single-wafer PIN diode designed for the detection of electrons with energies around and above the tritium beta-decay endpoint energy $E_0 \approx 18.6\,\mathrm{keV}$. The band gap between valence and conduction band in silicon is $E_{\mathrm{gap}} \approx 1.12\,\mathrm{eV}$ (at $T = 300\,\mathrm{K}$) and the mean energy to generate an electron-

[1] Comsol Multiphysics GmbH, Robert-Gernhardt-Platz 1, 37073 Göttingen, Germany.

hole pair in silicon is $W = 3.66\,\mathrm{eV}$ (at $T = 300\,\mathrm{K}$) [155]. Electrons from the tritium β-decay endpoint energy $E_0 \approx 18.6\,\mathrm{keV}$ will generate roughly 5000 electron-hole (e/h) pairs. KATRIN's post-acceleration electrode raises the electron energy by 10 keV, which leads to about 7800 e/h pairs.

The drift velocity $v_D = \mu \cdot E$ in an electric field E depends on the charge carrier mobility μ and can be $v_D \approx 50\,\mu\mathrm{m/ns}$ [156]. With a typical thickness of silicon detectors $d \approx 300\,\mu\mathrm{m}$, the approximated drift time of these charge carriers is [156]

$$t = d/v_D \approx \frac{300\mu\mathrm{m}}{50\mu\mathrm{m/ns}} \approx 6\,\mathrm{ns}. \tag{6.1.1}$$

That means, silicon detectors are fast compared to many other types. Electrons of 28.6 keV energy will be stopped after approximately 4.3 µm in silicon [157].

In PIN diodes, the p/n-junction of the strongly doped p^+- and n^+-layer is separated by an intrinsically (weakly) doped n- or p-layer in between[2]. The large difference in charge carriers between p^+ and n^+ zone results in a larger active detector volume than in a simpler PN diode. When a reverse voltage U is applied to the PIN diode, the depletion zone propagates via $d \approx \sqrt{U}$ into the intrinsic layer until it is fully depleted. A PIN diode is fully depleted when the electric field reaches $E = 0\,\mathrm{V/m}$ upon arrival at the n^+-layer. It is under-depleted, if the electric field reaches $E = 0\,\mathrm{V/m}$ within the intrinsically n-doped bulk and over-depleted, if the voltage is increased after the full-depletion voltage is reached, which leads to a constant addition of an electric field. The latter can be described as a plate capacitor for large voltages [156]. When the breakdown voltage is reached, the silicon becomes conducting and a large current may flow and, in severe cases, destroy the device.

The information of an energy deposition needs to arrive at the electrodes in order for a signal to be detected. The incoming particle, therefore, needs to deposit its energy in an area with non-zero electric field that allows separation of electron-hole-pairs and subsequent charge drifting. On the one hand, the drifting charges induce an influence signal as long as they drift. On the other hand, the charges are measured as they arrive at the collection electrode. In order to fully measure the deposited energy, both e and h need to be collected completely.

Electrons and holes have drift mobilities of $\mu_e = 1450\,\mathrm{cm^2/Vs}$ and $\mu_h = 505\,\mathrm{cm^2/Vs}$ [155]. The factor of $\mu_e/\mu_h \approx 3$ is small compared to, e.g., gas detectors. The drift velocity v_e of electrons depends on the electric field $E(x)$ and is given by [156]

$$v_e = -\mu_e E_x(x) \approx \frac{1}{\tau_e}\left(\frac{\varepsilon_0\varepsilon_r}{eN_D} \cdot \frac{U}{d} + \frac{d}{2} - x\right) = \dot{x}_e \tag{6.1.2}$$

with the total depth d. This works analogously for holes and their drift velocity v_h. The characteristic time until charges are collected at the negative p^+-electrode is $\tau_{e,h} = \frac{\varepsilon_0\epsilon_r}{\mu_{e,h}eN_D}$

[2]For simplicity, the PIN diodes in this chapter are exclusively treated as diodes with an intrinsically n-doped bulk, which means that the depletion zone spreads from the p-doped side into the intrinsically n-doped layer.

[156]. For silicon, where the relative permittivity is $\varepsilon_\mathrm{r} = 11.9$ and a typical intrinsic doping concentration is $N_D = 10^{12}\mathrm{cm}^{-3}$, with $d = 300\,\mu\mathrm{m}$ the characteristic times for electrons/holes are $\tau_e \approx 5\,\mathrm{ns}$ and $\tau_h \approx 15\,\mathrm{ns}$, respectively [156].

The charges contribute to the influence signal while drifting in a non-zero electric field. A simplified description assumes a constant electric field: The generated current i is given by the change of charges q over time t' on the total thickness d,

$$i = \frac{\mathrm{d}q}{\mathrm{d}t'} = Q\frac{v_e}{d}. \tag{6.1.3}$$

The current charges the plate capacitor, which can be assumed in case of over-depletion, with the total number of charges

$$Q = \int i\mathrm{d}t = Q\frac{v_e}{d}t = Q\frac{v_e}{d}\frac{d-x}{v_e} = Q\frac{d-x}{d}. \tag{6.1.4}$$

with x being the localization of an interaction. However, the plate capacitor analogy does not account for the dependence of the electric field on x: In reality, the charge carriers undergo an accelerated motion in the non-constant electric field up to a saturation velocity for large fields [156]. The total current is characterized by arriving electrons and holes. This is depicted in figure 6.1 for a point-like charge deposition at $x_0 = \frac{2}{3}d$. The measurement of the overall very small total current in the order of a few µA relies on potent amplifier systems.

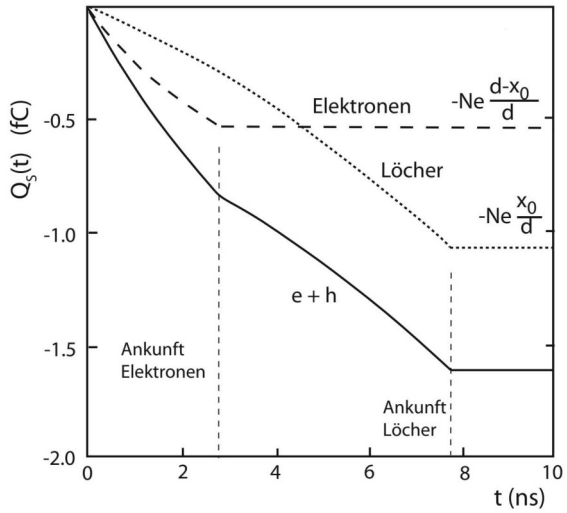

Figure 6.1 – Charge signal for $N = 10000$ charges starting (point-like) at $x_0 = \frac{2}{3}d$ in a detector with depletion voltage $U_\mathrm{dep} = 100\,\mathrm{V}$, bias voltage $U = 150\,\mathrm{V}$, total thickness $d = 300\,\mu\mathrm{m}$, from [156]. The electrons and holes that arrive at the negative electrode induce a measurable current. Overdepletion of the diode allows the electron drift time to be finite. However, a (smaller) signal is measured also at bias voltage $U < U_\mathrm{dep}$ via influence [156].

In addition to drifting, the charge carriers undergo diffusion, which can be described by the diffusion equation [156]. The diffusion coefficient for electrons is given by the

Einstein-Smoluchowski relation

$$D_e = \mu_e \frac{k_\mathrm{B} T}{e}, \tag{6.1.5}$$

analogously for holes h, and the mean value of displacement is calculated from the diffusion equation to

$$\sigma = \sqrt{2 D_e T}, \tag{6.1.6}$$

which can be expressed as [158]

$$\sigma = d \sqrt{\frac{2kT}{eU}}. \tag{6.1.7}$$

With $k_\mathrm{B}T \approx 25\,\mathrm{meV}$ at $T = 300\,\mathrm{K}$, the diffusion width of charge carriers through a $d = 300\,\mu\mathrm{m}$ thin (not microstructured) Hamamatsu S3590 PIN diode at $U_\mathrm{bias} = 60\,\mathrm{V}$ is

$$\sigma \approx 300\,\mu\mathrm{m} \sqrt{\frac{2 \cdot 25\,\mathrm{meV}}{60\,\mathrm{V}}} = 8.7\,\mu\mathrm{m} \tag{6.1.8}$$

Si-PIN diodes may be frontside- or backside-illuminated. When the intrinsic layer is n-doped, the *frontside* is the p^+-doped side and the *backside* is the n^+-doped side. The microstructure of a Si-aTEF can either be on the p^+-side (frontside-illumination) or on the n^+-side (backside-illumination). The implications of microstructuring either the n^+ or the p^+ side will be examined in the following sections.

6.2 Electric Potential in (Microstructured) Si-PIN Diodes

The depletion zone of a PIN diode marks the active detector volume. There, a non-zero electric potential gradient allows charge separation and, in the end, the generation of measurable signals. The electric potential is, thus, a direct indicator for the active detector volume. The electric potential in a 1-dimensional Si-aTEF geometry in dependence of the bias voltage is calculated in section 6.2.1 and helps to predict the spread of the depletion zone throughout the detector. The 2-dimensional Si-aTEF geometry is of greater value to understand the propagation of the depletion zone within the microstructure. There, COMSOL® semiconductor simulations are utilized and described in section 6.2.2.

6.2.1 Solution of the 1-dimensional Poisson Equation

A constant doping concentration with stepwise changes between the differently doped regions is assumed. Further, all dopants are ionized, i.e., $N_\mathrm{A}^- = N_\mathrm{A}$, $N_\mathrm{D}^+ = N_\mathrm{D}$ for the acceptors (N_A) and donors (N_D). The depletion zone is devoid of free charge carriers and the field inside of the junction area serves to move any free charge carriers out of the depletion zone. There is no electric field assumed outside of the junction area. The charge density in the respective region is given by

$$\rho(x) = \begin{cases} -eN_A, & \text{for} \quad -x_p \leq x \leq 0 \\ eN_D, & \text{for} \quad 0 \leq x \leq x_n \end{cases} \tag{6.2.1}$$

with x_p or x_n being the extension of the space-charge region into the p or n doped region of the semiconductor. Charge conservation implies

$$N_\mathrm{A} x_p = N_\mathrm{D} x_n. \tag{6.2.2}$$

Typical doping concentrations are $N_\mathrm{A} = 10^{19}\,\mathrm{cm}^{-3}$ and $N_\mathrm{D} = 2.3 \cdot 10^{12}\,\mathrm{cm}^{-3}$ [156]. The propagation into the p-layer is negligible while the depletion layer spreads into the n-layer of $x_n \approx 20\,\mu\mathrm{m}$ thickness, which is due to the considerably smaller density of minority (n-type) charge carriers compared to the majority (p-type) charge carrier density. The number of majority charge carriers will, therefore, change minimally with an external electrostatic potential. The width d of the depletion zone is given by [156]

$$d \approx x_n \approx \sqrt{\frac{2\varepsilon_r \varepsilon_0}{e} U_{bi} \frac{1}{N_\mathrm{D}}}. \tag{6.2.3}$$

A built-in voltage U_{bi} is inherent in the p-n-junction. The application of a reverse voltage U, i.e. a positive voltage at the n-doped side, leads to an increased depletion zone via

$$d \approx x_n \approx \sqrt{\frac{2\varepsilon_r \varepsilon_0}{e} (U + U_{bi}) \frac{1}{N_\mathrm{D}}}. \tag{6.2.4}$$

The electric potential and the charge density are related via Poisson's equation

$$\Delta\Phi = \frac{\rho}{\varepsilon} \tag{6.2.5}$$

with the field Φ, the charge density ρ, and the permittivity ε. Si-PIN diodes may be frontside- or backside-illuminated, i.e. the illuminated side is either the p-layer or the n-layer. The depletion zone extends from the frontside. This plays a crucial role for the Si-aTEF, since KATRIN's FPD is backside-illuminated and the Hamamatsu diodes used for the experiments in this work are frontside-illuminated. Differences in their behavior are, therefore, expected.

The general solution of the Poisson equation is

$$E(x) = \frac{1}{\varepsilon_0 \varepsilon_r} \int_{-\infty}^{x} \rho(x')\,\mathrm{d}x' \tag{6.2.6}$$

with the electric field $E(x)$ at depth x in the PIN diode.

The depletion zone depth d of a regular PIN diode increases with the reverse voltage U, following $d \propto \sqrt{U}$ according to eq. (6.2.4). In a backside-illuminated microstructured diode, however, the depletion zone propagation within the microstructure is reduced by the tenfold larger concentration of charge carriers in the n^+ side with respect to the p^+ side.

The open area ratio (OAR) defines the removed amount of the thin n^+ or p^+ layer and, thereby, drastically influences the solution of the 1d-Poisson equation. From the known behavior of charges within a p/n junction and the artificially modified charge distribution in a microstructured aTEF diode, one can calculate the depletion zone depth corresponding

to a bias voltage. For the frontside- and the backside-illuminated Si-aTEF, there are different cases to be considered, see fig. 6.2. In all cases, charge conservation is assumed and the analytical calculation is based on that. The partly removed doped n^+ or p^+ region, however, necessitates a modification of eq. (6.2.2) in case of Si-aTEF diodes.

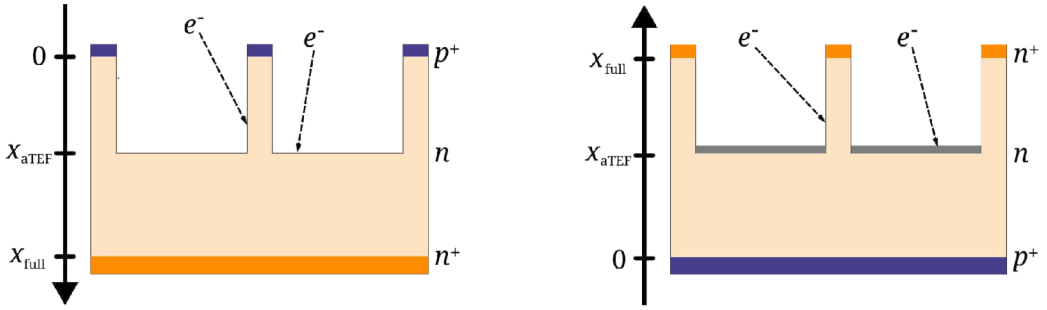

(a) Microstructure on p^+-side **(b)** Microstructure on n^+-side

Figure 6.2 – Sketch of two possible Si-aTEF concept implementations in an $n^+/n/p^+$ (a) or $p^+/n/n^+$ (b) doping ordering. The n^+ layer is shown in dark orange, the n layer in light orange, and the p^+ layer in dark blue. Incoming electrons from the top either hit the floor or frontal side of the structure or, under large incident angles, hit the channel walls. The floor of the etched channels does not register electrons either because of a missing electric field in the bulk material as in a, or because of a blocking layer, as shown in grey in (b). The electrodes on top and bottom are not shown. For convenience, $x = 0$ was chosen to be between n- and p^+-layer (as starting point of the depletion zone) was in the simplified 1d-models. Compare figure 6.3 for the doping profile of the 1d-models.

Frontside-illuminated Si-aTEF: The electric field inside of a PIN diode is given by

$$E(x) = \frac{1}{\varepsilon_0 \varepsilon_r} \int_{-\infty}^{x} \rho(x')\mathrm{d}x'. \tag{6.2.7}$$

When the depletion zone reaches the microstructure, $d = x_{\mathrm{aTEF}}$, the reverse voltage is $U(x_{\mathrm{aTEF}}) =: U_{\mathrm{aTEF}}$. In a PIN diode with a microstructured p^+ side with the charge density $\rho(x)$ and for $U < U_{\mathrm{aTEF}}$ the depletion zone spread d (from the p^+-doped side) is smaller than the microstructured depth, $d < x_{\mathrm{aTEF}}$. With eq. (6.2.1), the electric field is

$$\begin{aligned} E(x) &= \frac{1}{\varepsilon_0 \varepsilon_r}(-eN_A x_p + eN_D x) \\ &= \frac{eN_D}{\varepsilon_0 \varepsilon_r}(x - d). \end{aligned} \tag{6.2.8}$$

When the reverse voltage is enlarged, the depletion zone depth may overcome the microstructured depth, $d > x_{\mathrm{aTEF}}$. The electric field in the region $0 < x < x_{\mathrm{aTEF}}$ then

becomes

$$\begin{aligned} E(x) &= \frac{1}{\varepsilon_0\varepsilon_r}(-eN_A x_p + eN_D x) \\ &= \frac{eN_D}{\varepsilon_0\varepsilon_r}\left(x - x_{\mathrm{aTEF}} - \frac{d - x_{\mathrm{aTEF}}}{\delta}\right) \\ &=: \frac{eN_D}{\varepsilon_0\varepsilon_r}(x - d_1) \end{aligned} \tag{6.2.9}$$

with $d_1 = x_{\mathrm{aTEF}} + \delta^{-1} \cdot (d - x_{\mathrm{aTEF}})$ and the reduction factor $\delta = 1 - \mathrm{OAR} \approx 0.1$, where a Si-aTEF with $\mathrm{OAR} = 0.9$ is assumed. The electric field in the region $x > x_{\mathrm{aTEF}}$ is given by

$$\begin{aligned} E(x) &= \frac{1}{\varepsilon_0\varepsilon_r}(-eN_A x_p + eN_D x_{\mathrm{aTEF}} + eN_D \frac{(x - x_{\mathrm{aTEF}})}{\delta}) \\ &= \frac{eN_D}{\varepsilon_0\varepsilon_r}\left(\left(-x_{\mathrm{aTEF}} - \frac{d - x_{\mathrm{aTEF}}}{\delta}\right) + x_{\mathrm{aTEF}} + \frac{x - x_{\mathrm{aTEF}}}{\delta}\right) \\ &= \frac{eN_D}{\varepsilon_0\varepsilon_r}\frac{x - d}{\delta}. \end{aligned} \tag{6.2.10}$$

The electric potential is derived from the electric field via integration: For a frontside-illuminated Si-PIN diode the depletion zone spreads from the p-layer. The potential is given by

$$\begin{aligned} U(x) &= \int_{-\infty}^{x} E(x)\,\mathrm{d}x' \\ U(x) &= \frac{eN_D}{\varepsilon_0\varepsilon_r}\begin{cases} \frac{x^2}{2} - xd & \text{for} \quad U < U_{\mathrm{aTEF}} \\ x_{\mathrm{aTEF}}\left(\frac{x_{\mathrm{aTEF}}}{2} - d_1\right) - \frac{x_{\mathrm{aTEF}}}{\delta}\left(\frac{x_{\mathrm{aTEF}}}{2} - d\right) + \frac{x}{\delta}\left(\frac{x}{2} - d\right) & \text{for} \quad U > U_{\mathrm{aTEF}} \end{cases} \end{aligned} \tag{6.2.11}$$

Backside-illuminated Si-aTEF: Analogously to the previous case, the electric field within a backside-illuminated Si-PIN diode with depletion zone spread from the p^+-layer in case of a potential $U < U_{\mathrm{aTEF}}$ and, thus, $x < x_{\mathrm{aTEF}}$ is given by

$$E(x) = \frac{eN_D}{\varepsilon_0\varepsilon_r}(x - d). \tag{6.2.12}$$

When the bias voltage is enlarged to $U > U_{\mathrm{aTEF}}$, the depletion zone reaches the microstructure, where the lower charge density leads to an further spread of the depletion zone. The electric field for $x < x_{\mathrm{aTEF}}$ is given by

$$E(x) = \frac{eN_D}{\varepsilon_0\varepsilon_r}\left(x - x_{\mathrm{aTEF}} - \delta(d - x_{\mathrm{aTEF}})\right) =: \frac{eN_D}{\varepsilon_0\varepsilon_r}(x - d_2) \tag{6.2.13}$$

with $d_2 = x_{\mathrm{aTEF}} + \delta \cdot (d - x_{\mathrm{aTEF}})$. For $x > x_{\mathrm{aTEF}}$ the electric field becomes

$$E(x) = \frac{eN_D}{\varepsilon_0 \varepsilon_r} \delta(x - d). \tag{6.2.14}$$

The electric potential within a backside-illuminated Si-PIN diode is then given by

$$U(x) = \frac{eN_D}{\varepsilon_0 \varepsilon_r} \cdot \begin{cases} \frac{x^2}{2} - xd & \text{for} \quad U < U_{\mathrm{aTEF}} \\ \\ \frac{-x_{\mathrm{aTEF}}^2}{2} + \delta \left(\frac{x_{\mathrm{aTEF}}^2}{2} + \frac{x^2}{2} - dx \right) & \text{for} \quad U < U_{\mathrm{aTEF}}. \end{cases} \tag{6.2.15}$$

The potential within the diode and the bias-voltage dependent spread of the depletion zone was calculated and is shown in figure 6.4 for frontside- and backside-illuminated Si-aTEF diodes, together with the simulation results from the following section. The rapid depletion in case of the frontside-illuminated Si-aTEF diode at small bias voltages within the "microstructure", i.e. within the region of 90% reduced doping concentration, is in opposition of the slow depletion of the microstructure within the backside-illuminated Si-aTEF diode.

6.2.2 COMSOL™ Multiphysics Simulation

The one-dimensional solution of the Poisson equation helps to predict the behavior of microstructured PIN diodes, as it allows the calculation of the depletion zone propagation and, thereby, the active detector region. It does, by definition, not examine the depletion zone propagation within the microstructure and ignores any border effects. This information is gathered by a two dimensional diode model in COMSOL™ with the Semiconductor Module.

In addition, a one-dimensional model of microstructured Si-PIN diodes is calculated in COMSOL™ in order to verify the results of the solution of the one-dimensional Poisson equation in the previous chapter.

6.2.3 1-dimensional PIN-Diode

The one-dimensional model consists of a 300 µm long Si-PIN diode with, in this order, a 30 µm deep n^+-doped region (backside), an n-doped region in the center and a 30 µm deep p^+-doped region (frontside). The doping concentrations of n^+ and p^+ are $N_D = N_A = 10^{20}\mathrm{cm}^{-3}$. The doping concentration of the bulk is $N_i = 10^{12}\,\mathrm{cm}^{-3}$. Metal contacts on the ends allow to apply a reverse bias voltage. Here, the n^+-doped side is positively biased with V_n, while the p^+-doped side is kept at $V_p = 0\,\mathrm{V}$. Compared to a non-microstructured diode, the microstructure with a depth of 150 µm reduces the material and – in the 1d-model – the doping concentration by 90%, for instance. As before, two cases need to be considered:

If the microstructure is on the p^+-doped side, i.e. in the region between $0\,\mu\mathrm{m} < x < 150\,\mu\mathrm{m}$, the p-doping concentration is reduced to $n_A = 0.1 \cdot N_A$ and the intrinsic layer in

this region is reduced to $n_i = 0.1 \cdot N_i$.

If the microstructure is on the n^+-doped side, i.e. in the region of $150\,\mu\text{m} < x < 300\,\mu\text{m}$, the n-doping concentration is reduced to $n_D = 0.1 \cdot N_D$ and the intrinsic layer in this region is reduced to $n_i = 0.1 \cdot N_i$.

The doping profile of the 1d-model is shown in figure 6.3. The one-dimensional model

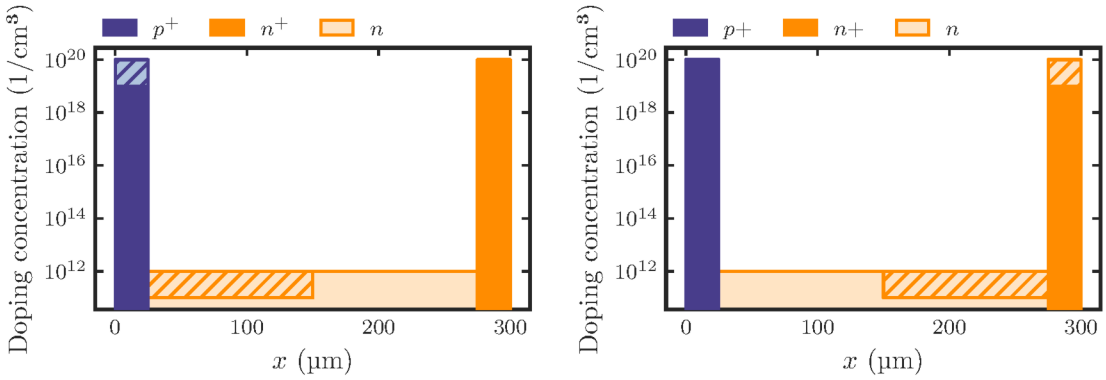

(a) Microstructure on p^+-side **(b)** Microstructure on n^+-side

Figure 6.3 – Doping profiles of the (a) frontside-illuminated and (b) backside-illuminated 1d model of a Si-PIN diode. The doping concentration is reduced by a factor of 10 in the microstructured part, as indicated by the hatched area.

does agree well with the analytical solution of section 6.2.1, as it is based on the same geometry. The results of both are shown in figure 6.4.

The results lead to the conclusion that the microstructure of the frontside-illuminated Si-aTEF in figure 6.4b is depleted already at small bias voltages, while full-depletion of the non-structured region requires much higher voltages. Therefore, electron detection at small bias voltages may only be possible in the microstructure. That can allow a p^+-microstructured Si-PIN diode to function as a Si-aTEF.

In the backside-illuminated Si-aTEF in figure 6.4c, the non-microstructured intrinsic region will be depleted at first. Higher voltages are then necessary to propagate the depletion zone into the microstructure. Electron detection in the microstructured region will, therefore, only be possible for higher bias voltages, and electrons will also be detected in the bulk.

6.2.4 2-dimensional PIN-Diode

The two-dimensional model consists of an $n^+/n/p^+$-diode with a microstructure either on the n^+ or the p^+ side. The doped region extends, as in the one-dimensional model, 10% into the n-doped region. The total thickness of the diode is chosen to $d = 300\,\mu\text{m}$. The depth of the microstructure is varied. Figure 6.5 shows results of different parameter variations and their effects.

The *frontside-illuminated* Si-aTEF model, see fig. 6.5 a, shows depletion of the channel walls (pillars) even at small reverse voltages and a non-depleted bulk region beneath the

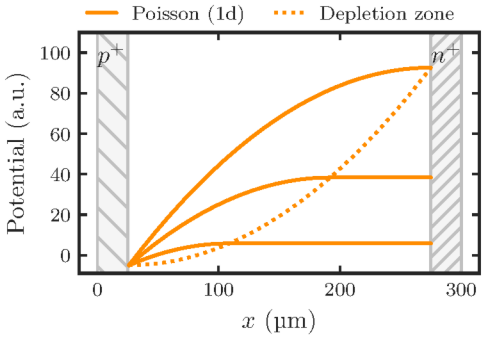

(a) Non-microstructured diode

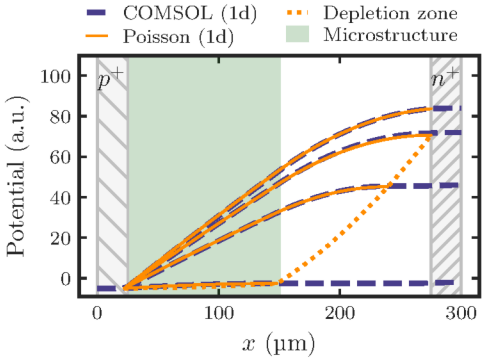

(b) Microstructure on p^+-side

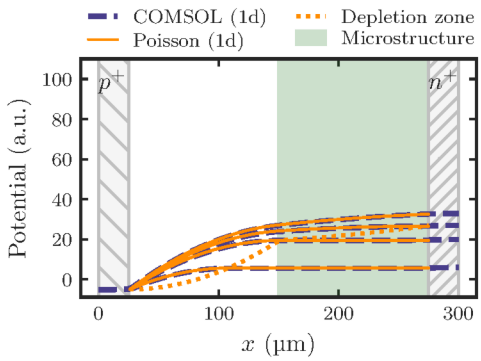

(c) Microstructure on n^+-side

Figure 6.4 – Potential curve within an unmodified (a) and within "microstructured" 1-dimensional diodes (b) and (c). The applied bias voltage is equal to the difference between minimum and maximum of each potential curve. The curves are either calculated via 1-dimensional Poisson equation (dashed blue) or via 1-dimensional diode model in COMSOL (solid orange). The solution of the 1-dimensional Poisson equation is scaled to fit the COMSOL-solution in order to show their close resemblance. The border of the depletion zone (dotted orange) spreads from the p^+-side with increasing bias voltage.

channels. The p^+-region is between $y = 300\,\mu m$ and $y = 270\,\mu m$. The non-microstructured bulk region can be depleted, too, but larger voltages than depicted here are necessary. The active detector area in this case is the microstructured channel wall, where a potential gradient exists. That is the searched-for effect that is needed for a realisation of the Si-aTEF. In addition to the channel sidewalls, the outer, non-structured regions behave as regular Si-PIN diode. The depletion voltage in that region is smaller than for the frontside-illuminated Si-aTEF and the active area extends deeper into the diode. This non-structured border area is built into the simulation for comparison, but such a region may also be present in an actual Si-aTEF wafer for manufacturing or stability reasons.

The depletion zone propagation in the *backside-illuminated* Si-aTEF model, see fig. 6.5 b, begins to spread from the non-structured p^+-doped side. Here, the p^+-region is between $y = 0\,\mu m$ and $y = 30\,\mu m$, which was chosen for illustrative purposes. Larger reverse voltages provide a potential gradient in the microstructure, too, but the bulk region will remain active. The potential curve steepens after the depletion zone reaches the

microstructure. The negative charges from the p^+-side are balanced with positive charges, which induces a spread of the depletion zone with higher reverse bias voltages. The number of partners is diminished in the microstructure when compared to the bulk. Therefore, the depletion zone will spread further at lower voltages. In the 1d-case, the depletion zone spreads further at lower voltages, as well, but in 2d the spread within the microstructure is not generated by a smaller charge carrier density: The reason for the faster spread is the spatial reduction on a fraction of the original material. The depletion zone moves through a smaller area (or volume in the 3-dimensional case). The 1d-calculation cannot resemble that. To bypass the problem, there is a smaller overall charge carrier density assumed in the microstructured region. Since the non-structured bulk is depleted at lower voltages than the microstructure, the detector will work as a Si-aTEF only if a blocking layer of the channel floor as shown in figure 6.2 is realized. That passivation may be, for example, a SiO_2 layer of a few µm thickness in order to absorb 18.6 keV-electrons with small angles.

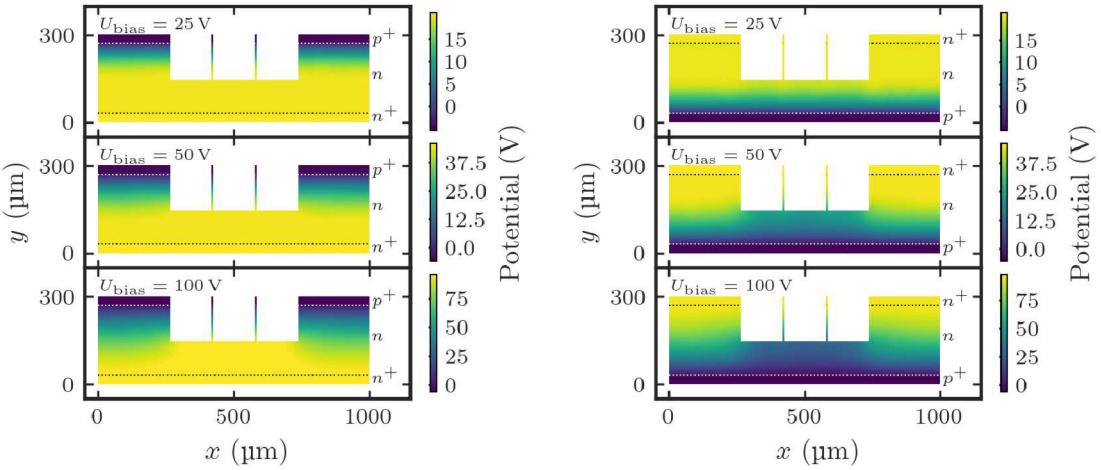

(a) Microstructure on p^+-side

(b) Microstructure on n^+-side.

Figure 6.5 – Geometry of the 2-dimensional Si-PIN diode model in COMSOL. The doping zone borders are marked by dotted lines. The n^+ and p^+ zones extend 10% (here: 30 µm) into the diode. (a) shows the potential for a microstructure on the p^+-side and (b) for a microstructure on the n^+-side, when the (positive) bias voltage is applied on the n^+-side.

There is an important implication of these simulations for the frontside-illuminated Si-aTEF: Reverse voltages below the full-depletion voltage need to be applied in order to keep the bulk passive. However, non-fully depleted PIN-diodes face disadvantages: The thermal/Johnson noise is increased by the finite electrical resistance of the dead layer on the backside [159]. In addition, timing properties tend to be worsened from the slow charge carrier velocities in the field-free region at the depletion zone edge. Further, the active area and the capacitance and, thereby, the detector response depend on the applied reverse voltage. That is not the case in fully-depleted detectors and needs to be taken into account.

In figure 6.6a the electric field is shown for a frontside-illuminated Si-aTEF. The electric field in the microstructure is larger compared to the non-microstructured case. Therefore,

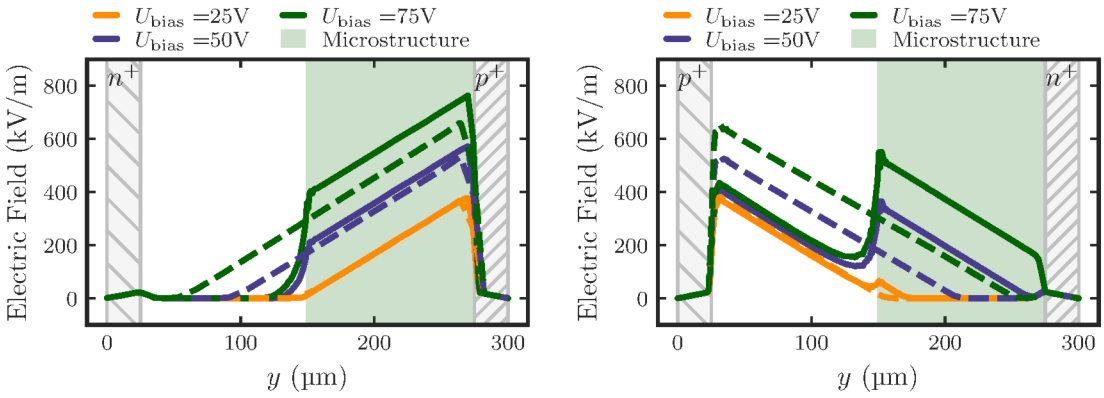

(a) Microstructure on p^+-side **(b)** Microstructure on n^+-side

Figure 6.6 – Electric field within microstructured diode and depletion zone spread. The solid lines are cuts through the centre of the thin pillars at $x = 420\,\mu m$, compare model in 6.5. The dashed lines are cuts through the bulk material at the outer area at $x = 120\,\mu m$. (a) shows the field for a microstructure on the p^+-side and (b) for a microstructure on the n^+-side, when the (positive) bias voltage is applied on the n^+-side.

in the case of frontside-illuminated Si-aTEF the breakdown potential will be reached at smaller voltages than in a non-microstructured Si-PIN diode. Below the breakdown voltage charges should be separated efficiently by the strong electric field in the microstructure. In the bulk material beneath the microstructure, however, an electric field and, thereby, charge separation is only apparent at much larger bias voltages.

In case of the backside-illuminated Si-aTEF in figure 6.6b, the electric field strength increased as soon as the depletion zone reached the microstructure. That means, charges would be effectively separated upon incident in the microstructure, when the bias voltage is large enough.

Additional simulations under variation of the depth of the microstructure were carried out. These are shown in figure 6.7. A shallower microstructure in a frontside-illuminated diode required a smaller bias voltage to fully deplete the microstructure. In case of a backside-illuminated diode, the shallower microstructure required larger reverse voltage for full depletion of the microstructure. The corresponding depletion voltage in a deeper microstructure was larger in a frontside-illuminated and smaller in a backside-illuminated diode.

To conclude, the propagation of the depletion zone through the Si-aTEF of both cases, frontside- and backside-illuminated, is understood with the help of analytical calculations and simulations. They predict that Si-aTEF diodes can, as intended, suppress electrons of small pitch angles. The simulations point to the problem of an active floor region in backside-illuminated Si-aTEF detectors, which can be solved by an additional blocking layer. In this work, though, the focus was laid on testing the the functionality of first Si-aTEF prototypes. Further, the simulations do not predict charge-collection efficiency and charge-collection times.

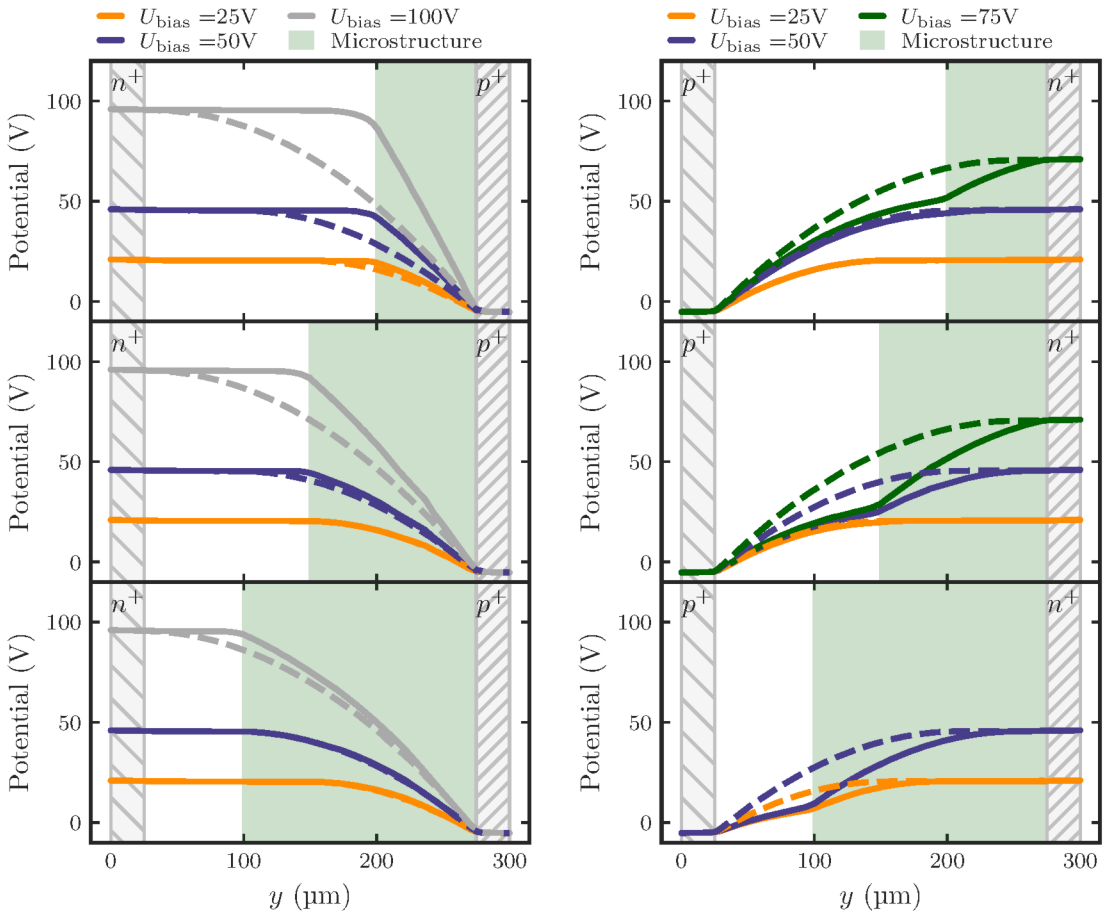

(a) Microstructure on p^+-side

(b) Microstructure on n^+-side

Figure 6.7 – Potential curve within the thin pillar of the diode at $x = 420\,\mu\text{m}$ (solid line) and within the outer region at $x = 120\,\mu\text{m}$ (dashed line), compare model in 6.5. The depth of the microstructure is varied (grey area). The solution for $U_{\text{bias}} = 75\,\text{V}$ in the case when the microstructure is on the n^+ side and 200 µm deep did not converge, see lower panel in (b).

6.3 Experimental Proof of Angle-selective Electron Detection

The intermediate goal of the Si-aTEF measurements on the Si-aTEF prototypes was a proof for the angle-selective electron detection. In this section, tests of Si-aTEF prototype iterations on important characteristics are shown. These characteristics are the incident angle-dependent electron detection, their (temperature-dependent) noise performance and leakage current and, further, the detection homogeneity over the surface. Over the course of the experiments with Si-aTEF prototypes, the methods and test environment have evolved: A second test setup had to overcome essential limitations that prohibited a smooth workflow and measurement of the incident angle-dependent detection efficiency.

Initial tests on the first microstructured Si-PIN diodes were carried out in the test setup described in chapter 4.3.1, here referred to as setup I. That setup was modified in

order to not use the MCP-filter in the center and the detector was replaced by a Si-aTEF prototype. The incident angle on the detector was varied by changing the photoelectron source plate angle. Due to the macroscopical period length of the cyclotron motion and cyclotron radius, however, the incident angle strongly depended on the starting magnetic field. Simulations with KASSIOPEIA in [134] revealed adiabaticity issues and very limited reachable incident angles of the electrons. In [134] measurements of Si-aTEF prototypes were presented that actually showed detection probability in dependence of the plate angle of the photoelectron source, but since the resulting incident angle on the detector remained unclear even with extended simulations the need of a new setup arose.

In general, the incident angle of electrons on a detector can be varied by either influencing the electron beam or by rotating the detector. The latter allows much more precise experiments: When the detector is rotated with regard to the electron beam the electron the incident angle is directly controllable. Therefore, the dedicated Si-aTEF test setup was designed under the lead of Sonja Schneidewind [69] with a rotatable detector, referred to as setup II. A static (non-tiltable) photoelectron source, a magnetic guiding field and a charge-sensitive preamplifier that was thermally linked to a LN_2-coolable cold finger were installed.

Si-PIN Detector and Charge-sensitive Preamplifier

The Si-PIN diode used as detector and as Si-aTEF prototype in both setups I and II was the Hamamatsu S3590-09. It featured a $10 \times 10\,\mathrm{mm}^2$ active area and a depletion layer thickness of 0.3 mm. Its maximum reverse voltage was $U_{\mathrm{bias}} = -100\,\mathrm{V}$ and full depletion of the volume was reached at around $U_{\mathrm{bias}} = -60\,\mathrm{V}$. A guard ring reduced surface leakage currents. The low terminal capacitance was 40 pF at $U_{\mathrm{bias}} = -70\,\mathrm{V}$ reverse voltage [143], which allowed small $1/f$-noise and Johnson noise contributions. An examination of the signal generation within Si-PIN diodes is given in chapter 6.1.

The signals generated by these Si-PIN diodes were small and required amplification with low noise contribution, which was obtained with a charge-sensitive preamplifier. The preamplifier transforms the high detector impedance into a low-ohmic impedance and amplifies the weak outgoing signal by translating the collected charges into a voltage signal. Its output voltage is directly proportional to the incoming charges.

The preamplifier layout of setup II was originally developed for the Mainz Neutrino Experiment [160, 161]. It was developed further and used in [162] for an APD-based single-photon detector for laser spectroscopy on highly charged ions, where noise-reduction was very crucial to detect single photons.

The charge-sensitive preamplifiers of both setups I and II were divided into two stages. The first preamplifier stage is located inside the vacuum chamber to minimize the signal path, reduce parasitic inductivities and capacitances and, thereby, noise. Its components were chosen with regard to the noise contributions and further design constraints: The feedback resistance, for example, was chosen large to reduce white noise, but the time

constant prolongs with larger resistance, which reduces the possible maximum count rate [161]. The performance of the JFET (Johnson-gate field-effect transistor) on the first stage is very critical, since noise components that are generated in the first stage are amplified along with the signal. Thus, the first stage is placed as close to the detector as possible to reduce sources of stray capacitance. Stiff cables and connections of the first preamplifier stage reduce microphonic noise [162]. A schematic circuit diagram is shown in figure 6.8. The first stage contains two matched Vichay U430 n-channel JFET transistors, which are connected in parallel to reduce the shot noise. The time constant τ is adjusted by the resistance and capacitance of the feedback loop. If the HV resistance is chosen too small, an extensive amount of current can destroy the electronic components. If the HV resistance is too large, the current becomes too small to be measurable. A 500 MΩ high-voltage resistance is installed in order to enhance the resolution of the current measurement in contrast to the original 5 GΩ resistance. A short-circuited (defect) diode that is biased with $U_{\text{bias}} = -60\,\text{V}$ would show a reverse current of $I = \frac{|U_{\text{bias}}|}{R} = \frac{60\,\text{V}}{500\,\text{M}\Omega} = 120\,\text{nA}$.

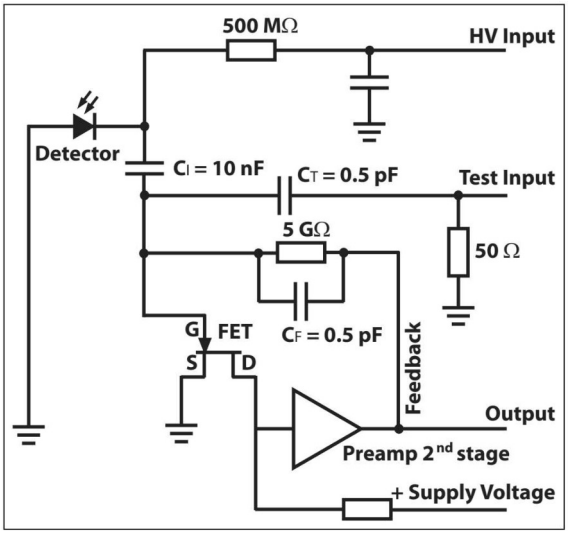

Figure 6.8 – Preamp circuit from [162].

The second stage of the preamplifier is placed outside of the chamber to minimize the amount of components within the vacuum system. The HV-connection, the ±12 V and ±24 V connection via D-Sub 9 to an NIM spectroscopy amplifier, and the energy (E) and timing (T) output are accessible by its aluminum casing.

The energy to generate an electron-hole pair in silicon is $W = 3.66\,\text{eV}$ (at $T = 300\,\text{K}$) [155]. An electron of $E = 100\,\text{keV}$ energy will induce a number of charges

$$Q = \frac{E}{W} = \frac{1 \cdot 10^5\,\text{eV}}{3.66\,\text{eV}} \cdot e = 4.3 \cdot 10^{-15}\,\text{C} \tag{6.3.1}$$

and a pulse height of

$$U = \frac{Q}{C_T} = 8.6\,\text{mV} \tag{6.3.2}$$

with $C_T = 0.5\,\mathrm{pF}$ [162].

The preamplifier housing consisted of copper to allow large temperature conductance and efficient cooling.

6.3.1 Setup I – Modified ToF Test Setup

Setup I was described in chapter 4.3.1. It consisted of the photoelectron source and the beamline, where electrons were guided via a system of coils. The MCP-detector and its readout was exchanged for an Si-aTEF prototype with a charge-sensitive preamplifier. The LN_2-coolable preamplifier and detector mount were modified from a setup used in [162]. An CAEN N968 spectroscopy amplifier and a CAEN N957 multichannel analyzer (MCA) were used. The MCA delivered the signals to the readout-PC, where the software iMCAr[3] was used to access and save the data [163]. Due to the $R_\mathrm{I} = 100\,\mathrm{M\Omega}$ HV resistance of the preamplifier, a short-circuited (defect) diode with bias $U_\mathrm{bias} = -60\,\mathrm{V}$ leads to a maximal current of $I = \frac{|U_\mathrm{bias}|}{R_\mathrm{I}} = \frac{60\,\mathrm{V}}{100\,\mathrm{M\Omega}} = 600\,\mathrm{nA}$ in setup I. On the contrary, in setup II the HV resistance was chosen to $R_\mathrm{II} = 500\,\mathrm{M\Omega}$. That lead to a maximum current $I = \frac{|U_\mathrm{bias}|}{R_\mathrm{II}} = \frac{60\,\mathrm{V}}{500\,\mathrm{M\Omega}} = 120\,\mathrm{nA}$ in setup II.

The performance of the photoelectron source decreased over time and the source was stable only if operated at $U_\mathrm{back} \leq -14\,\mathrm{kV}$. The noise increased further over time until a broken voltage supply line on the vacuum side of the flange lead to failure and made a repair necessary after the measurements with Si-aTEF prototype A and B. All other prototypes were tested in setup II, which is explained below.

The magnetic guiding of electrons from the photoelectron source to the detector was described before. The magnetic field was generated by air coils at the source position, at the center and at the detector. In addition, there were coils directly wound around the beam tube chambers, see chapter 4.3.1. Magnetic steering with the additional two parallel pairs of coils at the detector that were aligned transversally to each other and to the beamline was required for electrons to hit the detector. The beam was steered by adjusting the current through the coil pairs until a signal was detected. The magnetic steering, however, altered the angle of the magnetic field line and, even more severely, the incident angle of the electrons on the detector. Additional simulations in Kassiopeia were carried out in order to reconstruct the incident angle from the coil currents, but non-adiabatic effects and the macroscopic cyclotron length with the induced large phase and its influence on the angle (see chapter 4.3.2) led to extreme uncertainties on the predictions [134]. Therefore, the tests only allowed judgement on the general function of Si-aTEF prototypes as electron detectors. Diodes A and B were examined in this setup, but the key property – their angle-dependent effciency – could not be proven. That gave motivation to construct the dedicated test setup described in section 6.3.2.

[3]The MCA software was written by B. Bieringer and remains continually updated and upgraded as open source. It was renamed to iMCAr (interactive MCA recorder). It features a GUI, where the recorded data of the ADC-channels be inspected live. Further, it allows basic data analysis.

6.3.2 Setup II – Dedicated aTEF Test Setup

Setup II was mainly developed within the PhD thesis of Sonja Schneidewind [69]. It is described here for the sake of explaining the first characterization measurements of Si-aTEF prototypes. Setup II included a rotatable preamplifier and detector section, see figure 6.9a. In combination with a fixed-angle photoelectron source, it allowed measurement of incident angle-dependent electron detection properties. The photoelectron source (figure 6.9d) is, as well, developed and built within the PhD thesis of S. Schneidewind [69]. It is a reduced-complexity variant of the high-energy photoelectron source used for, i.a., calibration and energy loss measurements in KATRIN, as carried out within [69]. Its design and working principle is based on the source described in 4.3.1, but altered to allow, i.a., higher electron energies. The high voltage is generated by a Knürr-Heinzinger PNC5-30000 neg high-voltage supply. The back plate potential is set to a negative value U_{back}. The front plate voltage is provided by a voltage divider with a resistance ratio of 73 %, i.e. the front plate voltage is 73 % of the back plate voltage, as suggested by S. Schneidewind, which is a compromise between a sharp angular distribution and a high front plate voltage, where too large voltages can inflict damage, and optimized for back plate voltage between 18 keV and 30 keV. The voltage difference accelerates the photoelectrons in the electric field between back plate and front plate. An aperture of 15 mm diameter lets the electrons pass and they are further – non-adiabatically – accelerated by the surrounding ground potential. The plate angle between front and back plate is fixed to $\alpha_p = 0°$.

As in setup I, the LVL TO39 250-270 nm deep UV-LED is supplied via a Tektronix AFG 3102 frequency generator with a rectangular voltage pulse of determined frequency and width. The UV light is coupled into an optical fiber of 200 µm diameter that is suited for UV-light and connected to a vacuum feedthrough. From there, the light is guided through another UV-fiber directly onto the backside of the thin gold cathode on the back plate.

The electrons are guided by a solenoid coil that can achieve a magnetic field strength of approximately 15 mT at 30 A current in its center [164]. It is placed on a set of rotatable and translatable tables (2 ×PT8625, 1 ×HT25, 1 ×DT36025-PAE) by MM Engineering[4] with a translation precision of 0.05 mm and a rotation precision of 0.1°, respectively. For a large cyclotron displacement length h the incident angle heavily depends on the cyclotron phase, as seen in section 4.3.2. The electrons' cyclotron radius in setup II is kept small via proper alignment of the field lines and the electron beam, so that the cyclotron phase is less relevant. Thus, by keeping the plate angle at $\alpha_p = 0°$ and rotating the preamplifier instead of the photoelectron source, the main problem of setup I is eliminated. A possible remaining misalignment of the magnetic field is not relevant, since the rotation axis of the detector is on the detector surface.

The photoelectron source chamber is placed on a rail system. In order to exchange the detector, the photoelectron source chamber can be detached and moved away from the rest of the setup on a rail system. That allows the detector exchange to be performed by a

[4] MM Engineering GmbH, Lärchenstrasse 21, 85625 Baiern-Berganger, Germany.

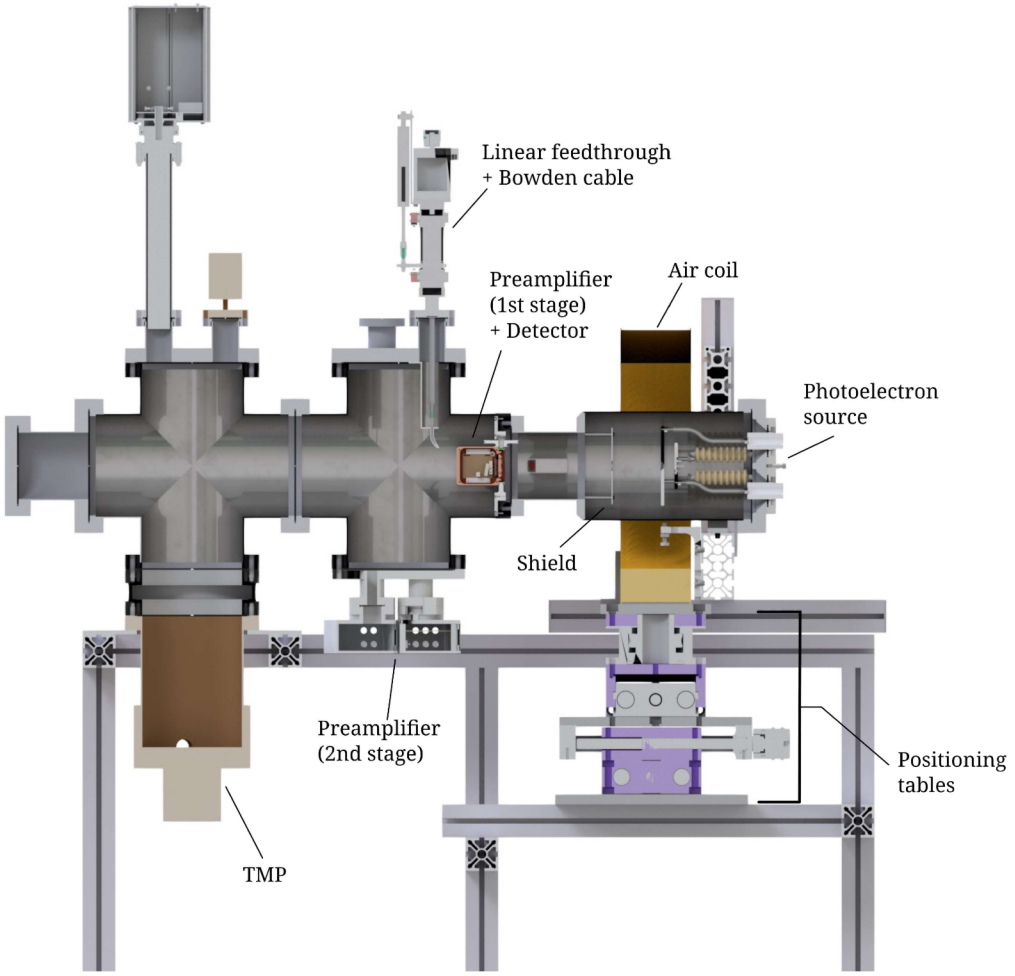

(a) CAD drawing by Hans-Werner Ortjohann

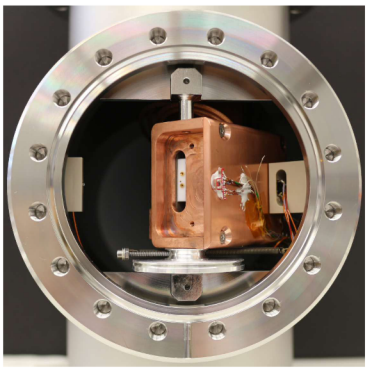

(b) Rotatable preamplifier

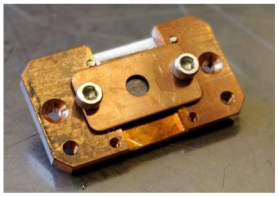

(c) Diode adapter

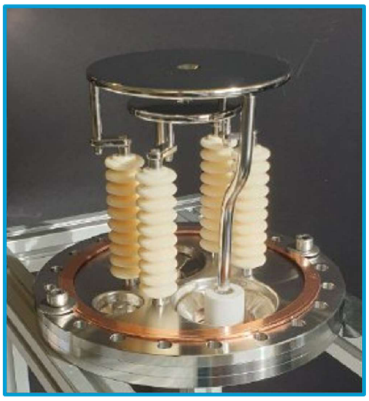

(d) Photoelectron source

Figure 6.9 – Setup II is shown in a. Its main components are the rotatable and LN_2-coolable charge-sensitive preamplifier (b), the adapter (c) for an uncomplicated diode installation to the preamplifier, and the photoelectron source (d). The electric field of the photoelectron source is shielded from the detector and preamplifier. A Bowden cable mechanism provides the control of the detector rotation angle α_D. The mechanism was planned and carried out by H.-W. Ortjohann. Photo of the photoelectron source by S. Schneidewind.

single person.

An oil-free Leybold SC 15D scroll pump generates the pre-vacuum and a Leybold TURBOVAC MAG W 400 iP turbomolecular pump generates the ultra high vacuum of approximately 10^{-7} mbar to 10^{-8} mbar. The pressure is read-out via Pirani-sensor Leybold THERMOVAC TTR 91S and ultrahigh-vacuum sensor Leybold IE 514 and the accompanying controller IONIVAC IM 540.

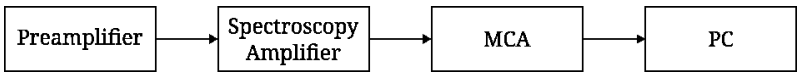

Figure 6.10 – The DAQ chain for both, setup I and setup II, consisted of the two-staged charge-sensitive preamplifier, a CAEN N968 spectroscopy amplifier, a CAEN N957 multichannel analyzer (MCA) and the readout-PC with `iMCAR` software.

The detector is installed on an adapter made of copper, see figure 6.9c. It is insulated with PTFE to guide the electrical contacts. Additional Kapton® tape is applied to avoid short circuits. The adapter allows installation of regular Hamamatsu S3590 PIN diodes as well as microstructured Si-aTEF prototypes at a desk. Since the adapter is removable, this installation can be performed at a desk, in contrast to the installation procedure in setup I, where soldering very close to the vacuum chamber was necessary to install a detector. Upon installation in the vacuum chamber, the adapter with the diode is carefully plugged into the PTFE-surrounded contacts on the preamplifier circuit board.

The vacuum chamber that contains the photoelectron source needs to be removed in order to reach the preamplifier and install the detector adapter. To minimize disturbance of the alignment and for ease of use, the chamber is placed on rails that allow to move it without manually bearing it.

The data acquisition system consists of the two-staged charge-sensitive preamplifier, an CAEN N968 spectroscopy amplifier, and a CAEN N957 multichannel analyzer with a PC with iMCAr-Software (see footnote 3), as schematically shown in figure 6.10. An Agilent InfiniiVision DSO-X 2024A is used for diagnostic purposes and to directly record signal waveforms.

The first preamplifier stage is coupled via four 1 cm thick flexible copper strands to the copper cold finger. The cold finger is fed from the outside into the vacuum and can be cooled with LN_2 that is stored in a cryogenic Dewar underneath. This LN_2 cooling arrangement allows temperatures of up to $-110°C$ at the preamplifier housing. PT1000 sensors are installed in the cold finger close to the connection to the preamplifier housing and on the preamplifier housing for temperature monitoring. The temperature and the voltage and current of the iseg NHQ224M power supply are written into a file by a dedicated LabView program, which was collaboratively written together with S. Schneidewind and L. Pöllitsch [136].

6.3.3 Characterization of (Microstructured) Si-PIN diodes

The KATRIN detector section in principle allows cooling of the detector to approximately $-40°$C. As an intermediate aim, the Si-aTEF prototypes should work as efficient electron detectors at this temperature. A first measure for the performance is the measured reverse current: If the reverse (dark) current falls below $1 - 2$ nA, the noise level is typically acceptable and does not overshadow the measurement. At room temperature, the Si-aTEF prototypes show large amounts of reverse current and noise, which can be drastically reduced by cooling. The reverse current can, further, be efficiently lowered by a surface passivation treatment as post-processing after the ICP-RIE. That is successfully tested in [69, 144] and is not investigated in this work.

The performance of diodes A and B in setup I and of diode C and diode D in setup II with focus on the angle-selective electron detection is described in this chapter. Different investigations were used to find properties and main differences to unmodified Hamamatsu S3590, which were used as reference. The reverse current is used as a measure for the leakage current and, thereby, noise of the diode. It was measured with an iseg NHQ 224M 4 kV high voltage supply, that featured a 100 pA-precision current-readout [165]. It was also used to deliver the bias voltage.

6.3.3.1 Diodes A and B

Setup I was used for first tests on diodes A and B. These were prepared simultaneously, with diode A being etched less deep, compare chapter 5.5. In both cases the noise at room temperature was too high for electron signals (or artificial pulser signals) to be measured. Table 6.1 lists the forward voltage and reverse current of both diodes before and after the etch process. A slight decrease in forward voltage and a drastic increase in reverse current were measured. Cooling resulted in a significantly reduced amount of reverse current and, as a consequence, lower noise. While the reverse current of diode A was outside its specified range before the etching process, diode B was fully working before the treatment, see table 6.1. The small leakage current of 3 nA at room temperature at $U_{\text{bias}} = -60$ V indicated a regularly working diode B. The etching process damaged both diodes, so that the forward voltage decreased and the reverse current increased. A separate preamplifier with 100 MΩ HV resistance was used to measure the reverse current depending on the bias voltage of both diodes: After the etch process, diode B at room temperature showed the maximum current of $I_{\text{reverse}} = 100$ nA at $U_{\text{bias}} = -10$ V, which is a sign of excessive damage that allows the flow of high leakage currents. The reverse current of diode A at room temperature was slightly lower at $I_{\text{reverse}} = 85$ nA.

The leakage current I can be described as function of temperature T via

$$I(T) \propto T^2 e^{-E_G/2kT}, \tag{6.3.3}$$

which shows a strong temperature dependence [156]. A guard ring usually hinders charges

and charge traps, which mainly come from the cutting edge of the chip, to generate a surface current. In case of the Si-aTEF, where the damage to the silicon crystal is inflicted within the guarded area, surface currents can only be reduced by lower temperatures via eq. (6.3.3), by surface treatments with, e.g. SiO_2 [69, 144], and – supposedly – by a cleaner etched surface with minimal amount of irregularities.

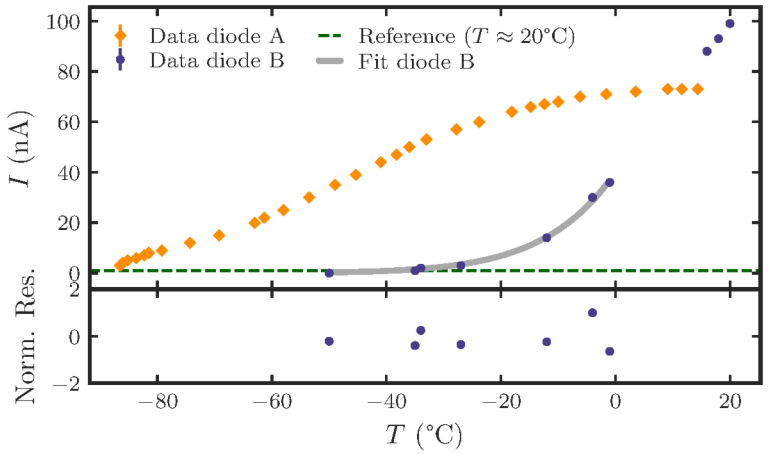

Figure 6.11 – Reverse current of diodes A and B over temperature. While diode B worked as electron detector for different electron energies, no signal could be detected with diode A after the microstructuring treatment. The values were read from the iseg NHQ 224M high-voltage power supply and denoted manually. Diode A was supplied with $U_{\text{bias}} = -40\,\text{V}$, diode B with $U_{\text{bias}} = -60\,\text{V}$ with a 500 MΩ HV resistance in the preamplifier. The current would saturate at 80 nA for $U_{\text{bias}} = -40\,\text{V}$ and at 120 nA for $U_{\text{bias}} = -60\,\text{V}$. The saturation influences the curve shape for larger currents and, therefore, the fit was carried out in a limited range. The reading-error of the power supply display and the manufacturer-specified uncertainty [165] were used as uncertainty for the current measurement, although the manufacturer-specified uncertainty is supposedly too large. The fit resulted in a χ^2_r-value of $\chi^2_r = 1.86/5 = 0.37$.

For both diodes A and B, cooling was indeed an efficient measure to reduce the reverse current, as shown in figure 6.11. The reduction in reverse current with decreasing temperature of diode B is in accordance with eq. (6.3.3). The effective band width from the fitted data is $E_{\text{G,eff}} = (0.96 \pm 0.07)\,\text{eV}$. Defects supposedly cause intermediate states and, thereby, the value to be smaller than the literature value for silicon of $E_{\text{G}} \approx 1.12\,\text{eV}$ [155]. Diode A showed a very different behavior, which did not follow eq. 6.3.3 and, thus, malfunction of this diode was suspected. Diodes A and B were subsequently installed in setup I and their response to electrons of 14 keV from the photoelectron source was measured. Diode A was not able to measure electrons and discarded as Si-aTEF prototype. Measuring electrons with diode B required magnetic beam deflection via the parallel coils centered around the detector: The electrons were magnetically guided from the source through the beamline towards the detector. In order for the beam to reach the detector, which had a circular aperture 5 mm diameter in front of it to only expose the microstructure, the beam was deflected in the detector region. The plate angle α_{p} of the photoelectron source was varied from 0° to 8°. The electron beam was guided through the aperture. For every α_{p} the measured rate was maximized by variation of the deflection coil currents. The maximized

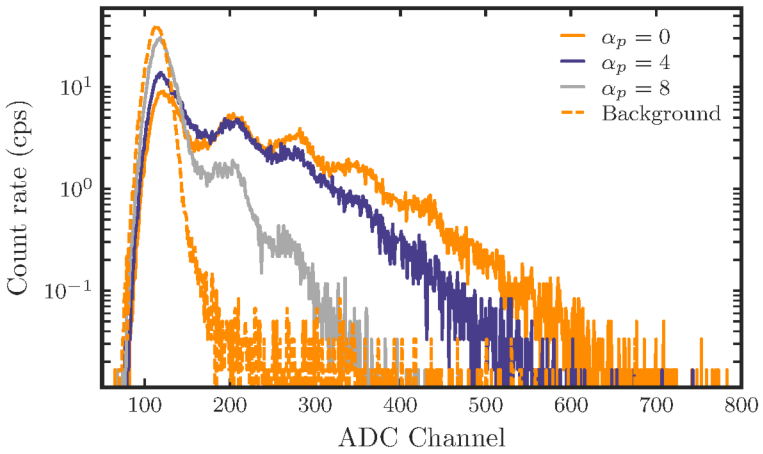

Figure 6.12 – The electron spectrum of 14 keV electrons from the photoelectron source shows that diode B is functional after ICP-RIE treatment, measured in setup I. It was cooled to approximately −70°C. The beam tube coils and air coils were powered by constant currents. The deflection coils were varied to direct the electron beam through the small 5 mm aperture onto the microstructured surface of the diode. The plate angle α_p of the photoelectron source does not reflect the incident angle. Multiple electron peaks are visible, indicating high efficiency and full charge collection at least in parts of the diode surface. The non-microstructured part was covered by an aperture of 5 mm diameter that only revealed the microstructure. The UV-LED of the photoelectron source was driven with an 8 V-pulse of 1 µs width at a frequency of 1 kHz. The diode B was biased with $U_\mathrm{bias} = -60$ V.

rate and multiplicity was highest for $\alpha_\mathrm{p} = 0°$. While the peak position remained constant, the rate and the multiplicity diminished with larger α_p, see figure 6.12.

On first sight, that seemed to exclude an increasing detection efficiency of electrons with large incident angles. However, the assumption that larger plate angles mean larger incident angles on the detector turned out wrong when detailed simulations were obtained by R. Salomon [134]. These simulations revealed violation of adiabaticity of the electrons on their way through the beamline and, thereby, eq. (3.1.6) was not valid [134]. There may have been multiple reasons for an increase of count rate for smaller α_p: The small aperture in front of the detector required a precise adjustment of the deflection coils at every α_p. In turn, the change of the deflection coil current influenced the incident angle of the electrons on the detector. Further, the electrons with larger initial angles arrived on the detector with a broader variety of angles due to the violation of adiabatic guidance, according to simulations [134]. That spread also lead to a broader beam spot, which exceeded the aperture and reduced the measured electron rate and multiplicity [134].

The inconclusive results and unresolved deviations between measurements and accompanying KASSIOPEIA simulations, described in detail in [134], lead to the conclusion that test setup I was not suited for the proof of angle-selective detection of Si-aTEF prototypes.

Unfortunately, diode B malfunctioned during commissioning tests with setup II before the rotation mechanism of the detector module was fully working. Although diode B was a promising Si-aTEF prototype, angle-selective electron detection was not shown nor disproven. That it was able to measure electrons despite the damage from the etch

Table 6.1 – Forward voltage U_{forward} and leakage current I_{leakage} of diodes A and B before and after ICP-RIE. U_{forward} was measured with a multimeter and I_{leakage} with the iseg NHQ 224M high-voltage supply, which was also used to apply U_{bias}. The HV resistance of the charge-sensitive preamplifier was 100 MΩ.

Voltage/current	**pre/post**	**A**	**B**
U_{forward}		456 mV	464 mV
I_{leakage} at $U_{\text{bias}} = -10$ V	pre	36 nA	2 nA
I_{leakage} at $U_{\text{bias}} = -60$ V		126 nA	3 nA
U_{forward}		424 mV	395 mV
I_{leakage} @ $U_{\text{bias}} = -10$ V	post	85 nA	100 nA
I_{leakage} @ $U_{\text{bias}} = -60$ V		514 nA	600 nA

process was, however, seen as remarkable result, which lead to the continued development of Si-aTEF prototypes.

6.3.3.2 Diode C

After diodes A and B malfunctioned, more diodes were prepared. Similar to diode B, the Si-aTEF prototype diode C (see chapter 5.5) showed a reduced forward voltage of 372 mV instead of the typical approx. 470 mV. It was able to detect photons from a 100 Hz light source. The photoresist mainly detached from the surface after the etching process, leaving the unetched face side of the diode uncovered during the measurements. The performance of diode C was examined in setup II.

The stabilization time of the noise at low temperatures around $T \approx -100$°C was measured at a bias voltage of $U_{\text{bias}} = -18$ V and is shown in figure 6.13. The noise-rate

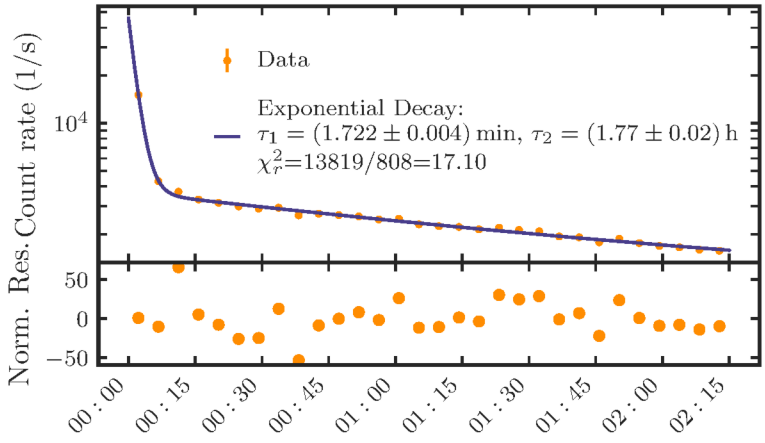

Figure 6.13 – Stabilization of diode C after bias voltage of $U_{\text{bias}} = -18$ V was applied at constant temperature $T \approx -110$°C. The voltage was ramped up in steps of a few V until −18 V was reached after approximately 30 s. The noise count rate approximately follows two exponential decays. No pile-up correction and no multiplicity correction were applied, which supposedly leads to the increased χ^2_r-value.

decrease over time can be described phenomenologically by two exponential decays. After a first, fast decline in noise count rate within a few minutes, the count rate finally decreased with a larger exponential time constant $\tau_2 \approx 1.8\,\mathrm{h}$. That behavior was only measured for diode C, but may also occur in other specimen. It should be monitored in future Si-aTEF detectors.

The increased noise rate and its reduction over time in etched Si-aTEF detectors probably were due to the detector damage: There was, on the one hand, significant damage induced on the surface and the passivation layer. On the other hand, the etching process significantly altered and damaged the volume, which lead to phonon excitation, crystal structure deformations, and other distortions [156]. The leakage current is generally increased with damage [156]. While surface damage decreases the charge collection, the volume damage induces parasitic currents [156]. Structural defects can be vacancies or interstitials, which act as acceptors or donors [159]. Charge trapping effectively decreases the mean free path of charge carriers and, thereby, reduces the induced signal. When reverse bias voltage is applied, charge carriers are caught and released in traps until equilibrium is reached. The release of a trap induces a current, which may be registered by the charge-sensitive preamplifier and, thereby, contributes to the noise counts. The small number of noise events made this effect non-measurable in untreated reference diodes, but the rather heavily altered Si-aTEF prototype diode C showed this behavior after the ICP-RIE process.

The leakage current may contain surface ($I \propto U$) and volume ($I \propto \sqrt{U}$) proportions [156]. The relation between current and bias voltage can elucidate which proportion dominates. Surface proportions often stem from defects or residues on the surface [156], of which both are inflicted to the Si-aTEF prototypes by the microstructuring process and, thus, a linear correlation was measured, as shown in figure 6.14.

With a shaping time of 0.5 µs, the spectroscopy amplifier was optimized for the Si-aTEF test, see figure 6.15. The MCA threshold was lowered to Thr = 3 in order to reveal the electron signals in the spectrum. The pulse height spectrum was dominated by noise in the lower channels, see figure 6.16. Pile-up then induced an additional noise peak in higher ADC channels. The spectra of diode C did not show a considerable energy resolution, which was a stark contrast to the performance of non-microstructured Hamamatsu S3590 Si-PIN diodes. That hinted to incomplete charge collection. The phenomenon is further contemplated in the next section 6.3.3.3.

The background count rate B could be removed from the spectrum to measure the electron signal count rate S: B was subtracted from the total spectrum T via $S(f) = T - f \cdot B$, where a factor $f = 1$ implies that no differences in pile-up or dead time were prevalent between B and T. When the subtraction factor f minimized the background contribution, $\mathrm{d}S/\mathrm{dCh_{ADC}}$ showed the lowest amount of variation. Thus, the sum over the derivative of S is minimal, when the subtraction factor f fully eliminates the background. The mean value of f for all spectra in the measurement series is $\mu(f) = 0.150$ with standard deviation $\sigma(f) = 0.006$. The same background spectrum was used for all signal spectra. This method

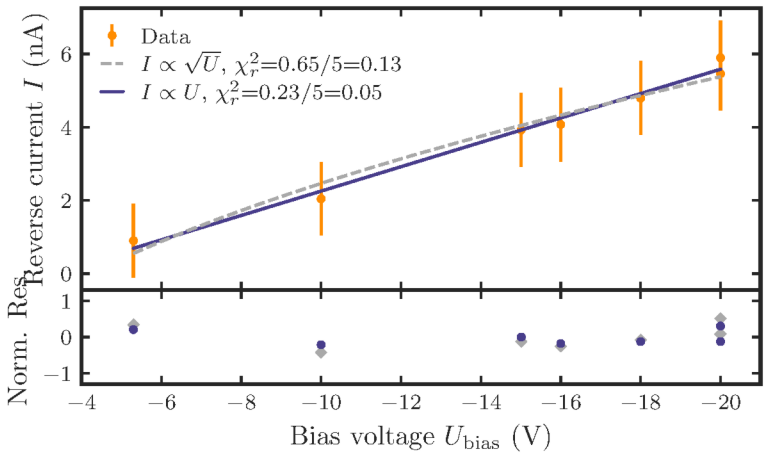

Figure 6.14 – Reverse current over bias voltage of diode C. In order to not increase the reverse current by electron flux from the photoelectron source, the UV-LED was turned off during the measurements. The temperature was constant at $T = (-102.7 \pm 0.5)°\mathrm{C}$. The small variation of the temperature had a marginal effect on the leakage current in the order of $< 5 \times 10^{-5}\,\mathrm{nA}$. The χ_r^2-value of the linear correlation is smaller and describes the data more fittingly: The central values of the data more closely follows $I \propto U$. However, the manufacturer-specified current uncertainty was in the order of 1 nA [165], which appears to be rather large and is probably overestimated.

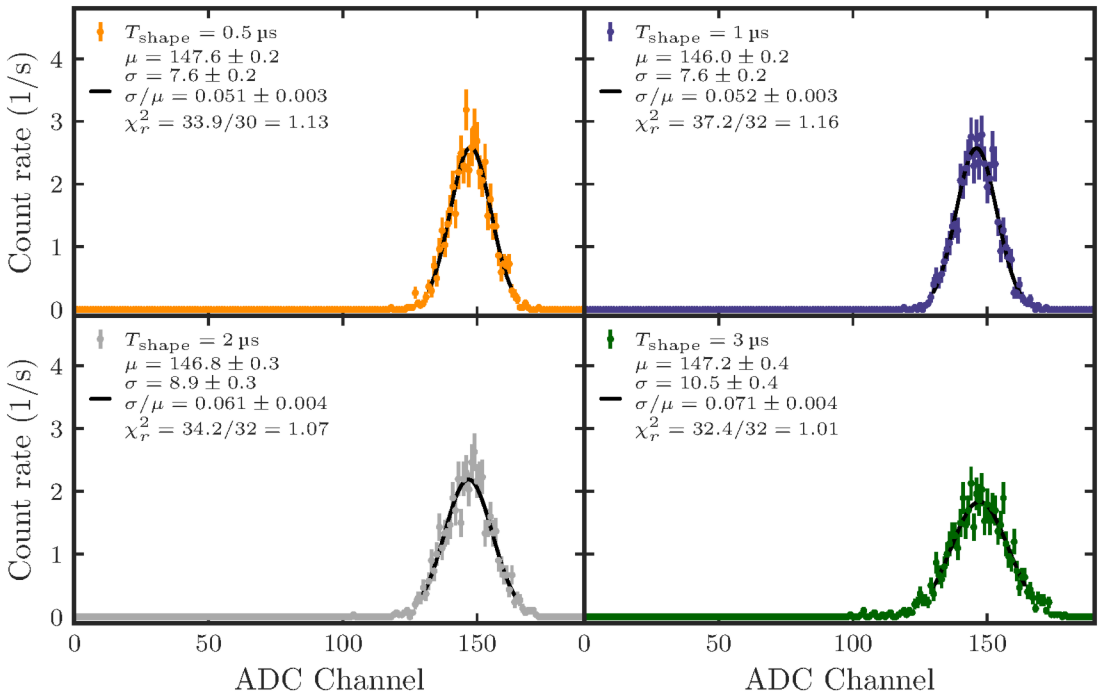

Figure 6.15 – The shaping time was varied for diode C, which was biased with $U_{\mathrm{bias}} = -17\,\mathrm{V}$ and cooled to approximately $T = -100°\mathrm{C}$. The MCA threshold was set to Thr = 10, where the noise contribution was suppressed, so that pile-up was avoided. A test pulse that was large enough to overcome the threshold was used. The short shaping times of $T_{\mathrm{shape}} = 0.5\,\mu\mathrm{s}$ to $T_{\mathrm{shape}} = 1\,\mu\mathrm{s}$ of the spectroscopy amplifier were suited best to resolve the pulse.

of background subtraction is only valid if the background contribution is stable over time and does not change its spectral shape. As seen below and, more severely, in [136], the background of a Si-aTEF prototype in setup II can change over time, which introduces an additional (non-quantified) uncertainty on f.

The fundamental property of a Si-aTEF is the angle-selective electron detection. For the measurement of the count rate under variation of the incident angle, the linear feedthrough and the Bowden cable mechanism were used to rotate the detector with respect to the electron beam. The translation of linear feedthrough set position and detector angle α_D was measured in [136]. The electron count rate was measured for a fixed coil position and different Bowden cable elongations, i.e. for rotation angles $-40°$ to $33°$. The photoelectron source was operated with back plate voltage $U_{\text{back}} = -20\,\text{kV}$. The UV-LED was triggered with 10 kHz at 100 ns width and 8 V pulse height. The magnetic coil current was 30 A and the detector was biased with $U_{\text{bias}} = -18\,\text{V}$, where a stable operation was possible. The measurement is illustrated in figure 6.17, where larger detector angles $|\alpha_D|$ resulted in larger electron count rates. Since the face side of the diode was not covered by photoresist and the open area ratio is $\text{OAR} = (73.3 \pm 0.6)\%$ – leaving more than a quarter of the original surface area exposed – the count rate under $\alpha_D = 0°$ was of significant magnitude: The forward directed electrons either hit the channel wall, the floor, or the front of the channels. However, the count rate increased for large detector angles and was minimal for a rotation angle of $\alpha_D = 0°$. That means, diode C showed the first proof that Si-aTEF prototypes possess angle-dependent detection efficiency and that the Si-aTEF is a valid detector principle to differentiate between electrons based on their incident angle.

Measurements of the electron rate were, in addition, carried out while changing the position of the coil, thereby scanning the surface of the diode. Regions of different detection efficiencies were identified by scanning the surface on sub-mm-level via step-wise displacement of the coil, which was placed on a precisely movable and translatable table, see section 6.3.2. The measurement of the rate in dependence of the coil position is shown in figure 6.18 for different electron energies. For a pointlike electron beam, a rectangular shape was expected. However, the signal count rate strongly depended on the position of the coil. Its irregularity showed that the surfaces was inhomogeneously active. The optical microscope images in section 5.5 of this diode shows defects, e.g. silicon needles, that may contribute to imperfect charge collection by increased surface damage and electron trapping.

6.3.3.3 Diode D

The diode D with an $\text{OAR}_\text{D} = (43.0 \pm 0.2)\%$ had its photoresist still persistant on the surface. It was installed in the detector section of setup II and examined for its reverse current, the shape of e^--spectra, the angle-selective detection efficiency and the detection homogeneity over its surface.

Figure 6.19 shows the temperature-dependent reverse current. It was reduced to sub-

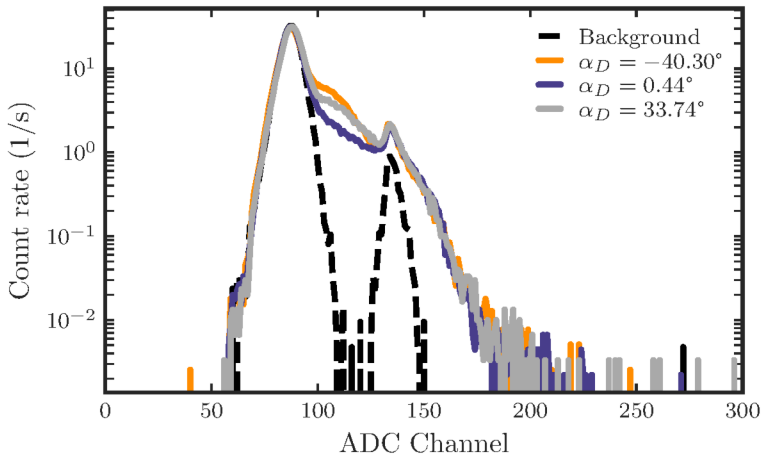

(a) 18 kV

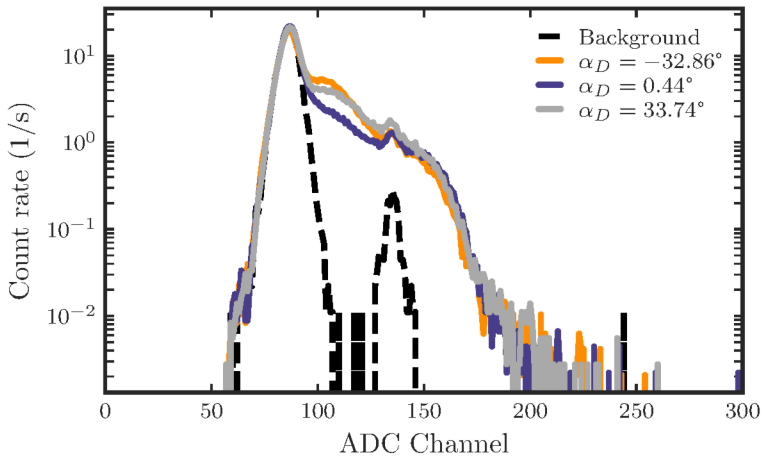

(b) 20 kV

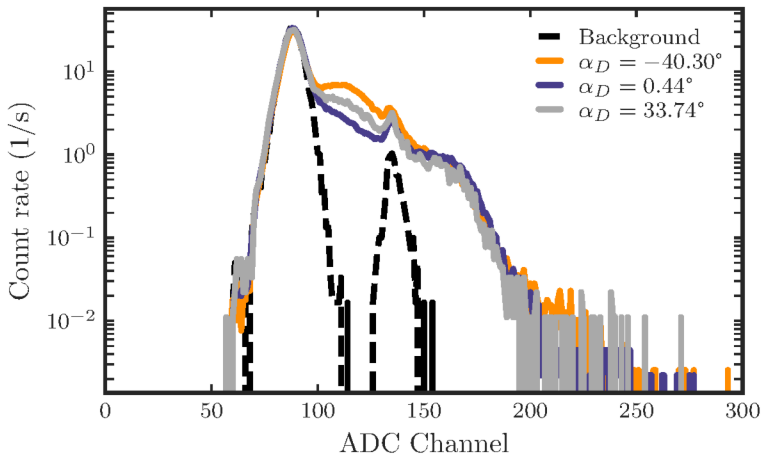

(c) 22 kV

Figure 6.16 – Pulse height spectra of diode C for different electron energies at different detector angles α_D. The noise peak featured a double structure, the cause of which is not fully clarified and which diminishes at larger thresholds. The count rate increased with larger α_D.

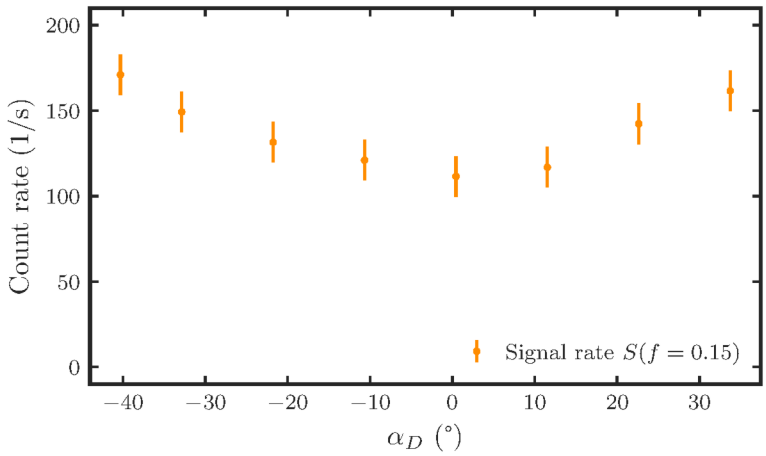

Figure 6.17 – Angle-dependent detection of electrons with 20 keV energy for different detector angles α_D in diode C. The background count rate was subtracted with the method described in section 6.3.3.2. The standard deviation of f was added to the uncertainty. The standard deviation of the rather inhomogeneous count rate over x – as seen in figure 6.18 – was taken into account, as well. The count rate ratio at $\alpha_D = -40°$ to $\alpha_D = 0°$ is 1.53 ± 0.19.

nA-level by cooling to $T < -60°\mathrm{C}$, which lowered the noise level in the spectrum. The effective band width $E_{\mathrm{G,eff}} = (0.98 \pm 0.02)\,\mathrm{eV}$ is smaller than the literature value for silicon of $E_{\mathrm{G}} \approx 1.12\,\mathrm{eV}$ [155], which is likely caused by defects. The result is consistent with the previous measurement in 6.3.3.1.

While the energy resolution of a reference diode improved with lower temperatures and most of the primary electrons were detected at the $1e^-$ peak, see figure 6.20b, the determination of the incident-electron energy for diode D appears unfeasible: The charge collection efficiency of diode D was overall drastically reduced with respect to the reference diode. Further, it strongly depended on the temperature: Lower temperatures enhanced the charge collection. Figure 6.20a shows this effect.

A reduced charge collection is generally due to a decreased charge carrier lifetime, which can be attributed to the large amount of defects in the Si-aTEF prototypes induced by the microstructuring process. The pulse shape of the charges, if released for example at the p^+ contact of a planar PIN detector, is affected by trapping and detrapping. A linear rise of the pulse is expected, when no trapping occurs. Permanent trapping lowers the amplitude and induces a curvature in the rise of the pulse, while non-permanent trapping releases charge carriers after a finite trapping time [159, 166]. Thus, a large number of trapped charges diminishes the collected charges, alters the pulse shape and, in the end, decreases the position in the pulse height spectrum of the incident electrons. An increased charge collection at cryogenic temperatures was also found in [167], which suggests properties of amorphous silicon to be prevalent in irradiated and reverse-annealed (i.e., temperature-cycled between 4.2 K and room temperature) silicon detectors as explanation. The implications on a Si-aTEF detector and possibilities to increase charge collection at higher temperatures are to be investigated further.

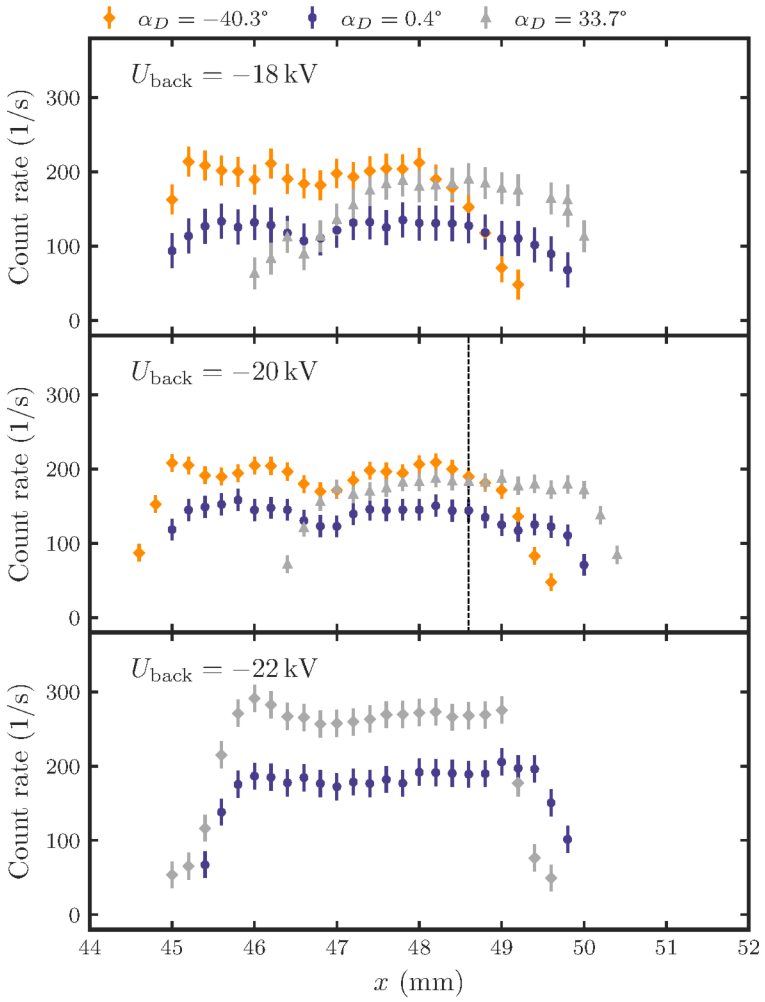

Figure 6.18 – Scans of the x-position of the coil at different back-plate voltages of the photoelectron source, i.e. at different electron energies $E = eU_{\text{back}}$, of diode C. The aperture was of 5 mm diameter, which is resembled in the width of the distributions. The effective aperture as seen from the front becomes smaller for larger $|\alpha_D|$. Further, since the rotation axis is the detector surface, the aperture rotates slightly off-axis. The scans show a slight dependence in the count rate of the coil position, with resembling local minima and maxima in different energies and angles at the same x-position. The count rate depends on α_D. Figure 6.17 was measured with electrons of 20 keV at $x = 48.6$ mm, which is indicated by the black dashed vertical line.

Figure 6.21 shows that the count rate and spectral shape strongly depend on the incident angle. The back plate of the photoelectron source was set to $U_{\text{back}} = -20\,\text{kV}$. The current through the coil was set to 30 A and its position was fixed. The background in 6.21 (b) was subtracted with the method described in section 6.3.3.2. The count rate drastically diminished with a smaller detector angle $|\alpha_D|$. Since the top face side of the channels was covered in photoresist, the detector response was entirely generated by hits of the inner surface. The floor region of the channels appears to be inactive, as the diminishing count rate at small α_D shows.

The increased detection efficiency with larger detector angle is also visible in figures 6.22,

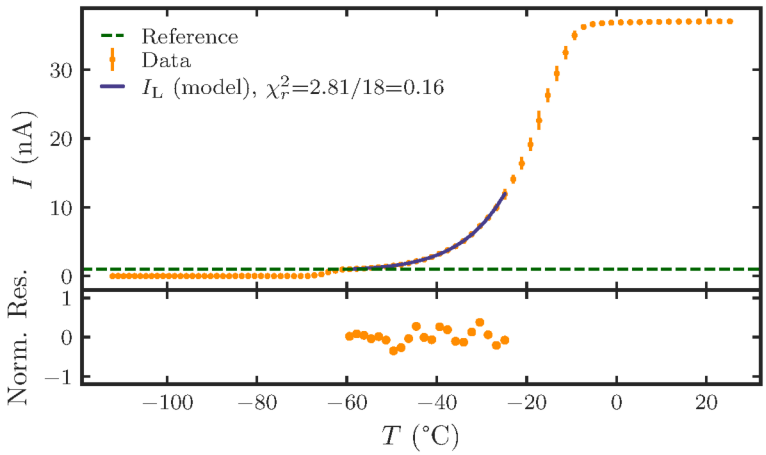

Figure 6.19 – Temperature dependent leakage current of diode D, when biased with $U_{\text{bias}} = -18\,\text{V}$. The leakage current can be described by eq. (6.3.3). The temperature was measured in 1°C steps. For each temperature step, the measured leakage currents were averaged and their standard deviation was used as uncertainty. The supposedly too large uncertainty of the high-voltage power supply of $\mathcal{O}(1\,\text{nA})$ was not added.

where, further, a strong dependence on the coil displacement is revealed. The coil was used to move the electron beam across the detector, as described in section 6.3.3.2. The overall count rate rised with α_D. However, there were multiple (local) features depending on the coil displacement x and on the detector angle α_D. In figure 6.22 at 20 keV electron energy, for example, the rate decreases continually for $\alpha_D = -40.3°$. At the same energy, but at $\alpha_D = 33.7°$, a minimum appears at $x = 49.6\,\text{cm}$. These inhomogeneities may be linked to the surface damage of a diode. They seem to depend on the direction of electrons and are not linked to visible surface defects.

The detection efficiency of diode D was directly compared to a reference diode in a dedicated measurement, where the experimental circumstances were kept as fixed as possible. The measurements were conducted directly after each other, with the only known difference being the detector angle and the temperature: The diode D was set to $\alpha_D = -40°$ and the reference diode to $\alpha_D = 28°$, which was moved once due to the exchange of the diode adapter. The spectra are shown in figure 6.23 (a). Diode D was operated at a temperature of the preamplifier housing of $T_{\text{D}} = -107°\text{C}$ and the reference diode at $T_{\text{Ref}} = -50°\text{C}$. The difference in temperature does not significantly affect the efficiency of the reference diode, but its energy resolution becomes sharper with lower temperatures. The non-zero detector angle of the reference diode in this case is an effect of approximately 3% between $\alpha_D = -40°$ and $\alpha_D = 28°$, see figure A.1a in the appendix. However, the exchange of a diode in setup II is a hardware change, which may slightly alter – for example – the alignment and can induce an additional uncertainty. The background

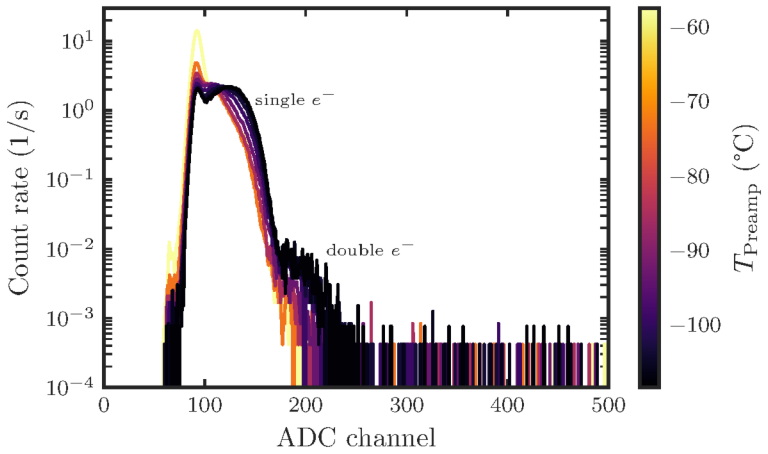

(a) Diode D

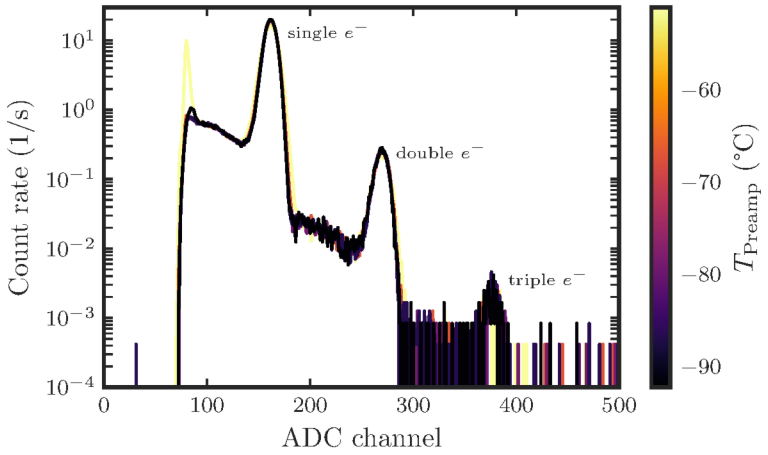

(b) Reference diode

Figure 6.20 – Spectra of 20 keV electrons during detector cooling from room temperature to about −105°C. The color scale indicates the preamplifier temperature T_{Preamp}. The spectra of diode D in (a) are each averaged from 20 consecutively recorded spectra. The shoulder in the highest populated MCA channels likely stem from simultaneous detection of two electrons. The charge collection is significantly increased with lower temperatures and highest for the lowest reached temperatures close to −100°C. The spectral shape of the reference diode in (b) was slightly improved by cooling, but the charge collection efficiency is unaffected by the temperature change. The simultaneous detection of two or more electrons is clearly visible by the secondary and tertiary peaks.

factor f was found to be

$$f_{\mathrm{D}} = 1.22 \pm 0.12 \tag{6.3.4}$$

$$f_{\mathrm{Ref}} = 0.87 \pm 0.04 \tag{6.3.5}$$

at back-plate voltage $U_{\mathrm{back}} = -20\,\mathrm{kV}$ of the photoelectron source and for a fixed position of the coil. The uncertainty of f was estimated by variation of the full spectrum T and background spectrum B within their 1σ-margins. The signal spectra ($S = T - f$) are shown

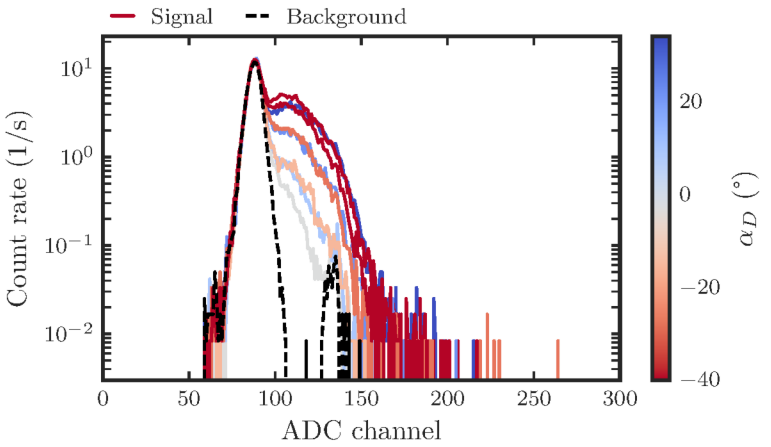

(a) Spectra of electrons depending on rotation angle.

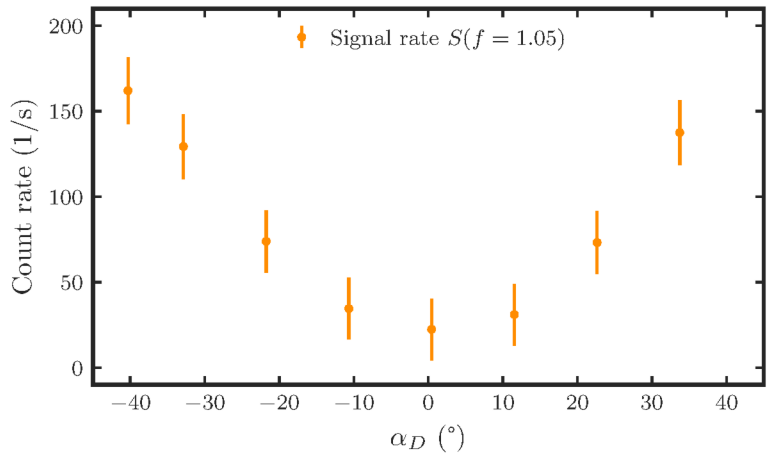

(b) Angle-dependent 20 keV electron detection.

Figure 6.21 – Spectra and count rate at different detector angles α_D for diode D. The position of the coil was fixed during the measurements. The count rate shown in (b) is the signal with eliminated background via the method explained in section 6.3.3.2. (b) was recorded at a fixed coil position at $x = 48.8\,\text{mm}$ and $y = 13.5\,\text{mm}$. However, the count rate depends on the position of the coil (see figure 6.22). The errorbars incorporate the standard deviation of the count rate depending on x. The count rate ratio at $\alpha_D = -40°$ to $\alpha_D = 0°$ is 7.2 ± 5.9.

in figure 6.23b. The remaining count rate in the spectrum after background subtraction in the relevant region up to ADC-Channel $\text{Ch}_{\text{ADC}} = 300$ is:

$$\sum_{\text{ch.}=0}^{300} S_{\text{D}} = (50.0 \pm 2.4)\,\text{cps} \tag{6.3.6}$$

$$\sum_{\text{Ch.}=0}^{300} S_{\text{Ref}} = (163.2 \pm 9.4)\,\text{cps}. \tag{6.3.7}$$

That allows to calculate the efficiency of diode D at $\alpha_D = -40°$ with respect to the

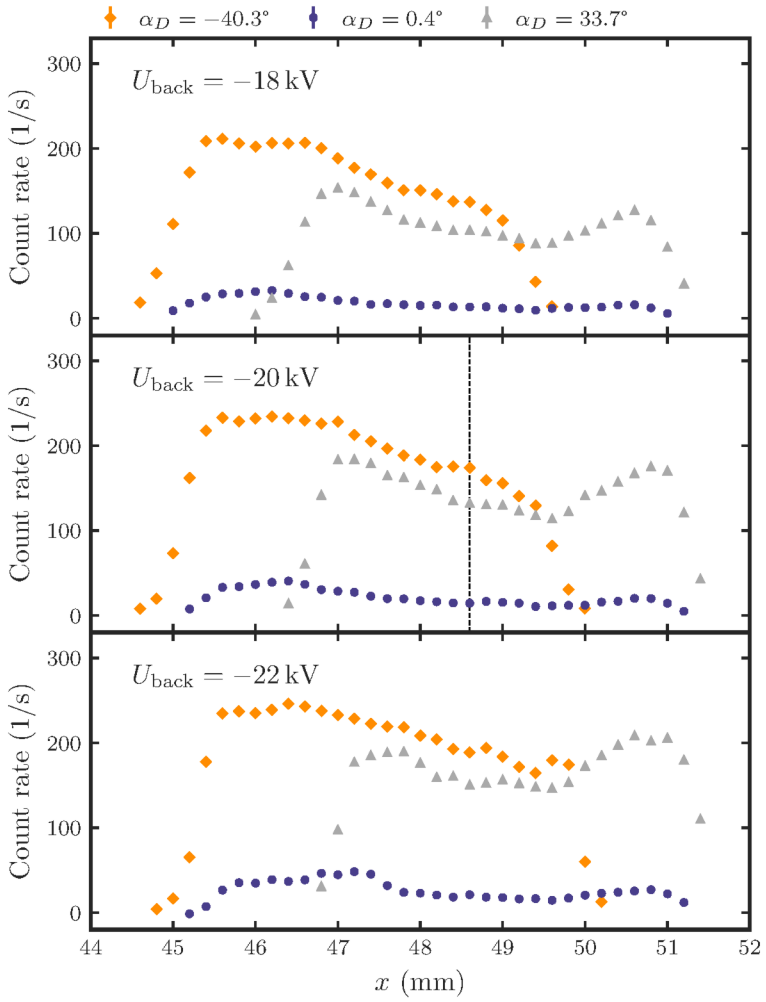

Figure 6.22 – Scans over x-positions of the coil at different back-plate voltages U_{back} of the photoelectron source reveal a huge dependency of the count rate on the detector angle α_D in diode D. Further, there appears to be inhomogeneous detection efficiency over x, as seen in figure 6.18 before. The reason for the different widths and the shifted central position of the distributions is the change of the effective aperture size in frontal view when the detector is rotated. The angle-selective detection efficiency in figure 6.21 was measured with electrons of 20 keV energy at $x = 48.6\,\text{mm}$, as indicated by the black dashed line.

efficiency of a reference diode to

$$\text{Eff}_\text{D} = \frac{\sum_0^{300} S_\text{D}}{\sum_0^{300} S_\text{Ref}} \cdot \frac{1}{\text{OAR}_\text{D}} = 0.71 \pm 0.05. \tag{6.3.8}$$

It is suspected that the photoresist-covered area and the bottom of the channels is fully inactive and that the detection of electrons occurs only in the channel side walls. The count rate is, further, expected to increase when the photoresist is removed, which bears a risk of performance issues or even destroying the detector. In order to preserve the functionality of diode D, the photoresist was left on the device.

Operation of an FPD-sized Si-aTEF with the angle-dependent detection efficiency of

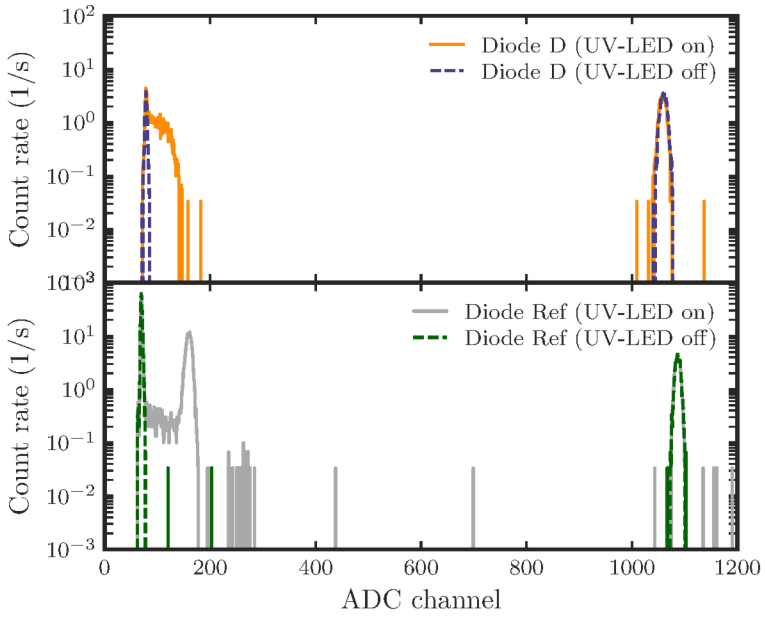

(a) Electron spectra of diode D and reference diode.

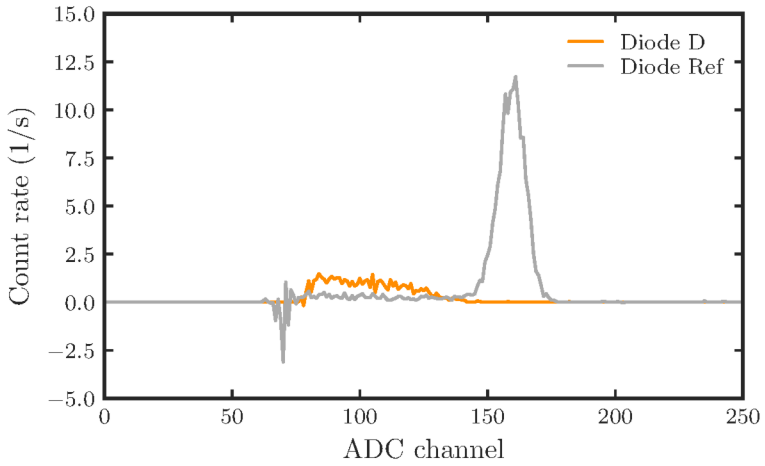

(b) Signal spectra, background subtracted with factor f_{D} or f_{Ref}.

Figure 6.23 – Spectra of diode D and of a reference Si-PIN diode of the same type (Hamamatsu S3590), which was not microstructured. The position of the coil was fixed and not altered between both measurements. The count rate shown in (b) is the signal S with eliminated background B via the method explained in section 6.3.3.2. A pulse counter was activated during the measurements, with 99.9% (diode D) or 99.6% (reference diode) of the counts being registered by the MCA. The dead time was, thus, negligible.

diode D in KATRIN would reduce the count rate at the detector. A rough measure of the performance of such a Si-aTEF was estimated as follows: The angle-dependent detection efficiency was fitted with a polynomial, see figure A.2 in the appendix, to allow a continuous description. It was multiplied to the known angular distribution of the signal (up to 40° to avoid extrapolation) from 3.15. The signal spectrum at $\alpha = 40°$ was scaled by $\mathrm{Eff_D} = 0.71 \pm 0.05$ multiplied with $\mathrm{OAR_D}$. The multiplication of the OAR was necessary,

since the photomask is thought to remain on the surface. When the photomask is removed, the efficiency rises to $\mathrm{Eff_D} \cdot \mathrm{OAR_D} + 100\% \cdot (1 - \mathrm{OAR_D})$.

The detection efficiency for Rydberg-background electrons (at small angles) was derived from the signal spectrum: The ratio of the original signal count rate at 5° was compared to the Si-aTEF signal count rate at 5°. The ratio was used to scale the Rydberg-background angular distribution by the same amount. Figure 6.24 shows the resulting angular distributions. The relative count rate of diode D as Si-aTEF with the angle-dependent efficiency (up to 40°) would be $(18.2 \pm 1.2)\%$ for signal electrons and $(4.6 \pm 0.3)\%$ for Rydberg-background electrons when compared to the reference diode. The hypothetical removal of the photomask would deliver an efficiency of $(66.2 \pm 4.7)\%$ for signal electrons and $(43.2 \pm 3.1)\%$ for Rydberg background electrons.

To conclude, diode D was the first successful Si-aTEF prototype with an outstanding suppression of electrons with small incident angles. For KATRIN, the strong reduction of Rydberg-background would be a success. However, the signal reduction by approximately 80% (with photomask) would be very detrimental to KATRIN's neutrino mass sensitivity, which is also the case for a 33% reduction (without photomask). In addition, background components with larger angles are demonstrably prevalent, as explained in section 4.1.2, which would enlarge the estimated efficiencies for its detection. An optimal Si-aTEF would strongly reduce the background, but retain most of the signal. The obtained relative count rates are expected to change drastically for Si-aTEF detectors without photoresist and with an optimal OAR. The measured rate at small angles would strongly depend on the OAR, since the front side of the Si-aTEF channels would be active and without angle-dependent detection efficiency. Thus, the reasearch for optimization of Si-aTEF prototypes is ongoing.

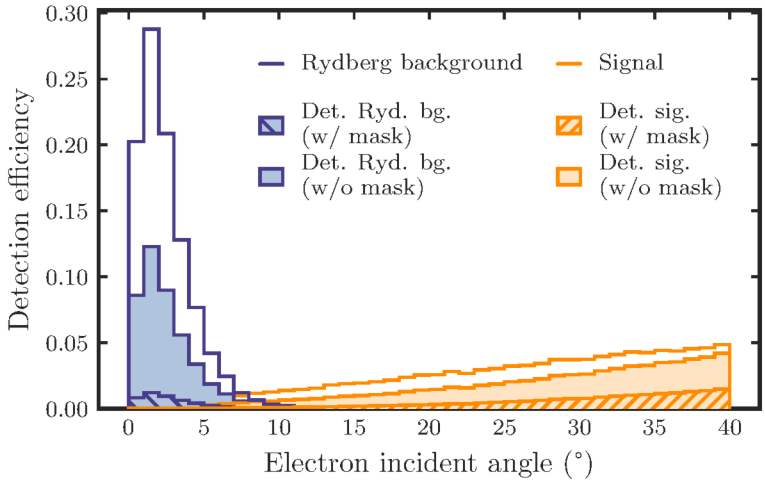

Figure 6.24 – Angular distribution of 10^5 β-decay electrons and 10^5 Rydberg background electrons of up to 40° incident angle on the detector in KATRIN. The efficiency of diode D relative to the reference diode was applied to the "detected signal" (orange) and "detected Rydberg background" (blue). With photomask on diode D (hatched area), an efficiency of $\mathrm{Eff_D} \cdot \mathrm{OAR_D} = 30\%$ is expected at electron incident angles of 40°. A strong reduction at small angles is observed. Although affected less, the signal is reduced by more than 80%. In the scenario with removed photomask (filled area), an efficiency of $\mathrm{Eff_D} \cdot \mathrm{OAR_D} + 100\% \cdot (1 - \mathrm{OAR_D}) = 87.5\%$ is expected at 40°, which retains significantly more signal and background. The result is transferable to a KATRIN-scenario only with caveats: The efficiency was measured with electrons of 20 keV energy instead of 18 keV or 28 keV (without/with KATRIN's post-acceleration), but the detection efficiency probably depends non-negligibly on the energy. Further, the electron angular distribution of the photoelectron source of setup II is unknown and was not considered and the detector angle α_D was used equivalently to the incident angle. The missing energy resolution of diode D, which would affect the region-of-interest energy-cut of the currently used FPD and increase the background, was not accounted for. The thickness of the photoresist and its shadowing effect at large angles was neglected in the estimation. The backscattering of electrons off the silicon surface was neglected, too. Finally, the Rydberg background in KATRIN is accompanied by backgrounds from autoionizing atoms of larger incident angles, which is detrimental for the differentiation with an aTEF. Still, the simulation allows a first estimation of the performance of an actual Si-aTEF prototype in KATRIN.

6.4 Towards an aTEF for the KATRIN Experiment

The previous chapter showed the feasibility of angle-selective electron detection with microstructured Si-PIN diodes. Further, test procedures of Si-aTEF prototypes were developed: These were, i.a., the angle-selective detection efficiency, detection homogeneity over the surface, the stabilization time after application of U_{bias}, the temperature-dependent noise and reverse current, and the temperature-dependent charge collection. Deviations of the protoype performance from reference diodes were found in all of these categories, which makes these tests crucial. In contrast to reference diodes, the charge collection of prototypes was temperature-dependent in the examined temperature range. Due to that and the broad distribution of the count rate over the pulse-height spectrum, an energy resolution was not measurable and the Si-aTEF was used as a mere counting detector. Within the KATRIN-system that would introduce systematic uncertainties, since

a region-of-interest within the spectrum cannot be defined. This problem may be mitigated with an improved etch process: It is suspected that the charge collection efficiency becomes less temperature-dependent when the surface incorporates fewer defects.

All Si-aTEF prototypes in this work suffered from an increased distance between photomask and photoresist during the lithography process, which resulted in broader sidewalls than anticipated. More results on Si-aTEF prototype performances will be investigated in [69], where Hamamatsu Si-PIN diodes with a plane ceramic packaging are used. These allow a much more precise lithography process, which reportedly results in much sharper microstructures. Currently, it remains open whether they possess a similar angle-selectivity: It was not yet experimentally shown whether the very thin sidewalls allow for sufficient charge collection.

The final Si-aTEF would consist of a full-sized microstructured FPD. Until now the angle-selectivity was tested only in frontside-illuminated Si-aTEF prototypes. The electronic setup in the KATRIN detector section would require a major modification, if a frontside-illuminated Si-aTEF should be installed. While the simulations presented in section 6.2 predict backside-illuminated Si-aTEFs to work, if an additional blocking layer is applied on the channel floor, it was not yet experimentally tested.

A Si-aTEF for KATRIN would, further, need a highly homogeneous detection efficiency throughout its surface. It can be suspected that a cleaner etch result, including the elimination of artifacts like silicon needles, would result in larger homogeneity and in a lower leakage current – especially, if a suitable passivation layer is added. The detection homogeneity can be tested in KATRIN with the isotropically emitting gaseous ^{83m}Kr source.

A major systematic uncertainty contribution of a Si-aTEF detector is the backscattering of electrons on its various surfaces. The backscattering probability is known to drastically increase with larger angles to the surface normal. It would have to be understood deeply, accompanied by dedicated simulations (e.g. GEANT4) and measurements.

Long-term stability of the Si-aTEF prototypes was not yet tested. It was, however, seen that repeated cooling to approximately -100°C and warming up to room temperature had a detrimental effect on the Si-aTEF prototypes. For example, the epoxy encasing of the wire bonds was destroyed in case of diode B.

Further, the mechanical stability of a Si-aTEF for KATRIN in full size of the FPD is of concern: The pogo-pin assembly applies significant pressure on the FPDs pixelated frontside to establish an electrical connection. In addition to the stresses induced by the pogo pins, which are estimated in [91], the ICP-RIE may leave edges that lead to increased risk of breakage along crystal planes. On the other hand, thin silicon becomes more flexible, which may help to preserve the integrity of the wafer.

7 Conclusion and Outlook

The neutrino mass remains to be an unknown, but essential characteristic of the universe. It has, i.a., critical influence on the structure formation of the early universe. The mass and its generation mechanism resemble a missing ingredient for an updated Standard Model of particle physics.

Up to now, complementary experiments did not yield a direct estimation: Neither cosmological observations nor neutrinoless double-beta decay could reveal the neutrino mass. Both impose strong limits on the neutrino mass, but depend on the correctness of the underlying models. Direct measurements, which rely on the kinematics of the β-decay but do not make assumptions on the mass generation process, measure the electron energy of weakly decaying isotopes. About 15 years after the last neutrino mass data from the Troitsk tritium β-decay experiment were taken [168], the KATRIN experiment was able to find new upper limits on the incoherent sum of the neutrino mass eigenstates via an integral measurement of the electrons' energy spectrum: Analysis of the first data delivered a result $m_\nu < 1.1\,\mathrm{eV/c^2}$. It was surpassed by the first sub-eV result that stems from combination of the first two science runs. After the (tentative) end of KATRIN's neutrino mass search, KATRIN's focal plane detector will be exchanged by the TRISTAN detector, i.e. a sophisticated silicon drift detector, which allows precise differential energy spectrometry [169]. That will allow to cover undisclosed areas in the parameter space of (keV-)sterile neutrino masses.

Reducing background always was a crucial part of the KATRIN experiment. Various measures were successfully implemented, e.g. reduction of Penning traps via grounded metal rods to catch ions and electrons from the spectrometer volume, or the efficient reduction of radioactive radon from vacuum pumps via cryogenic baffles before it can reach spectrometer volume. Many more were already foreseen in the technical design report, which included the installation of the inner electrode to shield against external radiation and charged particles from the inner spectrometer wall. The installation of the inner electrode was, however, the very likely reason for an elevated background from radioactive contamination with ^{210}Pb in the spectrometer wall. The subsequent α-decay of ^{210}Po sputters off various species of ionized and neutral atoms, which may be in highly-excited Rydberg state. Neutral Rydberg atoms can pass the inner electrode and enter the spectrometer volume. Upon de-excitation (via black body radiation), they release low-energetic electrons, which are accelerated to the detector and, in terms of energy, are indistinguishable from β-decay electrons. The specific property, according to the model, is their sharp angular distribution: The isotropic angular distribution is adiabatically

transformed on the way to the detector and – due to the small initial energy, which is smaller than the transverse energy that β-decay electrons can have – into a sharp angular distribution. However, additional autoionizing states may contribute to a larger angular distribution and extend the angular distribution at the detector, but further measurements are needed for clarification.

The silicon PIN detector is not able to differentiate between angular distributions. The aTEF project aims to add angular selectivity to KATRIN's detector. It builds on the idea of a transverse energy filter, which was thought model of a two-staged grid that blocks the direct line of sight to the detector. Electrons with large cyclotron radii would have a higher chance to pass, while small-angled background would be filtered. The concept was ruled out, as the signal would be reduced too strongly, but sparked ideas of active filters in the beamline: Microchannel plate detectors, Si-PIN detectors, and scintillator-based detectors all may be fabricated such that only electrons with large pitch angles come in contact with the active detector region.

This work proved that MCP-detectors show angle-selective detection. The conceptual idea of an MCP-aTEF was shown, but its implementation would require a dedicated fabrication procedure and testing. Many unknowns, e.g. the reachable secondary electron gain, hinder the project from being prioritized.

An aTEF-detector that utilizes the existing KATRIN focal plane detector would be an optimal solution. The development of a so-called Si-aTEF within this work concentrated on the fabrication of prototypes and the understanding, whether and why angle-selective electron detection can work in microstructured Si-PIN diodes. Their fabrication procedure is obtained by a deep reactive ion etch process with preceding UV-lithography. The cryogenic silicon-etching technique was made available by the Münster Nanofabrication Facility (MNF) and optimized within the aTEF project. Although the photoresist masks for the diodes could not be prepared properly due to their protruding ceramic housing, a microstructure could be applied and 100 µm to 150 µm deep etched diodes were produced. The main finding is the evidence of angle-selectivity within microstructured Si-PIN diodes, with commercial Si-PIN diodes being the prototypes. However, the charge collection of the prototypes suffered and their energy resolution was drastically impaired. The operation temperature of $T \approx -60°\mathrm{C}$ was below KATRIN's requirement of $-40°\mathrm{C}$. Surface passivation can help to increase the operation temperature, as e.g. shown in [69, 144].

After the experimental part of this work was finished, diodes with a specifically produced flat ceramic housing arrived. These allow better processing: Very precise photomasks and etches can be achieved. Results are found mainly in [69, 135, 144]. Further, the microstructuring of a spare FPD was ordered, which can in principle be tested in the KATRIN beamline. The commissioned Fraunhofer IZM Berlin tested its etch process on blank Si-wafers of original detector size and shape. These (non-active) wafers were used for an assessment of the mechanical stability.

Before the risk is taken to exchange the focal plane detector for a Si-aTEF, extensive studies of the consequences of an angular selective electron detector in KATRIN would

be necessary: Systematic effects like the increased backscattering probability at larger incidence angles or a broader region-of-interest in the energy spectrum need to be considered, as well as the practical consequence of immeasurable 0°-electrons of calibration sources, especially KATRIN's photoelectron source. Further, the prototypes would need to be tested in KATRIN environment. A suitable device is a side access to the beamline between KATRIN's superconducting detector magnet and pinch magnet, which can be separated from the beamline by a gate valve. It would allow to introduce Si-aTEF prototype detectors (or other R&D-devices) and measure in-situ the response and performance – depending on the exact flux tube position and field strength. First steps of the preparation of the side access are described in [135].

With the aTEF, an improvement of the sensitivity in the order of 11% to 23% within a typical KATRIN measurement campaign is, according to statistical sensitivity studies (neglecting systematic effects), when either autoionizing oxygen as additional background source is considered or the Rydberg background is considered as only source [140]. That is significant, but complementary methods, e.g. de-excitation of Rydberg states via THz radiation, remain crucial.

A Appendix

Lithography Recipes

The lithography recipes were utilized for the respective samples as explained in section 5.2.

Table A.1 – Recipes with parameters for the Nano Imprint Lithography System EVG620 NT: Separation, proximity, thickness (mask), and thickness (resist) are given in µm, thickness (substrate) in mm, and the UV-exposure dose is given in mJ/cm^2. The large substrate thickness of 1.9 mm for the FPD was due to additional spacers, which allowed the correct positioning. The substrate thickness of 2.7 mm for the Hamamatsu S3590 Si-PIN diodes was due to their ceramic housing and additional spacers.

Recipe	Sep.	Prox.	Mask	Substr.	Resist	Dose	Filename
L-ChipE2	500	150	2.83	0.525	350	250	`SU8-pinDiode_v2.rp`
L-Wafer	500	150	2.63	0.2	150	250	`SU8-Si-200umwafer_closer[...].rp`
L-S3590v2	500	200	2.63	2.7	350	250	`SU8-pinDiode_v2.rp`
L-S3590v3	500	50	2.83	0.75	350	250	`SU8-pinDiode_v3.rp`
L-FPD	700	300	2.93	1.9	300	250	`SU8-pinDiode_FPD2.rp`

Reference diode

The measurements were obtained in setup II with the aim to allow comparison of Si-aTEF prototypes to a reference.

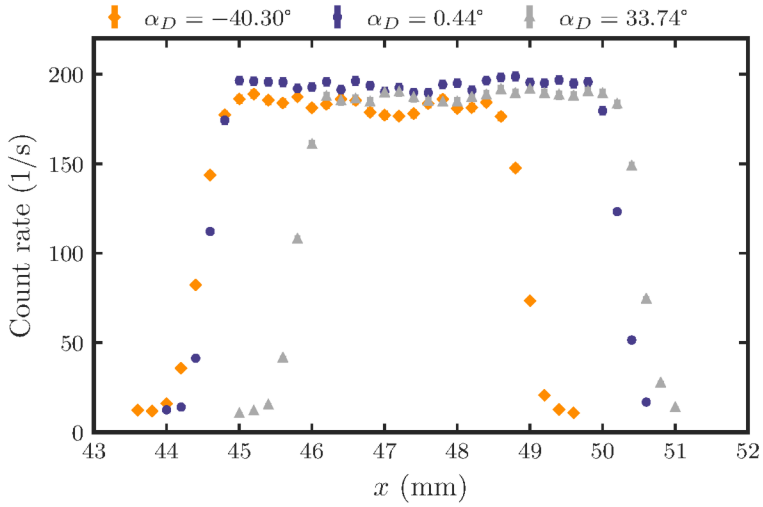

(a) $U_{\text{back}} = -20\,\text{kV}$

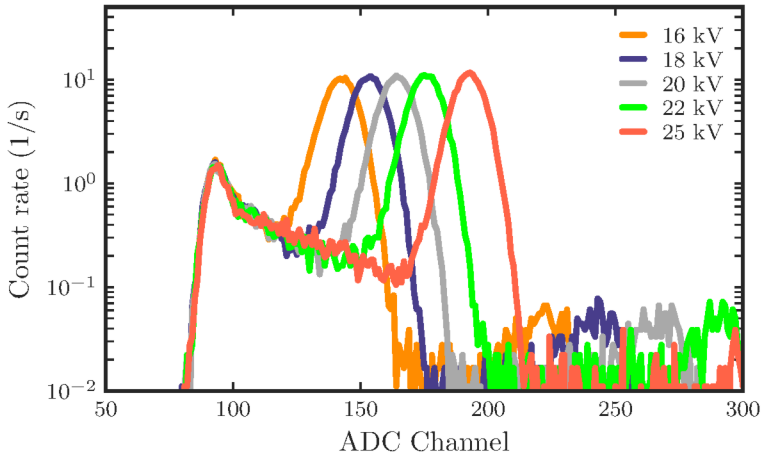

(b) Pulse-height spectrum at different electron energies

Figure A.1 – The count rate was measured with the reference diode at various x-positions of the coil at electron energies of 20 keV in (a). The mean count rate of the reference diode at $\alpha_D = -40.30°$ in the region between $x \in [45.4\,\text{mm}, 48.2\,\text{mm}]$ is (187.7 ± 2.4) cps. For $\alpha_D = 0.44°$ the mean count rate in $x \in [45.2\,\text{mm}, 49.6\,\text{mm}]$ is (194.2 ± 2.6) cps and for $\alpha_D = 33.74°$ the mean count rate in $x \in [46.4\,\text{mm}, 49.8\,\text{mm}]$ is (182.3 ± 3.4) cps. The count rate at larger angles diminishes because of an increased electron backscattering probability at larger incident angles. As expected, the peak-position of the electrons detected with the reference diode moves to higher ADC channels with larger electron energies, as shown in (b).

Diode D

The angle-selective detection rate of figure 6.21 (b) was fitted with a polynomial fit. The large error bars do not allow an unambiguous description, but the fit delivers a sufficient illustration of the trend of the angle-dependency.

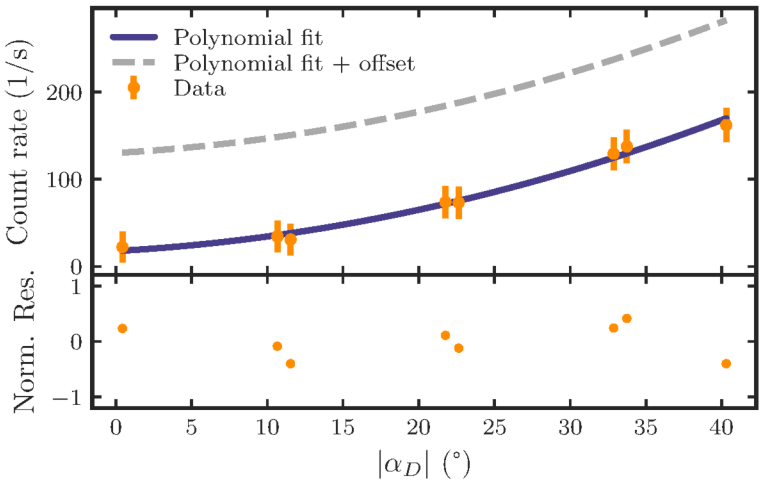

Figure A.2 – Polynomial fit to the angle-dependent detection efficiency of diode D. The absolute value of the detector angle α_D was used, thereby assuming that the angle-dependency is symmetric around $\alpha_D = 0°$. Due to the large error margin, the $\chi^2_r \approx 0.64/8 \approx 0.08$ is excessively small. The offset is added to account for the additional active detector area: The dashed grey line is the expected outcome when the photomask is removed.

Bibliography

[1] W. Pauli, "Offener Brief an die Gruppe der Radioaktiven bei der Gauvereins-Tagung zu Tübingen," typed Copy. [Online]. Available: http://cds.cern.ch/record/83282

[2] E. Fermi, "Versuch einer Theorie der β-Strahlen. i," *Zeitschrift für Physik*, vol. 88, no. 3-4, pp. 161–177, mar 1934.

[3] C. L. Cowan, F. Reines, F. B. Harrison, H. W. Kruse, and A. D. McGuire, "Detection of the Free Neutrino: a Confirmation," *Science*, vol. 124, no. 3212, pp. 103–104, 1956.

[4] "The Nobel Prize in Physics 1995." [Online]. Available: https://www.nobelprize.org/prizes/physics/1995/summary/

[5] M. Aker, A. Beglarian, J. Behrens, A. Berlev, U. Besserer *et al.*, "Direct neutrino-mass measurement with sub-electronvolt sensitivity," *Nature Physics*, vol. 18, no. 2, pp. 160–166, 2022.

[6] KATRIN collaboration, "KATRIN Design Report," Forschungszentrum Karlsruhe, Tech. Rep. 7090, 2005. [Online]. Available: https://publikationen.bibliothek.kit.edu/270060419

[7] Z. Maki, M. Nakagawa, and S. Sakata, "Remarks on the Unified Model of Elementary Particles," *Progress of Theoretical Physics*, vol. 28, no. 5, pp. 870–880, 1962.

[8] B. Pontecorvo, "Mesonium and Antimesonium," *Soviet Journal of Experimental and Theoretical Physics*, vol. 6, p. 429, 1958.

[9] B. T. Cleveland, T. Daily, J. Raymond Davis, J. R. Distel, K. Lande *et al.*, "Measurement of the Solar Electron Neutrino Flux with the Homestake Chlorine Detector," *The Astrophysical Journal*, vol. 496, no. 1, pp. 505–526, 1998.

[10] "The Nobel Prize in Physics 2002." [Online]. Available: https://www.nobelprize.org/prizes/physics/2002/summary/

[11] Y. Fukuda, T. Hayakawa, E. Ichihara, K. Inoue, K. Ishihara *et al.*, "Evidence for Oscillation of Atmospheric Neutrinos," *Physical Review Letters*, vol. 81, no. 8, pp. 1562–1567, 1998.

[12] Q. R. Ahmad, R. C. Allen, T. C. Andersen, J. D.Anglin, J. C. Barton *et al.*, "Direct Evidence for Neutrino Flavor Transformation from Neutral-Current Interactions in the Sudbury Neutrino Observatory," *Physical Review Letters*, vol. 89, no. 1, p. 011301, 2002.

[13] "The Nobel Prize in Physics 2015." [Online]. Available: https://www.nobelprize.org/prizes/physics/2015/summary/

[14] K. Abe, C. Bronner, Y. Haga, Y. Hayato, M. Ikeda *et al.*, "Atmospheric neutrino oscillation analysis with external constraints in Super-Kamiokande I-IV," *Physical Review D*, vol. 97, no. 7, p. 072001, 2018.

[15] M. G. Aartsen, M. Ackermann, J. Adams, J. A. Aguilar, M. Ahlers *et al.*, "Determining neutrino oscillation parameters from atmospheric muon neutrino disappearance with three years of IceCube DeepCore data," *Physical Review D*, vol. 91, no. 7, p. 072004, 2015.

[16] F. Kaether, W. Hampel, G. Heusser, J. Kiko, and T. Kirsten, "Reanalysis of the Gallex solar neutrino flux and source experiments," *Physics Letters B*, vol. 685, no. 1, pp. 47–54, 2010.

[17] B. Aharmim, S. N. Ahmed, A. E. Anthony, N. Barros, E. W. Beier *et al.*, "Combined analysis of all three phases of solar neutrino data from the Sudbury Neutrino Observatory," *Physical Review C*, vol. 88, no. 2, p. 025501, 2013.

[18] Y. Nakajima, "Recent results and future prospects from Super-Kamiokande." The XXIX International Conference on Neutrino Physics and Astrophysics, 2020, conference talk.

[19] G. Bellini, J. Benziger, D. Bick, S. Bonetti, G. Bonfini *et al.*, "Precision Measurement of the ^{7}Be Solar Neutrino Interaction Rate in Borexino," *Physical Review Letters*, vol. 107, no. 14, p. 141302, sep 2011.

[20] A. Himmel, "New Oscillation Results from the NOvA Experiment." The XXIX International Conference on Neutrino Physics and Astrophysics, 2020, conference talk.

[21] P. Dunne, "Latest Neutrino Oscillation Results from T2K." The XXIX International Conference on Neutrino Physics and Astrophysics, 2020, conference talk.

[22] D. Adey, F. An, A. Balantekin, H. Band, M. Bishai *et al.*, "Measurement of the Electron Antineutrino Oscillation with 1958 Days of Operation at Daya Bay," *Physical Review Letters*, vol. 121, no. 24, p. 241805, 2018.

[23] S.-H. Seo, "New results from RENO using 1500 days of data," *Journal of Physics: Conference Series*, vol. 1342, no. 1, p. 012045, 2020.

[24] *New Results from the Double Chooz Experiment.* The XXIX International Conference on Neutrino Physics and Astrophysics, 2020, conference talk.

[25] M. C. Gonzalez-Garcia, M. Maltoni, and T. Schwetz, "NuFIT: Three-Flavour Global Analyses of Neutrino Oscillation Experiments," *Universe*, vol. 7, no. 12, p. 459, 2021.

[26] A. de Gouvêa, K. Pitts, K. Scholberg, G. P. Zeller, J. Alonso *et al.*, "Neutrinos," 2013.

[27] S. Schael, R. Barate, R. Brunelière, D. Buskulic, I. De Bonis *et al.*, "Precision electroweak measurements on the Z resonance," *Physics Reports*, vol. 427, no. 5-6, pp. 257–454, 2006.

[28] R. L. Workman, V. D. Burkert, V. Crede, E. Klempt, U. Thoma *et al.*, "Review of Particle Physics," *Progress of Theoretical and Experimental Physics*, vol. 2022, no. 8, 2022.

[29] P. Vogel, L. Wen, and C. Zhang, "Neutrino oscillation studies with reactors," *Nature Communications*, vol. 6, no. 1, 2015.

[30] I. Esteban, M. C. Gonzalez-Garcia, A. Hernandez-Cabezudo, M. Maltoni, and T. Schwetz, "Global analysis of three-flavour neutrino oscillations: synergies and tensions in the determination of θ_{23}, δ_{CP}, and the mass ordering," *Journal of High Energy Physics*, vol. 2019, no. 1, 2019.

[31] E. W. Otten and C. Weinheimer, "Neutrino mass limit from tritium β decay," *Reports on Progress in Physics*, vol. 71, no. 8, p. 086201, 2008.

[32] T. Yanagida, "Proc. Workshop on Unified theory and the baryon number in the universe," vol. 95, 1979.

[33] N. Aghanim, Y. Akrami, M. Ashdown, J. Aumont, C. Baccigalupi *et al.*, "Planck 2018 results," *Astronomy & Astrophysics*, vol. 641, p. A6, 2020.

[34] S. Alam, M. Aubert, S. Avila, C. Balland, J. E. Bautista *et al.*, "Completed SDSS-IV extended Baryon Oscillation Spectroscopic Survey: Cosmological implications from two decades of spectroscopic surveys at the Apache Point Observatory," *Physical Review D*, vol. 103, no. 8, p. 083533, 2021.

[35] E. D. Valentino, A. Melchiorri, and J. Silk, "Cosmological constraints in extended parameter

space from the Planck 2018 Legacy release," *Journal of Cosmology and Astroparticle Physics*, vol. 2020, no. 01, pp. 013–013, 2020.

[36] R. Allison, P. Caucal, E. Calabrese, J. Dunkley, and T. Louis, "Towards a cosmological neutrino mass detection," *Physical Review D*, vol. 92, no. 12, p. 123535, 2015.

[37] G. Zatsepin, "Probability of determining the upper limit of the neutrino mass from the time of flight," *Soviet Journal of Experimental and Theoretical Physics Letters*, vol. 8, p. 205, 1968.

[38] K. S. Hirata, T. Kajita, M. Koshiba, M. Nakahata, Y. Oyama *et al.*, "Observation in the Kamiokande-II detector of the neutrino burst from supernova SN1987A," *Physical Review D*, vol. 38, no. 2, pp. 448–458, 1988.

[39] T. Haines, C. Bratton, D. Casper, A. Ciocio, R. Claus *et al.*, "Neutrinos from SN1987a in the IMB detector," *Nuclear Instruments and Methods in Physics Research Section A: Accelerators, Spectrometers, Detectors and Associated Equipment*, vol. 264, no. 1, pp. 28–31, 1988.

[40] T. J. Loredo and D. Q. Lamb, "Bayesian analysis of neutrinos observed from supernova SN 1987A," *Physical Review D*, vol. 65, no. 6, p. 063002, 2002.

[41] J. Schechter and J. W. F. Valle, "Neutrinoless double-β decay in $SU(2) \times U(1)$ theories," *Physical Review D*, vol. 25, no. 11, pp. 2951–2954, 1982.

[42] M. J. Dolinski, A. W. Poon, and W. Rodejohann, "Neutrinoless Double-Beta Decay: Status and Prospects," *Annual Review of Nuclear and Particle Science*, vol. 69, no. 1, pp. 219–251, 2019.

[43] M. Agostini, G. Araujo, A. Bakalyarov, M. Balata, I. Barabanov *et al.*, "Final Results of GERDA on the Search for Neutrinoless Double-β Decay," *Physical Review Letters*, vol. 125, no. 25, p. 252502, 2020.

[44] S. Abe, S. Asami, M. Eizuka, S. Futagi, A. Gando *et al.*, "Search for the majorana nature of neutrinos in the inverted mass ordering region with kamland-zen," *Physical Review Letters*, vol. 130, no. 5, p. 051801, 2023.

[45] C. Alduino, F. Alessandria, K. Alfonso, E. Andreotti, C. Arnaboldi *et al.*, "First Results from CUORE: A Search for Lepton Number Violation via $0\nu\beta\beta$ Decay of ^{130}Te," *Physical Review Letters*, vol. 120, no. 13, p. 132501, 2018.

[46] P. Filianin, C. Lyu, M. Door, K. Blaum, W. Huang *et al.*, "Direct Q-Value Determination of the β-Decay of ^{187}Re," *Physical Review Letters*, vol. 127, no. 7, p. 072502, 2021.

[47] M. Medina Restrepo and E. G. Myers, "Mass Difference of Tritium and Helium-3," *Physical Review Letters*, vol. 131, no. 24, p. 243002, 2023.

[48] C. Velte, F. Ahrens, A. Barth, K. Blaum, M. Braß *et al.*, "High-resolution and low-background ^{163}Ho spectrum: interpretation of the resonance tails," *The European Physical Journal C*, vol. 79, no. 12, 2019.

[49] M. Kleesiek, J. Behrens, G. Drexlin, K. Eitel, M. Erhard *et al.*, "β-decay spectrum, response function and statistical model for neutrino mass measurements with the KATRIN experiment," *The European Physical Journal C*, vol. 79, no. 3, 2019.

[50] K. Zuber, *Neutrino Physics*. CRC Press, 2020, ISBN: 978-1-315-19561-2.

[51] J. Bonn, B. Bornschein, L. Bornschein, L. Fickinger, B. Flatt *et al.*, "The Mainz neutrino mass experiment," *Nuclear Physics B - Proceedings Supplements*, vol. 91, no. 1-3, pp. 273–279, 2001.

[52] V. Lobashev, V. Aseev, A. Belesev, A. Berlev, E. Geraskin *et al.*, "Direct search for neutrino mass and anomaly in the tritium beta-spectrum: Status of "Troitsk neutrino mass" experiment," *Nuclear Physics B - Proceedings Supplements*, vol. 91, no. 1-3, pp. 280–286, 2001.

[53] P. J. Doe, J. Kofron, E. L. McBride, R. G. H. Robertson, L. J. Rosenberg *et al.*, "Project 8: Determining neutrino mass from tritium beta decay using a frequency-based method," 2013.

[54] M. Sisti, C. Arnaboldi, C. Brofferio, G. Ceruti, O. Cremonesi *et al.*, "New limits from the Milano neutrino mass experiment with thermal microcalorimeters," *Nuclear Instruments and Methods in Physics Research Section A: Accelerators, Spectrometers, Detectors and Associated Equipment*, vol. 520, no. 1-3, pp. 125–131, 2004.

[55] J. A. Formaggio, A. L. C. de Gouvêa, and R. H. Robertson, "Direct measurements of neutrino mass," *Physics Reports*, vol. 914, pp. 1–54, 2021.

[56] L. Gastaldo, K. Blaum, K. Chrysalidis, T. D. Goodacre, A. Domula *et al.*, "The electron capture in ^{163}Ho experiment – ECHo," *The European Physical Journal Special Topics*, vol. 226, no. 8, pp. 1623–1694, 2017.

[57] M. Borghesi, B. Alpert, M. Balata, D. Becker, D. Bennet *et al.*, "An updated overview of the HOLMES status," *Nuclear Instruments and Methods in Physics Research Section A: Accelerators, Spectrometers, Detectors and Associated Equipment*, vol. 1051, p. 168205, 2023.

[58] P.-O. Ranitzsch, C. Hassel, M. Wegner, D. Hengstler, S. Kempf *et al.*, "Characterization of the ^{163}Ho Electron Capture Spectrum: A Step Towards the Electron Neutrino Mass Determination," *Physical Review Letters*, vol. 119, no. 12, p. 122501, 2017.

[59] K. Assamagan, C. Brönnimann, M. Daum, H. Forrer, R. Frosch *et al.*, "Upper limit of the muon-neutrino mass and charged-pion mass from momentum analysis of a surface muon beam," *Physical Review D*, vol. 53, no. 11, pp. 6065–6077, jun 1996.

[60] R. Barate *et al.*, "An upper limit on the τ neutrino mass from three- and five-prong tau decays," *The European Physical Journal C*, vol. 2, no. 3, pp. 395–406, apr 1998.

[61] M. Aker, M. Balzer, D. Batzler, A. Beglarian, J. Behrens *et al.*, "KATRIN: status and prospects for the neutrino mass and beyond," *Journal of Physics G: Nuclear and Particle Physics*, vol. 49, no. 10, p. 100501, 2022.

[62] N. R.-M. Trost, "Modeling and measurement of Rydberg-State mediated Background at the KATRIN Main Spectrometer," Ph.D. dissertation, Karlsruhe Institute of Technology, 2018.

[63] F. Fränkle, A. Schaller, K. Blaum, L. Bornschein, G. Drexlin *et al.*, "KATRIN background due to surface radioimpurities," *Astroparticle Physics*, vol. 138, p. 102686, 2022.

[64] D. F. Hinz, "Background systematics and extensions to the KATRIN background model," Ph.D. dissertation, Karlsruhe Institute of Technology, 2022.

[65] M. Carminati, M. Gugiatti, D. Siegmann, K. Urban, P. King *et al.*, "The TRISTAN 166-pixel detector: Preliminary results with a planar setup," *Nuclear Instruments and Methods in Physics Research Section A: Accelerators, Spectrometers, Detectors and Associated Equipment*, vol. 1049, p. 168046, 2023.

[66] L. Kuckert, "The Windowless Gaseous Tritium Source of the KATRIN Experiment - Characterisation of Gas Dynamical and Plasma Properties," 2016.

[67] M. Aker, K. Altenmüller, J. Amsbaugh, M. Arenz, M. Babutzka *et al.*, "The design, construction, and commissioning of the KATRIN experiment," *Journal of Instrumentation*, vol. 16, no. 08, p. T08015, 2021.

[68] J. Behrens, P. C.-O. Ranitzsch, M. Beck, A. Beglarian, M. Erhard *et al.*, "A pulsed, mono-energetic and angular-selective UV photo-electron source for the commissioning of the KATRIN experiment," *The European Physical Journal C*, vol. 77, no. 6, 2017.

[69] S. Schneidewind, "Improvement of the neutrino mass sensitivity and background reduction of the KATRIN experiment," Ph.D. dissertation in preparation, University of Münster, to be published 2024.

[70] R. Sack, "Measurement of the energy loss of 18.6 keV electrons on deuterium gas and determination of the tritium Q-value at the KATRIN experiment," Ph.D. dissertation, University of Münster, 2020.

[71] M. Sturm, M. Schlösser, R. J. Lewis, B. Bornschein, G. Drexlin *et al.*, "Monitoring of all hydrogen isotopologues at tritium laboratory Karlsruhe using Raman spectroscopy," *Laser Physics*, vol. 20, no. 2, pp. 493–507, 2009.

[72] J. Sentkerestiová, O. Dragoun, O. Lebeda, M. Ryšavý, M. Sturm *et al.*, "Gaseous ^{83m}Kr generator for KATRIN," *Journal of Instrumentation*, vol. 13, no. 04, pp. P04 018–P04 018, 2018.

[73] C. Rodenbeck, "A method for determining the transition energies of ^{83m}Kr at the KATRIN experiment," *The European Physical Journal C*, vol. 82, no. 8, 2022.

[74] E. McCutchan, "Nuclear Data Sheets for A = 83," *Nuclear Data Sheets*, vol. 125, pp. 201–394, 2015.

[75] F. Friedel, C. Röttele, L. Schimpf, J. Wolf, G. Drexlin *et al.*, "Time-dependent simulation of the flow reduction of D2 and T2 in the KATRIN experiment," *Vacuum*, vol. 159, pp. 161–172, 2019.

[76] C. Röttele, "Tritium suppression factor of the KATRIN transport section," Ph.D. dissertation, Karlsruhe Institute of Technology, 2019.

[77] S. A. Nepijko, I. Rabin, and W. Schulze, "Morphology of Frozen Rare-Gas Layers," *ChemPhysChem*, vol. 6, no. 2, pp. 235–238, 2005.

[78] K. Jousten, *Handbook of Vacuum Technology.* Wiley-VCH, ISBN: 978-3-527-40723-1.

[79] B. Bieringer, "Improving the systematic uncertainties of KATRIN," Ph.D. dissertation in preparation, University of Münster, to be published 2025.

[80] M. Böttcher, "Measurement of nuclear transition energies of Kr-83m for tritium Q value determination at KATRIN," Ph.D. dissertation in preparation, University of Münster, to be published 2025.

[81] A. Lokhov, B. Bieringer, G. Drexlin, S. Dyba, K. Gauda *et al.*, "Background reduction at the KATRIN experiment by the shifted analysing plane configuration," *The European Physical Journal C*, vol. 82, no. 3, 2022.

[82] G. Beamson, H. Q. Porter, and D. W. Turner, "The collimating and magnifying properties of a superconducting field photoelectron spectrometer," *Journal of Physics E: Scientific Instruments*, vol. 13, no. 1, pp. 64–66, jan 1980.

[83] V. Lobashev and P. Spivak, "A method for measuring the electron antineutrino rest mass," *Nuclear Instruments and Methods in Physics Research Section A: Accelerators, Spectrometers, Detectors and Associated Equipment*, vol. 240, no. 2, pp. 305–310, 1985.

[84] M. Aker, K. Altenmüller, M. Arenz, M. Babutzka, J. Barrett *et al.*, "Improved Upper Limit on the Neutrino Mass from a Direct Kinematic Method by KATRIN," *Physical Review Letters*, vol. 123, no. 22, p. 221802, 2019.

[85] M. Aker, K. Altenmüller, A. Beglarian, J. Behrens, A. Berlev *et al.*, "Suppression of Penning discharges between the KATRIN spectrometers," *The European Physical Journal C*, vol. 80, no. 9, 2020.

[86] T. Thümmler, R. Marx, and C. Weinheimer, "Precision high voltage divider for the KATRIN experiment," *New Journal of Physics*, vol. 11, no. 10, p. 103007, 2009.

[87] S. Bauer, R. Berendes, F. Hochschulz, H. W. Ortjohann, S. Rosendahl *et al.*, "Next generation KATRIN high precision voltage divider for voltages up to 65kV," *Journal of Instrumentation*, vol. 8, no. 10, pp. P10 026–P10 026, 2013.

[88] K. Valerius, "The wire electrode system for the KATRIN main spectrometer," *Progress in Particle and Nuclear Physics*, vol. 64, no. 2, pp. 291–293, 2010.

[89] J. Amsbaugh *et al.*, "Focal-plane detector system for the KATRIN experiment," *Nuclear Instruments and Methods in Physics Research Section A: Accelerators, Spectrometers, Detectors and Associated Equipment*, vol. 778, pp. 40–60, 2015.

[90] B. L. Wall, "Karlsruhe Tritium Experiment: Detector System Commissioning and In-Situ PIN-Diode Array Dead-Layer Measurement," Ph.D. dissertation, University of Washington, 2013.

[91] B. A. VanDevender, L. I. Bodine, A. W. Myers, J. F. Amsbaugh, M. A. Howe *et al.*, "Performance of a TiN-coated monolithic silicon pin-diode array under mechanical stress," *Nuclear Instruments and Methods in Physics Research Section A: Accelerators, Spectrometers, Detectors and Associated Equipment*, vol. 673, pp. 46–50, 2012.

[92] M. Howe, G. Cox, P. Harvey, F. McGirt, K. Rielage *et al.*, "Sudbury neutrino observatory neutral current detector acquisition software overview," *IEEE Transactions on Nuclear Science*, vol. 51, no. 3, pp. 878–883, 2004.

[93] M. Aker, K. Altenmüller, A. Beglarian, J. Behrens, A. Berlev *et al.*, "Analysis methods for the first KATRIN neutrino-mass measurement," *Physical Review D*, vol. 104, no. 1, p. 012005, 2021.

[94] C. Karl, P. Eller, and S. Mertens, "Fast and precise model calculation for KATRIN using a neural network," *The European Physical Journal C*, vol. 82, no. 5, 2022.

[95] A. V. Lokhov and F. V. Tkachov, "Confidence intervals with a priori parameter bounds," *Physics of Particles and Nuclei*, vol. 46, no. 3, pp. 347–365, 2015.

[96] K. Altenmüller, M. Arenz, W.-J. Baek, M. Beck, A. Beglarian *et al.*, "Gamma-induced background in the KATRIN main spectrometer," *The European Physical Journal C*, vol. 79, no. 9, 2019.

[97] ——, "Muon-induced background in the KATRIN main spectrometer," *Astroparticle Physics*, vol. 108, pp. 40–49, 2019.

[98] F. Fränkle, L. Bornschein, G. Drexlin, F. Glück, S. Görhardt *et al.*, "Radon induced background processes in the KATRIN pre-spectrometer," *Astroparticle Physics*, vol. 35, no. 3, pp. 128–134, 2011.

[99] S. Mertens, G. Drexlin, F. Fränkle, D. Furse, F. Glück *et al.*, "Background due to stored electrons following nuclear decays in the KATRIN spectrometers and its impact on the neutrino mass sensitivity," *Astroparticle Physics*, vol. 41, pp. 52–62, 2013.

[100] G. Drexlin, F. Harms, A. Jansen, M. Krause, F. Müller *et al.*, "Calculations and TPMC simulations of the reduction of radioactive decays of a noble gas by cryo-panels," *Vacuum*, vol. 138, pp. 165–172, 2017.

[101] S. Görhardt, J. Bonn, L. Bornschein, G. Drexlin, F. Fränkle *et al.*, "Impact of a cryogenic baffle system on the suppression of radon-induced background in the KATRIN Pre-Spectrometer," *Journal of Instrumentation*, vol. 13, no. 10, pp. T10 004–T10 004, 2018.

[102] S. Dyba, "Background reduction by the inner wire electrode and set-up of the condensed krypton source at the neutrino mass experiment KATRIN," Ph.D. dissertation, University of Münster, 2018.

[103] A. Schaller, "Characterization and mitigation of the background in KATRIN," Ph.D. dissertation, Technical University of Munich, Max Planck Institute for Physics Munich, 2020.

[104] "Radioactive decay chains of uranium," 2015, Accessed: 13th Dec 2023. [Online]. Available: https://commons.wikimedia.org/wiki/File:Decay_chain(4n+2,_Uranium_series).svg

[105] J. F. Ziegler, M. Ziegler, and J. Biersack, "SRIM – the stopping and range of ions in matter (2010)," *Nuclear Instruments and Methods in Physics Research Section B: Beam Interactions with Materials and Atoms*, vol. 268, no. 11-12, pp. 1818–1823, 2010.

[106] K. Gauda, S. Schneidewind, G. Drexlin, A. Fulst, V. Hannen *et al.*, "An active transverse energy filter to differentiate low energy particles with large pitch angles in a strong magnetic field," *Eur. Phys. J. C*, vol. 82, no. 10, 2022.

[107] A. Fulst, "A Novel Quasi-Differential Method for MAC-E Filters and Determination and Control of the Electric Potentials of the KATRIN Experiment with a Stabilized Condensed Krypton Source and a UV Illumination System," Ph.D. dissertation, University of Münster, 2020.

[108] N. M. N. Steinbrink, "Beyond-Standard Model Neutrino Physics Sensitivity with KATRIN," Ph.D. dissertation, University of Münster, 2017.

[109] E. L. Martin, "Electron detection systems for KATRIN detector and spectrometer section," Ph.D. dissertation, University of Washington, 2017.

[110] T. Wolz, C. Malbrunot, M. Vieille-Grosjean, and D. Comparat, "Stimulated decay and formation of antihydrogen atoms," *Physical Review A*, vol. 101, no. 4, p. 043412, 2020.

[111] M. Vieille-Grosjean, E. Dimova, Z. Mazzotta, D. Comparat, T. Wolz *et al.*, "Induced THz transitions in Rydberg caesium atoms for application in antihydrogen experiments," *The European Physical Journal D*, vol. 75, no. 1, 2021.

[112] R. G. H. Robertson, "Transverse Energy Filter," 2019, Center for Experimental Nuclear Physics and Astrophysics and Department of Physics, University of Washington, Seattle.

[113] K. Gauda, "Investigation of Transverse Energy Filter Configurations," 2020, 39th KATRIN Collaboration Meeting.

[114] D. Furse, S. Groh, N. Trost, M. Babutzka, J. P. Barrett *et al.*, "Kassiopeia: a modern, extensible C++ particle tracking package," *New Journal of Physics*, vol. 19, no. 5, p. 053012, May 2017.

[115] D. Hinz, "Ionisation mechanisms of ^{206}Pb induced Rydberg atoms," Master's thesis, Karlsruhe Institute of Technology, 2018.

[116] R. H. Garstang, "Energy Levels and Transition Probabilities in P2 and P4 Configurations," *Monthly Notices of the Royal Astronomical Society*, vol. 111, no. 1, pp. 115–124, 1951.

[117] A. Omholt and L. Harang, "Measurements of the mean lifetime of the metastable 1S-state of the oxygen atom in the upper atmosphere during auroral displays," *Journal of Atmospheric and Terrestrial Physics*, vol. 7, pp. 247–253, jul 1955.

[118] W. B. Colson, J. McPherson, and F. T. King, "High-gain imaging electron multiplier," *Review of Scientific Instruments*, vol. 44, no. 12, pp. 1694–1696, 1973.

[119] "Microchannel plates from Photonis reduce background noise up to 100x," Accessed 09th October 2023. [Online]. Available: https://www.laserfocusworld.com/detectors-imaging/article/16565294/microchannel-plates-from-photonis-reduce-background-noise-up-to-100x

[120] G. Heusser, "Low-Radioactivity Background Techniques," *Annual Review of Nuclear and Particle Science*, vol. 45, no. 1, pp. 543–590, 1995.

[121] C. Gönner, "Investigations on a custom-made silicon-based microchannel plate as active transverse energy filter for the KATRIN experiment," Bachelor's Thesis, University of Münster, 2022.

[122] A. U. Mane and J. W. Elam, "Atomic Layer Deposition of W:Al2O_3 Nanocomposite Films with Tunable Resistivity," *Chemical Vapor Deposition*, vol. 19, no. 4-6, pp. 186–193, 2013.

[123] C. P. Beetz, R. Boerstler, J. Steinbeck, B. Lemieux, and D. R. Winn, "Silicon-micromachined microchannel plates," *Nuclear Instruments and Methods in Physics Research Section A: Accelerators, Spectrometers, Detectors and Associated Equipment*, vol. 442, no. 1-3, pp. 443–451, 2000.

[124] A. U. Mane, Q. Peng, J. W. Elam, D. C. Bennis, C. A. Craven *et al.*, "An Atomic Layer Deposition Method to Fabricate Economical and Robust Large Area Microchannel Plates for Photodetectors," *Physics Procedia*, vol. 37, pp. 722–732, 2012.

[125] W. Cao, B. Zhu, X. Bai, P. Xu, B. Wang *et al.*, "High-Sensitivity and Long-Life Microchannel Plate Processed by Atomic Layer Deposition," *Nanoscale Research Letters*, vol. 14, no. 1, 2019.

[126] R. W. J. Salomon, "Development of a Setup to test Time-Of-Flight Methods for the KATRIN Experiment," Bachelor's Thesis, University of Münster, 2019.

[127] B. Flatt, "Designstudien für das KATRIN-Experiment," Master's thesis, Johannes-Gutenberg-Universität Mainz, 2001.

[128] M. Aker, A. Beglarian, J. Behrens, A. Berlev, U. Besserer *et al.*, "Precision measurement of the electron energy-loss function in tritium and deuterium gas for the KATRIN experiment," *The European Physical Journal C*, vol. 81, no. 7, 2021.

[129] J. Behrens, "Design and commissioning of a monoenergetic photoelectron source and active background reduction by magnetic pulse at the KATRIN experiment," Ph.D. dissertation, University of Münster, 2016.

[130] *tectra MCP-050-D-L-A-F*, tectra GmbH, Reuterweg 51-53, Frankfurt/M., Germany, Manual.

[131] W. R. Leo, *The NIM Standard*. Springer Berlin Heidelberg, 1994, pp. 257–261.

[132] P. Oelpmann, "Angular selective electron detection using microchannel plates for a possible background reduction at the KATRIN experiment," Master's thesis, University of Münster, 2021.

[133] T. König, "Simulations and measurements of angular selectiveelectron transmission and detection for the KATRIN experiment," Bachelor's Thesis, University of Münster, 2021.

[134] R. W. J. Salomon, "Simulations on an angular-selective photoelectron source and on an active transverse energy filter for the KATRIN experiment," Master's thesis, University of Münster, 2022.

[135] K. Blümer, "New test setup for testing active transverse energy filters in the KATRIN beamline," Bachelor's thesis, University of Münster, 2023.

[136] L. Pöllitsch, "Charakterisierung des neuen Teststands für aktive Transversalenergiefilter für das KATRIN-Experiment," Bachelor's Thesis, University of Münster, 2022.

[137] J. N. Lauer, "Application Cases of Transverse Energy Filters in the KATRIN Experiment," Master's thesis, Karlsruhe Institute of Technology, 2022.

[138] E. Morenzoni, K. Oba, E. Pedroni, and D. Taqqu, "Performance of microchannel plates in high magnetic fields," *Nuclear Instruments and Methods in Physics Research Section A: Accelerators, Spectrometers, Detectors and Associated Equipment*, vol. 263, no. 2–3, pp. 397–400, 1988.

[139] R. J. Nikolic, A. M. Conway, C. E. Reinhardt, R. T. Graff, T. F. Wang *et al.*, "Fabrication of pillar-structured thermal neutron detectors," in *2007 IEEE Nuclear Science Symposium Conference Record*. IEEE, 2007.

[140] S. Schneidewind, K. Gauda, K. Blümer, C. Gönner, V. Hannen *et al.*, "Background reduction at the KATRIN experiment with an active transverse energy filter (aTEF)," in *Verhandlungen der DPG*. DPG Frühjahrstagung Dresden, 2023.

[141] *SU-8 3000 Technical Data Sheet*, Ver. 1 ed., Kayaku Advanced Materials, 200 Flanders Road, Westborough, MA 01581 USA, 2020, Data Sheet.

[142] H. Gehring, M. Blaicher, W. Hartmann, and W. H. P. Pernice, "Python based open source design framework for integrated nanophotonic and superconducting circuitry with 2D-3D-hybrid integration," *OSA Continuum*, vol. 2, no. 11, p. 3091, 2019.

[143] *Si PIN photodiodes S3590 series*, HAMAMATSU PHOTONICS K.K., Solid State Division, 1126-1 Ichino-cho, Higashi-ku, Hamamatsu City, 435-8558 Japan, 2023, Data Sheet.

[144] S. Wein, "Charakterisierung der Detektionseigenschaften von mikrostrukturierten Si-PIN-Dioden fur das KATRIN-Experiment," Bachelor's Thesis, University of Münster, 2023.

[145] D. L. Flamm, "Mechanisms of silicon etching in fluorine- and chlorine-containing plasmas," *Pure and Applied Chemistry*, vol. 62, no. 9, pp. 1709–1720, 1990.

[146] M. D. Henry, C. Welch, and A. Scherer, "Techniques of cryogenic reactive ion etching in silicon for fabrication of sensors," *Journal of Vacuum Science and Technology A. Vacuum, Surfaces, and Films*, vol. 27, no. 5, pp. 1211–1216, 2009.

[147] J. A. Bondur, "Dry process technology (reactive ion etching)," *Journal of Vacuum Science and Technology*, vol. 13, no. 5, pp. 1023–1029, 1976.

[148] F. Laermer and A. Urban, "Milestones in deep reactive ion etching," in *The 13th International Conference on Solid-State Sensors, Actuators and Microsystems, 2005. Digest of Technical Papers. TRANSDUCERS '05.* IEEE, 2005.

[149] A. S. F Laermer, DE Patent 4 241 045C1, 1994.

[150] U. Sökmen, A. Stranz, S. Fündling, H.-H. Wehmann, V. Bandalo *et al.*, "Capabilities of ICP-RIE cryogenic dry etching of silicon: review of exemplary microstructures," *Journal of Micromechanics and Microengineering*, vol. 19, no. 10, p. 105005, 2009.

[151] T. D. Bestwick, G. S. Oehrlein, and D. Angell, "Cryogenic reactive ion etching of silicon in SF_6," *Applied Physics Letters*, vol. 57, no. 5, pp. 431–433, 1990.

[152] Accessed: 05th Jun 2023. [Online]. Available: https://plasma.oxinst.com/products/icpcvd/plasmapro-100-icpcvd

[153] M. de Boer, J. Gardeniers, H. Jansen, E. Smulders, M.-J. Gilde *et al.*, "Guidelines for etching silicon MEMS structures using fluorine high-density plasmas at cryogenic temperatures," *Journal of Microelectromechanical Systems*, vol. 11, no. 4, pp. 385–401, 2002.

[154] Z. Fan, D. Cui, Z. Zhang, Z. Zhao, H. Chen *et al.*, "Recent progress of black silicon: From fabrications to applications," *Nanomaterials*, vol. 11, no. 1, p. 41, 2020.

[155] S. M. Sze, *Semiconductor devices, physics and technology.* Wiley, 2011, ISBN: 978-0470-53794-7.

[156] H. Kolanoski and N. Wermes, *Teilchendetektoren.* Springer Berlin Heidelberg, 2016, ISBN: 978-3-662-45349-0.

[157] S. Seltzer, "Stopping-Powers and Range Tables for Electrons, Protons, and Helium Ions, NIST Standard Reference Database 124," 1993.

[158] A. Einstein, "Elementare Theorie der Brownschen Bewegung," *Zeitschrift für Elektrochemie und angewandte physikalische Chemie*, vol. 14, no. 17, pp. 235–239, 1908.

[159] G. F. Knoll, *Radiation detection and measurement.* Wiley, 2000, ISBN: 0-471-07338-5.

[160] C. Weinheimer, M. Schrader, J. Bonn, T. Loeken, and H. Backe, "Measurement of energy resolution and dead layer thickness of LN2-cooled PIN photodiodes," *Nuclear Instruments and Methods in Physics Research Section A: Accelerators, Spectrometers, Detectors and Associated Equipment*, vol. 311, no. 1-2, pp. 273–279, 1992.

[161] M. Schrader, "Rauschoptimierung eines ladungsempfindlichen Vorverstärkers für Halbleiterdetektoren und digitale Filterung des analogen Ausgangssignals," Diploma Thesis, Johannes Gutenberg Universität Mainz, 1990.

[162] R. Jöhren, "Spectroscopy of the hyperfine transition in lithium-like bismuth at the esr at gsi and an apd-based single-photon detector for laser spectroscopy on highly charged ions," Ph.D. dissertation, University of Münster, 2013.

[163] B. Bieringer, ""MCA Recorder", a platform independent, open graphical MCA controller software," in *Verhandlungen der DPG*, 2019. [Online]. Available: https://www.dpg-verhandlungen.de/year/2019/conference/muenchen/part/hk/session/54/contribution/71

[164] B. Hillen, "Untersuchung von Methoden zur Unterdrückung des Spektrometeruntergrunds beim KATRIN Experiment," Ph.D. dissertation, University of Münster, 2011.

[165] *Präzisions NIM Hochspannungsquelle der Baureihe NHQ HIGH PRECISON RS232 - Interface*, 3rd ed., iseg Spezialelektronik GmbH, Bautzner Landstr. 23, 01454 Radeberg/Rossendorf, Germany, 2001, Manual.

[166] M. Martini and T. McMath, "Trapping and detrapping effects in lithium-drifted germanium and silicon detectors," *Nuclear Instruments and Methods*, vol. 79, no. 2, pp. 259–276, mar 1970.

[167] W. H. Bell, L. Casagrande, C. D. Via, V. Granata, and V. G. Palmieri, "Temperature dependence of the charge collection efficiency in heavily irradiated silicon detectors," *Nuclear Instruments and Methods in Physics Research Section A: Accelerators, Spectrometers, Detectors and Associated Equipment*, vol. 435, no. 1–2, pp. 187–193, 1999.

[168] V. N. Aseev, A. I. Belesev, A. I. Berlev, E. V. Geraskin, A. A. Golubev *et al.*, "Upper limit on the electron antineutrino mass from the Troitsk experiment," *Physical Review D*, vol. 84, no. 11, p. 112003, 2011.

[169] S. Mertens, A. Alborini, K. Altenmüller, T. Bode, L. Bombelli *et al.*, "A novel detector system for KATRIN to search for keV-scale sterile neutrinos," *Journal of Physics G: Nuclear and Particle Physics*, vol. 46, no. 6, p. 065203, 2019.

Danksagung

Ich möchte mich bei Prof. Christian Weinheimer für das Ermöglichen der Promotion in seiner Gruppe bedanken. Die Motivation und der Ansporn, die vielen Herausforderungen zu bestehen, waren sehr wertvoll. Ebenso wertvoll waren die gute Betreuung und das rücksichtsvolle Miteinander. Prof. Christian Klein-Bösing möchte ich für die Übernahme der Zweitbetreuung, für die hilfreichen Ratschläge und für ein offenes Ohr danken.

Der gesamten KATRIN-Kollaboration danke ich für die schöne und lehrreiche Zeit und das Einberaumen eines so großen Stellenwertes "neuer Technologien" wie des aTEF-Projekts.

Prof. Wolfram Pernice danke ich für die Unterstützung bei der Umsetzung des aTEF-Projekts. Aus seiner Gruppe möchte ich besonders Maik Stappers erwähnen, der dem aTEF-Team die ersten Schritte zur Nanofabrikation im Reinraum des Münster Nanofabrication Facility (MNF) gezeigt hat. Das MNF hat dadurch das aTEF-Projekt und die Infrastruktur für die Herstellung der Detektor-Prototypen direkt vor Ort erst ermöglicht. Mein Dank gilt den Mitarbeiter*innen, die mir und dem gesamten aTEF-Team die Bedienung diverser Gerätschaften ermöglichten, ohne die das Projekt so nicht möglich gewesen wäre. Für einen Kern- und Teilchenphysiker war das eine herausfordernde, aber auch sehr spannende Aufgabe.

Vielen Dank an Uta Mayer und Michaela Erdmann für die vielfältige administrative Unterstützung und das tolle Miteinander. Mit den Werkstätten des IKP – der Dank gilt hier stellvertretend den Leitern Roland Berendes und Georg Bourichter – war die Umsetzung vieler toller Apparaturen möglich. Aber auch abseits der schnellen Hilfe war das freundliche Miteinander immer toll. Besonders möchte ich Hans-Werner Ortjohann danken, der für jede Anforderung die passende Apparatur plante und aufbaute und, abseits davon, auch für Hilfseinsätze immer bereit ist. Die Zusammenarbeit war nicht nur lehrreich, sondern durch die wertschätzende Art auch sehr angenehm. Auch danke ich Christian Huhmann und Daniel Bonaventura, die mir und dem ganzen aTEF-Team jederzeit die benötigte Unterstützung zukommen ließen.

Der gesamten Arbeitsgruppe möchte ich für eine schöne Zeit, gegenseitige Unterstützung, die tolle Arbeitsatmosphäre und anregende Kaffeepausen danken. Besonderer Dank geht an Sonja Schneidewind – für bewundernswerten Einsatz, an vielen anderen Stellen wie auch bei unserem Projekt. Ohne den Austausch und die Experimente und Fehlversuche in Labor und Reinraum wäre das nicht möglich gewesen. Vielen Dank auch fürs Korrekturlesen! Ein weiterer besonderer Dank gilt Volker Hannen für die vielfältige Betreuung und Unterstützung und das tolle Miteinander auch abseits von Arbeitsthemen. Für die

gute Zusammenarbeit, das tolle Miteinander und die Hilfe möchte ich Benedikt Bieringer, Richard Salomon, Christian Gönner, Kyrill Blümer, Sebastian Wein, Lukas Pöllitsch sowie den ehemaligen Mitgliedern Alexey Lokhov, Alexander Fulst, Stephan Dyba, Tim König und Patrick Oelpmann großen Dank aussprechen. Lutz, Johanna, Henning, Simon-Nis, Ken, Matthias, David, Daniel, Christian, Andria, Justus und Philipp danke ich herzlich für die schöne, lehrreiche und aufregende Zeit während der gesamten Promotion!

Ich danke Niklas (seine Voraussage scheint sich zu bewahrheiten), Ayleen, Juli und Roger dafür, dass ich immer auf sie zählen kann. Die anstrengenden Zeiten fielen mir mit ihnen viel leichter, die schönen Zeiten waren umso schöner! Meinen Eltern Anke und Rainer möchte ich für die großartige Unterstützung bei meinem Studium und der Promotion und für die stete Bestärkung bei all meinen Vorhaben ganz herzlich danken.

Ruth danke ich für die schönen Momente abseits der Promotion, aber auch den steten Glauben in mich und die Kraft, die sie mir gibt. Für alles, für jetzt und für immer.